Errata

Study of phase transitions in atmospheric aerosols: freezing and efflorescence of complex aqueous mixtures

On p. 11, in Eq. (2.1) and in lines 25, 26, 29 and 30 ΔG_i should be replaced by ΔG.

On p. 11, line 21 should be read as: where v_{ice} is the volume of a H_2O molecule in ice and k is the Boltzmann constant.

On p. 11, line 26 should be read as: If $S(T) > 1$, ΔG has both a negative contribution from the volume-dependent term and a positive contribution from the surface-dependent term.

On p. 12, the correct version of figure 4 is:

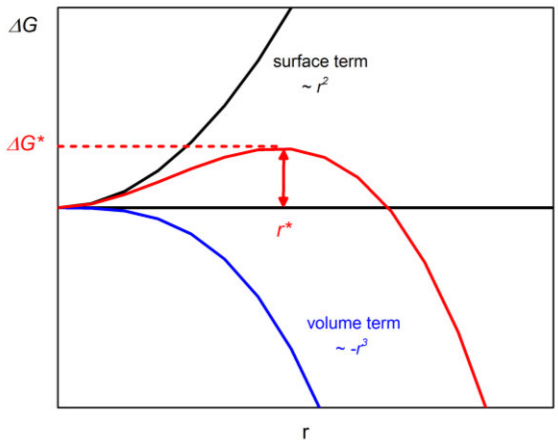

Figure 4: Free energy of the ice nucleus formation depending on the ice nucleus radius.

On p. 12, the paragraph from line 3 to line 6 should be read as:

The maximum of the free energy ΔG^* corresponds to a critical cluster size r^* and can be calculated by setting the first derivative with respect to the radius to zero:

$$r^* = \frac{2v_{ice}\sigma_{sl}}{kTln(S(T))} \qquad (2.3)$$

The free energy of the ice nucleus formation can be written as:

$$\Delta G^*(T) = \frac{16\pi}{3}\frac{{v_{ice}}^2{\sigma_{sl}}^3}{[kTln(S(T))]^2} \qquad (2.4)$$

On p. 12, line 15 should be read as follows: where n_w is defined as the volume number density of water molecules in liquid water. In Ickes et al.[1], the value of n_w is reported to be in the range from $3.1 \cdot 10^{28} m^{-3}$ to $3.35 \cdot 10^{28} m^{-3}$.

On p. 14, in Eq. (2.11) and in the lines 8 and 15 θ_{Nl} and θ_{sn} should be replaced by θ.

On p. 15, in line 2, θ_{sl} should be replaced by σ_{sl} and in Eq. (2.12) θ_{sn} should be changed to θ.

On p. 15, the Eqs. (2.14) and (2.15) should be:

$$\Delta G^*(T)f(\theta) = \frac{16\pi}{3}\frac{{\nu_{ice}}^2{\sigma_{sl}}^3}{[kTln(S(T))]^2}f(\theta) \qquad (2.\ 14)$$

$$J_{het}(T,\theta) = n_{w,het}\left(\frac{kT}{h}\right)exp\left(\frac{-\Delta F_{diff}(T)}{kT}\right)exp\left(\frac{-\Delta G^*(T)f(\theta)}{kT}\right) \qquad (2.\ 15)$$

where $n_{w,het}$ is defined as the number density of water molecules at the ice nucleus/water interface. Ickes et al.[1] reported $n_{w,het}$ in the range from $5.85 \cdot 10^{18}m^{-2}$ to $1 \cdot 10^{19}m^{-2}$.

On p. 16, the correct version of figure 7 is:

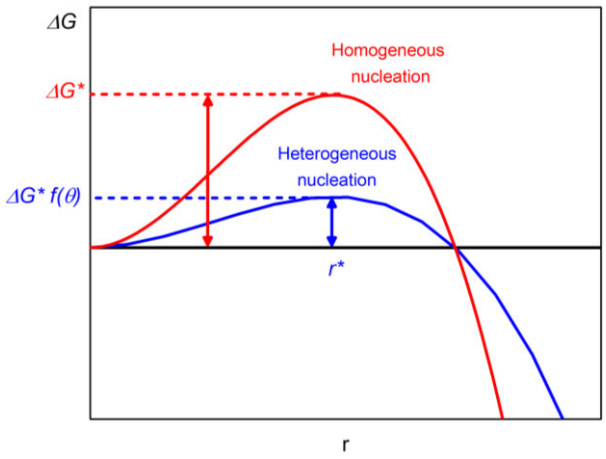

Figure 7: Free energy of ice nucleus formation for homogeneous and heterogeneous ice nucleation. The free energy barrier of heterogeneous ice nucleation is reduced compared to the case of homogeneous ice nucleation.

On p. 23, in line 22 “µm” must be replaced by “nm” and in Eq. (2.26) the minus sign must be omitted.

On p. 24, in Eq. (2.28) the minus sign must be omitted, ΔF_{cr} should be changed to $\Delta F_{cr,eff}$ and in line 12 (2.28) must be replaced by (2.29).

On p. 25, line 2 should be read as: ν_{s0} and ν_{c0} are the molar volumes of salt in a solution and a solid and ρ_{s0} and ρ_{c0} are the corresponding specific densities of the salt in a solution and a crystal.

On p. 26, in Eq. (2.35) the minus sign must be omitted and ΔF_{cr} should be changed to $\Delta F_{cr,eff}\ f(m_{cs},x)$.

On p. 27, in Eq. (2.36) $\Delta F_{cr,eff}$ in the exponent should be multiplied by $f(m_{cs},x)$.

On p. 32, Eq. (3.29) should be changed to:

$$\alpha(Q_i) = \alpha_0 + \left(\frac{\partial\alpha}{\partial Q_i}\right)_0 Q_i + \cdots \qquad (3.\ 29)$$

On p. 33, the correct versions of Eqs. (3.31) and (3.33) should have the form:

$$\mu = \left[\alpha_0 + \left(\frac{\partial \alpha}{\partial Q_i}\right)_0 Q_i^0 \cos(2\pi\nu t)\right] E_0 \cos(2\pi\nu_0 t) \tag{3. 31}$$

$$\mu = \underbrace{\alpha_0 E_0 cos(2\pi\nu_0 t)}_{Rayleigh} + \underbrace{\frac{1}{2}\left(\frac{\partial \alpha}{\partial Q_i}\right)_0 E_0 Q_i^0 \, cos[2\pi t(\nu_0 - \nu)]}_{Stokes}$$

$$+ \underbrace{\frac{1}{2}\left(\frac{\partial \alpha}{\partial Q_i}\right)_0 E_0 Q_i^0 \, cos[2\pi t(\nu_0 + \nu)]}_{Anti-Stokes} \tag{3. 33}$$

On p. 33, the paragraph from line 13 to line 17 should be read as:

The intensity I of light radiated by a dipole oscillating at the frequency ν_0 can be written as:

$$I = \frac{(2\pi\nu_0)^4}{3c^3} |\mu|^2 \tag{3. 35}$$

This means that the total scattered intensity of light is given by:

$$I = \frac{(2\pi\nu_0)^4}{3c^3} {\alpha_0}^2 {E_0}^2 cos^2(2\pi\nu_0 t) + \frac{1}{4}\frac{[2\pi(\nu_0 - \nu)]^4}{3c^3}\left(\frac{\partial \alpha}{\partial Q_i}\right)_0^2 {E_0}^2 {Q_i^0}^2 \, cos^2[2\pi t(\nu_0 - \nu)]$$

$$+ \frac{1}{4}\frac{[2\pi(\nu_0 + \nu)]^4}{3c^3}\left(\frac{\partial \alpha}{\partial Q_i}\right)_0^2 {E_0}^2 {Q_i^0}^2 \, cos^2[2\pi t(\nu_0 + \nu)] + \cdots \tag{3. 36}$$

For the sake of simplicity the cross terms in Eq. (3.36) are neglected. Please note that the phases of the different electromagnetic waves are not explicitly considered for the derivation of the equations[2, 3].

References:

1. L. Ickes, A. Welti, C. Hoose and U. Lohmann, *Physical Chemistry Chemical Physics*, **2015**, 17, 5514-5537.
2. B. Dietzek, D. Cialla, M. Schmitt and J. Popp, in *Confocal Raman Microscopy*, eds. T. Dieing, O. Hollricher and J. Toporski, Springer Berlin Heidelberg, Berlin, Heidelberg, **2011**, pp. 21-42.
3. C. J. H. Schutte, *The Theory of Molecular Spectroscopy Volume1: The Quantum Mechanics and Group Theory of Vibrating and Rotating Molecules*, North-Holland Publishing Company, Amsterdam, **1976**.

Dissertation

submitted to the

Combined Faculties for the Natural Sciences and for Mathematics

of the Ruperto-Carola University of Heidelberg, Germany

for the degree of

Doctor of Natural Sciences

Put forward by

Master of Science Chemistry: Andreas Peckhaus

Born in: Essen

Oral examination: 06.07.2016

Study of phase transitions in atmospheric aerosols:

freezing and efflorescence of complex aqueous mixtures

Referees: Prof. Dr. Thomas Leisner

Prof. Dr. Hans-Robert Volpp

Zusammenfassung

Die vorliegende Arbeit befasst sich mit homogenen und heterogenen Nukleationsprozessen in atmosphärischen Aerosolpartikeln. Zum einen wurde das heterogene Gefrieren von unterkühlten Feldspat-Suspensionstropfen mit einem neuartigen Coldstage-Aufbau untersucht. Zum anderen wurde die Effloreszenz von NaCl Dihydrat in unterkühlten NaCl- und Seesalz-Topfen mit einem elektrodynamischen Levitator und einem Raman-Mikroskop studiert. Die Untersuchung hatte zum Ziel, die fundamentale stochastische Natur der homogenen und heterogenen Nukleation in metastabilen Aerosolsystemen aufzuklären.

Um die Fähigkeit von Feldspat-Partikeln zur Eisnukleation zu untersuchen, wurden mehrere hundert Tropfen auf einem Siliziumsubstrat deponiert. Es wurden Experimente mit verschiedenen Temperaturrampen, bei konstanter Temperatur und wiederholte Gefrier- und Aufwärmvorgänge durchgeführt. Die beobachteten Ergebnisse konnten im Rahmen der klassischen Nukleationstheorie (Soccer Ball Model, SBM) gedeutet werden. Das SBM-Model beschrieb sowohl die Verschiebung der Gefrierkurven zu tieferen Temperaturen aufgrund zunehmender Verdünnung als auch die Kühlratenabhängigkeit und die Oberflächendichte eisaktiver Stellen $n_s(T)$ über einen großen Temperaturbereich. Weiterhin war das SBM-Model in der Lage die Variation der Oberflächendichte eisaktiver Stellen $n_s(T)$ mit der Konzentration und die Abflachung der $n_s(T)$-Kurven bei tiefen Temperaturen korrekt wiederzugeben. Durch wiederholte Gefrier- und Aufwärmexperimente konnte die stochastische Natur der heterogenen Eisnukleation belegt werden. Im Rahmen der internationalen FIN02 Kampagne wurde die Zuverlässigkeit des Coldstage-Aufbaus gezeigt.

Einzelne Lösungstropfen, die entweder aus reinem NaCl oder simuliertem Seesalz bestanden, wurden bei definierten Temperaturen und relativen Feuchten in den elektrodynamischen Levitator eingebracht. Eine statische Analyse mehrerer hundert einzelner Effloreszenzereignisse zeigte, dass die Wahrscheinlichkeit der Kristallisation von NaCl Dihydrat eine Funktion der Temperatur, des Tropfenvolumens und der Konzentration der gelösten Stoffe ist. Zudem wurden die temperaturabhängigen homogenen und heterogenen Nukleationsratenkoeffizienten von NaCl Dihydrat ermittelt. Die Unstimmigkeiten früherer experimenteller Untersuchungen zur Bildung von NaCl Dihydrat konnten erstmals aufgrund der Messungen quantitativ erklärt werden. Weiterhin wurde bei den Experimenten mit Seesalz-Tropfen eine verstärkte Bildung von NaCl Dihydrat beobachtet, da eine schnellere Kristallisation von sekundären Seesalz-Komponenten die heterogene Nukleation von NaCl Dihydrat begünstigt.

Abstract

This work addresses homogeneous and heterogeneous nucleation phenomena in atmospheric aerosol particles. First, the heterogeneous freezing of supercooled droplets containing feldspar particles has been investigated in a novel droplet freezing assay instrument. Second, the efflorescence of NaCl-dihydrate in supercooled NaCl and sea salt solute droplets has been studied with a technique combining electrodynamic balance (EDB) and Raman microscopy. The study was aimed to clarify the fundamental stochastic nature of homogeneous and heterogeneous nucleation in metastable aerosol systems.

The ice nucleation efficiency of feldspar particles has been measured by depositing several hundred suspension droplets onto continuously cooled silicon substrate. Three types of experiments have been conducted: cooling ramp, isothermal freezing at constant temperature and freeze-thaw cycles. The observed freezing behavior have been interpreted in a framework of classical nucleation theory (Soccer Ball Model, SBM). The SBM was shown to adequately describe the shift of the freezing curves towards lower temperature with dilution, the cooling rate dependence and the ice nucleating active sites (INAS) surface density $n_s(T)$ in a wide temperature range. Moreover, the SBM was capable of reproducing the variation of INAS surface density $n_s(T)$ with concentration of IN in the suspension droplets and correctly predicting the leveling-off of the $n_s(T)$ at low temperature. The freeze-thaw experiments have clearly shown that the heterogeneous freezing induced even by very active ice nucleating species still possesses a stochastic nature, with the degree of randomness increasing towards homogeneous nucleation. The reliability of the experimental approach has been also demonstrated during the Fifth Ice Nucleating intercomparison campaign (FIN02).

Single solution droplets consisting of pure NaCl or simulated sea salt were suspended into the EDB maintained at constant temperature and relative humidity. A statistical analysis of several hundreds of individual efflorescence events allowed to describe the probability of NaCl dihydrate crystallization as a function of temperature, droplet volume, and solute concentration, and to derive the homogeneous and heterogeneous nucleation rate coefficients of NaCl dihydrate. Based on these measurements, the discrepancies between temperature dependent efflorescence of NaCl dihydrate observed in the previous experiments could be quantitatively explained for the first time. Furthermore, the experiments with the sea salt solution droplets showed an enhanced formation of NaCl dihydrate due to the faster crystallization of secondary sea salt components triggering the heterogeneous nucleation of NaCl dihydrate.

List of contents

1 Introduction

1.1 Motivation

The earth's energy budget is influenced by a variety of natural and anthropogenic climate drivers complicating the prediction of the future development of climate due to their mutual dependencies and feedback mechanisms. The radiative forcing (RF) is defined as the change in net irradiance at the tropopause after allowing for stratospheric temperatures to readjust to radiative equilibrium, but with surface and tropospheric temperatures and state held fixed at the unperturbed values[1]. The concept of RF is used to assess the impact of anthropogenic and natural drivers of climate change. The RF from emissions of well-mixed greenhouse gases (e.g. CO_2, CH_4, N_2O and halocarbons) is well-established and is on the order of $3Wm^{-2}$ for 2011 relative to 1750 (i.e. the preindustrial period)[2]. As can be seen from figure 1, the warming effect of black carbon aerosols is nearly balanced by the cooling effect of mineral dust particles, sulfate and nitrate containing aerosol. Overall, the RF of aerosols and precursors has a negative sign ($-0.27Wm^{-2}$). However, the level of scientific understanding of the indirect aerosol effect, e.g. the aerosol-cloud interaction remains low compared to the previous IPCC assessment reports and far from being completely understood. The RF of the cloud adjustments due to aerosols is assessed with $-0.55Wm^{-2}$, but the associated error bar is quite large. Based on these uncertainties the need arises to understand the underlying microphysical properties of clouds and aerosol particles. Atmospheric research should address this topic and design and perform experiments, which can potentially contribute to a reduction of the uncertainties. This may allow to constrain both regional and global scale climate models and facilitate a better prediction of the climate change.

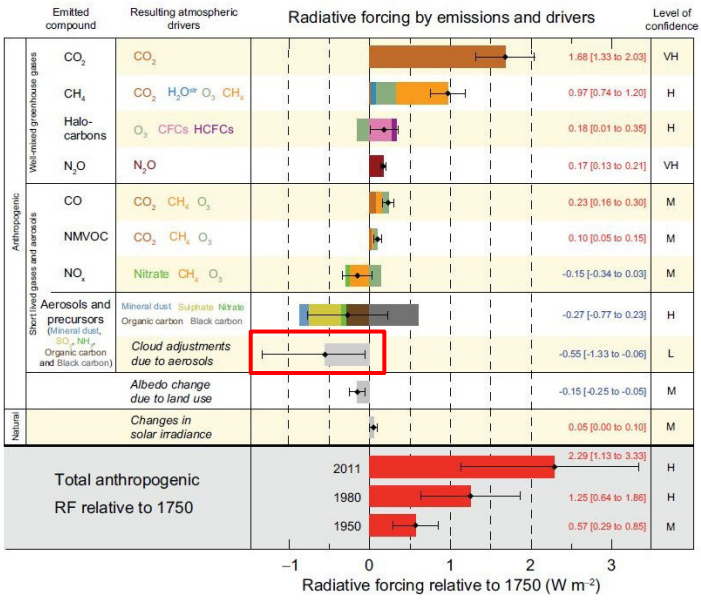

Figure 1: Radiative forcing estimates in 2011 relative to 1750 and the uncertainties for the main drivers of climate change[2].

1.2 State of the art

One important aspect of the aerosol-cloud interaction is the ability of atmospheric aerosol particles to act as cloud condensation nuclei (CCN)[3] or ice nuclei (IN)[4]. Recently, K-rich feldspar was found to be an efficient ice nucleus compared to other investigated mineral dust particles immersed in supercooled water droplets[5]. Furthermore, it was suggested that K-feldspar as a surrogate for primary emitted mineral dust particles accounts for much of the ice nucleation ability observed globally. But so far, no conclusive explanation for its high ice nucleation efficiency is given.

Beside heterogeneous ice nucleation, atmospheric aerosol particles can undergo solute crystallization as another important nucleation process. Chemical composition, relative humidity (RH) and temperature have been identified as key determinants influencing the phase state of aerosol particles[6-8] and thus their crystallization processes. Aqueous aerosol particles containing NaCl and sea salt are an abundant aerosol type in the atmosphere. Recent laboratory studies indicated that micron-sized and submicron-sized NaCl droplets predominately nucleated NaCl dihydrate at very low temperatures[9, 10]. It has been demonstrated that the NaCl dihydrate particles exhibited ice nucleation efficiencies in deposition freezing experiments comparable to those of mineral dust particles[11]. However, significant discrepancies in the temperature-dependent partitioning between anhydrous NaCl and NaCl dihydrate were observed. Results reported by Schill et al. revealed that simulated sea salt aerosol (SSA) particles were ice active via immersion in solution nucleation, but the potential contribution and formation of NaCl dihydrate in SSA was not discussed by the authors[12].

Furthermore, internal morphological changes of organic/inorganic aerosol particles proceeding after phase separation are well known, but these changes were only observed for deposited particles and not confirmed for levitated particles[13].

1.3 Objectives of the work

The objectives of this thesis are to understand the ice nucleation efficiencies of different feldspar particles and to describe their ice nucleation behavior within a classical nucleation theory (CNT)-based formalism. This could help to understand the glaciation of clouds since very effective ice nuclei such as K-feldspar particles may lead to an increase of the amount of precipitation and therefore lower the cloud coverage and the lifetime of clouds[4]. Outcomes of the CNT-based formalism could help to improve cloud and climate modelling studies.

The second aim of this work is to elucidate the conditions for the formation of NaCl dihydrate and to reconcile different experimental approaches, i.e. cloud chamber and environmental cell studies by considering the influence of temperature, droplet volume and solute concentration on the nucleation process. It is also intended to investigate the effect of additional ionic species on the solute crystallization of NaCl dihydrate in efflorescing SSA solution droplets. The formation NaCl dihydrate in SSA solution droplets could potentially give some information about the ability of these particles to nucleate ice at low temperatures which are relevant for ice clouds in the upper troposphere.

1.4 Approach

To study the heterogeneous ice nucleation of feldspar particles a novel droplet freezing assay is used. This technique was selected due to the capability of investigating a large number of droplets simultaneously in a single experimental run. The number of investigated droplets provides both good statistical validity and high sensitivity for the detection of rare freezing events. Different types of nucleation experiments can be performed without large modifications of the apparatus. This makes the techniques suitable for the study of stochastic processes such as heterogeneous ice nucleation.

Moreover, the combination of an electrodynamic balance (EDB) coupled to a Raman microscope is used for the examination of the solute crystallization of solution droplets. This combined approach has the advantage that single solution droplets can be trapped in the EDB without contact to foreign surfaces. By using the EDB, the influence of foreign surfaces triggering the nucleation process can be ruled out. The Raman microscope allows to determine the size and shape of the levitated particle on the one hand and the phase state and chemical composition on the other hand.

1.5 Structure of the thesis

This thesis is organized as follows: First, the theoretical background concerning the aerosol properties, cloud microphysics and the fundamentals of homogeneous and heterogeneous ice nucleation and solute crystallization are provided. Then the experimental apparatus and the realization of the experiments are described in detail. The following presentation and discussion of the results is divided into two sections: In the first section, the results of a comparative study of K-rich and Na/Ca-rich feldspar ice nucleating particles conducted in a nanoliter droplet freezing assay and the results of the off-line instrument intercomparision campaign (Fifth International ice nucleation workshop, FIN02) at the Institute of Meteorology and Climate research - Atmospheric Aerosol Research (IMK-AAF) are summarized. In the second section, the solute nucleation experiments with pure NaCl and simulated sea salt solution droplets are presented. Finally, the thesis concludes with the major findings and gives a perspective.

2 Theoretical basics

2.1 Atmospheric aerosol

Sea salt aerosol (SSA) belongs to the primary aerosol particle type and contributes 50%-70% of the aerosol mass at oceanic remote site. The emissions flux from the ocean surface is estimated to be in the range from 1400-6800Tg/yr[2]. Currently, only two major sources of SSA are believed to be responsible for the SSA production[14]: Bursting of bubbles formed primarily by breaking waves and the mechanical disruption of wave crests by wind erosion. The mechanisms are shown in figure 2 (left panel). Many factors can influence the SSA production e.g. wind speed, sea and air temperatures, RH, etc. During their ascent, air bubbles can be enriched by dissolved organic substances that may be present in the uppermost layers of the ocean. SSA droplets ejected from the sea surface microlayer (SSM) may contain a significant amount of organic material beside the major ionic species. The size of the SSA particles critically depends on the production mechanism. Most small particles (≤1µm) originate from film droplets, medium droplets (from 1µm to 25µm) are predominately formed by jet droplets. The larger SSA droplets are jet and spume droplets (right panel of figure 2). All these production mechanism contribute to a rather broad size distribution of SSA particles with three distinct modes[15]. Each aerosol species has its own source, sink, lifetime and size distribution. Besides the sea salt aerosol, mineral dust is the second major contributor of natural coarse-mode aerosols worldwide[16]. Approximately, 1000-3000Tg is aerosolized per year[17]. Primary mineral dust particles e.g. feldspar particles are mainly produced by wind erosion, soil resuspension, agricultural and industrial activities[2]. Feldspars are normally only a minor part of the dust particles. Depending on the source, the bulk is composed of quartz and clay minerals. Clays are secondary i.e. weathered minerals[17].

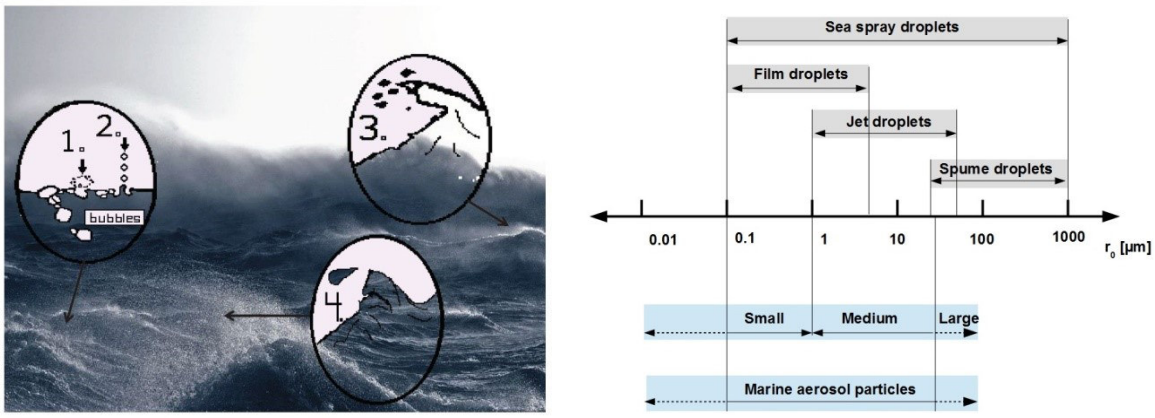

Figure 2: Left: Sea salt aerosol generating mechanisms: 1. Film droplets are produced from bubble bursting and the filaments of the bubble are left above the water surface. 2. Jet droplets are emitted from the break-down of the voids left at the ocean surface by the bubble. 3. Spume droplets are produced by the mechanical disrubtion of wave crests (whitecap). 4. The last mechanism shows the formation of large splash droplets[18]. Right: Size ranges of the produced sea salt droplets and marine aerosol particles[14, 19, 20]. The right panel is adapted and modified from the PhD thesis of M. D. Anguelova[21].

2.2 Cloud microphysics

The theoretical description of cloud microphysics is given in the textbooks of Pruppacher and Klett[22] and Seinfeld and Pandis[15]. A brief summary of cloud microphysics is provided here. A minor fraction of the total aerosol load has the ability to condense water vapor and form liquid cloud droplet. These aerosols particles are termed cloud condensation nuclei (CCN). The process of condensational growth below critical size is quantitatively described by the Köhler theory. The Köhler theory makes use of both the Kelvin equation for curved surfaces and the Raoult's law for diluted solutions. Both effects are combined to describe the critical particle diameter and supersaturation with respect of water to activate an aerosol particle to a cloud droplet. If the particle is activated, then the droplet grows further as long as the actual supersaturation is higher than or equal to the critical supersaturation. It should be keep in mind that the Kelvin effect is only important for very small particle sizes, i.e. usually smaller than 1µm. Droplets that are not activated to cloud droplets completely evaporate and contribute to the interstitial aerosol load. In warm clouds (i.e. containing no ice crystals), cloud droplets can grow to precipitation size by the so-called collision-coalescence mechanism. During their fall path, the larger droplets pick up smaller droplets and grow to rain droplet size (several millimeters in diameter). An important prerequisite for the activation to cloud droplets is the presence of CCN, otherwise several hundred percent of supersaturation with respect to water would be necessary to nucleate a liquid water droplet from the vapor phase. Precipitation is only generated by warm clouds, in mixed-phase clouds the ice phase is involved in the formation of precipitation. The figure 3 shows schematically the processes in a mixed-phase cloud. Ice nucleating particles (INPs) can trigger the formation of ice via a heterogeneous nucleation mechanism (described in more detail in section 2.6.3). The ice particles grow via vapor deposition. This process describes the growth of ice crystals through vapor deposition at the expense of liquid water droplets in mixed-phase clouds. The ice particles can gain additional mass by riming (contact freezing of supercooled water droplets on the ice particle's surface) and by aggregation processes (collision and sticking of ice crystals). If the ice particles exceed a certain mass, then they can fall out of the cloud. Melting of the ice particles may occur when the ambient temperatures and metrological conditions are suitable, so that they can reach the ground as rain droplets.

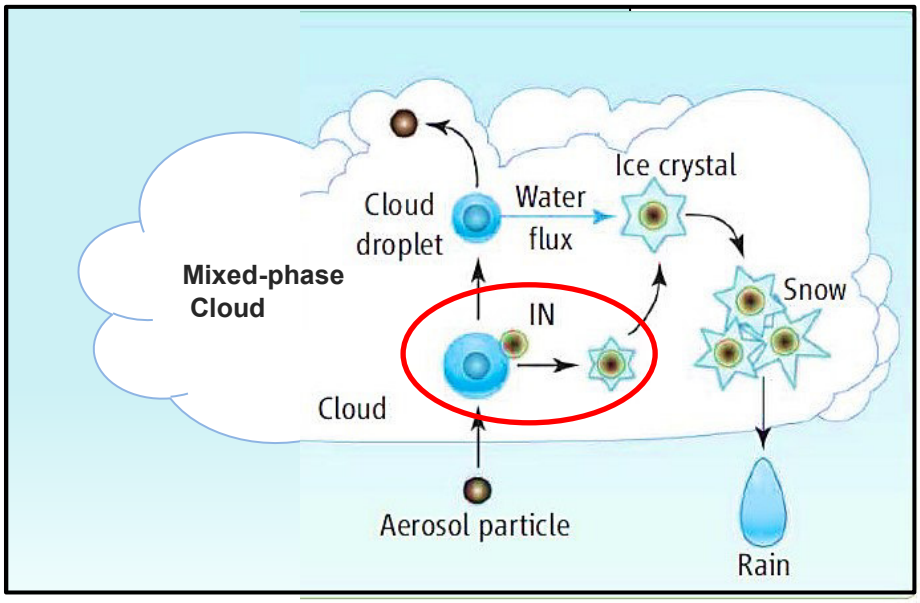

Figure 3: Schematic illustration of the processes inside a mixed-phase cloud. Ice crystals are formed via heterogeneous ice nucleation. The water vapor is transported from the liquid water droplets to the ice crystals due the difference in the saturation vapor pressures between ice and liquid water. Cloud droplets can eventually evaporate. This means that the clouds may serve as both sink and source of atmospheric aerosol particles. The red ellipse highlights the importance of the formation of ice in mixed-phase clouds. The illustration is adapted and modified from U. Baltensperger[23].

2.3 Feldspars and SSA as INPs? - State of the art of IN research

Up to now, feldspar was studied with various experimental methods and in different freezing modes. Deposition freeing experiments carried out in an environmental scanning electron microscope (ESEM) have shown that K-rich feldspar (microcline) had the lowest onset freezing temperature and supersaturation with respect to RH_{ice} (onset RH_{ice} of 105% at -12°C)[24]. In contrast, Na/Ca-rich feldspar (albite) showed only a weak temperature dependence of RH_{ice}, whereas K-feldspar exhibited an increase of onset RH_{ice} with decreasing temperature. Diffusion chamber experiments have led to the conclusion that K-feldspar (orthoclase) is an effective deposition IN at a temperature of -40°C (onset RH_{ice} of 135.0% ± 3.6% at the threshold of 0.1% of ice activated particles)[25]. Long term suspension of K-feldspar in water slightly increased the onset RH_{ice} value (127.1% ± 6.3%). It was concluded that the washing-out did not significantly changed the ability to nucleate ice.

In a number of droplet freezing assay experiments the K-feldspar particles have been investigated in immersion freezing mode and found that K-feldspar particles initiate freezing at higher temperatures than other mineral dust particles[5, 26, 27]. It was hypothesized that the fraction of K-feldspar in naturally mineral dusts samples correlates with the ice nucleation efficiency[5]. Size-selected measurements of K-feldspar (microcline) aerosol particles carried out in the Leipzig aerosol cloud interaction simulator (LACIS) have revealed that the frozen fraction of droplets containing individual feldspar aerosol particles could reached a plateau value well above -38°C[28]. This behavior was interpreted in terms of a specific average number of ice nucleating sites per particle reaching unity inside the temperature range where the freezing curve starts to level off. Na/Ca-feldspar particles studied with a Cold Stage/Raman microscope setup featured ice activity in both deposition and immersion freezing presumably due to K-feldspar impurities[29].

Several experiments addressed the influence of ageing on the ice nucleation efficiency of feldspar particles. Chemical treatment with sulfuric acid was shown to cause a reduction of ice activity of K-feldspar particles depending on the coating conditions[30, 31]. The ice activity of aged K-feldspar was similar to other chemically treated minerals i.e. Arizona test dust (ATD), kaolinite and illite NX. Mechanical milling of K-feldspar particles caused a slight increase in their ice activity, while enzymatic treatment significantly reduced their ice activity probably due to blocking of ice active sites[27]. Subsequent heating led to a restoration of the ice efficiency.

Laboratory studies of ice nucleation of feldspar in condensation and contact freezing mode are scarce. In particular, condensation freezing experiments conducted in the Manchester ice cloud chamber (MICC) fall tube have shown the temperature dependence of $n_s(T)$ values being less steep[32] compared to immersion freezing experiments reported in Atkinson et al[5]. In contact freezing experiments, K-feldspar particles have shown IN efficiency comparable to that of ATD and rhyolitic ash in the same temperature range[33]. Note that in this study the particle size distribution was rather broad and therefore the results should be interpreted with caution.

Although a large amount of the earth's crust consists of feldspar mineral (~51%[34]) only a minor fraction (~13%[17]) of this primary mineral contributes to the mineral-containing atmospheric aerosol particles. In particular, field campaigns showed that the mass fraction of K-feldspar collected on filter substrates in Taifou (Morocco) was 10 wt% in dust storm and 25 wt% in low-dust conditions[35]. Similar results were observed at Cape Verde with 20 wt% (“dust period”) and 25 wt% ("maritime period")[36]. These field campaigns have been carried out in the vicinity of Sahara desert and may exhibit strong gradients of particle concentration with distance from the source[37]. Mineral dust particles collected in Asia contained 11 wt% Na/Ca-rich feldspar and 8 wt% of K-rich feldspar[38].

Several potential candidates have been hypothesized for the ice activity of marine particles. The heterogeneous IN activity of marine aerosol particles in the immersion and deposition mode is summarized in the following. Early work suggested that biological matter in natural sea water sampled at the Bedford basin caused high IN activity starting already at -3.5°C[39, 40]. Follow-up studies conducted screening experiments in the immersion mode to directly identify the ice active marine microorganisms. Schell et al.[41] showed that cultures of the phytoplankton species *Cachonina niei*, *Ochromonus danica* and *Porphyridium aerugineum* featured IN activity. Furthermore, Fall et al.[42] screened 21 marine species and found out that among them the marine dinoflagellate *Heterocapsa niei* had the highest median freezing temperature (T_{50}) of -11.5°C. Parker et al.[43] described one ice active sea ice sample at different concentrations. In addition, several Antarctic marine diatoms (*Synedra sp.*, *Chaetoceros dichaeta*, *Chaetoceros flexuosum*, *Porosira glacialis*, and *Pososira pseudodenticulata*) were tested and showed no significant ice nucleation ability at temperatures higher than -12°C. In the same article, one out of eleven investigated marine bacteria strains showed IN activity between -2.0°C and -3.5°C (HK-31). More recent studies reported both the immersion and deposition ice nucleation of the diatom species *Thalassiosira pseudonana*[44, 45] and of the two phytoplankton species *Nannochloris atomus* and *Emiliania huxleyi*[46]. Intact and fragmented diatoms (*T. pseudonana*) immersed into NaCl solution droplets were able to nucleate ice ∼10K and up to ∼30K compared to the homogeneous freezing at high and low water activities respectively[44]. A marked difference in the IN efficiency of two phytoplankton species *N. atomus* and *E. huxleyi* was observed in the immersion mode with *N. atomus* being more ice active than *E. huxleyi*[46]. However, all three phytoplankton species exhibited a comparable IN activity in the deposition mode for $T<240K$ ($S_{ice}>1.2$)[45, 46]. In a similar direction point very recent results of Wilson et al.[47], who demonstrated that water samples from the sea surface microlayer (SML) collected at different locations including the Arctic Ocean, the North Atlantic Ocean, the North Pacific Ocean and the Coast of British Columbia (CB) are very efficient in nucleating ice. The authors provided strong evidences that exudates of the diatom *T. pseudonana* may trigger ice nucleation in both the immersion and deposition mode. This conclusion is further supported by filtration tests indicating a size range of the INPs from 0.2µm to 0.02µm and heating tests pointed to thermally labile biological INPs. Ladino et al.[48] substantiated these findings by showing that the phytoplankton exudates (*T. pseudonana*, *N. atomus* and *E. huxleyi*) and the marine bacterium (*Vibrio harveyi*) are very effective ice nucleators in the deposition mode (105% RH_{ice} at -40°C). In contrast, commercial sea salt particles, natural organic matter (NOM) particles and mixed sea salt/NOM particles were poor heterogeneous INPs (from 140.8 to 144.6% RH_{ice} at -40°C). The value for homogeneous freezing was 145.5% RH_{ice} at -40°C. Two recent studies showed that marine biological activity i.e. high phytoplankton and chlorophyll α (Chl α) levels are related to SSA IN emissions[49, 50]. High IN concentrations were also proposed to be associated with marine biogenic INPs over ocean-dominated environments (especially in the Sothern Ocean)[51].

A different line of reasoning focuses on the potential capability of non-biological constituents of sea spray aerosol acting as heterogeneous INPs. Wise et al.[9] observed a temperature-dependent partitioning between substrate-supported anhydrous NaCl and NaCl dihydrate particles in the temperature range from 236K to 252K. The NaCl dihydrate particles were effective depositional INPs in the range from 221K to 238K (S_{ice}=1.00-1.11). In the intermediate temperature range from 235K to 239K both depositional ice nucleation and deliquescence competed with each other. At temperatures above 239K, only deliquescence of the solid NaCl particles was observed. AIDA cloud chamber experiments reported by Wagner et al.[10] indicated that the partitioning of the two solid NaCl phases proceeded in the temperature range from 235K to 210K (i.e. a temperature shift of ~13K compared to Wise et al.). The NaCl dihydrate particles initiated depositional ice nucleation in the range from 227K to 213K (S_{ice}=1.15-1.25), which is comparable to mineral dust particles such as Arizona test dust (ATD) with S_{ice}=1.02-1.20 in the same temperature range[11]. By comparing the results of Wise et al. with those of Wagner et al., it is evident that the temperature-dependent partitioning is situated at lower temperatures and the onset S_{ice} values are slightly higher in Wagner et al. Schill et al.[12] investigated the ice nucleation behavior of simulated SSA particles and mixed SSA/sucrose particles in the temperature range from 235K to 215K. Above 230K the SSA particles fully deliquesced and below 225K immersion-in-solution nucleation was prevalent (S_{ice}=1.05-1.3) due to the presence of hygroscopic components in the salt mixture facilitating the water uptake prior to the ice nucleation. However, a different picture was obtained for mixed SSA/sucrose particles showing deliquescence above 225K and depositional ice nucleation below 220K. The observation of deposition freezing of mixed SSA/sucrose particles was explained by the formation of a glassy salt/organic matrix at low temperatures.

As a further candidate for heterogeneous ice nucleation activity, glassy organic aerosol can be considered. Under low temperature and relative humidity conditions, certain organic aerosol particles can turn into amorphous or highly viscous particles (via the glass transition), in which the diffusion coefficient of water is extremely low leading to a retarded interaction between the condensed and gas phase[52]. It was been shown that these glassy particles can nucleate ice in the deposition mode[53, 54].

The laboratory investigations are supported by analyses of ice residuals (IR) collected during aircraft measurement campaigns between 2002 and 2011 over North and Central America and nearby ocean in cirrus clouds. These observations revealed that sea salt can made up 25% of the IRs over open ocean fights and only 3% of the other fights[55]. Pratt et al. analyzed IRs sampled from an orographic wave cloud (i.e. a high-altitude mixed-phase cloud) over Wyoming (North America) in 2007 and found that only a minor fraction of the IRs (about 9%) contained sea salts (e.g. NaCl/KCl)[56].

2.4 Ice nucleation on aerosol particles

2.4.1 Homogeneous ice nucleation

In classical nucleation theory, it is assumed that density and temperature fluctuations of supercooled metastable water lead to the formation of a new ice phase. With decreasing temperature, the size of the randomly forming ice clusters grows. The process of cluster formation is reversible. Water molecules stick together forming a cluster and according to the Boltzmann law the clusters have a probability and size depending on temperature. At a critical cluster size, the further growth of the clusters is thermodynamically favorable. The formation of a critical ice cluster in supercooled water causes the freezing of the whole water droplet, i.e. the formation of a new ice phase inside the existing metastable liquid phase triggers the transition from a liquid to a frozen droplet.

In classical nucleation theory the formation of ice is considered to be related to a surface-dependent and a volume-dependent free energy term. The free energy for the formation of a new surface is associated with an interface of curvature r and the interface tension σ_{sl}, i.e. the creation of a boundary between the ice embryo and the metastable liquid phase generates an interfacial tension. On the other hand, the free energy for the formation of the ice bulk phase depends on the supersaturation $S(T)$, the volume of a H_2O molecule in ice and the radius of the ice embryo. Both the surface-dependent and the volume-dependent free energy contribution have to be considered for the formation of an ice nucleus in the metastable phase.

$$\Delta G = 4\pi\sigma_{sl}r^2 - \frac{4\pi}{3}\frac{kTln\big(S(T)\big)}{v_{ice}}r^3 \qquad (2.\ 1)$$

where v_{ice} is the volume of a H_2O molecule in ice and k is the Boltzmann constant. The supersaturation $S(T)$ is expressed as the quotient of the vapor pressures over liquid water $p_{H_2O}(T)$ and ice $p_{ice}(T)$ as a function of temperature:

$$S(T) = \frac{p_{H_2O}(T)}{p_{ice}(T)} \qquad (2.\ 2)$$

Figure 4 shows the free energy of the ice nucleus formation as a function of r. As can be seen from figure 4, if $S(T) < 1$, both terms in equation (2.1) are positive and ΔG increases with the radius. If $S(T) > 1$, ΔG has both a negative contribution from the volume-dependent term and a positive contribution from the volume-dependent term. For small ice clusters, the surface-dependent term dominates in equation (2.1) as compared to the behavior of ΔG in the case of $S(T) > 1$. If the radius of the ice nucleus increases, the volume-dependent term becomes more important. ΔG reaches a maximum value and then decreases with increasing radius[15].

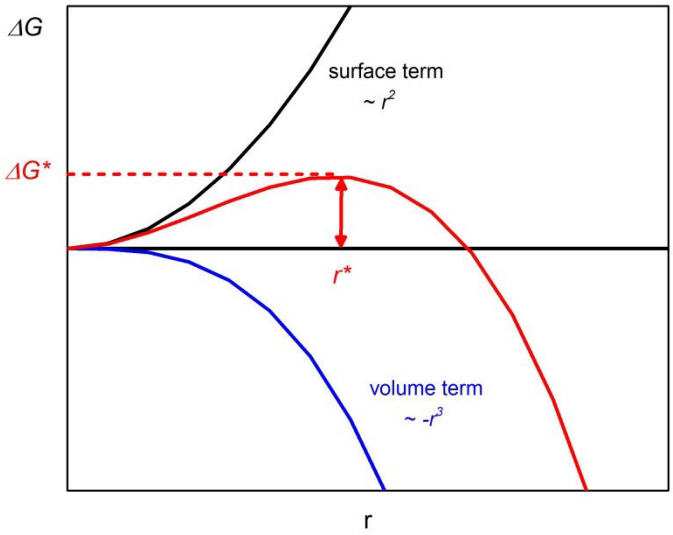

Figure 4: Free energy of the ice nucleus formation depending on the ice nucleus radius[22].

The maximum of the free energy ΔG^* corresponds to a critical cluster size r^* and can be calculated by setting the first derivative with respect to the radius to zero:

$$r^* = \frac{2\nu_{ice}\sigma_{sl}}{kTln(S(T))} \tag{2. 3}$$

The free energy of the ice nucleus formation can be written as:

$$\Delta G^*(T) = \frac{16\pi}{3}\frac{{\nu_{ice}}^2{\sigma_{sl}}^3}{[kTln(S(T))]^2} \tag{2. 4}$$

The diffusion activation energy is given by[57]:

$$\Delta F_{diff}(T) = \frac{\partial ln(D_v(T))}{\partial T}kT^2 \approx \frac{kT^2\Delta E}{(T-T_0)^2} \tag{2. 5}$$

where $D_v(T)$ is the diffusion coefficient of water. The diffusion activation energy can be reformulated using the Vogel-Fulcher-Tammann equation. It should be mentioned that the quantities σ_{sl}, ν_{ice} etc. are macroscopic quantities which are parameterized by experimental measurements.

The homogeneous nucleation rate coefficient $J_{hom}(T)$ is defined as the number of nucleation events per volume of liquid water and time. $J_{hom}(T)$ is composed of three different parts: a preexponential, a kinetic and thermodynamic factor[58]:

$$J_{hom}(T) = n_w\left(\frac{kT}{h}\right)exp\left(\frac{-\Delta F_{diff}(T)}{kT}\right)exp\left(\frac{-\Delta G^*(T)}{kT}\right) \tag{2. 6}$$

where n_w is defined as the volume number density of water molecules in liquid water. In Ickes et al.[58], the value of n_w is reported to be in the range from $3.1 \cdot 10^{28}m^{-3}$ to $3.35 \cdot 10^{28}m^{-3}$. The term $\left(\frac{kT}{h}\right)$ is the jump frequency of water molecules to overcome the

activation energy barrier. The kinetic term is related to the diffusion activation energy required for a water molecule to pass through the ice/water boundary and the thermodynamic term contains the free energy of ice nucleus formation[22, 58]. To measure the homogeneous nucleation rate it is assumed that the nucleation process can be described by a first-order rate equation, where N_u is the number of unfrozen droplets and V is the volume of the droplets:

$$\frac{dN_u}{dt} = -J_{hom}(T)VN_u \tag{2. 7}$$

Integration of equation (2.7) yields:

$$\int_{N_0}^{N_u} \frac{dN_u}{N_u} = -J_{hom}(T)V \int_0^t dt \tag{2. 8}$$

The logarithm of the number of unfrozen droplets divided by the number of total droplets is directly proportional to the homogeneous nucleation rate, i.e. the homogeneous nucleation rate can be extracted from the slope of a $ln\left(\frac{N_u}{N_0}\right)$ versus time plot:

$$ln\left(\frac{N_u}{N_0}\right) = -J_{hom}(T)Vt \tag{2. 9}$$

For practical purposes, it is useful to define the fraction of liquid and frozen droplets ($f_{liquid}(T)$ and $f_{ice}(T)$ respectively) as a function of temperature:

$$f_{liquid}(T) = 1 - f_{ice}(T) = \frac{N_u(T)}{N_0} \tag{2. 10}$$

2.4.2 Heterogeneous ice nucleation

In the atmosphere, the formation of an ice phase often proceeds via a heterogeneous ice nucleation pathway. There are four distinct heterogeneous ice nucleation modes: In deposition freezing, water vapor forms directly ice onto an ice nucleating particle without involving a liquid phase. In condensation freezing, water vapor first condenses on the ice nucleus and then the liquid water freezes. Contact freezing describes the instantaneous ice nucleation of a supercooled water droplet via a single collision with an INP. At least, in immersion freezing, an INP is immersed in the water droplet. If the water droplet is sufficiently supercooled, ice nucleation can occur. Deposition and condensation freezing are closely connected to the vapor phase and start at subsaturated conditions with respect to water. While immersion and contact freezing need supersaturated conditions with respect to water (see figure 5)[22].

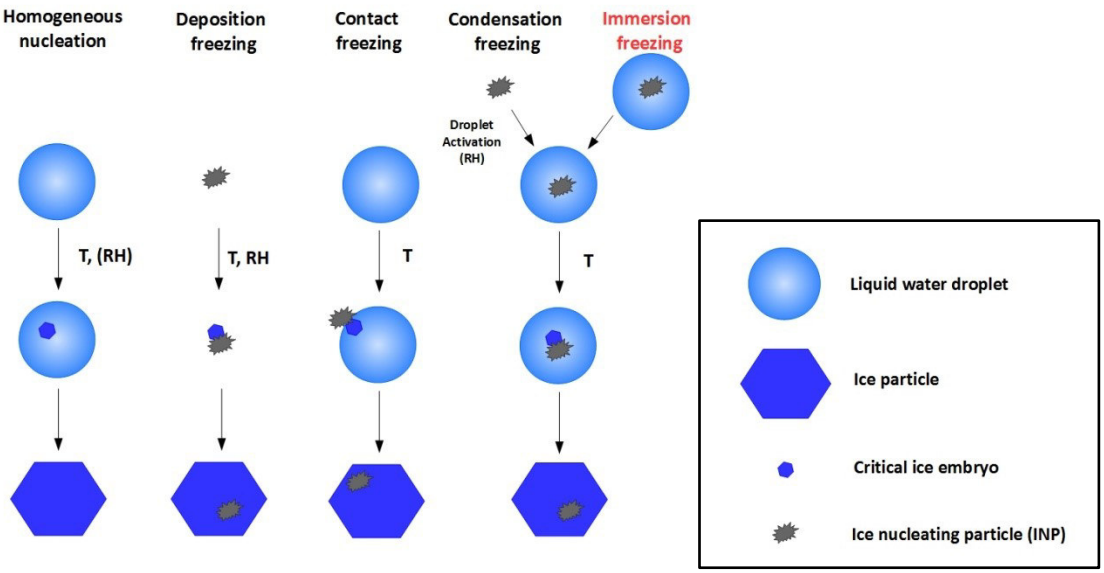

Figure 5: Schematic illustration of the homogeneous and heterogeneous ice nucleation pathways according to the nomenclature of Vali et al[59].

For the theoretical understanding of heterogeneous ice nucleation one considers a solid nucleus forming on a planar surface. The solid nucleus adopts the shape of a spherical cap. The nucleus is in contact with the surrounding liquid phase. The geometry of the spherical cap is characterized by two parameters: the radius of the sphere and a contact angle θ between the solid nucleus and the underlying substrate (see figure 6). The red dot in figure 6 indicates the point, where all three phases are in contact with each other.

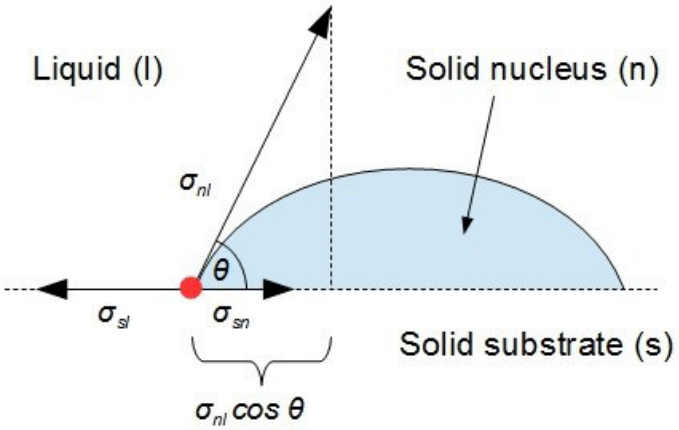

Figure 6: Illustration of a spherical ice nucleus in contact with liquid water and the solid substrate[60]. At the red dot all three phases are in contact with each other.

The contact angle is determined by the surface tensions at the three interfaces. The cosine of the contact angle θ is defined by the Young's equation for the balance of forces at the boundary of the solid nucleus and the solid substrate:

$$\sigma_{nl} cos\theta + \sigma_{sn} = \sigma_{sl} \qquad (2.\ 11)$$

where σ_{nl} is the surface tension between the solid nucleus and the liquid surrounding, σ_{sn} is the interface tension between the solid substrate and the nucleus and σ_{sl} is the surface tension between the solid substrate and the liquid phase. Equation (2.11) can be rewritten as:

$$m_{nl} = cos\theta = \frac{(\sigma_{sl} - \sigma_{sn})}{\sigma_{nl}} \tag{2. 12}$$

m_{nl} is defined as the wettability coefficient, because the parameter allows to access the interaction between the solid substrate and the nucleus. Additionally, a compatibility function $f(\theta)$ is described as[15]:

$$f(\theta) = \left(\frac{1}{4}\right)(2 + cos(\theta))(1 - cos(\theta))^2 \tag{2. 13}$$

The contact angle is more a concept or a convenient parameter in the compatibility function to account for the ice nucleation efficiency of a specific INP, rather than a directly observable quantity obtained from the measurements. It should be mentioned that the compatibility function is derived from a planar solid substrate. In reality, the geometry can deviate from a solid ice nucleus residing on a planar solid substrate. Therefore, several formal expressions exist to correct for the non-planar shape of the solid substrate.

The homogenous free energy of ice nucleus formation is multiplied by the compatibility function $f(\theta)$ resulting in the free energy needed to from an ice nucleus on a heterogeneous surface:

$$\Delta G^*(T) f(\theta) = \frac{16\pi}{3} \frac{{\nu_{ice}}^2 {\sigma_{sl}}^3}{[kTln(S(T))]^2} f(\theta) \tag{2. 14}$$

The introduction of a compatibility function leads to homogeneous ice nucleation in case of $\theta = \pi$. In the case of $\theta = 0$, the free energy for the formation of an ice embryo vanishes and ice nucleation is only diffusion-limited. Figure 7 shows that for $\theta < \pi$, the presence of an INP significantly reduces the free energy barrier meaning that heterogeneous ice nucleation is more favorable than homogeneous ice nucleation i.e. ice nucleation starts at higher temperatures and/or at lower supersaturations with respect to ice. Analogous to the homogenous nucleation coefficient, the heterogeneous nucleation coefficient is given by:

$$J_{het}(T, \theta) = n_{w,het} \left(\frac{kT}{h}\right) exp\left(\frac{-\Delta F_{diff}(T)}{kT}\right) exp\left(\frac{-\Delta G^*(T) f(\theta)}{kT}\right) \tag{2. 15}$$

where $n_{w,het}$ is defined as the number density of water molecules at the ice nucleus/water interface. Ickes et al.[58] reported $n_{w,het}$ in the range from $5.85 \cdot 10^{18} m^{-2}$ to $1 \cdot 10^{19} m^{-2}$.

Similar to the homogenous ice nucleation a first-order rate equation can be formulated, i.e. the change in the number of liquid droplets with time can be written as:

$$\frac{dN_u}{dt} = -N_u J_{het}(T) S_A \tag{2. 16}$$

Integrating and rearranging of equation (2.16) results in:

$$f_{ice} = 1 - exp(J_{het}(T)S_A t) \quad (2.\ 17)$$

The stochastic approach assumes that heterogeneous ice nucleation is a time-dependent process. As a consequence, a cooling rate dependence of the frozen fraction and a continuously decrease of the liquid fraction with increasing time at a constant temperature should be observed. Also in repeated freeze and thaw cycle experiments of single droplets, small deviations from the average freezing temperature of the single droplets should be measured. The difference between homogenous and heterogeneous freezing is that nucleation events occur more frequently on a foreign solid substrate due to the reduced free energy barrier, i.e. the heterogeneous nucleation rate is higher at the same temperature.

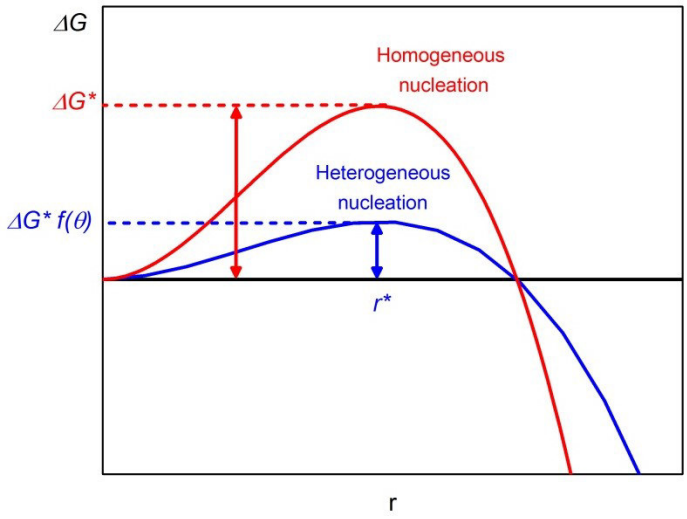

Figure 7: Free energy of ice nucleus formation for homogeneous and heterogeneous ice nucleation[22]. The free energy barrier of heterogeneous ice nucleation is reduced compared to the case of homogeneous ice nucleation.

2.4.3 Singular approach

The singular approach was developed by Levine[61] and Langham et al.[62]. It postulates that ice nucleation takes place on specific ice active surface sites. Each of the ice active sites is associated with a characteristic temperature. If a liquid water droplet containing an INP is supercooled to the characteristic temperature, ice nucleation immediately sets in. Ice nucleation should not occur above the characteristic temperature. This singular approach assumes that heterogeneous ice nucleation is a time-independent process, i.e. no decrease in the liquid fraction of a population of water droplets in isothermal experiments should be visible. Additionally, a single water droplet subjected to repeated freeze and thaw cycle experiments should always freeze at the same characteristic temperature. If a water droplet contains multiple nucleation sites, then the ice active site with the highest characteristic temperature initializes freezing of the whole droplet. A distribution of different IN types

among a population of water droplets results in a distribution of characteristic temperatures. The fraction of frozen droplets could be described by[63, 64]:

$$f_{ice}(T) = \frac{N_{ice}(T)}{N_0} = 1 - exp(n_s(T)S_A) \quad (2.\ 18)$$

where $N_{ice}(T)$ is the number of frozen droplets, $n_s(T)$ is the ice nucleation active sites (INAS) surface density and S_A is the total particle surface area. The total particle surface area is either derived from surface area distributions or calculated from the mass of particles per droplet multiplied by the specific surface area measured with BET approach[65] (BET-SSA). The INAS surface density is defined as the negative logarithm of the fraction of liquid droplets scaled to the total particle surface area per droplet:

$$n_s(T) = \frac{-ln(1 - f_{ice}(T))}{S_A} \quad (2.\ 19)$$

The concept of ice nucleation active site surface density was introduced in order to assess the ice nucleating efficiency of a variety of aerosol particles regardless of the experimental measurement conditions[63, 66].

2.4.4 Combined approaches

There are several combined approaches that try to bridge the gap between the stochastic and singular description of heterogeneous ice nucleation. In more detail, the time-dependent freezing rate (TDFR) model combines assumptions of the singular approach with a cooling rate dependence[67], multicomponent stochastic models make use of a simple linear expression of the temperature dependence of nucleation rate coefficient[68] and CNT based approaches use a distribution of active sites or contact angles to represent the variability in ice nucleation behavior[69, 70]. In this work, the focus is on the so-called Soccer ball model (SBM). SBM approach assumes that the surface area of a particle S_P is divided into a number of surface sites n_{site}, which are identical for all particles. Each surface site is assigned to a specific contact angle θ. The distribution of contact angles follows the Gaussian probability density function (PDF):

$$p(\theta) = \frac{1}{\sqrt{2\pi}\sigma_\theta} exp\left(-\frac{(\theta - \mu_\theta)^2}{2\sigma_\theta^2}\right) \quad (2.\ 20)$$

where μ_θ is the mean contact angle and σ_θ is the standard deviation of the Gaussian probability density function. The surface area s_{site} of an ice active site depends on the total particle surface area S_P divided by the number of surface sites:

$$s_{site} = \frac{S_P}{n_{site}} \quad (2.\ 21)$$

In the SBM approach, s_{site} varies with n_{site}, but could also be set to a fixed value independent of the surface area. In such case the probability P_{unfr} of a single suspension droplet to remain liquid after time *t* at given supercooling temperature *T* is given by[71]:

$$P_{unfr}(T,\mu_\theta,\sigma_\theta,t) = \int_0^\pi p(\theta)\exp(-J_{het}(T,\theta)s_{site}t)\,d\theta + \int_{-\infty}^0 p(\theta)\exp(-J_{het}(T,0)s_{site}t)\,d\theta + \int_\pi^\infty p(\theta)\exp(-J_{het}(T,\pi)s_{site}t)\,d\theta \quad (2.22)$$

The sum of the three terms in equation of (2.22) ensures that possible contributions outside of the interval [0, π] are considered, i.e. without the two terms integrating from [0,-∞] and [∞,π], it is equivalent to the α-PDF approach. J_{het} represents the heterogeneous ice nucleation rate coefficient a given temperature T and contact angle θ. The necessary parametrizations for the calculation of J_{het} are taken from the literature[57]. The freezing probability is given by:

$$P_{fr}(T,\mu_\theta,\sigma_\theta,t) = 1 - P_{unfr}(T,\mu_\theta,\sigma_\theta,t) \quad (2.23)$$

The freezing probability i.e. the frozen fraction of the population of droplets containing INPs with n_{site} is given by the following equation[28]:

$$f_{ice} = 1 - \exp\left[-n_{site}\left(1 - P_{unfr}(T,\mu_\theta,\sigma_\theta,t)\right)\right] \quad (2.24)$$

In case of cooling ramp experiments, the cooling rate $c = dT/dt$ has to be introduced to relate the temperature and time: $T = T_{start} + ct$, where T_{start} is the start temperature of the cooling ramp (typically 273K). The parameters n_{site}, μ_θ and σ_θ can be obtained by fitting the equation (2.24) to the experimentally measured fraction of frozen droplets as a function of freezing temperature (in cooling ramp experiments) or freezing times in isothermal experiments. The goodness of fit is described by r^2 correlation coefficient.

Equation (2.24) can be used to explore the relationships between the apparent fraction of frozen droplets and material properties, described as combination of μ_θ and σ_θ. Since the experimental parameter (particle number or mass per droplet) is represented by n_{site}, this equation provides also a basis for comparison between experiments conducted with the same material but under different experimental conditions (different droplet size and particle concentration). Moreover, it can be used to explore the relationship between the median freezing temperature and the cooling rate, which is often referred to as an indicator of stochastic or singular description of ice nucleation. The INAS surface density can be derived from the CNT-based parameterization by substituting Eq. (2.24) into (2.19):

$$n_s(T) = \frac{n_{site}}{S_p}\left(1 - P_{unfr}(T, \mu_\theta, \sigma_\theta, t)\right) \quad (2.\ 25)$$

In this relationship, the quotient of n_{site} divided by S_p converges to n_s^* when the freezing probability P_{unfr} reaches zero. n_s^* is defined as the maximum possible number of ice nucleation sites per particle surface area.

2.5 Phase behavior of solute aerosol particles

The hygroscopicity determines the interaction of an aerosol particle with water vapor. Deliquescence and efflorescence are common phenomena describing the phase transitions from one to another physical state in an aerosol particle. As can be seen from figure 8, a pure solid NaCl particle absorbs only a negligible amount of water from the vapor phase as the relative humidity (RH) increases (red line). However, at the deliquescence relative humidity (DRH) of about 75% for anhydrous NaCl, a spontaneous uptake of water occurs, resulting in a saturated NaCl solution droplet. A further increase of the RH leads to a continuous growth of the NaCl droplet and a dilution of the solute. As the RH decreases, water evaporates from the aqueous solution droplet. Crystallization does not occur at the DRH value due to the absence of a critical germ. The aqueous droplet shrinks continuously until the supersaturated solution spontaneously crystallizes with the accompanying release of crystallization enthalpy and the evaporation of remaining water to the vapor phase (blue line). The efflorescence relative humidity (ERH) of NaCl is situated at approximately 45% at ambient temperature. The hysteresis gap between the ERH and DRH value of NaCl is apparent from figure 8. This difference between the deliquescence and efflorescence is quite common for various aqueous salt particles[6] (not only NaCl). In the bulk case, the deliquescence and efflorescence points coincide due to the large volume and the contact to catalyzing surfaces (e.g. the container wall).

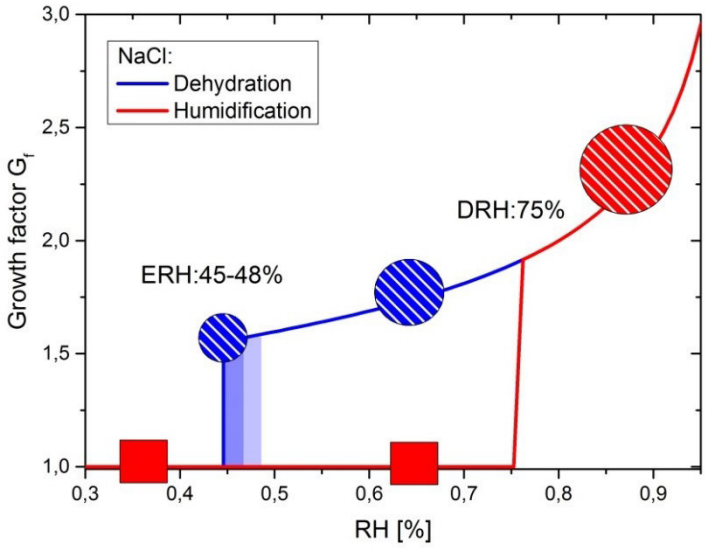

Figure 8: The hydration hysteresis diagram of sodium chloride (NaCl). The growth factor G_f as a function of relative humidity was calculated using the Extended Aerosol Inorganic model (E-AIM, version III at 298.15K, http://www.aim.env.uea.ac.uk/aim/aim.php)[72].

The phase diagram of NaCl/H_2O is depicted in figure 9. This diagram shows the relevant phases of the NaCl/H_2O system in the temperature vs. humidity space. The ice melting curve, the solubility curves of NaCl dihydrate and anhydrous NaCl enclose the stability region of the liquid phase. In particular, the solubility curve of anhydrous NaCl is equivalent to the temperature dependent DRH curve of anhydrous NaCl. The solubility curve of NaCl dihydrate is obtained by connecting the peritectic and eutectic points. At the eutectic temperature and composition, all three phases (i.e. ice, solid NaCl dihydrate and brine solution are in thermodynamic equilibrium. In contrast, at the peritectic temperature and composition, NaCl dihydrate decomposes into anhydrous NaCl and brine solution. Both points are so-called invariant, i.e. the NaCl/H_2O system has adopted a configuration, which has no degree of freedom. Below 0.15°C, NaCl dihydrate is the thermodynamically favorable solid NaCl phase. Further lowering the temperature or relative humidity leads to a metastable liquid. The homogeneous freezing curve and the temperature-dependent ERH curve define the boundaries of the stability region of the metastable liquid solution. At lower temperatures and/or relative humidities, only the solid crystalline phases are stable. The homogeneous freezing and the ERH curves exhibit a larger spread in the measurement data compared to the melting and deliquescence curves because the later ones are thermodynamic phase transitions. To be more specific, a linear fit to the ERH(T) data shows that the ERH decreases slightly with decreasing temperature, i.e. the ERH value is reduced from 43.4% to 37.7% in the range from 20°C to -20°C[73, 74]. A slightly increasing ERH value with decreasing temperature found was by Wise et al.[9]. The ERH values of anhydrous NaCl and NaCl dihydrate are nearly undistinguishable, while the DRH of the NaCl dihydrate (~85-87%) is significant higher than the DRH of the anhydrous NaCl form (~75%). Koop et al. showed that the phase diagram of NaCl/H_2O serve in the first approximation as a good proxy for the phase diagram of sea salt/H_2O [74].

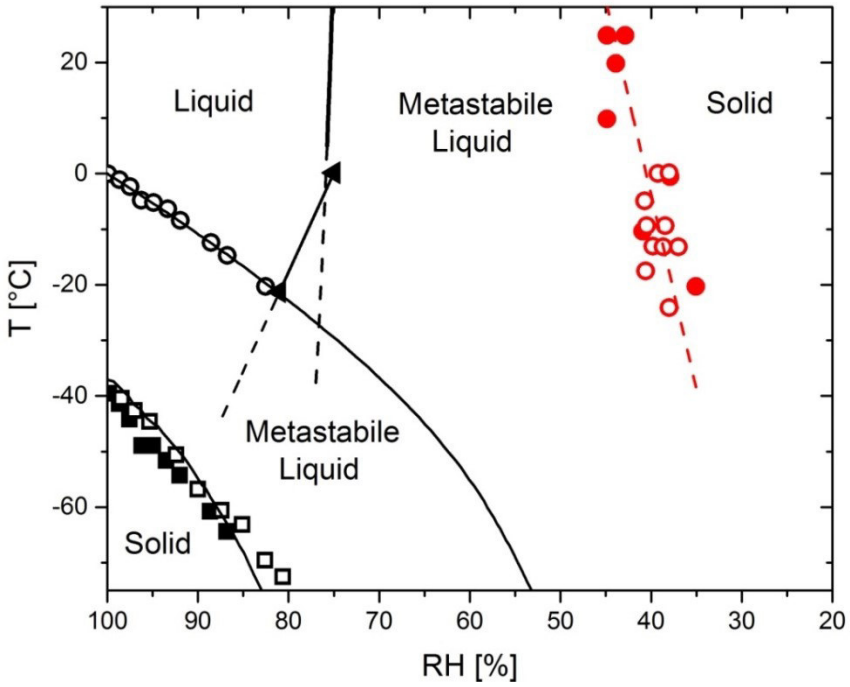

Figure 9: Phase diagram of sodium chloride (NaCl). The phase diagram is adapted from Koop et al.[74] and the references therein[75-79]. The black filled squares are taken from Koop and Zobrist[80]. The black line (solubility curve) based on Tang et al[81]. The black triangles denote the peritectic point: T=0.15°C at RH=75% and the eutectic point: -21.25°C at RH=81%[11]. The black dashed lines are linear extrapolations of the curves to lower temperatures. The red dashed curve is a linear fit to the efflorescence data points indicating the temperature dependence of the ERH.

However, previous measurements indicated that NaCl dihydrate has not been formed during the efflorescence of micron-sized NaCl solution droplets. In particular, Koop et al. conducted efflorescence and deliquescence experiments of NaCl droplets in an environmental cell in the temperature range from 249K to 273K and found no indication of NaCl dihydrate[74]. To a similar conclusion arrived Cziczo et al., who investigated the phase behavior of submicron-sized NaCl droplets with a flow tube setup coupled to an IR spectrometer in the temperature range from 298K to 253K[79]. The formation of NaCl dihydrate was actually observed in emulsion and bulk samples in homogeneous freezing experiments of NaCl solutions droplets by means of differential scanning calorimetry (DSC)[74].

Wise et al. studied the temperature-dependent partitioning between anhydrous NaCl and NaCl dihydrate by using an environmental cell equipped with a Raman microscope. The authors reported the temperature range from 236K to 252K, in which the transition between both phases occurred[9]. In contrast, Wagner et al. used the AIDA cloud chamber to investigate the temperature-dependent partitioning between the two solid phases of NaCl and observed the formation of NaCl dihydrate at much lower temperatures in the range from 235K to 210K[10]. The disagreement with Wise el al. was attributed to differences in the size of the NaCl particles, the humidity conditions and the possible influence of the substrate.

Extending the perspective to the more chemical complex sea salt system, the phase transitions of natural and simulated SSA particles containing no organic material were characterized by numerous studies with different experimental techniques[74, 82-85]. In general, the SSA particles have the ability to pick up significant amounts of water prior to the full deliquescence at 74% RH[82]. This behavior is probably related to the presence of hygroscopic inorganic salts such as $MgCl_2 \cdot 6H_2O$, which has a rather low DRH of 33%[77]. As opposed to solid anhydrous NaCl particles, after the efflorescence of the SSA particles residual water in the liquid state remained in the SSA particles as inferred from D_2O exchange experiments[77].

The formation of ice and NaCl dihydrate in emulsion samples and additionally the formation of magnesium chloride dodecahydrate ($MgCl_2 \cdot 12H_2O$) in bulk samples was confirmed by DSC experiments of homogeneous freezing of simulated sea water as reported by Koop et al.[74] The authors concluded that SSA particles are likely in a liquid state most of their residence time in the polar marine boundary layer.

Schill et al. described both the water uptake and the ice nucleation behavior of simulated SSA particles and mixed SSA/sucrose particles in the temperature range from 235K to 215K. Water uptake was recognized by the appearance of spectral features in the Raman spectra of deposited SSA particles already at 17% RH and 215K[12]. In addition, Schill et al. stated that above 230K the SSA particles fully deliquesced and below 225K immersion-in-solution nucleation was obtained. Very soluble components in the salt mixture probably enhance the water uptake prior to the ice nucleation. For mixed SSA/sucrose particles deliquescence above 225K and depositional ice nucleation below 220K was obtained. The observation of deposition ice nucleation of mixed SSA/sucrose particles was interpreted in terms of the formation of a glassy salt/organic matrix at low temperatures. Unfortunately, NaCl dihydrate was not observed in the SSA particles due the procedure of particle generation at ambient temperatures (~25°C).

2.6 Nucleation in solute aerosol particles

2.6.1 Homogeneous efflorescence

Efflorescence is considered as a process of homogeneous nucleation of a salt crystal in a solution supersaturated with respect to the solute. The theoretical treatment is analogous to the homogeneous ice nucleation[60]. Homogeneous efflorescence exhibits a stochastic nature of crystal nucleation. RH-cycle experiments of aqueous NaCl droplets at 20.1°C conducted in an electrostatic levitator showed a large variation in the incubations times (i.e. the time between reaching the equilibrium of the supersaturated state at 51% RH and the nucleation event). These observations were interpreted in terms of a stochastic process driven by random fluctuations in the metastable solution[86]. In a similar experiment, a single NaCl particle was cycled serval times in an electrodynamic balance to observe the reproducibility of the efflorescence RH. A spread of mole fractions at which crystallization occurred around the expectation value of 0.17 for NaCl was observed indicating the non-deterministic behavior of efflorescence[87]. Homogeneous efflorescence or solute crystallization can be viewed as a specific process within the more encompassing concept of crystallization[6].

Another similarity to homogeneous ice nucleation is the volume or size dependence of homogeneous efflorescence. The mean freezing temperature of a water droplet scales with the volume or size of the droplet, i.e. the larger the volume of the droplet, the less it can be supercooled before it freezes. The lowest freezing temperatures range from -33°C to -44°C for several millimeter to $2 \cdot 10^{-5} cm$ diameter droplets [22]. Gao et al. found that the ERH of NaCl decreases with decreasing particles size from 48% at d=20µm to a minimum ERH of 44% at 60-70µm. For smaller particles (d< 60-70µm) the ERH increased again due to the Kelvin effect[88], in agreement with other experimental data[89, 90]. Larger ERH values than 48% are expected to originate from heterogeneous nucleation due to impurities in the solution. These findings emphasize a similar treatment of both solute and ice nucleation bearing in mind that the thermodynamic driving forces for homogeneous ice nucleation are the temperature gradient (i.e. supercooling) and the difference in the vapor pressures of ice and supercooled water and for homogeneous efflorescence the difference in the vapor pressures of the solution and the surrounding gas phase (i.e. supersaturation with respect to the solute). The next paragraph gives a brief theoretical description of homogeneous efflorescence.

The theoretical considerations of homogeneous efflorescence follow the textbook of Khvorostyanov and Curry[60]. An expression for the critical radius r_{cr} of a salt germ can be derived by analogy to the homogeneous freezing:

$$r_{cr} = \frac{2\nu_c \sigma_{cs}}{kT ln(S_*)} \qquad (2.\ 26)$$

where ν_c is the specific volume of the solid salt, σ_{cs} is the surface tension at the interface of a salt crystal and solution, k is the Boltzmann constant and S_* is the critical salt supersaturation. S_* is defined as follows:

$$S_* = \frac{a_{s,eff}}{a_{s,del}} \tag{2. 27}$$

The salt supersaturation is the quotient of the solute activities at nucleation, i.e. the efflorescence RH and at the deliquescence RH with a saturated salt concentration of the solution droplet. The critical energy ΔF_{cr} for the formation of a salt germ can be expressed as:

$$\Delta F_{cr,eff} = \frac{16\pi}{3} \frac{{\nu_c}^2 {\sigma_{cs}}^3}{[kTln(S_*)]^2} \tag{2. 28}$$

To obtain the critical supersaturation S_* directly from the experimental measurements, a two-component system consisting of the solute and water is considered. If the Gibbs-Duhem equation at constant temperature and pressure is applied, then the following equation can be obtained:

$$dln(a_s) = -\left(\frac{x_w}{x_s}\right) dln(a_w) \tag{2. 29}$$

Integration of equation (2.29) between the solute activities at deliquescence and efflorescence yields[91]:

$$ln(S_*) = -\int_{a_{w,del}}^{a_{w,eff}} \left(\frac{x_w}{x_s}\right) dln(a_w) \approx -\int_{a_{w,del}}^{a_{w,eff}} \left(\frac{x_w}{x_s}\right) dln(RH_w) \tag{2. 30}$$

The ratio of the partial pressure of water $p_{H_2O}(T)$ to its saturation vapor pressure $p_{H_2O,sat}(T)$ for a given temperature is the relative humidity. The relative humidity with respect to water RH_w and the water activity a_w are directly related in the case of an aqueous solution phase in equilibrium with the surrounding vapor phase:

$$a_w = \frac{p_{H_2O}(T)}{p_{H_2O,sat}(T)} = \frac{RH_w}{100\%} \tag{2. 31}$$

The nucleation rate coefficient for homogeneous efflorescence can be written as:

$$J_{hom}^{eff} = c_{hom}^{eff} exp\left(\frac{-\Delta F_{cr,eff}}{kT}\right) exp\left(\frac{-\Delta F_{act,eff}}{kT}\right) \tag{2. 32}$$

where c_{hom}^{eff} is the kinetic coefficient of efflorescence, $\Delta F_{cr,eff}$ is the free energy of salt germ formation and $\Delta F_{act,eff}$ is the activation energy for the diffusion of solute molecules to the salt germ. The kinetic coefficient is defined as:

$$c_{hom}^{eff} = 2N_{cc}\left(\frac{\nu_{s0}}{\nu_{c0}}\frac{kT}{h}\right)\left(\frac{\sigma_{cs}}{kT}\right)^{1/2} = 2N_{cc}\left(\frac{\rho_{c0}}{\rho_{s0}}\frac{kT}{h}\right)\left(\frac{\sigma_{cs}}{kT}\right)^{1/2} \tag{2. 33}$$

where N_{cc} is the number of salt molecules in a crystal in contact with the unit area of a solution, ν_{s0} and ν_{c0} are the salt molar volumes in solid and solution respectively and ρ_{s0} and ρ_{c0} are the corresponding specific densities of the crystal and the salt in solution respectively.

2.6.2 Modelling of homogeneous efflorescence

From a modelling perspective, NaCl nucleation from a supersaturated solution can be viewed as a two-step mechanism[92]. At first, random concentration fluctuations give rise to higher concentrated regions, where less ordered arrangements of hydrated ions exist. It is argued that this loosely arrangements are described by Ostwald's rule of stages, which suggests that the prenucleation stage resembles more the metastable NaCl solution than the final anhydrous NaCl crystal[93]. These suggestions are in opposite to the predictions of the classical nucleation theory. In the early stages of nucleation, small clusters of partially hydrated Na^+ ions appeared in the trajectories of molecular dynamics (MD) simulations suggesting that these are the centers of stability[94]. The centers are characterized by Na^+ ions surrounded by no (i.e. six Cl^- ions) or at most one water molecule (i.e. five Cl^- ions).

The second step is associated with the spatial ordering of ions from a loosely arrangement of ions to a nanocrystal of critical size. This step constitutes the rate determining step. According to the literature, several values are estimated for the size of the critical NaCl nucleus ranging from ~40-70 atoms[95] to ~75 ions[92] (corresponding to a critical nucleus of ~1nm). After formation, the nucleus irreversibly grows and consumes the supersaturation in the solution. Zimmermann et al. [96] underlined that NaCl nucleated via the common rock-like structure in their MD simulations, but the attachment of ions is governed by ion desolvation rather than by diffusion of ions through the aqueous solution to the crystal site. In the course of crystal growth, aggregation and coalescence of nanocrystals can occur due to imperfections of the ion attachment leading to the formation of polycrystalline structures with non-uniform shape in the resulting (macro)crystal. These MD simulations represent a non-classical pathway of nucleation and crystal growth and illustrate how MD simulations can contribute to the ongoing debate of solute nucleation from an atomistic point of view.

2.6.3 Heterogeneous efflorescence

Heterogeneous efflorescence can be triggered via a solid nucleus either immersed into a solution droplet or colliding with a solution droplet. In immersion mode efflorescence, a relatively insoluble nucleus is immersed in an aqueous solution droplet and initializes solute nucleation at higher ERH values compared to the homogeneous ERH value, i.e. a lower supersaturation with respect to the solute is required to nucleate the solution droplet. Oatis et al. have studied the substances $CaCO_3$ and $BaSO_4$ immersed into aqueous ammonium sulfate (AS) solution droplets and found out that efflorescence occurred at ERH values of 49% and 46% respectively[91]. Without heterogeneous nuclei the efflorescence of AS was observed in the RH range from 33-37%. Richardson and Snyder showed at in the ternary system consisting of $NaCl/KCl/H_2O$, the less soluble component, KCl, can be a potential heterogeneous catalyst for the efflorescence of NaCl. ERH values of 62% and 65% for KCl and NaCl respectively were obtained[81, 97].

More recently, Davis et al. reported that contact mode efflorescence can be atmospherically relevant pathway of heterogeneous efflorescence[98]. In an optical levitator, solid AS particles as contact nuclei collide with supersaturated AS solution droplets inducing efflorescence close to the DRH value of AS (ERH =77±1%)[99]. An ERH value near or rater close to the respective DRH value is the highest RH at which crystallization is thermodynamically possible. In a follow-up study, several solute-contact nuclei pairs were investigated. The authors come to the conclusion that isochemical systems (where seed crystal is of the same composition as the anticipated crystalline phase of the solution droplet) exhibited higher ERH values than the heterochemical systems. These observations were interpreted in terms of a better lattice match for the isochemical solute-contact nuclei pairs[98].

It is assumed that heterogeneous efflorescence can be similarly treated as the heterogeneous ice nucleation in section (2.4.2). More sophisticated approaches have been developed to account for the geometry of nucleus on the substrate. An expression of the geometric factor for nucleation on a planar substrate is given by equation (2.13). For a curved substrate, i.e. a convex insoluble solid particle, the geometric factor $f(m_{cs}, x)$ has the form:

$$f(m_{cs}, x) = \frac{1}{2}\left[1 + \left(\frac{1 - m_{cs}x}{y}\right)^3 + x^3(2 - 3\psi + \psi^3) + 3m_{cs}x^2(\psi - 1)\right] \quad (2.\ 34)$$

where $\psi = (x - m_{cs})/y,\ y = (1 - 2m_{cs}x + x^2)^{1/2},\ x = r_N/r_{c,eff}$ and $m_{cs} = cos(\theta)$. r_N and $r_{c,eff}$ refer to the radii of the foreign substrate inside the solution droplet and the salt germ respectively. The free critical energy of heterogeneous efflorescence is modified by the geometric factor:

$$\Delta F_{cr,eff} f(m_{cs}, x) = \frac{16\pi}{3} \frac{{\nu_c}^2 {\sigma_{cs}}^3 f(m_{cs}, x)}{[kTln(S_*)]^2} \quad (2.\ 35)$$

The heterogeneous nucleation rate coefficient on the entire surface of the salt germ can be calculated using the following equation:

$$J_{het}^{eff} = c_{het}^{eff} exp\left(\frac{-\Delta F_{cr,eff} f(m_{cs}, x)}{kT}\right) exp\left(\frac{-\Delta F_{act,eff}}{kT}\right) \quad (2.\ 36)$$

The kinetic coefficient of heterogeneous efflorescence becomes:

$$c_{hom}^{eff} \approx N_{cc}\left(\frac{kT}{h}\right) c_{1cs} 4\pi r_{c,eff}^2 \quad (2.\ 37)$$

where c_{1cs} is the number of molecules adsorbed on the surface of the crystal. $4\pi r_{c,eff}^2$ describes the surface area of the salt germ which means that heterogeneous solute nucleation is proportional to the size of the salt critical germ.

2.7 Liquid-liquid phase separation (LLPS)

Liquid-liquid phase separations are thought to be of atmospheric importance for the change of the gas-particle partitioning of organic species[100], in the suppression of reactive uptake of N_2O_5 onto aerosol particles[101] and in heterogeneous ice nucleation processes[102]. LLPS are observed during the dehydration of multinary aqueous aerosols consisting of inorganic and organic components. Several mechanisms are proposed via LLPS can proceed: 1) spinodal decomposition, 2) nucleation-and-growth and 3) growth of a second phase at the surface of the particle depending on the organic to inorganic ratio (OIR)[13]. From a theoretical perspective, bimodal demixing is distinguished from spinodal decomposition[103]. Binodal demixing can be similarly treated as homogeneous nucleation. Statistical fluctuations induce the nucleation process, which is associated with a distinct nucleation barrier. On the other side, spinodal decomposition is a diffusion-limited process. There exists no nucleation barrier in spinodal decomposition and small fluctuations lead to the spontaneous formation of a new liquid phase in the entire droplet.

An example of LLPS is illustrated in figure 10. In the case of the dicarboxylic acids/ammonium sulfate/water (C6/AS/H_2O) mixture with an OIR of 0.5, first indications of LLPS are observed at 73.4%RH[13]. At RH=71.9%, an inner phase and satellite inclusions have formed consisting of aqueous ammonium sulfate. Further lowering the RH results in the coagulation of the AS inclusions into larger ones. At this stage, the internal configuration of the phases resembles a core-shell structure with small inclusions. Continuous drying tended the inner phase to move from the center to the edge of the droplet. At 67.2%RH, the droplet has adopted a partially engulfed morphology. Finally at 46.3RH%, the AS phase effloresced and may initiated the nucleation of the organic C6 phase. It was underlined that the LLPS of the C6/AS/water system with a mass fraction of solute (mfs) of 0.5 proceeded via spinodal decomposition (mfs between 0.4 and 0.7). At lower compositions (mfs between 0.07 and 0.4) predominantly nucleation-and-growth is expected.

The spatial separation of organic and inorganic components during the dehydration process seems to be a quite common feature of multinary organic/inorganic/water aerosols[104, 105]. Peckhaus et al. showed that spatial separation in ternary aerosols including the dicarboxylic acids (glutaric and malonic acid) and the inorganic salts (ammonium sulfate and nitrate) occurred during the efflorescence and can be detected in the effloresced particles by Raman mapping experiments[104].

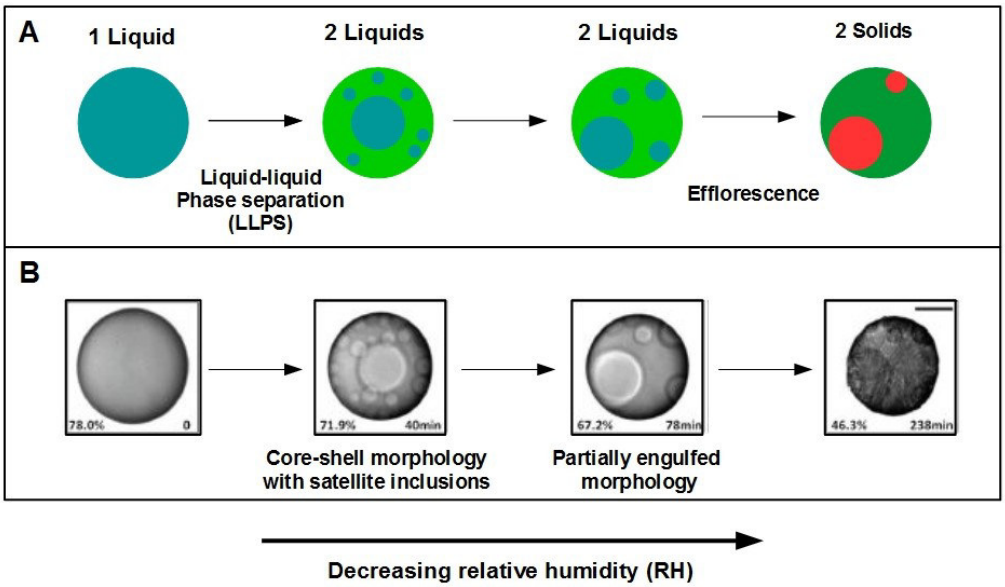

Figure 10: A) Schematic representation of the liquid-liquid phase separations and phase transitions occurring in mixed dicarboxylic acids/ammonium sulfate/water (C6/AS/H_2O) aerosol particles. B) Sequence of optical microscope images of a single aerosol particle consisting of C6/AS/H_2O with an organic-inorganic ratio (OIR) of 0.5. The optical microscopic images are taken from Song et al[13].

3. Methods

3.1 Principles of electrodynamic levitation

The principle of operation of an electrodynamic balance (EDB) goes back to the work of Paul et al.[106], who described successfully the basics of the quadrupole electric mass filter in 1955. As described in Davis et al.[107], since then many other configurations of an EDB have been developed for single microparticle studies. A brief recapitulation of the theoretical basics is provided here following the doctoral thesis of Dr. Denis Duft[108] and Dr. Nadine Hoffmann[109].

Several forces act on a charged particle suspended in an electrodynamic balance. The electric force F_e counteracts the gravitational force F_g and the drag force F_d. The gravitational force is defined as the product of the mass of the particle multiplied by the acceleration of gravity. The drag force originates from the friction of the particle on the air flow passing through the EDB. The balance of forces can be set up as follows:

$$F_e - F_g - F_d = 0 \tag{3. 1}$$

After substitution of equation (3.1):

$$qE - mg - 6\pi\eta r v = 0 \tag{3. 2}$$

where q is the charge, E is the electric field strength, m is the mass of the particle, g is the acceleration of gravity, η is the dynamic viscosity, r is the radius of the particle and v is the flow velocity. For the stabile storage of a charged particle in the EDB a temporally constant force field has to be applied. At the location of the particle $P(x_0, y_0, z_0)$ all external forces are compensated and the particle is located in a potential minimum. The potential $\Phi(x_0, y_0, z_0)$ must satisfy the following conditions:

$$\nabla\Phi(x_0, y_0, z_0) = 0$$
$$\Delta\Phi(x_0, y_0, z_0) > 0 \tag{3. 3}$$

An electrostatic force field contradicts the Laplace equation. This equation does not allow a minimum of the electrical potential in a charge free space:

$$\Delta\Phi(x_0, y_0, z_0) = 0 \tag{3. 4}$$

This restriction excludes the permanent storage of electrically charged particles with an electrostatic force field. To overcome is constraint, an electrodynamic field can be considered. In an electrodynamic field, the particle experiences only the force of a time-averaged field. This allows to stably trap a particle in all directions. To calculate the time-averaged force acting on the particle, let us first consider the motion of the charged particle in an electric field of the form:

$$E(z, t) = E_0(z)cos(\omega t) \tag{3. 5}$$

The amplitude $E_0(z)$ of the vibration of the particle is small compared to the time averaged motion for the particle. The motion of the particle $z(t)$ is assumed to be a superposition of two components:

$$z(t) = \bar{z}(t) + \xi(t) \tag{3. 6}$$

$$\xi(t) = \xi_0 cos(\omega t) \tag{3. 7}$$

The average motion $\bar{z}(t)$is given by the following equation:

$$\bar{z}(t) = \frac{\omega}{2\pi} \int_{t}^{t+\frac{2\pi}{\omega}} z(\tau) d\tau \tag{3. 8}$$

After substitution of equations (3.7) and (3.8) in (3.6), the motion of a particle $z(t)$ has the form:

$$z(t) = \frac{\omega}{2\pi} \int_{t}^{t+\frac{2\pi}{\omega}} z(\tau) d\tau + \xi_0 \, cos(\omega t) \tag{3. 9}$$

The equation of motion follows the formula:

$$m\ddot{z} = qE(z,t) = qE_0(z)cos(\omega t) \tag{3. 10}$$

A series expansion gives the equation:

$$m\ddot{z} = m\ddot{\bar{z}} + m\ddot{\xi} = qE(\bar{z},t) + q\xi \frac{\partial E(\bar{z},t)}{\partial \bar{z}} \tag{3. 11}$$

The amplitude of oscillation is related to the strength of the electric field as a good approximation for small amplitudes:

$$m\ddot{\xi} = qE(\bar{z},t) \tag{3. 12}$$

Integration of equation (3.12) yields:

$$\xi(\mathrm{t}) = -\frac{q}{m\omega^2} E_0(\bar{z}) \cos(\omega t) \tag{3. 13}$$

The time-averaged force on the particles can then be written as:

$$\overline{\mathrm{m}\ddot{z}} = \overline{qE(\bar{z},t)} + \overline{q\xi \frac{\partial E(\bar{z},t)}{\partial \bar{z}}} = q \frac{\partial E_0(\bar{z})}{\partial \bar{z}} \xi_0 \overline{cos^2(\omega t)} \tag{3. 14}$$

The time-averaged force can be expressed as:

$$\bar{F}(\bar{z}) = -\frac{1}{2} \frac{q^2}{m\omega^2} E_0(\bar{z}) \frac{\partial E_0(\bar{z})}{\partial \bar{z}} \tag{3. 15}$$

The quadratic dependency of the averaged force on the particle charge indicates that the average force is independent of the polarity of the charged particle. The averaged force can be written as the derivative of the pseudo potential:

$$\bar{F}(\bar{z}) = -q\,\nabla\Phi_{pseudo}(\bar{z}) \tag{3. 16}$$

The pseudo potential has the form:

$$\Phi_{pseudo}(\bar{z}) = \frac{1}{4}\frac{q}{m\omega^2}E_0^2(\bar{z}) \tag{3. 17}$$

In the minimum of the pseudo potential a time-averaged force acts on the particle and allows to capture the particle.

In the case of a quadrupole field, the pseudo potential has the form:

$$\Phi(x,y,z) = \Phi_0(\alpha x^2 + \beta y^2 + \gamma z^2) \tag{3. 18}$$

To fulfill the requirements of the Laplace equation the sum of the coefficients must be zero:

$$2\Phi_0(\alpha + \beta + \gamma) = 0 \tag{3. 19}$$

For example, a possible solution of equation (3.19) is:

$$\alpha = \beta \ \wedge\ \gamma = -2\alpha \tag{3. 20}$$

Then, the pseudo potential becomes:

$$\Phi(x,y,z) = \Phi_0\alpha(x^2 + y^2 - 2z^2) \tag{3. 21}$$

A representation of the pseudo potential in cylindrical coordinates simplifies equation (3.21) to:

$$r^2 = x^2 + y^2 \tag{3. 22}$$

and

$$\alpha = \frac{1}{r_0^2} \tag{3. 23}$$

Substituting equations (3.22) and (3.23) in (3.21) results in:

$$\Phi = \frac{\Phi_0}{r_0^2}(r^2 - 2z^2) \tag{3. 24}$$

The equipotential surfaces of this pseudo potential describe a rotationally symmetric object with a hyperboloidal geometry. The form of the electrodes of the electrodynamic balance used in the experimental setup (see section 4.2) exhibit the described design to stably levitate a charged microparticle.

3.2 Fundamentals of Raman spectroscopy

The Raman effect was first theoretically predicted by Adolf Smekal[110] in 1923 and then experimentally discovered by Raman and Krishnan[111] and by Landsberg and Mandelstein[112] in 1928. The Raman effect can be described by a scattering process, in which overall two photons are involved. In the scattering process, an incident photon is absorbed by the molecular system and immediately after the absorption a second photon is emitted. The inelastically scattered Raman photons exhibit a different frequency and energy as the incident photons.

The following derivation of the important equations based on the textbooks of C.J.H. Schutte[113] and E. B. Wilson[114]. In the framework of the classical electromagnetic theory, it is assumed that light is emitted from the molecular system as a result of the induced dipole oscillations of the molecule by an irradiating electromagnetic field. In the case of Rayleigh scattering, the dipole oscillations of the molecule have the same frequency as the incoming light. The time-dependent electric field strength $E(t)$ with the amplitude E_0 and the frequency of the incident light ν_0 follow the relation:

$$E(t) = E_0 cos(2\pi\nu_0 t) \tag{3. 25}$$

The induced dipole moment μ of the molecule depends on the polarizability tensor α, a quantity for the deformation of the electron shell by the electromagnetic field of the incident light and the electric field strength vector E:

$$\mu = \alpha E \tag{3. 26}$$

The polarizability tensor α can be written in the matrix notation as:

$$\alpha = \begin{pmatrix} \alpha_{xx} & \alpha_{xy} & \alpha_{xz} \\ \alpha_{yx} & \alpha_{yy} & \alpha_{yz} \\ \alpha_{zx} & \alpha_{zx} & \alpha_{zz} \end{pmatrix} \tag{3. 27}$$

The induced dipole moment is not parallel to the electromagnetic field which perturbs the molecule. By combining the equations (3.25) and (3.26) yields:

$$\mu = \alpha E_0 \cos(2\pi\nu_0 t) \tag{3. 28}$$

For a molecular system executing small vibrations, the polarizability may be expanded in terms of normal coordinates. If Q_i is a vibrational normal mode of the molecule, then the polarizability can be written as follows:

$$\alpha(Q_i) = \alpha_0 + \sum_i \left(\frac{\partial\alpha}{\partial Q_i}\right)_0 Q_i + higher\ terms \tag{3. 29}$$

For simplicity terms of higher order are neglected in the following derivation and only the first two terms are considered. Assuming that the normal mode is periodic in time, then Q_i will be of the form:

$$Q_i = Q_i^0 \cos(2\pi\nu t) \tag{3. 30}$$

If the equations (3.29) and (3.30) are substituted in equation (3.28), then an expression for the dipole moment is obtained:

$$\mu = \left[\alpha_0 + \left(\frac{\partial \alpha}{\partial Q_i}\right)_0 Q_i^0 \cos(2\pi\nu t)\right] E_0 \cos(2\pi\nu_0 t) \tag{3. 31}$$

By using a trigonometrical addition theorem, the product of two cosine functions can be transferred into the sum of two cosine functions:

$$cos(A)\, cos(B) = \frac{1}{2}[cos(A+B) + cos(A-B)] \tag{3. 32}$$

If this addition theorem is used, then the equation for the dipole moment (3.31) becomes:

$$\mu = \underbrace{\alpha_0 E_0 cos(2\pi\nu_0 t)}_{Rayleigh} + \underbrace{\frac{1}{2}\left(\frac{\partial \alpha}{\partial Q_i}\right)_0 E_0 Q_i^0\, cos[2\pi t(\nu_0 - \nu)]}_{Stokes}$$

$$+ \underbrace{\frac{1}{2}\left(\frac{\partial \alpha}{\partial Q_i}\right)_0 E_0 Q_i^0\, cos[2\pi t(\nu_0 + \nu)]}_{Anti-Stokes} \tag{3. 33}$$

The last formula shows that there are three types of scattered light in the linear expansion. The first term in this equation is equivalent to the Rayleigh scattering (an elastic scattering process), the other two terms describe the anti-Stokes and the Stokes scattering and refer to inelastic scattering. As can be seen from equation (3.33), an important prerequisite for the Raman scattering is the change in polarizability during the displacement of the atomic cores.

This requirement for Raman active vibrations in the spectra can be expressed as:

$$\left(\frac{\partial \alpha}{\partial Q_i}\right)_0 \neq 0 \tag{3. 34}$$

The total intensity I_R radiated by an oscillating dipole is related to the induced dipole moment and can be written as:

$$I_R = \frac{(2\pi\nu_0)^4}{3c^3} |\mu|^2 \tag{3. 35}$$

If equation (3.33) is substituted in (3.35), the total scattered intensity can be obtained:

$$I_R = \frac{(2\pi\nu)^4}{3c^3} {\alpha_0}^2 {E_0}^2 cos^2(2\pi\nu_0 t) + \frac{1}{4}\frac{(2\pi\nu)^4}{3c^3}\left(\frac{\partial \alpha}{\partial Q_i}\right)_0^2 {E_0}^2 {Q_i^0}^2\, cos^2[2\pi t(\nu_0 - \nu)]$$

$$+ \frac{1}{4}\frac{(2\pi\nu)^4}{3c^3}\left(\frac{\partial \alpha}{\partial Q_i}\right)_0^2 {E_0}^2 {Q_i^0}^2\, cos^2[2\pi t(\nu_0 + \nu)] \tag{3. 36}$$

This means that the intensity of the Rayleigh scattering depends strongly on the value of the molecular polarizability, while the Stokes and the anti-Stokes scattering depend on the square of the rate of change of the polarizability. The intensity of a particular Raman band (i.e. Stokes scattering) can be used for quantitative measurements. In Raman spectroscopy, the intensity of a band is directly proportional to the molecular species, unlike Infrared (IR) spectroscopy, in which the Beer-Lambert law describes the logarithmic dependence of the ratio between transmitted and incident light and the concentration of molecular species in the cuvette. The observed Raman intensity $I_R$can be expressed as:

$$I_R = \sigma(\lambda_0) L c I_0 k \tag{3. 37}$$

where σ is the apparent Raman scattering efficiency (depending on excitation wavelength), L is the interrogated volume, c is the concentration of species, I_0 is the incident intensity of the laser beam und k is the instrument specific throughput.

For practical proposes, the Raman shift $\Delta\tilde{\nu}$ is defined as the difference between the inverse of the excitation wavelength λ_0 and the wavelength of a specific Raman band λ_1. The following formula can be used to calculate the Raman shift in units of inverse wavenumbers:

$$\Delta\tilde{\nu} = \frac{1}{\lambda_0} - \frac{1}{\lambda_1} \tag{3. 38}$$

The wavenumber $\tilde{\nu}$ of a particular Raman band can be converted into the frequency via the speed of light and into the wavelength λ:

$$\tilde{\nu} = \frac{\nu}{c} = \frac{1}{\lambda} \tag{3. 39}$$

A quantum mechanical description of the Raman effect improved the understanding of i) the splitting of closely spaced lines (rotational-vibrational Raman spectra)[114], ii) the prediction of intensities for the Stokes and anti-Stokes lines and iii) the selection rules of Raman activity[113]. From the quantum mechanical perspective, Raman and Rayleigh scattering processes can be illustrated in terms of an energy level scheme. In elastic Rayleigh scattering, the energies of the incident and scattered photons are equal, i.e. no change in frequency or wavelength is observed (see left panel of figure 11). In the case of Raman scattering, the energy of the emitted photon deviates from the energy of the incident photon. The resulting energy difference is due to the transition between two different molecular states. If an incident light beam interacts with a molecular system, the molecule is excited from a vibrational level of the electronic ground state to a virtual state. The virtual state is an intermediate energy state with a short life time. The energy of this state strongly depends on the incident light frequency. Whether the molecule is in the lowest vibrational state or in an excited vibrational state of the electronic ground state, determines the emission of a Stokes photon or an anti-Stokes photon respectively.

The described scattering processes have a very weak Raman intensity (see right panel of figure 11). Only one out of 10^6 irradiated photons is involved in the Rayleigh scattering process. The fraction of Stokes and anti-Stokes scattered photons is significantly smaller. Due to the Boltzmann distribution of vibrational states, more molecules occupy the lowest accessible vibrational state and thus give rise to the higher intensity ($\sim 10^{-9}$) of the Stokes Raman band compared to the lower intensity of the anti-Stokes Raman band ($\sim 10^{-11}$).

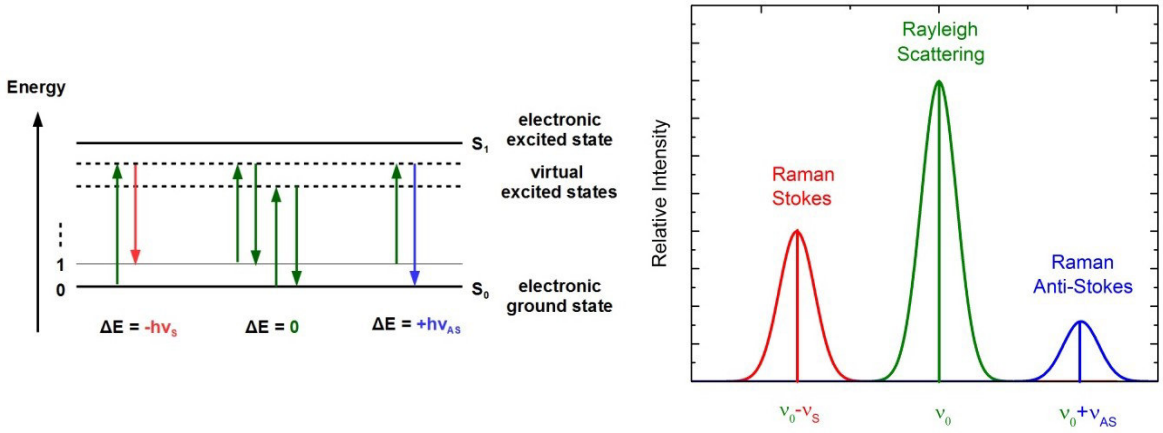

Figure 11: Left) Energy level scheme of the scattering processes. Right) The corresponding Raman spectra of the scattering processes. The relative signal intensities of the Raman bands are plotted as a function of frequency. The figure is adapted and modified from the textbooks[115, 116] and the doctoral thesis of S. Graß[117].

To illustrate the relationship between molecular structure and Raman activity, the fundamental vibrations of the sulfate ion (SO_4^{2-}) are considered. The free dissolved SO_4^{2-}-ion exhibit a T_d symmetry with 3N-6=9 fundamental vibrations. The irreducible representation of the point group T_d is $\Gamma_{vib}(T_d) = A_1 + E + 2F_2$.Thus the SO_4^{2-}-ion splits in four modes: The modes $\nu_1(A_1)$ and $\nu_2(E)$ are Raman active, whereas the two vibrations $\nu_3(F_2)$ and $\nu_4(F_2)$ are active in both the Infrared and Raman. The $\nu_1(A_1)$ is the symmetric stretching mode (figure 12A), $\nu_2(E)$ is the asymmetric stretching mode (figure 12B) and $\nu_3(F_2)$ and $\nu_4(F_2)$ are bending vibrations (figure 12C-D). The latter vibrations are energetically degenerated. The recapitulation of the Raman active modes of the sulfate molecule will be essential for the interpretation and analysis of vibrations in simulated sea salt particles (see section 5.5.2).

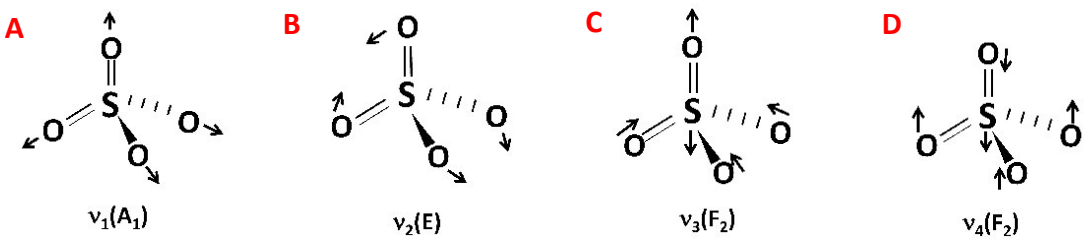

Figure 12: Raman normal modes of the sulfate molecule. The images are taken from the supplementary information of K. B. Mabrouk[118].

3.3 Analysis of Mie scattering

In 1908, Gustav Mie theoretically describes the elastic scattering of electromagnetic radiation by a homogeneous spherical particle[119]. A detailed description of the Mie theory is provided in Bohren and Huffman[120]. In short, the dimensionless size parameter x was introduced to discriminate between different scattering regimes:

$$x = \frac{2\pi r}{\lambda} \tag{3. 40}$$

where r is the radius of the droplet and λ is the wavelength. For the first case $x \ll 1$, Rayleigh scattering dominates, i.e. the scattering object is much smaller than the wavelength of light. In the second case $x \sim 1$, Mie scattering can be assumed, i.e. the object and the wavelength of light are of comparable size. In the last case $x \gg 1$, the classical (or geometric) scattering can be applied. For the droplets examined in this thesis, the Mie theory is appropriate for the determination of the size of the droplets. For the purpose of size determination, two dimensional angle-resolved optical scattering (TAOS) pattern are recorded (see section 5.6.5). These scattering pattern are intensity distributions of the elastically scattered light (in the polar and azimuthal angle range). A horizontal cross section of the scattering pattern delivers the phase function for a specific scattering angle range and at a given wavelength[109]. The distance between adjacent intensity maxima and minima is related to the size of the droplet. The phase function in turn is defined as the angular distribution of light intensity scattered by a spherical object at a given wavelength.

A more advanced approach is the Mie resonance spectroscopy. Typically, the spectra are expressed in the intensity vs. wavelength space and contain characteristic resonances (the so-called morphology-dependent resonances, MDRs), which can be illustrated as standing waves, with an integer number of wavelengths undergoing almost total internal inflections near the droplet surface[121]. Low resolution (light emitting diode, LED) Mie resonance spectroscopy allowed for the tracking of the size of the droplet, while the high resolution (tunable diode laser, TDL) Mie resonance spectroscopy is used to simultaneously determine the refractive index and the size of the droplet by comparing the measured spectra with Mie calculations[122]. The Mie resonances are characterized by the mode number and the mode order. The mode number is the angular variation of the internal mode intensity. The mode order is the number of radial maxima in the distribution of the mode intensity. It simply defines how deep a Mie resonance can penetrate into the droplet. The higher the mode order, the closer is the resonance at the surface and therefore more sensitive to changes at the liquid/air interface. For each mode number and order there exist a transversal electric (TE) and a transversal magnetic (TM) polarization, which have no radial electric or magnetic field component respectively[121]. In this thesis only TE-polarized Mie resonance spectra are presented (see section 5.6.3).

4. Experimental

The heterogeneous ice nucleation efficiencies of feldspar particles immersed into water droplets are studied with the novel cold stage apparatus. The working principle and the conducted experiments are outlined in section 4.1. Large parts of the section 4.1 are taken from Peckhaus et al[123]. The electrodynamic balance/Raman microscope setup which was used for the investigation of the solute crystallization of levitated NaCl and SSA droplets is described in subsequent section 4.2.

4.1 Cold Stage setup

The central part of the experimental setup is a cold stage (Linkham, Model MDBCS-196), which was used to carry out the cooling ramp and isothermal experiments (see figure 13). Cooling is achieved by pumping liquid nitrogen from a reservoir through the copper sample holder. The cold stage can operate in the temperature range from 77K to 400K. Controlled heating and cooling ramps can be performed at rates between 0.01 K/min to 100 K/min. The temperature stability is better than 0.1K.

A single crystal silicon substrate (Plano GmbH, 10×10 mm) was first cleaned with high grade acetone (p.a.) and then rinsed several times with NanoPure water (Barnstead Thermolyne Corporation, Infinity Base Unit, 18.2 MΩ·cm). Finally, the silicon wafer was purged with nitrogen to remove residual water. The cleaned silicon wafer was mounted into a square depression in the sample holder. It was shown before that a surface prepared in this way induces freezing of pure water drops only at temperatures very close to the temperature of homogeneous freezing[124].

The feldspar suspensions were prepared by adding the feldspar powder into 25 mL of NanoPure water and stirred for an hour. A piezo-driven drop-on-demand generator (GeSIM, Model A010-006 SPIP, cylindrical case) was used to print individual suspension droplets in a regular array onto the silicon substrate. Before dispensing, the substrate was cooled to the ambient dew point to reduce the evaporation of droplets. Up to 1000 suspension droplets of (215 ± 70) pL volume were deposited onto the silicon wafer resulting in droplets with (107 ± 14) µm diameter in spherical cap geometry with contact angle of 74°±10°. After printing, the droplet array was covered with silicone oil (VWR, Rhodorsil 47 V 1000) to prevent evaporation and any eventual interaction between the supercooled and frozen droplets. Measurements of the droplet geometry and volume are described in the appendix.

The temperature of the droplets was measured with a calibrated thin film platinum resistance sensor (Pt-100) that was fixed directly on the surface of the silicon substrate by a small amount of heat conducting paste (vacuum grade) as shown on the inset of figure 13. The Pt-100 sensor was calibrated against a reference sensor in the temperature range from -40°C to +30°C prior to the experiment. The single point temperature measurement error was estimated to be ± 0.1K.

A charge-coupled device (CCD)-camera (EO progressive) with a wide field objective (DiCon fiberoptics Inc.) was used to record the freezing of the suspension droplets. The substrate is illuminated by a ring light source mounted around the objective lens. Two polarizers (one in front of the light source and one in front of the objective) were used to enhance the brightness of the frozen droplets compared to the liquid ones. Video- and temperature recordings of the cooling and freezing process were taken at a frame rate of 1 to 8 frames per second (fps), allowing for identification of individual freezing events with time resolution of 0.125 to 1s and 0.1K temperature accuracy. Freezing of individual droplets can be recognized by a pronounced increase of the light scattered from the frozen droplets (detected through the crossed polarizer in front of the objective lens). An automated video analysis routine allows for extraction of the fraction of frozen droplets as a function of temperature from the raw data. Subsequent data processing with a LabView routine allowed for calculation of a fraction frozen vs. temperature curve.

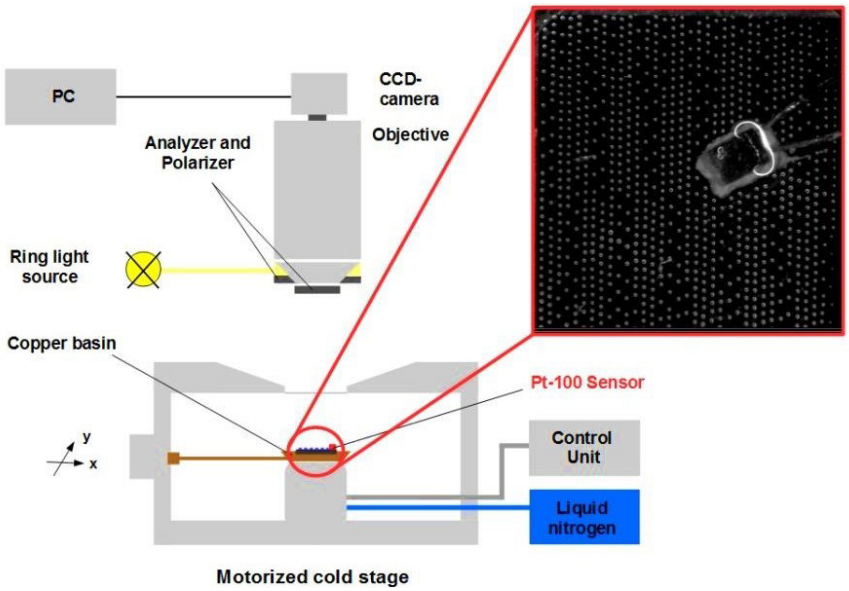

Figure 13: Schematic drawing of the nanoliter droplet freezing assay setup (side view). The inset shows the top view of 10×10 mm Si-wafer with ≈ 900 droplets immersed in silicone oil. The square shape near the center of the wafer is the Pt-100 temperature sensor.

4.1.1 Cooling ramp experiments

Two types of freezing experiments have been performed with this experimental setup: In cooling ramp (CR) experiments the temperature is linearly reduced with a constant cooling rate. Cooling ramp experiments from 273K to 233K were performed at three different cooling rates $c = dT/dt$ (-1 K/min, -5 K/min and -10 K/min) and the fraction of frozen droplets f_{ice} is recorded as a function of temperature with 0.1K resolution. After each CR experiment, the substrate is heated to 274K until every droplet has melted. Thereby the same sample can be used in repeated CR experiments allowing the correlation analysis of subsequent freezing runs.

4.1.2 Isothermal experiments

In isothermal (ISO) experiments (also known as temperature jump experiments) the temperature is reduced rapidly via initial ramp (-5 to -10 K/min) to a pre-set value and then held constant for about an hour, the individual freezing times being recorded continuously. The set point temperature was chosen such that maximum 25% of the droplets froze during the initial cooling ramp. These type of experiments addresses both the influence of temperature and time on the ice nucleation process of feldspar particles immersed in water droplets.

4.1.3 Sample preparation for chemical ageing experiments

To access the effect of ageing on the IN activity, the feldspar particles (FS01 und FS05) were left in water for over five months and the supernatant water was exchanged several times. Extreme care has been taken to avoid any contamination as a consequence of water exchange. The concentration of exchanged cations (K^+, Na^+, Ca^{2+}, Mg^{2+}) have been measured regularly during the first month (see section 5.1.8). For the cooling ramp experiments, the feldspar particles were centrifuged (Thermo scientific, 2000rpm for 20min), dried and re-suspended in 25 mL NanoPure water. Alternatively, fresh suspensions of feldspar (FS04) particles were heated to approximately +90°C for over an hour. Additionally, the FS04 feldspar sample has been suspended in 100 mL hydrogen peroxide aqueous solution (AppliChem GmbH, 30% p.a.) at +65°C und stirred for an hour or kept in hydrogen peroxide solution at room temperature overnight.

4.2 Electrodynamic balance (EDB)/Raman spectroscope setup

4.2.1 Droplet generation

Liquid droplet generation was achieved by a piezoelectric injector (GeSIM, model SPIP: A010-006, cylindrical PEEK housing with fluid connector for tubes). The microdispenser is made up of a silicon chip, on which a glass covering and a piezo-ceramic are attached (see figure 14). By applying an electrical pulse to the low-power piezoelectric actuator, the water reservoir is deformed and a monodisperse droplet is ejected. The volume accuracy is very high (around 1% as specified by the manufacturer). An amplitude of $U = 72V$ and a pulse duration of $100\mu s$ were used to generate micron-sized droplets with initial diameters between 51µm and 58µm. Since the EDB operates at subzero temperatures and the injector is placed inside the EDB throughout the experiments, the water reservoir must be protected from freezing. Resistance heating of the water reservoir by a thin film platinum sensor (Pt-100) ensures that the reservoir is not damaged by freezing. After the ejection, the droplet is charged via electrostatic induction by passing through a charging ring electrode, at which a voltage of about 300V is applied. It is assumed that the influence of additional surface charges ($\sim 10^6$ elementary charges) of the droplet is negligible[125, 126]. In the following, the operating

principle of the EDB, the contactless levitation of charged aerosol particles and the periphery devices will be discussed.

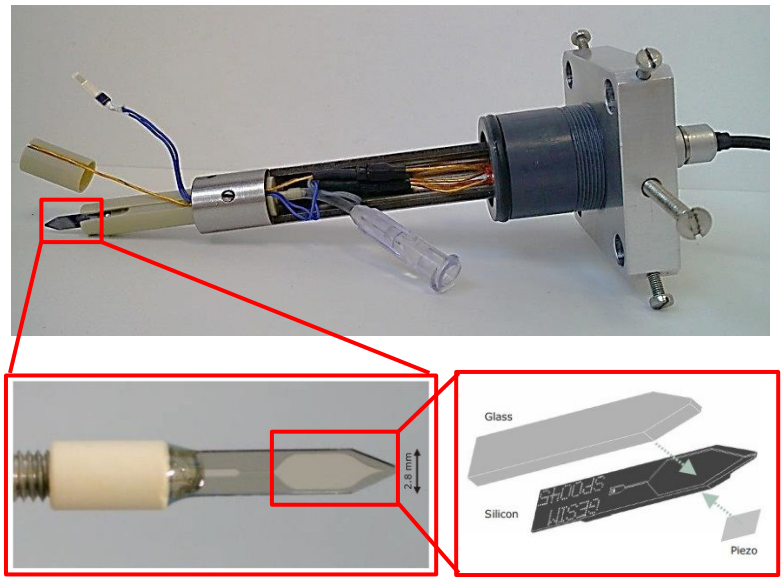

Figure 14: Above: Photographic image of the piezo-electric injector mounted on the holder. Below left: Close-up view of the microdispenser. Below right: Schematic representation of the microdispenser. A glass cover is fixed on top of a silicon chip. On the other side of the silicon chip a piezoelectric ceramic is glued. An electrical signal generates a monodisperse droplet emerging at the orifice of the dispenser (for details see http://www.gesim.de, brochure piezoelectric dispensers).

4.2.2 Description of the EDB

The EDB as the central part of the experimental setup is located in a vacuum housing for electrical and thermal isolation (see figure 15). Both a membrane and a turbo pump (Pfeiffer Vacuum, TMH 071P) are used to establish a vacuum of $p = 3.6 \cdot 10^{-4} mbar$ in the vacuum housing. The interior of the EDB is maintained at atmospheric pressure. As described in the previous section, a piezoelectric injector introduces a micron-sized droplet into the EDB, which can be trapped without contact to foreign surfaces. A superimposed AC/DC field is applied to the top and bottom electrodes whereas the center electrode is grounded due to the connection with the cooling system (i.e. the cold finger). An initial AC amplitude of $U = 1600V$ and a frequency of $f = 200Hz$ are chosen for the levitation of liquid droplets. Solid particles are captured at slightly higher frequencies ($f = 350 - 400Hz$). A delay time of $t = 700\mu s$ is selected to ensure that the droplets enter the EDB right at the moment of an arising slope of the oscillating AC signal. This setting facilitates that aerosol particles can be stored and analyzed in the EDB.

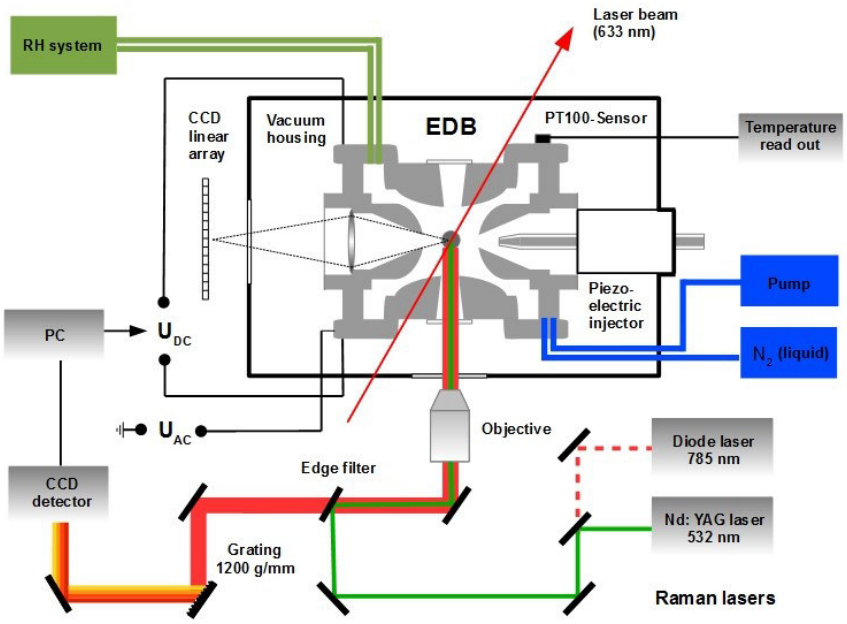

Figure 15: Schematic representation of the experimental EDB/Raman microscope setup including the surrounding instrumentation.

4.2.3 Peripheral devices

The cooling is achieved by pumping liquid nitrogen from a Dewar flask via a thermally isolated transfer tube to the cold finger of the EDB (CryoVac, PK 2001). The evaporating liquid nitrogen cools the cold finger and the attached ring electrode. A temperature controller (Lake Shore Cryotronics Inc., model 330 Autotuning) reads out the temperatures of the cold finger and the Pt-100 sensor mounted to the ring electrode of the EDB. An automatically controlled heater embedded in the cold finger counteracts the cooling flux ensuring that the temperature of the EDB is constant throughout the experiments. The temperature uncertainty is in the range of ±0.2°C. The other periphery devices and the confocal Raman microscope are described in the following paragraphs.

An unfocused and perpendicular polarized laser beam generated by a He-Ne laser (JDS Uniphase Corporation, 1107P, $\lambda = 632.81\text{nm}$, P < 4mW, diameter of laser beam: 0.48mm) is directed at the levitated droplet in the EDB (see left panel of figure 16). In 45° back scattering geometry, a linear charged coupled device (CCD) array (Spectronics devices) is installed. The backscattered light of the droplet is focused on the linear CCD-array via a X-Y positioner. A feedback mechanism actively regulated the DC voltage for the compensation of the gravitational force. The frequency of the AC field can be controlled both in an automatic and semi-automatic mode by the feedback mechanism. A CCD-camera (Imaging Source, DMK 21BF04.H, 640x480 pixel) is placed in 90° backscattering geometry relative to the incident He-Ne laser beam. Angle-resolved scattering pattern can be recorded allowing the size determination according to Mie theory and the phase discrimination of the particle. Regular and periodic interference fringes are characteristic for a liquid droplet and scattering

pattern with a totally irregular appearance are indicative for a crystallized particle. A commercial white light emitting diode (LED) mounted on top of the EDB is used to illuminate the particles. Shadow images of the particles are recorded by the Raman microscope providing additional information about the morphology, the phase state and the size of the particles. A red light bandpass filter mounted in front of the CCD-array enables the simultaneous adjustment of the DC voltage and the recording of shadow images of the particles by the Raman microscope.

For the visual inspection and spectroscopic characterization of the particles, an inverted confocal microscope (Olympus, IX71) coupled to a dispersive Raman spectrometer (Bruker, Senterra) is utilized. The Raman spectrometer is equipped with two diffraction gratings (400gr/mm and 1200gr/mm) and a spectroscopy CCD-camera (iDus Andor™, DU 420A-OE-152, 1025x255 pixels). The corresponding resolutions are 9-18cm^{-1} and 3-5cm^{-1} respectively. A laser wavelength of $\lambda = 532nm$ is used to excite Raman spectra in the spectral range from 80cm^{-1} to 4400cm^{-1}. Both short working distance (SWD) objectives (Olympus, MPlan, 20x/0.40, 50x/0.75 and EPlan, 10x/0.25) and long working distance (LWD) objectives (LMPlan FLN, 5x/0.13, 10x/0.25 and SLM Plan 20x/0.35) are available to investigate the particles. A moveable shutter is placed in front of the He-Ne laser to block the laser beam during the acquisition of Raman spectra. The acquisition and evaluation of Raman spectra was performed using the software program OPUS 7.2 (Bruker). The Raman spectra were baseline-corrected (concave rubberband method, 64 baseline points, 20 iterations) and exported in ASCII-file format for data postprocessing.

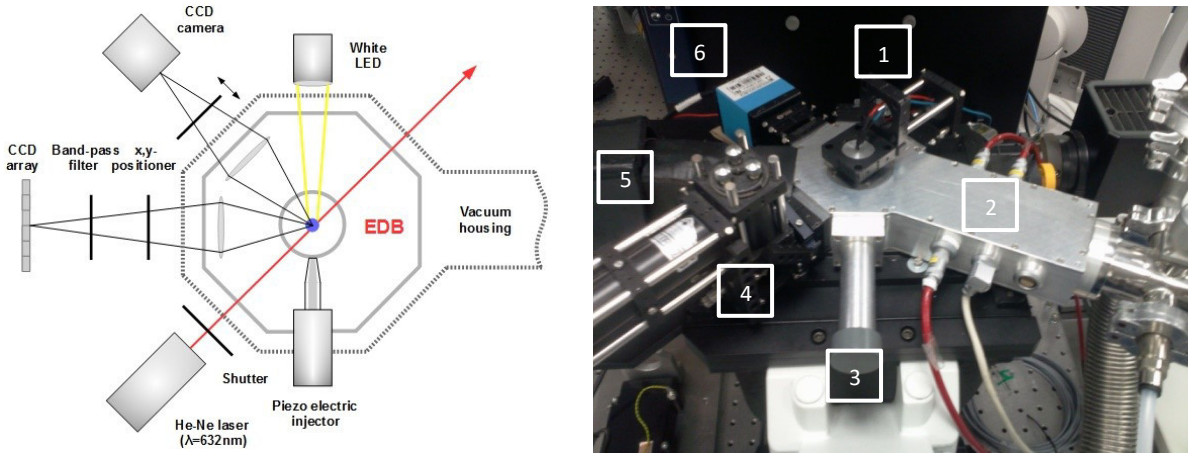

Figure 16: Left) Schematic representation of the central part of the EDB. Right) Photographic image of the EDB/Raman microscope setup. The surrounding instrumentation of the EDB is explained in more detail in the text.

4.2.4 Humidity control system

The flow diagram of the self-built RH system is depicted in figure 17. Compressed air is filtered by a high-efficient particulate arrestance (HEPA) filter and then splitted into three partial flows. The first flow is fed into the humidifier (Ansyco, Analytic systems and components GmbH, Sycos HS). The humidifier is specially designed for low output flows (0-100ml/min) and described in detail in the next section 4.2.5. The second flow is reduced by a needle valve and subsequently passes through a cold trap. The cold trap condenses water vapor form the compressed air into ice at the bottom of the cold trap. The third flow is mainly unchanged. To obtain a desired dew and frost point, the partial flows are recombined in different mixing ratios by using mass flow controllers (MFC). The MCFs are from the manufacturers Bronkhorst® (Low ΔP Flow, 2ln/min air) and Tylan (2900 Series, 1 SLPM and 50 SCCM). The partial vapor pressure of the mixed flow p_{tot} can be calculated as follows:

$$p_{tot} = \frac{p_1\dot{V}_1 + p_2\dot{V}_2 + \ldots}{\dot{V}_1 + \dot{V}_2 + \ldots} \qquad (4.\ 1)$$

where p_1, p_2,… are the partial vapor pressures and $\dot{V}_1$, $\dot{V}_2$,.. are the volumetric flow rates of the partial flows. The total humidified flow is fed into the chilled mirror hygrometer (MBW Calibration, 373L). The dew point mirror (DPM) operates in the temperature range from 20°C to -80°C. The accuracy of the DPM is ±0.1°C and the reproducibility: ±0.05°C. When the dew point and frost point are stabilized for about ~1h, a portion of the total humidified flow is diverted into the EDB. The volumetric flow rate is in the order of 40ml/min. The incoming and outcoming flows of the EDB were checked by a soap bubble flowmeter (Sensidyne, Gilan Gillibrator-2, flow range: from 20cc/min to 6L/min). This procedure guarantees that both the volumetric flow rate and the dew/frost point are accurately defined throughout the experiments. The dew and frost point temperatures are converted into the RH with respect to water (RH_w) and ice (RH_{ice}) according to Murphy et al.[127].

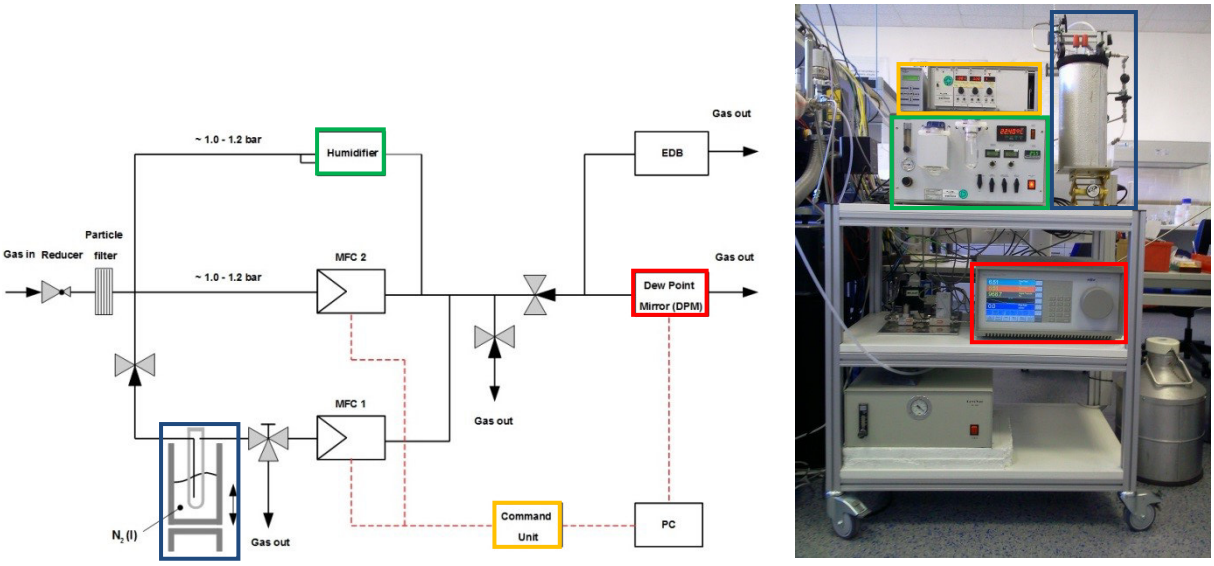

Figure 17: Left) Schematic representation of the relative humidity (RH) control system and Right) Photographic image of the apparatus.

In the following, a brief description of the humidifier is given (see figure 18). The incoming compressed air is splitted into two partial flows: A carrier gas flow is saturated with respect to water at 25-26°C by passing the gas through a glass frit into a water bath. Downstream of the saturator, a condensate separator removes entrained water droplets from the flow. Both the humidified carrier gas flow and the moisture gas flow enter the counterflow exchanger containing a permeable Nafion® membrane. A concentration gradient of water between the gas flows causes the transport of water molecules through the Nafion® membrane. Water molecules diffuse from the higher concentration (humidified carrier gas) to the lower concentration (moisture gas). By varying the carrier gas flow via a mass flow controller, the exchange of the two flows is enhanced or reduced, i.e. the RH of the moisture gas flow can be modified by adjusting the volumetric flow rate of the carrier gas flow. The carrier gas flow as well as the moisture gas flow can be varied between 0-100 ml/min by MFCs. The corresponding dew points temperatures are in the range from -45°C (as specified by the manufacturer) and the saturation temperature, i.e. 25°C. In reality, the Nafion® membrane contains substantial amounts of residual water, which complicates the adjustment of very low dew point temperatures in a sufficiently short time. Thus, the humidifier operates at fixed settings for the carrier gas und moisture gas flows and is afterwards mixed with additional dry flows in the relative humidity control system as described in the previous section 4.2.4.

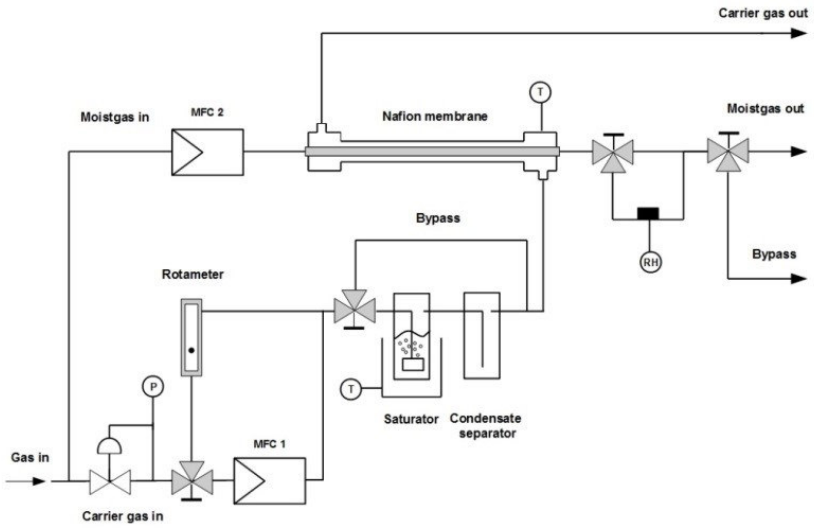

Figure 18: Schematic representation of the humidifier. The sketch based on a technical construction diagram of the humidifier from Ansyco, Analytic systems and components GmbH.

4.2.5 Preparation of NaCl and synthetic sea-salt solutions

For the preparation of a 10wt% aqueous solution, 2.22g of NaCl (Merck, ACS reagent, ≥99.5%) or simulated sea salt (Instant Ocean®, Aquarium Systems) are dissolved in 20ml deionized water (Barnstead-Thermolyne Corporation, NanoPure Infinity™ Ultrapure water system, 18.2MΩ·cm). A 10wt% aqueous solution of the ternary dicarboxylic acids/ammonium sulfate/water (C6/AS/H_2O) mixture with an organic to inorganic ratio (OIR) of 0.5 by mass is prepared in a similar manner. In total, 1.11g of solute, i.e. 0.55g of ammonium sulfate (Merck, for biochemistry, ≥99.5%) and 0.55g of C6 compounds are dissolved in 10mL deionized water. The organic fraction (i.e. C6 compounds) is composed of each 0.1851g (i.e. 33.3wt%) of 2-Methylglutaric acid (Merck, for synthesis), 3-Methylgluratic acid (Sigma Aldrich, 99%) and 2,2-dimethlsuccinic acid (Alfa Aesar, 99%). The molar mass is identical for all three C6 compounds (146.15g/mol).

Before each experiment, the injector is rinsed several times with deionized water to remove any contaminations from the water reservoir of the injector. Furthermore, syringe filters (Sartorius AG, white band, pore size of 0.45µm and red band, pore size of 0.2µm) are used to retain undissolved solid particles and contaminations. The reservoir of the injector is filled with freshly prepared aqueous solutions. The reproducibility of droplet generation of the injector is tested before each experiment. After the performance tests, the injector is mounted airtight through a port close to the center of the EDB. The experiments are described in the next section.

4.2.6 Isothermal and isohumid experiments

The EDB is purged several hours with dry compressed air prior to the experiments. Two types of experiments are performed in the EDB: Isothermal and isohumid efflorescence experiments and RH-ramp drying experiments at a constant temperature. These two types of experiments are exemplified in the following paragraphs.

The experimental conditions for efflorescence experiments with suspended SSA particles in the EDB at -16°C are shown in the left panel of figure 19. During the purging period, the temperature of the EDB and the relative humidity of the gas flow are adjusted. For the low-temperature efflorescence experiments, the relative humidity was chosen to be in the range between 38% and 45% (orange shaded area in the left panel of figure 19). It is assumed that the injected droplets are exposed to identical experimental conditions. This means that the RH and the temperature are constant throughout the experiments. Up to ∼70 identical solution droplets are studied in the course of a single efflorescence experiment at a predefined temperature.

4.2.7 RH-ramp experiments at constant temperature

In contrast, a RH-ramp drying experiment is conducted for the C6/AS/H_2O mixture at 15°C. After the initial purging, the relative humidity is increased (>90%) to ensure that the droplet is a fully liquid state. The injected particle is allowed to equilibrate with the environment and then the relative humidity is decreased stepwise (right panel of figure 19). A drying rate of about 0.23%/min is calculated. This type of experiment allows to investigate liquid-liquid phase separations and liquid-solid phase transitions of AS for a single levitated particle (see section 5.6). After the experiments, the humidified flow is switched off and the EDB is warmed up to room temperature (~20°C).

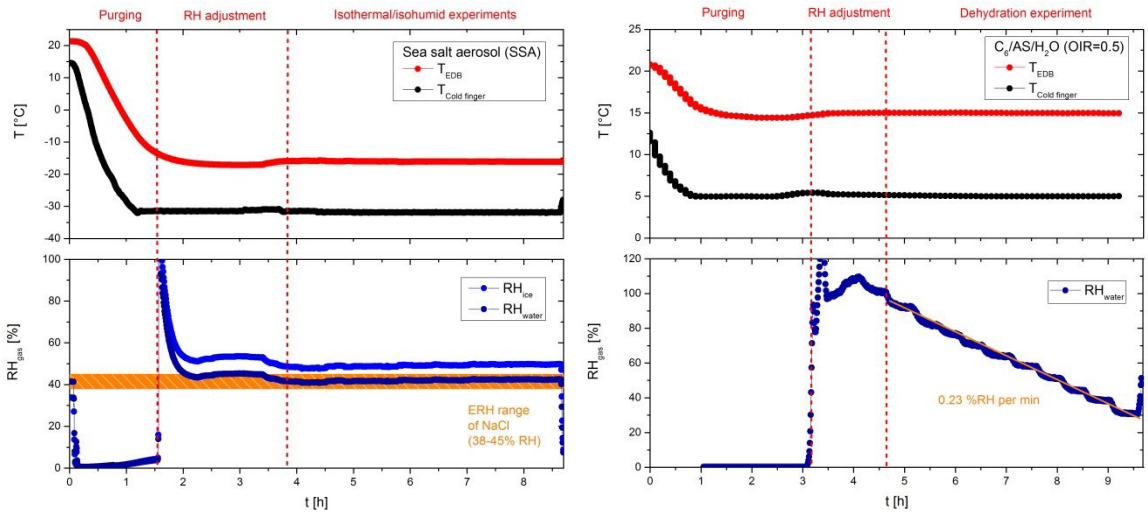

Figure 19: Temperature (top panels) and RH_w/RH_{ice} profiles (bottom panels) of an isothermal and isohumid experiment with sea salt aerosol particles at -16°C (left side) and a RH-ramp drying experiment at constant temperature (+15°C) with a C6/AS/H_2O aqueous solution droplet (right side). The red and black points denote the temperatures of the EDB and the cold finger respectively. The light blue and dark blue points denote the RH_{ice} and RH_w values respectively.

5. Results

5.1 Comparative study of feldspar ice nucleating particles

The results presented in section 5.1 are largely taken from Peckhaus et al[123].

5.1.1 Characterization of feldspar samples

The feldspar samples FS01, FS04 and FS05 were provided by the Institute of Applied Geosciences, Technical University of Darmstadt (Germany) and the feldspar sample FS02 was provided by the University of Leeds (UK). The samples FS01, FS04 and FS05 have been prepared by ball milling of single crystal mineral specimens. FS02 is the standard BCS 376 from the Bureau of Analyzed Samples, UK. All samples were studied during the Fifth International Ice Nucleation (FIN) measuring campaigns at AIDA cloud chamber in the framework of the Ice Nucleation Research Unit (INUIT) project of German Research Foundation (DFG). Table 1 gives an overview of the investigated feldspar samples.

An environmental scanning electron microscope (ESEM FEI, Quanta 650 FEG) was used to record images and energy dispersive X-ray (EDX) spectra of individual feldspar particles deposited on graphite and silicon substrates. For each sample, over one hundred individual spectra have been recorded for the individual particles separated by at least 10 µm from other particles or agglomerates. The program Esprit 1.9 (Bruker) was used to quantify the chemical composition of the feldspar samples. SEM images of feldspar particles showed agglomerates consisting of several large rocky particles with the smaller particle fragments on their surface (see figure 20). With respect to their morphology, both individual feldspar particles within one sample, and the particles from different feldspar samples were very similar.

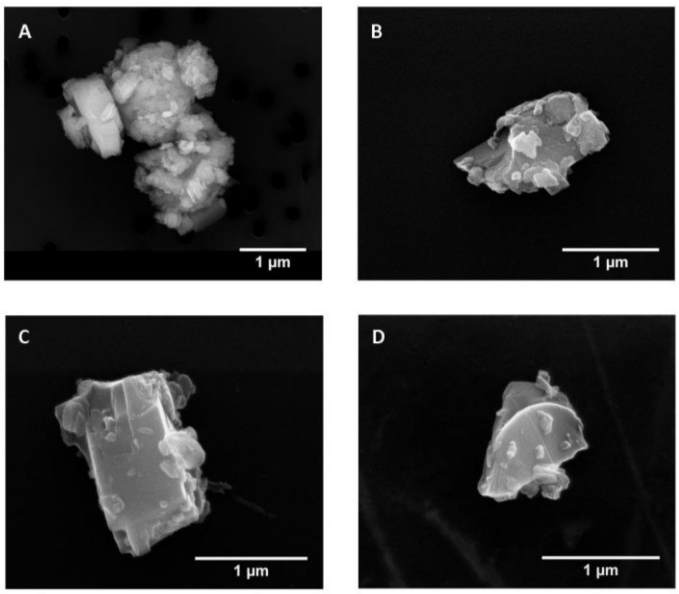

Figure 20: SEM images of A) FS01, B) FS02, C) FS04 and D) FS05 particles. Every size bar corresponds to 1µm.

The SEM images were used to measure the surface area of particles in the FS02 suspension droplets. The SEM images taken at different resolution were used to estimate the total projection area and the size distribution of the residual particles left after the droplet was evaporated (see figure 21). The projection area of individual residual particles has been measured with the program ImageJ 1.47v and used for derivation of the area equivalent particle diameter assuming particle sphericity. The projection area equivalent diameter of residual particles can either be converted into a size distribution by counting the frequency of residual particle diameters or to a total particle surface area per droplet by summing up the area of individual residual particles. The particle surface area derived from SEM images was in a good agreement with the BET-based particle SSA (see figure 22). This led to the assumption that the initial prepared concentrations were close to the final concentrations in the suspension droplets. Coagulation of feldspar particles in suspension may play a minor rule in concentrated feldspar suspensions[32] but was not observed in this study. Having demonstrated that the $S_{p,\,SEM} = S_{p,\,BET}$ for FS02 at the concentrations used in this work, it has relied on the $S_{p,\,BET}$ measurements for all other feldspar samples.

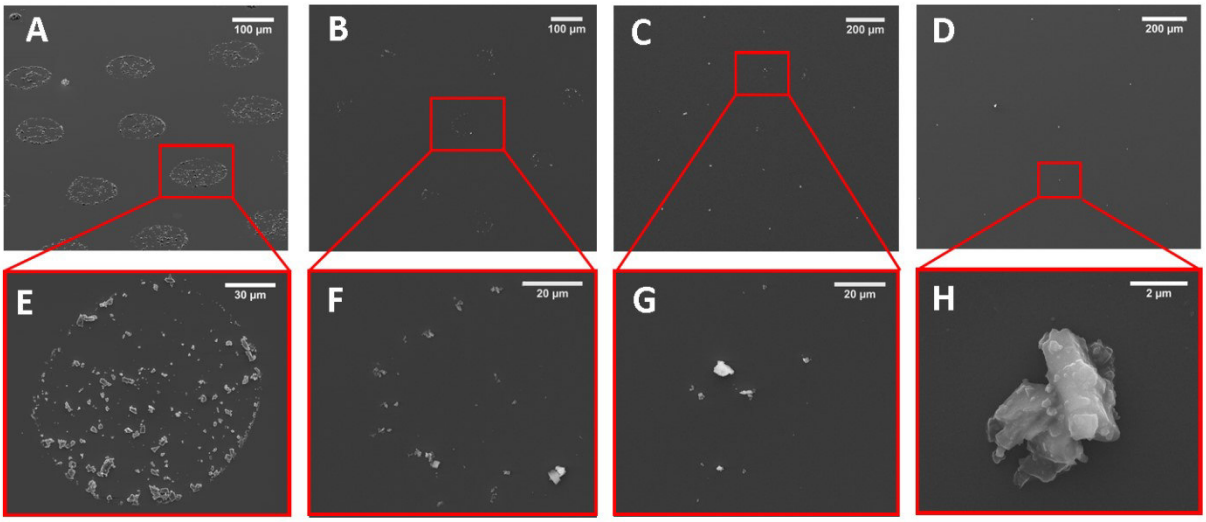

Figure 21: Footprints of the FS02 suspension droplets left after evaporation on the Si-wafer observed in the electron microscope: A) 0.8 wt%, B) 0.1 wt%, C) 0.05 wt% and D) 0.01 wt%. E)-H) Close-up SEM images showing residual particles of individual droplets. Note the different length of the size bars.

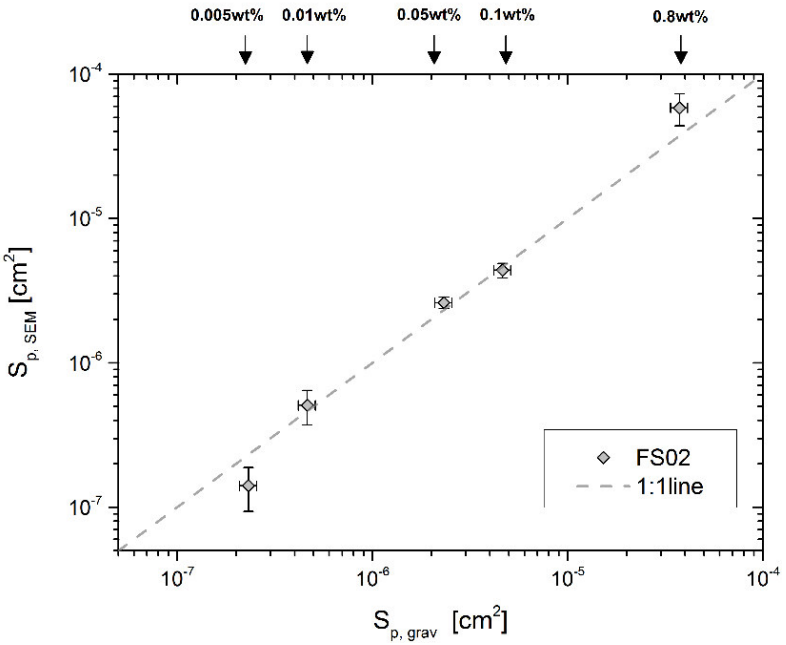

Figure 22: Particle surface area per droplet $\boldsymbol{S_p}$ derived from SEM images ($\boldsymbol{S_{p,SEM}}$) versus BET-based particle surface area per droplet ($\boldsymbol{S_{p,grav}}$). The black arrows in the top of the panel indicate the corresponding weight percentages.

Furthermore, the SEM images were used to determine the size distribution of feldspar particles per droplet. For that, the feldspar suspension of 0.1wt% was printed onto a silicon wafer and was allowed to evaporate. The projection area of individual residual particles has been measured and used to derive the area equivalent particle diameter under assumption of spherical particle geometry. The size distribution of FS02 particles ranged from 0.3µm to 4µm. The maximum is located at approximately 700 nm (see figure 23). The size distribution estimated from SEM images of residual FS02 particles agreed well with the size distribution obtained using laser diffraction analysis[5]. The resolution of SEM images is restricted to serval hundreds of nanometers, which limited the detection of very small FS02 particles.

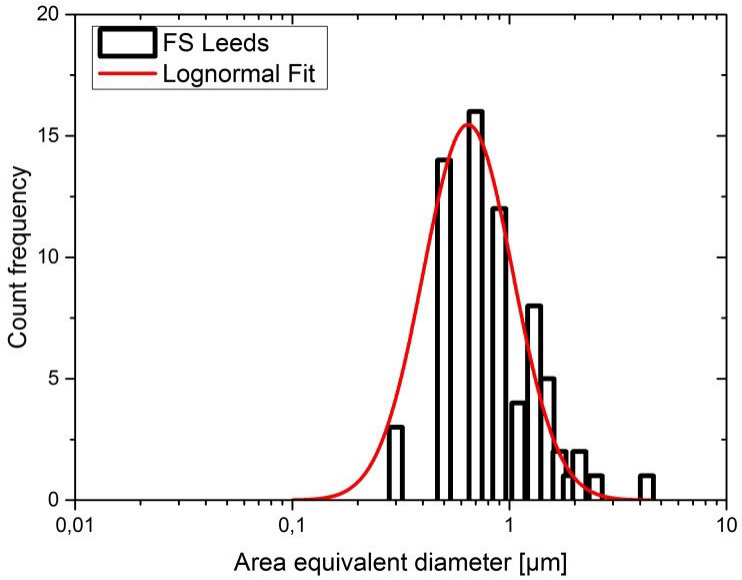

Figure 23: Size distribution of FS02 residual particles (0.1wt% suspension).

The specific surface area (S_{BET}) has been measured with N_2 gas adsorption technique following the Brunauer-Emmett-Teller method[65] (BET). The SSA of feldspar samples ranged from 1.79 to 2.94 m²/g (see table 1) which is lower than the BET surface areas reported by Atkinson et al.[5] (3.2 m²/g for FS02 and 5.8 m²/g for Na/Ca feldspar particles respectively) and slightly higher than the BET surface area reported by Schill et al.[29] (1.219 m²/g for Na/Ca feldspar particles). The SSA was then used to calculate the "gravimetric" particle total surface area using the relationship $S_p = W \cdot V_{drop} \cdot S_{BET}$. Both methods delivered similar values of S_p, as demonstrated in figure 22.

Table 1: The mineral composition and specific surface area (N_2 BET SSA) of feldspar samples.

Sample	Source	Mineral composition (XRD)	BET SSA [m²/g]
FS01	Minas Gerais, Brazil, supplied by IAG TU Darmstadt	76% K-feldspar (microcline) 24% Na/Ca-feldspar (albite)	1.79
FS02	Bureau of Analyzed Samples, UK, standard BCS 376 (provided by University of Leeds, UK)	80% K-feldspar* 16% Na/Ca-feldspar* 4% quartz	2.64
FS04	Mt. Maloso area (Malawi), supplied by IAG TU Darmstadt	80% K-feldspar (microcline) 18% Na/Ca-feldspar (albite) 2% quartz	2.94
FS05	IAG TU Darmstadt, in-house collection	>90% Na/Ca-feldspar (albite)	1.92

*mineral phase was not specified

The ternary phase diagram derived from EDX measurements of individual feldspar particles shows that particles of FS01, FS02 and FS04 have a similar chemical composition close to the end member microcline/orthoclase[128] (figure 24A). The compositional distribution of FS01 and FS02 are nearly overlapping, but also some particles richer in sodium and calcium were observed. The composition of FS04 was slightly closer to the end member microcline/orthoclase. Iron as a trace component was found in individual EDX spectra of FS02 and FS04 which can probably originate from trace impurities of aegirine (member of sodium pyroxene group) known to form in the alkaline igneous rocks also responsible for the formation of alkali feldspars[129], as in the region of Mount Malosa in Malawi. Note that the EDX spectra were measured on the single particle basis and therefore do not represent the weight average composition of the entire sample. The composition of the agglomerates may differ from that of the individual particles. In accordance with the solid solution series of plagioclase the majority of FS05 particles are situated in the region of andesine[128] (intermediate plagioclase, 30-50% anorthite) (figure 24B). However, individual particles were richer in sodium and closer to the end member albite. Based on the analysis of individual EDX spectra, the Al:Si ratio was found to be very close to 1:3. This ratio varies from 1:3 for albite to 2:2 for anorthite (end member of the plagioclase solution series). The EDX spectra of size selected FS05 particles (300 nm mobility diameter) do not significantly differ in their composition from larger coarse-grained particles. We therefore suggest that the FS05 sample predominantly consists of albite with minor heterogeneous inclusions of andesine. The observed steady rise of Ca^{2+} ion concentration measured in the suspension over the period of four weeks supports this conclusion (see figure 35). In the following, we refer to FS05 as a "Na/Ca-rich feldspar" and to FS01, FS02 and FS04 samples as "K-rich feldspar". Overall, the EDX results mainly confirmed the composition of feldspar samples derived from XRD analysis (see table 1).

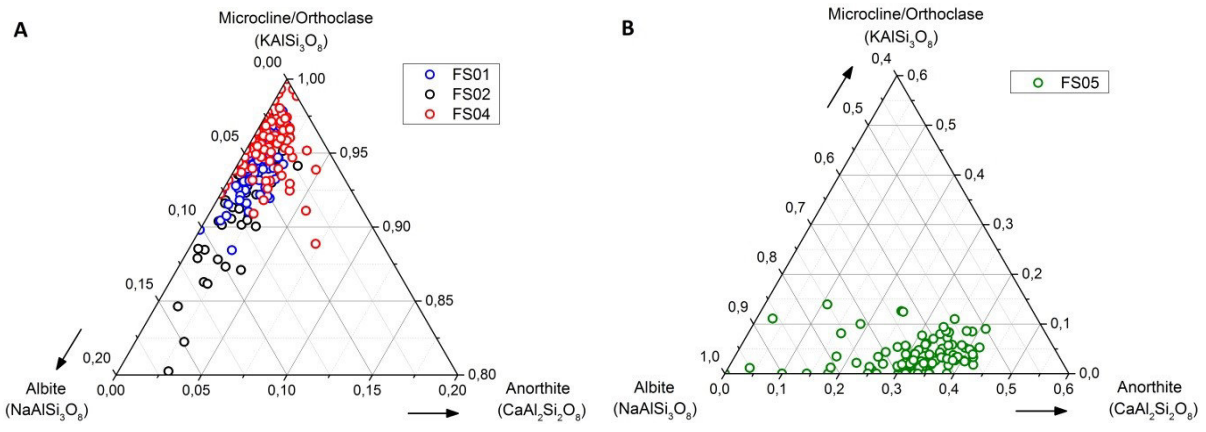

Figure 24: EDX data of individual feldspar particles plotted on the ternary phase diagram based on elemental mass percentages. A) Ternary phase diagrams of K-feldspar particles (FS01, FS02 and FS04) and B) Na/Ca-feldspar particles (FS05). Note the different scales of the ternary axis.

Raman spectra of feldspar powder samples were recorded with an optical microscope coupled to a dispersive Raman spectrometer. For acquisition of the bulk spectra, the feldspar samples were excited by a wavelength of 532nm and a power of 50 mW. For focusing of the particles, the short working distance (SWD) objective (Olympus, MPlan 50x/0.75) was used.

The feldspar samples FS01, FS02 and FS04 exhibited three distinct Raman bands (452cm^{-1}, 474cm^{-1} and 511cm^{-1}) in the range from 420cm^{-1} to 560cm^{-1}, which are characteristic for K-feldspar[130] (microcline) (see figure 25). In the same region, only two strong Raman bands appeared at 479 cm^{-1} and 507 cm^{-1} for the FS05 feldspar sample. The Raman spectra of FS05 could not be clearly assigned to albite[131] or andesine[132]. The absence of the third Raman band in the spectra range and the characteristic shift of the main Raman band at 507 cm^{-1} seems to be in accordance with the disordered albite (high-temperature modification), whereas for the ordered albite (low-temperature modification) three Raman bands were observed[130]. Note that in all the Raman spectra of feldspar samples, no evidence was found for typical vibrations of organic compounds (e.g. in the $\nu(CH)$ stretching region). Thus, these Raman spectra confirmed mainly the EDX and XRD results with regard to the composition of the feldspar samples.

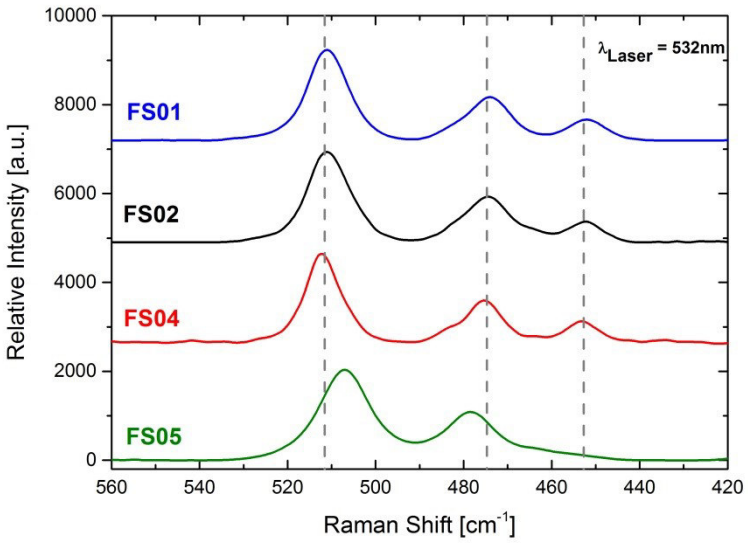

Figure 25: Raman spectra of investigated feldspar particles.

5.1.2 Cooling ramp experiments

Suspensions of FS01, FS02, FS04 and FS05 were investigated in the concentration range from 0.01wt% to 0.8wt% (see figures 26A-26D) at three different cooling rates: 1, 5 and 10 K/min. Supercooled water droplets containing feldspar particles froze well above the homogeneous freezing limit (which was found to be 237 K for 100 µm droplets on a pure silicon substrate, see doctoral thesis of Isabelle Steinke[124]). The concentrated suspensions (0.8wt%, dark coloured curves) have shown in general steeper freezing curves as compared to less concentrated suspensions. The freezing behavior of FS01 and FS02 was nearly identical. The freezing of Na/Ca-rich feldspar suspensions (FS05, figure 26C) occurred at lower temperature range (from 255.5K to 248K) as compared to K-rich feldspar suspensions. The concentrated (0.8wt%) suspension of FS04 was quite outstanding from the rest of samples as the droplets started to freeze already at 268K (figure 26D). All suspension droplets of FS04 were frozen at 255K. The effect of concentration was similar for all investigated feldspar sample suspensions. With decreasing concentration of feldspar suspensions, the frozen fraction curves covered a broader temperature range and the frozen fraction curves are shifted to lower temperatures. Additionally, the freezing curves of less concentrated FS04 suspensions (0.01 wt% to 0.1wt%) are very similar to those of FS01 and FS02 feldspar suspensions.

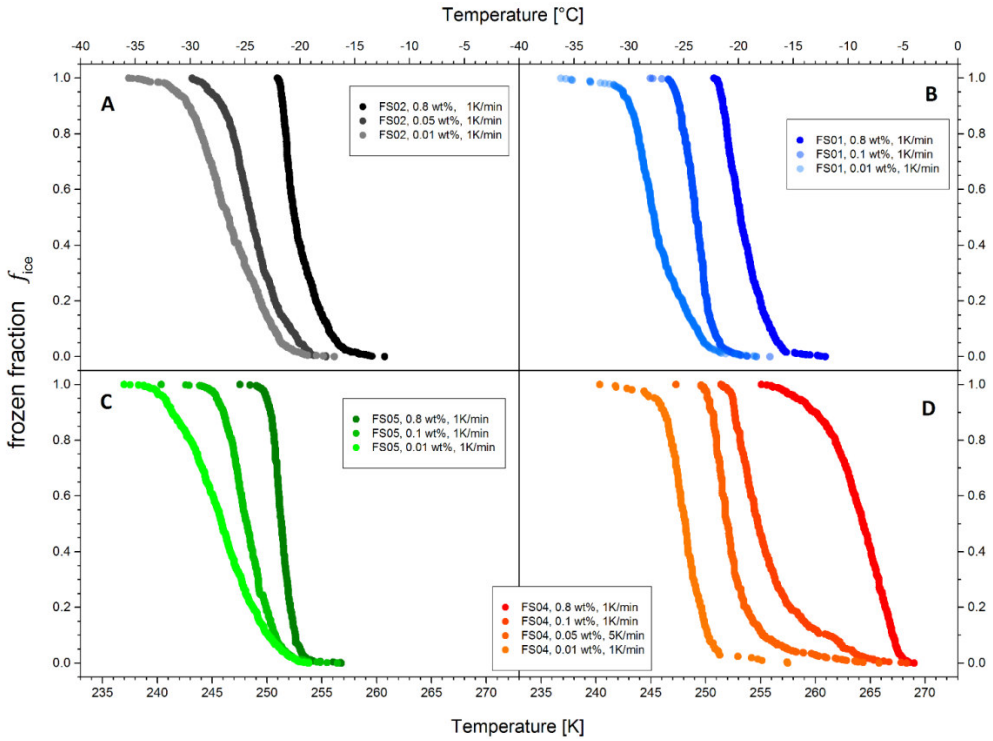

Figure 26: Frozen fraction curves of feldspar suspensions with various concentrations for A) FS02, B) FS01, C) FS05, and D) FS04. Note the initiation of freezing at 268K for FS04 0.8wt% suspension droplets.

5.1.3 Freeze-thaw cycle experiments

To investigate the repeatability of droplet freezing, freeze-thaw cycle experiments with identical cooling rates have been performed. Every individual droplet has been assigned a rank number according to its freezing time in two successive CR experiments, with rank number 1 corresponding to the first droplet frozen and so on. The pairs of rank numbers of the individual droplet have been plotted on a 2D coordinate grid as shown in the figure 27. Droplets that have disappeared in the second temperature ramp experiment or could not be detected automatically were excluded from consideration. A perfect correlation between rank orders in two cycle experiments would imply that every droplet froze exactly at the same temperature in both CR runs. On the other hand, no correlation between the freezing rank numbers would imply statistically independent freezing events or very steep temperature dependence of the heterogeneous nucleation rate coefficient (if the freezing times of individual droplets could not be distinguished within the time resolution of the video camera).

For NanoPure water droplets on a cleaned silicon wafer substrate no correlation between the ranking order of freezing events could be observed, as shown by Pearson's r coefficient equal to 0.14. However, a small fraction of droplet population near the beginning of a cooling cycle (figure 27A) showed local increase of correlation which could probably be associated with contamination of the silicon wafer or impurities in the water or in the silicon oil. For concentrated FS01 suspensions a higher correlation of freezing events was observed (r = 0.89, figure 27C). FS05 suspensions showed a lower correlation coefficient (r = 0.8, figure 27B). The highest correlation coefficient was obtained for concentrated FS04 suspensions (r = 0.92, figure 27D).

These observations suggest that the correlation coefficient is related to the IN efficiency of the suspension material. INPs initiating freezing at lower temperature also showed a lower correlation coefficient, while more efficient INPs nucleate ice at higher temperature and in a narrow temperature range showing higher correlation coefficients. A similar conclusion was drawn for the ice nucleation of collected rainwater samples[133]. Therein, a slight decrease of standard deviations of the median freezing temperatures at higher temperatures (i.e. reduced cooling rate dependence) has been reported. In Campbell et al.[134], a correlation plot was used for the characterization of silicon substrates roughened with diamond powder. It could be demonstrated that there was a strong correlation between freezing ranks of droplets in successive cooling runs on scratched silicon substrates. Similar experiments, investigating the repeatability of freezing temperatures of single droplets of distilled water and two soil dust samples were carried out with a microliter droplet freezing assay[135]. The derived Spearman rank correlation coefficients for pairs of runs were higher than 0.9 indicating a high repeatability of freezing temperatures. The standard deviation of the mean freezing temperature evaluated from the freeze-thaw cycle experiments on individual droplets containing ATD[136], soil dust[135] and Nonadecanol[57] was found to be less than 1 K. For volcanic ash[137] (Fornea et al., 2009) and black carbon[133], this value was larger (a few

degrees). These experiments corroborated the small variability of freezing temperatures of individual droplets. The presented correlation plots demonstrate both the random variability of freezing temperatures in successive cycle experiments as well as the variability of surface properties across the population of feldspar particles, while in the cycle experiments on individual droplets the variability of surface properties can be neglected[70]. The strong correlation between freezing events observed in our freeze-thaw cycles confirms the idea that the heterogeneous nucleation of ice is stochastic in nature, but its average observable characteristics (like fraction of frozen droplets) are governed by temperature dependent efficiency of individual IN active sites.

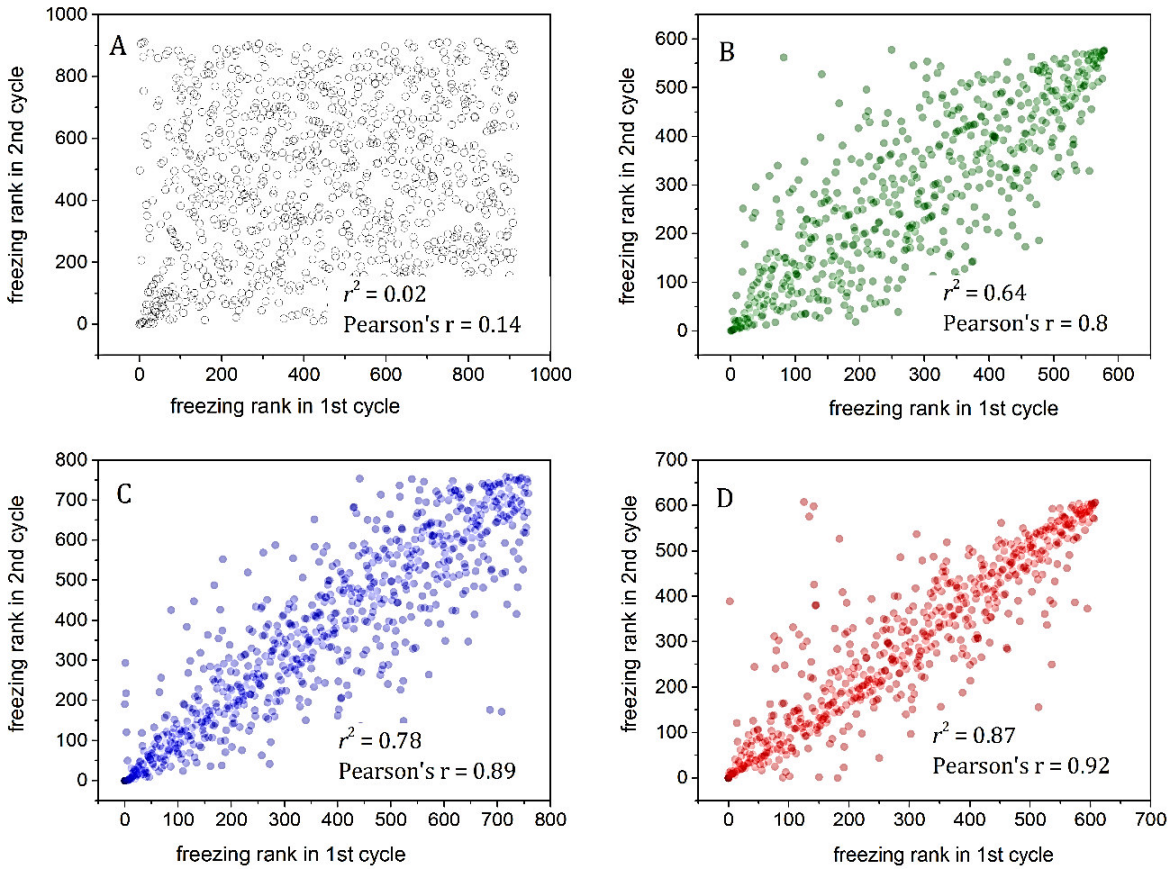

Figure 27: Correlations plots of freeze-thaw cycle experiments of feldspar suspensions (0.8wt%, 5 K/min). A) NanoPure water, B) FS05, C) FS01, and D) FS04. In the bottom right corner of every panel the adj. r^2 and the Pearson's r correlation coefficients describe the degree of correlation.

5.1.4 Isothermal experiments

For a droplet population containing single component INPs kept at constant temperature, the classical nucleation theory (CNT) predicts an exponential decay of the number of liquid droplets with time. To see if such behavior can be observed under realistic experimental conditions, we have conducted a series of isothermal experiments where droplets were cooled down rapidly (typically at rate of 10 K/min) and then kept at constant temperature T_{ISO} for an hour. These experiments have been conducted for concentrated (0.8 wt%) suspensions of FS02 at T_{ISO} = 253K, 254K, 255K, and 256K, and FS04 at T_{ISO} = 266K and 267K. The resulting decay curves are shown in Fig. 28 together with the SBM simulations that are discussed in the next section.

For droplets of FS02 suspensions, the decay of the liquid fraction $f_{liq}(t)$ is clearly deviating from the linearity (in log-log scale) indicating broad distribution of the active sites responsible for ice nucleation (see figure 28A). The deviation from linearity is more pronounced for lower temperatures, as more and more ice nucleating sites become active.

A different behavior is seen for the FS04 suspensions. The $f_{liq}(t)$ curve shows a nearly linear (in log-log scale) decrease with time (figure 28B), with decay rate becoming less steep at lower temperature. A linear decrease is usually attributed to a single component IN population with a uniform and narrow distribution of active sites and/or contact angles on the particle surface: AgI[17], kaolinite[138] and illite NX[139]. In contrast, a non-linear time dependence have been reported for a number of mineral dust particles immersed in water droplets. In droplet freezing assay experiments, FS02 suspensions[140], ATD suspensions[136] and less concentrated illite NX suspensions[68] featured a non-linear time behavior. Studies in the Zurich Ice Nucleation Chamber (ZINC) have found that size-selected kaolinite particles (Fluka, 400nm and 800nm) showed also a non-exponential decay with increasing residence time and temperature[141]. Non-exponential time dependence was associated with a multi-component system featuring a high degree of interparticle variability[140]. Other authors ascribe the deviation from the exponential behavior to the diversity of active sites and the finite number of droplets[136]. In addition, one type of cultivated cells of INA bacteria was found to exhibit a constant logarithmic of the fraction of liquid droplets with time indicating a narrow distribution of active sites and/or contact angles of the ice nucleating species[142].

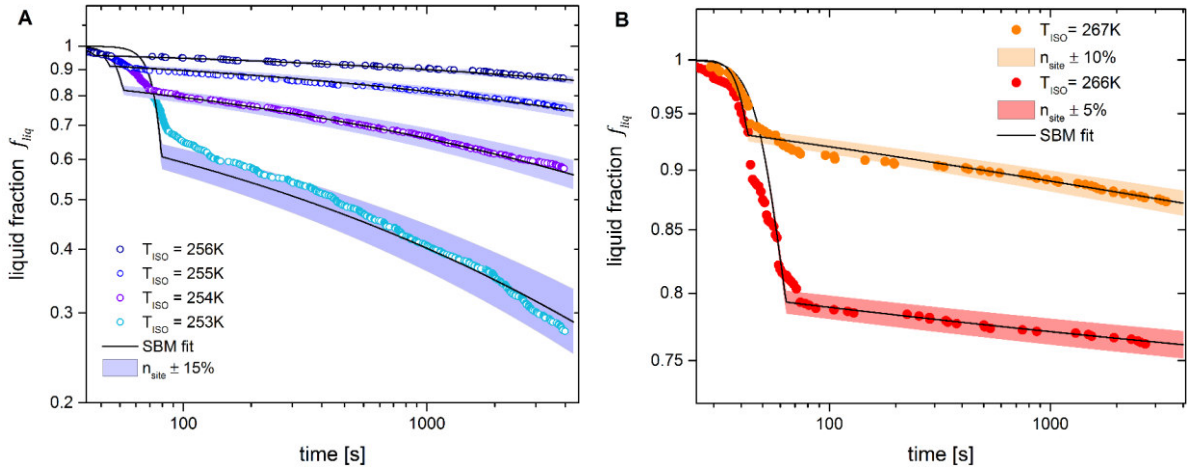

Figure 28: Decay of the liquid fraction with time for A) FS02 and B) FS04 for different T_{ISO} (log-log scale). Solid lines show composite SBM fit with parameters given in table 2 (see section 5.1.6 for detailed discussion). Shaded areas indicate the variability $\boldsymbol{n_{site}} \pm \Delta\boldsymbol{n_{site}}$ of a best fit value, with actual $\Delta\boldsymbol{n_{site}}$ given in the legend.

5.1.5 Cooling rate dependence

For all investigated concentrated feldspar suspensions a weak cooling rate dependence of the median freezing temperature ($T_{0.5}$) was observed (figure 29). For FS01, FS02 and FS05 the median freezing temperature was shifted by ΔT = 0.6 - 0.7K toward lower temperature as cooling rate $c = dT/dt$ increased from -1K/min to -10K/min. However, for concentrated FS04 suspensions (0.8 wt%) the $T_{0.5}$ value decreased by only 0.2 K.

Depending on the mineral dust type and the concentration of suspension, the reported influence of cooling rate on the median freezing temperature can vary strongly. A 0.1 wt% ATD suspension showed a temperature shift value of ΔT = 1.3K for a change in cooling rate from 0.01K/min to 5K/min[136]. This corresponds to a temperature shift of ΔT = 0.5K per ten-fold change in the cooling rate. In contrast, kaolinite[138], montmorillonite and flame soot suspensions[133] showed a very strong cooling rate dependence. For kaolinite suspensions (sample provided by Clay Minerals Society, CMS) a temperature shift of ΔT = 8 K (three orders of magnitude change in cooling rate) and ΔT = 3K for montmorillonite and flame soot suspensions (two orders of magnitude change in cooling rate) were obtained. For illite NX suspensions a complex cooling rate dependence was observed: on the one hand, suspension droplets with a large surface area of illite NX exhibited a temperature dependence in the order of 1-2K. On the other hand, a negligible cooling rate dependence for droplets containing a low surface area of illite NX was observed. These apparently contradicting observations could be explained consistently in the framework of a stochastic multicomponent model[68].

Unlike mineral dusts, biological INP showed a weaker cooling rate dependence. For Snomax® a weak increase of the $T_{0.5}$ value with decreasing cooling rate was found[133]. The cooling rate dependence of the $T_{0.5}$ value for Snomax® was quantified in a microliter droplet freezing

assay[143]: an increase in cooling rate by two orders of magnitude from -0.1 K/min to -10 K/min led to a temperature shift of ΔT = 0.55K and ΔT = 0.64K for highly concentrated (Class A type) and less concentrated (Class C type) Snomax® suspensions, respectively. This is consistent with the observation of a reduced cooling rate dependence for droplets containing highly effective IN particles.

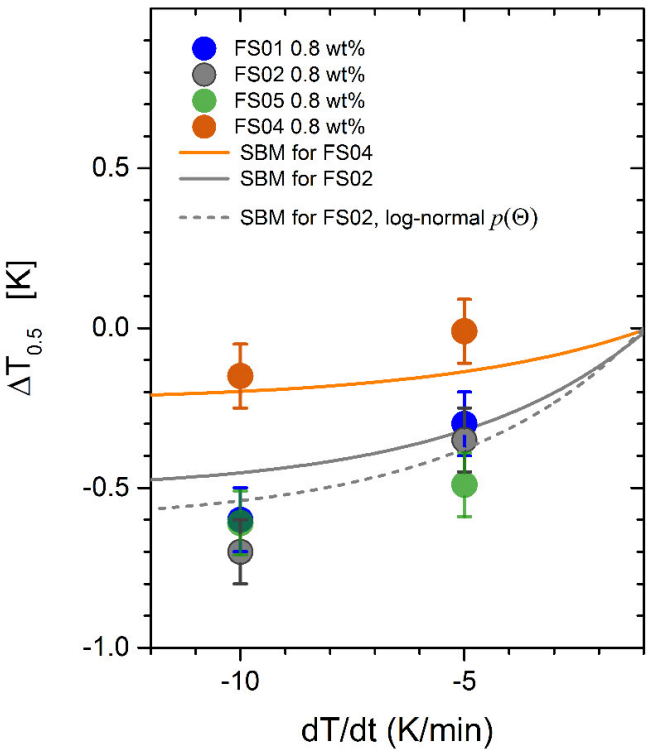

Figure 29: The shift $\Delta \boldsymbol{T_{0.5}}$ of the median temperature $\boldsymbol{T_{0.5}}$ relative to the $\boldsymbol{T_{0.5}}$ at 1K/min for different cooling rates $\boldsymbol{c = dT/dt}$. Solid lines represent expected $\Delta \boldsymbol{T_{0.5}}(\boldsymbol{c})$ calculated with fit parameters given in table 2. Dashed line is the theoretical temperature shift calculated with the same SBM parameters for FS02 but assuming the log-normal distribution of contact angles $\boldsymbol{p(\theta)}$.

5.1.6 SBM-based fit of experimental data

To demonstrate the common features and differences in freezing behavior of all feldspar suspensions, the SBM-based fit is applied to the experimental freezing curves of all feldspar samples obtained for various concentrations. The raw measurement data (as shown in figure. 26A and 26D) have been averaged within the 0.5K temperature intervals. These binned data have been fitted with Eq. (2.24) with adjustable fit parameters $n_{site,}$ μ_θ, and σ_θ (see figure 30). Binning improves the efficiency of minimization algorithm that has been programmed in Matlab. The values of fit parameters obtained for the best fit are given in table 2.

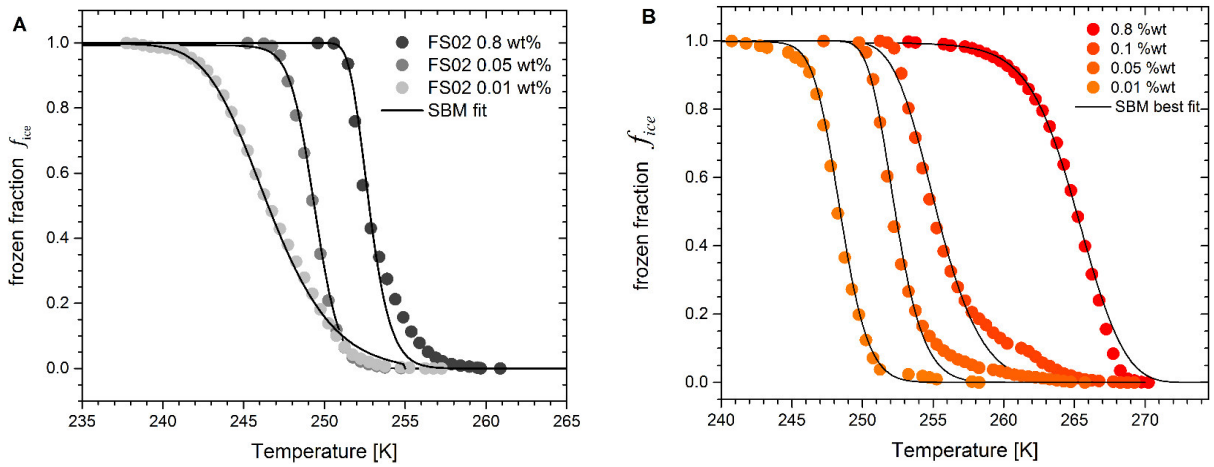

Figure 30: Freezing curves of A) FS02 and B) FS04, binned into 0.5K temperature intervals (filled symbols) and SBM best fit (solid curves). Fit parameters are given in table 2.

For isothermal experiments the fit routine has been modified to fit the entire decay curve of the liquid droplet fraction. This was achieved by applying the cooling ramp relationship $T = T_{start} + ct$ in the time interval $t_{start} \leq t \leq t_{ISO}$ until $T_{ISO} = T(t_{ISO})$ has been reached and then fixing $T(t) = T_{ISO}$. In this way the fit routine was forced to find the set of fit parameters capable of reproducing both frozen fraction at the end of the cooling ramp $f_{liq}(t_{ISO})$ and time evolution of the decay curve at constant temperature $f_{liq}(t), t > t_{ISO}$. The resulting "composite" fit curves are shown in figure 28A and 28B for FS02 and FS04, respectively and the resulting fit parameters are given in table 3.

By allowing all three SBM parameters being freely adjustable, different combinations of $n_{site,}$ μ_θ and σ_θ could be found that would represent the experimental results equally well. Therefore, a constraining condition is required to obtain a self-consistent set of fitting parameters. Such condition can be found in different ways: by analyzing the cooling rate dependence of $f_{ice}(T)$ or by finding the unique set of fit parameters adequately describing both CR and ISO experiments with the same INPs. First, we compare the observed shift of the median temperature with the theoretical values calculated with the help of Eq. (2.24), with $T_{0.5}$ being the temperature where $f_{ice} = 0.5$ and

$\Delta T_{0.5}(c) = T_{0.5}(c) - T_{0.5}(-1\,K/min)$ (solid lines in figure 29). The values of n_{site}, μ_θ and σ_θ have been taken from the SBM fit of the CR freezing curves as described above in this section. The absolute values of $\Delta T_{0.5}(c)$ are satisfactory reproduced by the model for FS01 and FS02 at $c = -5\,K/min$ and for FS04 at $c = -10\,K/min$ but are 0.2K off for FS01, FS02, and FS05 at $c = -10\,K/min$. The shift of the median temperature is less pronounced for better ice nuclei (compare $\Delta T_{0.5}(-10\,K/min) = -0.2K$ for FS04 vs. $\Delta T_{0.5}(-10\,K/min) = -0.5K$ for "generic" feldspars FS01, FS02, and FS05 and this feature is clearly captured by the SBM (see figure 29). Although the trend in the cooling rate dependence is adequately predicted, it should be noted that the $\Delta T_{0.5}(c)$ calculated with Eq. (2.24) is relatively insensitive to the variation of input parameters (see also the discussion in Herbert et al.[140]): therefore it is not possible to achieve more than $\Delta T_{0.5} = -0.5K$ for ten-fold change in the cooling rate. However, the cooling rate dependence seems to be sensitive to the symmetry of the contact angle distribution $p(\theta)$: by assuming the log-normal instead of Gaussian distributed contact angles but otherwise preserving all model parameters a better agreement with the measurements of $\Delta T_{0.5}$ at $c = -10\,K/min$ could be achieved (dashed line in figure 29). Therefore, it can be concluded that the cooling rate dependence of the freezing curve is adequately described by SBM but can hardly be used to constrain the fitting routine.

The allowed variability of fit parameters can be reduced if we consider that the same IN material has been used in CR experiments with different weight concentrations W. In this case the values of μ_θ and σ_θ can be kept constant in the simulation of the freezing curves and only n_{site} should be varied. The initial pair of μ_θ and σ_θ can be determined either by fitting the freezing curve measured for the lowest concentration or by assuming the fit parameters obtained from the ISO experiments (if available), as it has been done here for FS02.

The same considerations have been used to constrain the fit of isothermal data for FS02 and FS04 obtained for different values of T_{ISO}. For FS02, the initial values of $\mu_\theta = 1.32\,rad$ and $\sigma_\theta = 0.1\,rad$ have been obtained from the fit of composite liquid fraction decay curve at 256 K. This pair of parameters have been then used to fit the other ISO decay curves and the freezing curves measured in the CR experiments with various concentrations. Within this approach, a high quality fit ($r^2 > 0.95$) of all frozen fraction curves (figure 30A) and liquid fraction decay curves (figure 28A) could be achieved. Note that the number of IN sites per droplet n_{site} required to achieve the fit convergence increases with the rising concentration of FS02 suspension, which make sense as the number of sites per droplet is increasing with mass concentration of the particulate matter in the suspension. Note also, that obtained pair of fit parameters for FS02 is very close to the values $\mu_\theta = 1.29\,rad$ and $\sigma_\theta = 0.1\,rad$ obtained in Niedermeier et al.[28] by fitting the frozen fraction curves measured in diffusion channel LACIS for the same feldspar specimen (FS01).

The fit of the ISO measurements of FS02 has delivered a higher number of IN active sites n_{site} for higher T_{ISO} (see table 3). This contra-intuitive observation can be possibly explained

by the relationship between T_{ISO} and the final fraction of frozen droplet achieved at the end of ISO run. For higher T_{ISO} the final fraction of frozen droplets is lower, and the fit algorithm "compensates" for the reduction of available sites by increasing their total number. This effect was not very pronounced in case of FS04 (see table 3), probably because the final fraction of frozen droplet for both used T_{ISO} was very similar. This observation, however, hints that n_{site} should not be treated blindly as a number of active sites activated during the cooling ramp or isothermal freezing, but rather as a number of active site required by the numerical algorithm to reproduce the freezing curve. Thus, caution should be exercised when interpreting the fit results, as numerical features can be mistaken for physical relationships.

Almost the same distribution of contact angle ($\mu_\theta = 1.33\ rad, \sigma_\theta = 0.1\ rad$) as for FS02 was obtained by fitting the concentrated FS05 suspensions. This is a somewhat unexpected result since freezing curves are visibly shifted towards the lower temperature (by at least 2K, see Fig. 25A and 25C). If one would trust the physical interpretation of fitting parameters, the similarity of contact angle distributions would mean that the difference between K-rich feldspar (FS01, FS02) and Na/Ca-rich feldspar (FS05) is not in the activity of IN sites but in their number per unit particle surface ($n_{site} = 47$ for FS05 against $n_{site} = 181$ for FS02, with only 20% difference between total particle surface S_p). However, the same temperature shift can be obviously compensated by increasing the standard deviation from $\sigma_\theta = 0.1\ rad$ to $\sigma_\theta = 0.14\ rad$ (compare $n_{site} = 30$ for FS01 and $n_{site} = 181$ for FS02, which have a very similar freezing behavior). Such analysis demonstrates that fitting the freezing curves with freely variable three-parameter fit without providing additional constraint does not necessarily lead to a better understanding of IN nature. Therefore the intercomparison of the freezing behavior of different specimens or observed in different experimental setups based on such a fit should be done with extreme caution.

The sample FS04 is clearly standing out of the analyzed group of feldspars in several respects. For this specimen, it was not possible to fit all freezing curves obtained at various concentrations with a fixed pair of fit parameters μ_θ and σ_θ. The $\mu_\theta = 0.75\ rad$ found for freezing curve measured for the 0.8 wt% suspension indicates a very high IN efficiency. However, for the diluted suspensions (0.01 wt% to 0.1 wt%) the fit parameters that secured the best fit appeared to be close to the values obtained for the three other feldspar specimens (see table 2). Such behavior could only be interpreted in terms of bimodal population of active sites in the FS04 sample, with the sites belonging to the very active second mode present in scarce numbers and thus visible dominating the freezing curve of concentrated suspension droplets. In diluted suspensions the presence of the second mode is visible as a shoulder on the higher temperature side of the freezing curves for 0.1 wt% and 0.05 wt% suspensions (see figure 30B). This shoulder, however, does not affect the fit algorithm.

The two-component hypothesis of FS04 freezing behavior is strongly supported by the data of isothermal decay experiments and corresponding fit. The fit parameters that provided the

best fit of liquid fraction decay curves were identically apart for the 15% difference in the n_{site} value, so that the only experimental value actually different in the simulation is the T_{ISO} (266K and 265K). The value of $\mu_\theta = 0.56\,rad$ is even lower than the mean contact angle obtained from the fit of the freezing curve $\mu_\theta = 0.75\,rad$ and the standard deviation $\sigma_\theta = 0.04$ indicates a homogeneous population of IN active sites. The difference in μ_θ between the CR and the ISO fits should be attributed to the fact that in the CR experiment the whole distribution of freezing sites is involved in ice nucleation and therefore the contact angle obtained in the fit represents the whole distribution of active sites. On the contrary, in the ISO experiments only the most efficient sites are activated so that the less efficient sites are excluded from the freezing process. The homogeneity of the active sites distribution is consistent with the linearity of the decay curve in the log-log scale (see figure 28B).

Such low values and narrow distributions of contact angles (and hence high IN activity) have been previously obtained in SBM fit for freezing curves of biological INPs. For example, the INPs generated from Czech and Swedish birch pollen washing water (BPWW) have been characterized by $\mu_\theta = 1.01$ rad, $\sigma_\theta = 0.08$ rad, and $\mu_\theta = 0.83\,rad, \sigma_\theta = 0.0005\,rad$ respectively[144]. For Snomax® particles, the best INP known up to date[145], SBM parameters of $\mu_\theta = 0.595\,rad, \sigma_\theta = 0.04\,rad$ have been calculated based on the same approach[146]. Within this reference framework, the IN efficiency of high active mode of FS04 is higher than that of the BPWW and at least as high as that of the Snomax®.

Overall the IN activity of feldspars investigated in this study is situated at the upper end of ice activity scale. For ATD particles the range of SBM parameter was found between $\mu_\theta = 2.13\,rad$, $\sigma_\theta = 0.33\,rad$, and $\mu_\theta = 2.48\,rad$, $\sigma_\theta = 0.39$ rad[70]. The mean and standard deviation of the contact angle distribution of Illite NX was found to be $\mu_\theta = 1.90\,rad$ and $\sigma_\theta = 0.27$ rad respectively[147]. Similar SBM parameters were observed for size-selected kaolinite (Fluka) particles: $\mu_\theta = 1.87\,rad$ and $\sigma_\theta = 0.25$ rad[148]. Note, that these fit data were not constrained by isothermal freezing experiments. However, this comparison suggests that the SBM framework correctly reproduces the relative ice nucleation efficiency of natural and artificial mineral dust aerosols.

Table 2: SBM parameters obtained by fitting the CR freezing curves. The total particle surface area per droplet S_p is given for 0.8wt% suspensions and could be recalculated for all other mass concentrations. Pearson's r correlation coefficient was calculated from the freeze-thaw cycle experiments.

	FS01	**FS02**			**FS05**	**FS04**			
$W\ [wt\%]$	0.8	0.8	0.05	0.01	0.8	0.8	0.1	0.05	0.01
$S_p\ [cm^2]$	2.5×10^{-5}	3.7×10^{-5}			2.7×10^{-5}	4.2×10^{-5}			
$n_S^*\ [cm^{-2}]$	2.1×10^{7}				1.8×10^{7}	1×10^{4}	2.4×10^{7}		
$n_{site}\ [\#]$	30	181	8	2	47	3.5	63	25	6.8
$\mu_\theta\ [rad]$	1.3	1.32			1.33	0.75	1.32	1.3	1.35
$\sigma_\theta\ [rad]$	0.14	0.1			0.102	0.12	0.15	0.12	0.1
r^2	0.99	0.96	0.99	0.95	> 0.95	0.99	0.95	0.98	> 0.99
$Pearson's\ r$	0.89	-	-	-	0.8	0.92	-	-	-

Table 3: SBM parameters obtained by fitting the ISO decay curves.

	FS02				**FS04**	
$T_{ISO}\ [K]$	256	255	254	253	267	266
$S_P\ [cm^2]$	3.7×10^{-5}				4.2×10^{-5}	
$n_{site}\ [\#]$	4400	1565	705	410	0.42	0.36
$\mu_\theta\ [rad]$	1.32				0.56	
$\sigma_\theta\ [rad]$	0.1				0.04	
r^2	0.99	0.98	0.98	0.94	0.99	0.98

5.1.7 Surface density of IN active sites

The CR experiments performed with varying concentration allowed to calculate the INAS surface density via Eq. (2.19) in the temperature range from 238K to 260K for FS01 and FS02 (see figure 31). Both $n_s(T)$ curves for FS01 and FS02 are very similar and therefore put together in one plot. In the temperature range between 252K and 260K (occupied by the 0.8wt% suspension data), the $n_s(T)$ values are only slightly lower than those reported for FS02 in Atkinson et al.[5], denoted ATK2013 in the plot and elsewhere. The data of ATK2013 is shown in form of exponential parametrization and is used as a reference for all other $n_s(T)$ plots (black solid line in figures 31 to 33). Size-selected measurements of FS01 particles in LACIS also showed a similar slope of $n_s(T)$ curve but the values are shifted towards higher n_s values located at lower temperature (orange open triangles, Niedermeier et al.[28], denoted NIED2015 in the plot and in the following discussion). Both our $n_s(T)$ curves for FS01 and FS02 suspensions and the data from NIED2015 showed a leveling-off of $n_s(T)$ values with decreasing temperature. A qualitative explanation that was suggested in NIED2015 is that at colder temperature the INAS surface density is approaching asymptotic value n_s^*, equal to the maximum surface density of all possible INAS for the given particle population. The leveling off has not been reported in ATK2013, obviously because the suspension was not diluted sufficiently to reach the temperature range where the leveling-off would be expected.

The $n_s(T)$ curve can be easily related to the SBM fit parameters obtained from the CR and ISO experiments via Eq. (2.25). The shaded area in the figure 31 shows the range of $n_s(T)$ that can be obtained by assuming the fit parameters from table 2: $\mu_\theta = 1.32\,rad$, $\sigma_\theta = 0.1\,rad$, $c = -1\,K/min$, $n_{site} = 2$, and varying weight concentration of feldspar in the droplet suspension from 0.01 wt% to 0.8 wt% and therefore varying the total particle surface area since $S_p = W \cdot V_{drop} \cdot S_{BET}$. Note that varying the S_p has essentially the same effect on the $n_s(T)$ as varying the n_{site} since these two quantities appear as a ratio in the Eq. 2.25. The fact that all experimental data fall inside the shaded area demonstrates that the range covered by n_{site} variation corresponds to the variation range of total particle surface at different weight concentrations. One can immediately see that the SBM simulation captures the leveling-off of $n_s(T)$ at lower temperature.

As pointed out in Niedermeier et al.[28], the asymptotic value n_s^* is the limit of $n_s(T)$ when the probability of the suspension droplet to freeze at T, $P_{freeze} = 1 - P_{unfr}(T, \mu_\theta, \sigma_\theta, t)$, approaches 1 (recall Eq. (2.25)). It is therefore clear that the suspension droplet is bound to freeze when $n_s(T)$ reaches the value n_s^* and further increase of the IN active site efficiency (described in the model by decreasing the value of contact angle) would not result in the further increase of the freezing probability (or the fraction of frozen droplets). The value of n_s^* is therefore a true suspension property as compared to n_{site}, which is just a number required by the minimization algorithm to fit the experimental freezing curve. For combined FS02 and FS01 the upper boundary value of n_s^* was found to be 2.1×10^7 cm^{-2}, corresponding to the surface area occupied by a single IN active site $S_{site} \approx 5\ \mu m^2$, a square

patch with the side length of 2.2 µm, which is at least 6 orders of magnitude larger than the cross section area of a critical ice nucleus at low temperature[22].

We observe that the data of NIED2015 are laying outside the shaded area in figure 31. The values of $n_s(T)$ reported in NIED2015 have been obtained for single size selected feldspar particles, with the modal electrical mobility diameters ranging from 0.2µm to 0.5µm. If the geometric surface area (based on the aerodynamic diameter, as specified in NIED2015) of a 0.5µm particle is used as the S_p in Eq. (2.25) and the constant temperature and residence time of 1.6 s (LACIS condition), than the blue broken line can be obtained that agrees with the data of NIED2015 quite well. The ratio of the asymptotic n_s^* values is evidently equal to the ratio of S_p values in NIED2015 and in this study (red broken curve in figure 31). Thus, it can be concluded that the apparent INAS surface density in the plateau region is a function of the particle surface area per droplet, which is not obvious considering that per definition the INAS surface density is a number of frozen droplets normalized by the particle surface area.

For the asymptotic value of INAS surface density for NIED2015 data a value of $n_s^* = 4.7 \times 10^8\ cm^{-2}$ is calculated and the corresponding surface area occupied by a single IN in this case is reduced to $\approx 0.21\ \mu m^2$, a square patch with the side length of $\approx 460\ nm$, still "oversized" for a single critical ice germ. According to CNT, the active site area of a critical ice embryo was estimated to be 10nm² at 244K (varying from 1.2nm to 3.1nm in the temperature range from 235K to 255K)[69]. The fact that the "surface area per active site" is much larger than the cross section area of a critical ice germ supports the idea that "ice active sites" should be some local features (of morphological or chemical nature) and not the homogeneous patches of particle surface.

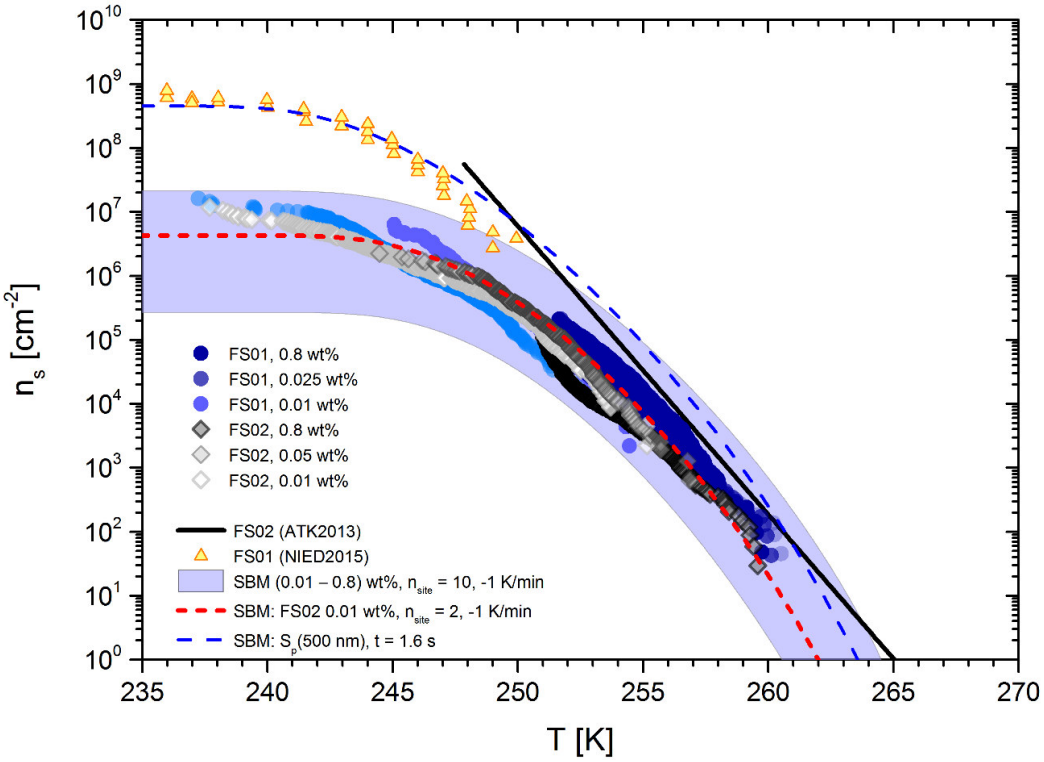

Figure 31: $\boldsymbol{n_s(T)}$ curves of K-feldspar particles FS01 and FS02. Shaded area shows the range of $\boldsymbol{n_s(T)}$ values predicted by equation (2.25) with fixed parameter set $\boldsymbol{\mu_\theta = 1.32\,rad, \sigma_\theta = 0.1\,rad}$, $\boldsymbol{n_{site} = 10}$, and suspension between 0.01wt% and 0.8 wt%. Red broken line corresponds to the best fit parameter set for FS02 (see table 2) with 0.01wt% and $\boldsymbol{dT/dt = -1\,K/min}$. The blue broken line is calculated with the same parameter set but assuming a single FS01 particle with Stokes diameter of 500nm per droplet and fixed temperature lasting for 1.6s (LACIS conditions) instead of constant cooling rate.

The $n_s(T)$ curves of FS05 suspensions are shifted to lower temperatures compared to FS01 and FS02 (see figure 32) but otherwise showed the same behavior (exponential growth in the range from 250K to 257K and gradual leveling-off at lower temperatures). Together with our values, both measurements reported recently in Atkinson et al.[5] and Schill et al.[29] fall nicely into the range of n_s values predicted by Eq. (2.25) by assuming the fit parameters: $\mu_\theta = 1.33\,rad$, $\sigma_\theta = 0.1\,rad$, $n_{site} = 5$, $c = -1\,K/min$ and varying the weight concentration of feldspar in the droplet suspension from 0.01 wt% to 0.8 wt%. The upper boundary value of n_s^* was found to be $1.8 \times 10^7\ cm^{-2}$, very close to that of FS01 and FS02.

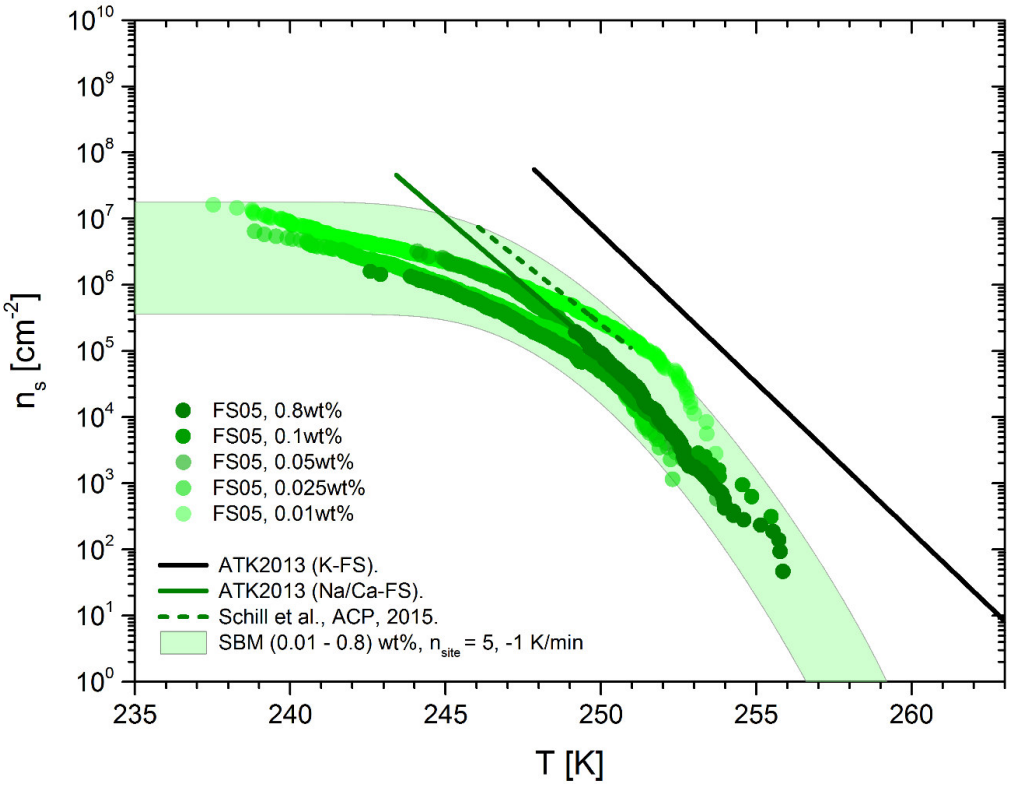

Figure 32: $\boldsymbol{n_s(T)}$ curves of Na/Ca-feldspar particles FS05. Shaded area shows the range of $\boldsymbol{n_s(T)}$ values predicted by equation (2.25) with fixed fit parameter set of $\boldsymbol{\mu_\theta = 1.33\,rad}$, $\boldsymbol{\sigma_\theta = 0.102\,rad}$, $\boldsymbol{n_{site} = 5}$ and concentration of feldspar suspensions varied between 0.01 wt% and 0.8 wt%. Black and green solid lines are exponential fits of data from ATK2013 for K-rich and Na/Ca-rich feldspar suspension droplets, respectively. The green dotted line is an exponential fit of the Na/Ca-feldspar data from Schill et al.[29].

The outstanding nature of FS04 becomes more evident on the $n_s(T)$ plot (see figure 33). The bimodal behavior is clearly visible with the first mode being active already at 268K, 5K below the melting point of water. The second mode is located at lower temperature and is almost coinciding with the $n_s(T)$ curve of FS01 and FS02 (shown as red broken line in figure 33). Both modes show the leveling-off starting below 266 K for the high-temperature mode and below 248 K for the low-temperature mode.

The coexistence of two independent sets of IN active sites can be reproduced by Eq. (2.25) by using two separate sets of fitting parameters (table 2) for calculation of $n_s(T)$. The $n_s(T)$ range covering the low-temperature mode is obtained by assuming the fit parameters: $\mu_\theta = 1.3\,rad$, $\sigma_\theta = 0.12\,rad, n_{site} = 10$ and varying the weight concentration of feldspar in the droplet suspension from 0.01 wt% to 0.1 wt%, whereas the high temperature mode is represented by fit parameters: $\mu_\theta = 0.75\,rad$, $\sigma_\theta = 0.12\,rad$ and varying the n_{site} from 0.2 to 10. Note that the $n_s(T)$ curve calculated with the SBM fit parameters obtained from the isothermal freezing experiments ($\mu_\theta = 0.56\,rad$, $\sigma_\theta = 0.04\,rad$, table 3) is only reproducing the rising slope of the measured curve. This means that the overall shape of the high-temperature part of the curve (above 255K) is influenced by IN active sites from both

active and less active modes, and is responsible for the higher value of μ_θ than the one obtained from isothermal freezing experiments.

A formal comparison of the asymptotic INAS surface densities n_s^* for two modes $2.4 \times 10^7 cm^{-2}$ for low temperature mode vs. $1.0 \times 10^4 cm^{-2}$ for high temperature mode suggests that the highly active sites constitute roughly 0.1% of all sites in the feldspar suspension droplets. Multiplying the n_s^* for the high temperature mode with the total particle surface area per droplet one can estimate $n_s^* \times S_p = 0.29$ implying that only 30% of the most highly concentered suspension droplets contain at least one high temperature active site at all. One can obtain approximately the same number by noting that only 75% of all droplets froze in the ISO experiment after cooling the droplet assay down to 266 K and waiting for an hour (see figure 28B). Since the amount of feldspar in our suspension droplets (0.8 wt%) corresponds roughly to 3.7×10^3 individual feldspar particles of 0.5µm diameter, one could estimate that only one in ≈ 12000 feldspar aerosol particles of this size would contain a single highly active ice nucleating site. This estimation might be helpful in understanding the nature of these sites, as discussed below.

A two-step ice nucleation behavior was previously obtained for pure size-selected ATD particles[149] and birch pollen washing water residual particles[144] in LACIS, for soil dust particles[150] and Snomax®[143, 145] particles in droplet freezing assay experiments. These measurements highlight that there could be multiple distinct populations of ice nucleating particles (INPs) present in a particular material. The concentration determines which IN population is visible in the fraction of frozen droplets. To our knowledge, however, multiple ice nucleating species in a single component mineral dust aerosol (illite NX, kaolinite, etc.) have not been observed before.

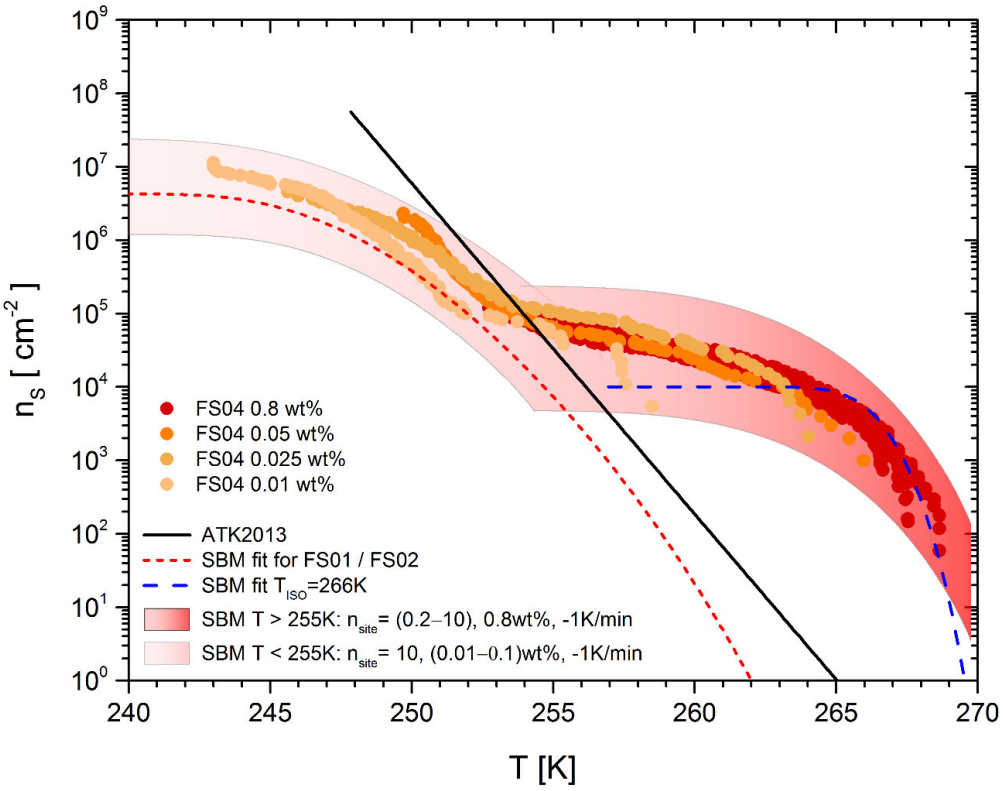

Figure 33: $\boldsymbol{n_s(T)}$ curves of K-feldspar particles FS04. The shaded areas show the range of $\boldsymbol{n_s(T)}$ values (for details see text). Black solid line is a fit of data from ATK2013 for FS02. Red broken line is a fit to our FS02 data (as in figure 31). Blue broken line is the $\boldsymbol{n_s(T)}$ curve predicted by Eq. (2.25) with parameters obtained from the isothermal freezing experiments (see table 3).

5.1.8 Influence of ageing

To examine the influence of aging on the ice activity of feldspars, K-feldspar (FS01) and Na/Ca-feldspar (FS05) particles were soaked in water for over five months and the supernatant water was exchanged twice. Soaking in water resulted in a decrease of the median freezing temperature by 2K for FS01 and by 3K for FS05 0.8 wt% suspensions. (see figure 34). The reduction of ice nucleating efficiency is thought to be correlated with the release of soluble components from the framework of the mineral (e.g. alkali metal ions, hydrated aluminum and silicon species), which might be repartitioned as amorphous material on the surface of feldspar particles[151, 152] and inhibit ice active sites. The stronger reduction in T_{50} values observed for FS05 might be a consequence of a higher dissolution rate of the Na/Ca-feldspar particles[151, 153]. The time evolution of the leaked cation concentrations (K^+, Na^+, Ca^{2+}, and Mg^{2+}) have been measured during the first month by liquid ion chromatography and is shown in figure 35. We have observed a steady rise of cation concentration during whole period of observation according to the $\sim t^{0.5}$ law, well known in petrology for the dissolution rates of tectosilicates[153]. This behavior clearly differs from the cation release from illite NX clay mineral in aqueous suspension, where no further increase of the cation concentration was observed after initial fast release occurring on the order of

several minutes[147]. The depletion of framework cations in the surface crystalline layers of feldspar might be another explanation of the observed reduction of ice activity. Due to the constant release of the framework cations the IN activity of the ageing feldspar should gradually reduce over long time period, as the feldspar is weathered to become a clay.

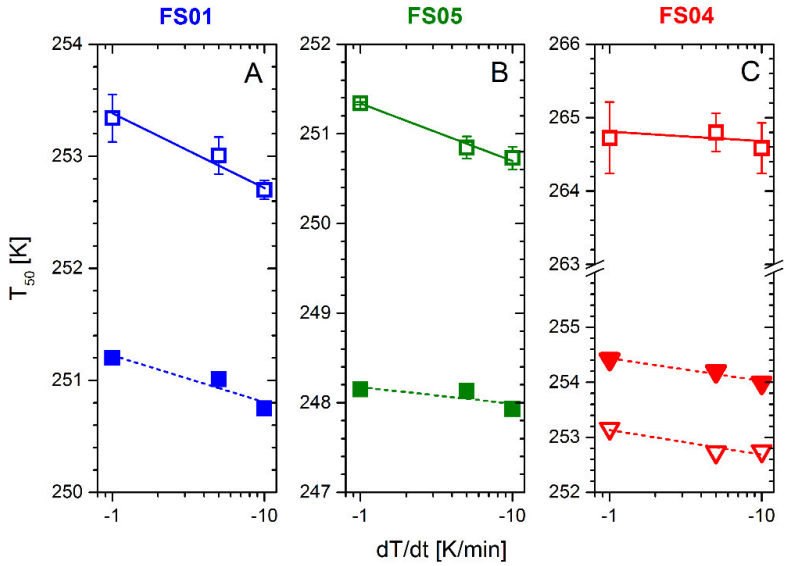

Figure 34: A, B) Median freezing temperature $\boldsymbol{T_{0.5}}$ for the aqueous suspensions of FS01 und FS05 aged for over five months (blue and green filled symbols). C) Median freezing temperature $\boldsymbol{T_{0.5}}$ of FS04 0.8wt% suspension treated with 30% H_2O_2 for an hour (filled triangles) and overnight (open triangles). $\boldsymbol{T_{0.5}}$ for the freshly prepared suspension is shown as open square symbols. Straight lines are non-weighted linear regressions of the averaged $\boldsymbol{T_{0.5}}$ values for three different cooling rates.

The effect of particle processing, such as removal of hydrophilic ions by water, in a water suspension was examined by ion chromatography. Suspended samples were prepared by stirring feldspar suspension (0.1g in 10mL of Nanopure water) over one month. IC (Dionex DX-500 IC System equipped with Dionex Conductivity Detector CD20) was used to determine the concentrations of washed out cations (K^+, Na^+, Ca^{2+} and Mg^{2+}) as a function of time. A weak solution of sulfuric acid (5mL H_2SO_4 (96wt%) diluted in 2L of Nanopure water) was used as the eluent. The measurements were conducted every 10sec within first 2min, every 10min within the first hour after immersion and then every 3 days for a 4-week period. The concentration of K^+ in the washing water of FS01 was steadily rising even after one month in the suspension (see figure 35), whereas the concentrations of Na^+ and Ca^{2+} in the FS05 suspension were gradually levelling off towards the end of the measurement period.

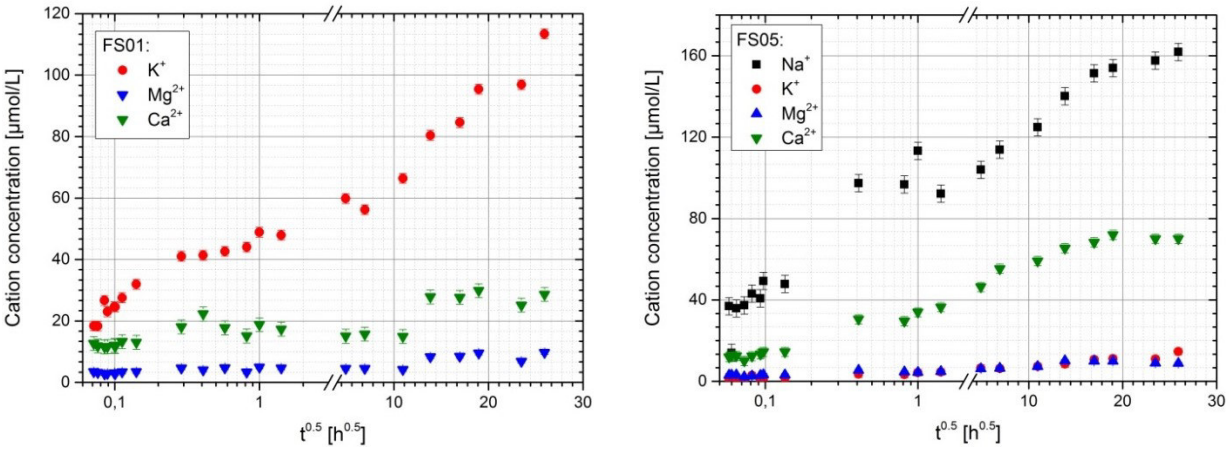

Figure 35: Evolution of cation concentrations in aqueous suspensions of 0.1g feldspar in 10ml deionized water with time derived from ion chromatography (IC) measurements. Left panel: FS01 and right panel: FS05.

It has been undertaken an attempt to shed some light onto the anomalously high ice nucleating efficiency of concentrated FS04 suspensions by treating them both thermally and chemically. The primary suspect was contamination with biological IN particles known to be the most active ice nucleating particles in immersion mode. To this matter, CR experiments with 0.8wt% suspensions heated up to 90°C for an hour were conducted. Heating is a common procedure to test for proteinaceous ice nuclei that are expected to degrade progressively with increasing temperature[154, 155]. Thus treated FS04 showed a slight decrease of the T_{50} value from 264.7K to 263.9K in 1K/min CR experiment, but the $n_s(T)$ curve preserved its bimodal shape and position (see figure 36). This clearly demonstrates that proteinaceous IN could not be responsible for the high ice activity of FS04 particles. Another test is the removal of thermally stable carbonaceous IN by digestion with hydrogen peroxide solution[150, 156]. This treatment, performed at 65°C for one hour, has indeed resulted in the significant reduction of the ice activity of FS04. Keeping the FS04 sample in hydrogen peroxide over night at room temperature lowered the T_{50} even further (figure 34C and figure 36). A weak cooling rate dependence of chemically treated FS04 particles was observed, with the 10-fold change is responsible for $\Delta T \approx 0.5K$. This is more than the ΔT observed for untreated suspensions by a factor of 2 (open symbols in figure 34C) and is characteristic for generic feldspars FS01 and FS02. By looking at $n_s(T)$ curves of thermally and chemically treated FS04 it becomes clear that the treatment has reduced its IN activity down to that of the generic K-feldspar (FS01 and FS02). A further reduction was not observed and is not expected since the generic K-feldspar particles showed no detectable change in ice activity after a thermal treatment[27, 150]. Based on these results alone, organic IN cannot be ruled out as a reason for the anomalous high freezing efficiency of FS04 particles.

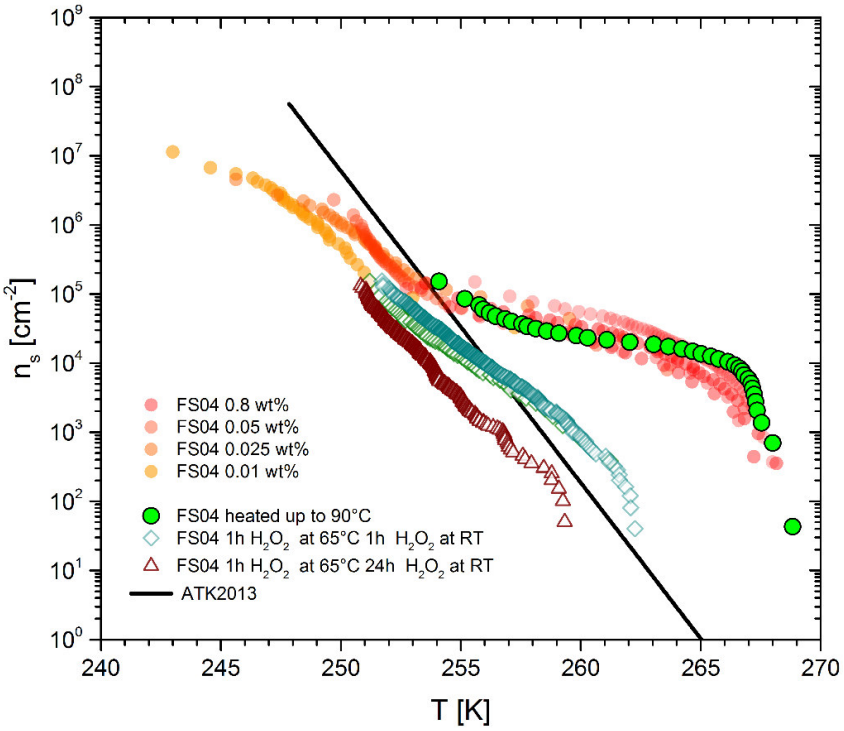

Figure 36: $\boldsymbol{n_s(T)}$ curves of K-feldspar particles (FS04) after heating to 90°C and chemical treatment with hydrogen peroxide.

The amount of "contamination" required to produce the observed enhancement of INAS surface density at high temperature can be calculated. The feldspar powder used for preparation of FS04 suspension was produced by ball milling of a single crystal feldspar specimen. Due to the usual precaution measures taken to avoid the contamination during and after the preparation, it is logical to assume that the contamination could be introduced on the surface of specimen prior to milling, and the amount of contamination should be proportional to the surface area of the original specimen. In the previous section it was concluded that only every third droplet in the experiment contained a highly active ice nucleating "entity". Since the mass of feldspar per $0.6\ nL$ droplet at 0.8wt% concentration is $V_d \times 0.008 \times \rho_{FS} = 1.2 \times 10^{-8}\ g$, one can estimate the mass concentration of active sites equal to $n_m = 2.7 \times 10^8\ g^{-1}$. Such value is characteristic for ice active fungal species[157] or most active component of Snomax® at 267K[145]. Suppose the specimen was a cube with a side of 1cm prior to milling, which is a typical size of low cost single crystal specimen of feldspar. Assuming that all high active INP were located on the surface of such a specimen, the surface density of INPs of $\approx 1.2\ \mu m^{-2}$ can be obtained, more than one ice nucleating particle per square micrometer. Such contamination is impossible and it can be drawn the conclusion that the active sites responsible for the high-temperature freezing mode are inherent for the feldspar itself. The question of the nature of this ice nucleating substance remains open.

Several studies addressed the influence of ageing processes on the IN activity of feldspar particles. In more detail, diffusion chamber studies showed no statistically significant change in ice nucleation ability of unwashed and washed feldspar (orthoclase) particles in deposition

mode freezing experiments[25]. K-feldspar treated with enzyme nucleated ice at much lower temperatures, but after heating the ice activity has been restored to the original level. For Na/Ca-feldspar particles (albite and andesine) no distinct change after thermal and chemical treatment was noticed[27]. A strong reduction of ice activity of K-feldspar particles (microcline) immersed in water droplets was achieved by treatment with sulfuric acid[30]. It was suggested that the treatment with sulfuric acid irreversibly modified the lattice structure of K-feldspar, as was also suggested by the ice nucleation experiments with bare and sulfuric acid coated K-feldspar particles[31]. To be more specific, in the deposition freezing experiments a reduced ice activity for coated feldspar particles was found, while no significant difference between bare and coated K-feldspar particles was observed in immersion freezing experiments. This behavior was explained in terms of dissolution of coating material under water-supersaturated conditions. However, these results are hardly comparable with our observations since sulfuric acid coatings have not been applied in our study.

5.2 FIN02 campaign

The FIN02 campaign was one of the three phases of the Fifth International Ice Nucleation Workshop (FIN). This workshop included: 1) The intercomparison of single particle mass spectrometers for the determination of IN composition (FIN01, Nov. 2014), 2) The intercomparison of online and offline IN instruments (FIN02, Mar. 2015) and 3) The intercomparison of sampling methods for ambient INPs (FIN03, Sep. 2015). Up to 23 research groups from US and Europe participated in the FIN02 campaign. The main objective of FIN02 campaign was to obtain a comprehensive picture about the capability and reliability of up-to-date IN measurement techniques.

5.2.1 Characterization of aerosol particles

Immersion freezing experiments of known and unknown aerosol samples were performed with the KIT Cold stage as a part of the off-line intercomparison at the IMK-AAF. The aerosol samples were collected via two impingers from the NAUA chamber (small evacuable aerosol chamber, 3.7m³)[158]. The operating principle and the collection efficiency of an impinger is described in Hader et al.[159] The settings of the instruments, washing and bottling protocols are specified in the FIN02 off-line tables. For the characterization of the aerosol samples, suspension droplets were printed onto the silicon substrate and the droplets were allowed to evaporate. The residual aerosol particles were subsequently analyzed by means of SEM/EDX measurements. The SEM images of the residual particles are shown in figure 37. As illustrated in figure 37, some of the residual particles form complex morphological structures encompassing aggregated smaller particles (e.g. illite NX, figure 37B) and coated particles (e.g. soil dust and Snomax®, figures 37A and 37D), which is probably due to the washing out of soluble material in water. Spatially separated residual particles were obtained for the K-feldspar and Tunisian desert dust samples (figures 37C and 37E). However, the arrangements of the residual particles give an idea of the size and shape of the evaporated aerosol suspension droplets. In the next paragraphs, the results of the FIN02 intercomparison campaign will be presented.

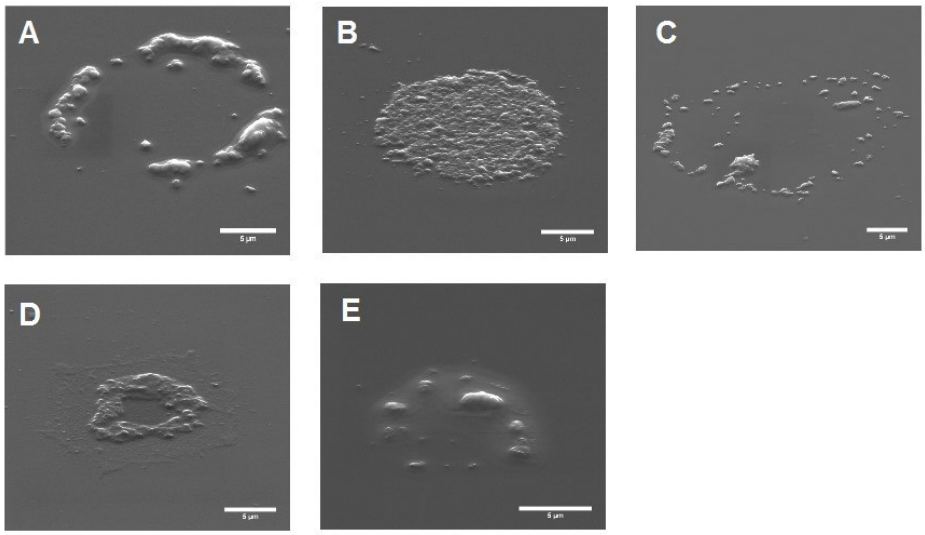

Figure 37: SEM images of A) soil dust, B) illite NX , C) K-feldspar, D) Snowmax® and E) desert dust residual particles deposited onto a silicon substrate. Every size bar corresponds to 5µm.

5.2.2 Cooling ramp experiments

Cooling ramp (CR) experiments were performed for known aerosol samples hereinafter referred to as non-formal intercomparison and for unknown blind test and mystery samples hereinafter referred to as formal intercomparison. Known and unknown aerosol samples were treated equally and at least two 1K/min CR runs were measured. The frozen fraction curves of the aerosol samples and the blind test/mystery samples are depicted in the figures 38A and 38B. Each aerosol sample of the non-formal intercomparison showed ice activity in a specific temperature range: Snomax® froze between -4.23°C and -11.85°C, K-feldspar between -17.15°C and -22.5°C, soil dust between -19.23°C and -30.17°C, desert dust between -20.24°C and -35.85°C and finally illite NX between -23.59°C and -33.94°C. The frozen fraction curves of individual CR runs for a specific sample nearly overlap indicating a high repeatability of the measurements. In addition, the frozen fraction curves of NanoPure water (1K/min and 5K/min) are included in figure 38A. All frozen fraction curves were very steep except for the Tunisian desert dust. The experimental results are consistent with the previous measurements of Snomax®[143, 145], K-feldspar[5], soil dust[150], desert dust[160] and illite NX[147] showing that the KIT Cold stage can quantitatively represent the ice nucleation efficiencies of various aerosol samples. Concerning the aerosol samples of the formal intercomparison, blind test 22 and mystery I sample froze in the temperature range from -18.48°C to -28.60°C, whereas the blind test 24 and the mystery II sample nucleated ice at lower temperatures (from -21.55°C to -31.39°C) and higher temperatures (from -13.12°C to -23.23°C) respectively.

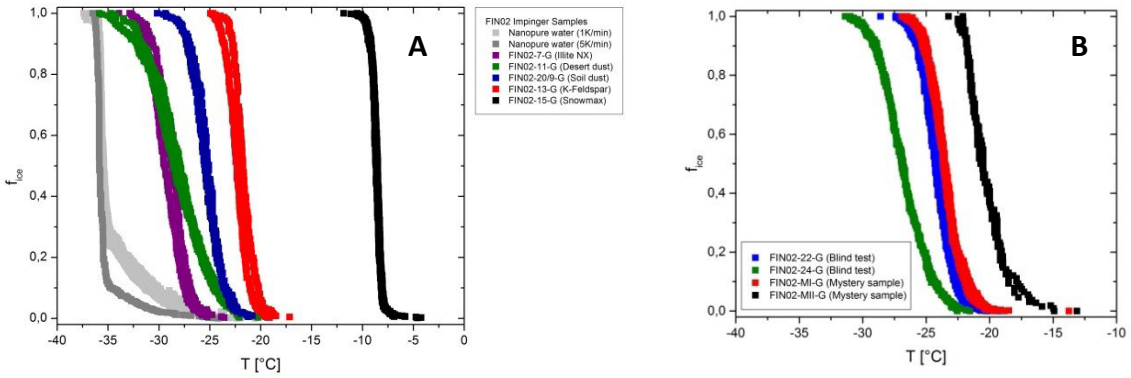

Figure 38: Frozen fraction curves of A) the aerosol impinger samples (non-formal intercomparison data) and B) the blind test/mystery samples (formal intercomparison data). Note that for every aerosol sample at least two runs are shown.

5.2.3 Calculation of the number concentration of IN

The procedure for the calculation of the number of IN per liter water and per cubic meter air follows the considerations of Hader et al.[159] At first, NanoPure water samples were measured with a cooling rate of 1K/min. The fraction of unfrozen droplets as a function of temperature is converted into the concentration of IN per picoliter via normalization to the volume of the droplet V_{drop}:

$$c_{IN}(T) = -\frac{lnf_{unfrozen}(T)}{V_{drop}} \qquad (5.\ 1)$$

The small fraction of water droplets that freeze at temperatures higher than the homogeneous freezing limit (~-36°C) is utilized for the parametrization of the background. It is assumed that heterogeneous nucleation by impurities in the water or defects on the surface of the silicon substrate induced the freezing of the water droplets. A third-order polynomial is used for the background parametrization:

$$c_{Impurities}(T) = exp(A + BT + CT^2 + DT^3) \qquad (5.\ 2)$$

where $c_{IN}(T)$ is the concentration of IN per liter water. The coefficients are $A = -30.768$, $B = -3.612$, $C = -0.086$ and $D = -7.277 \cdot 10^{-4}$ (red solid line in figure 39A, R^2=0.994). Alternatively, a second parametrization with $A = -33.039$, $B = -3.870$, $C = -0.098$ and $D = -8.922 \cdot 10^{-4}$ (blue solid line in figure 39A, R^2=0.998) was worked out. In the appendix, an exponential expression with base 10 is given, which is used for the following calculations. However, both parametrizations differ only slightly from each other. By using this functional relationship, the background can be calculated for a particular temperature and subtracted from the IN concentration of the impinge aerosol sample. Second, the impinger aerosol sample curves were temperature-binned in 0.5°C intervals resulting in a strong reduction of the data points. Third, several runs (1K/min) were averaged to estimate the statistical uncertainty of the IN concentration. The confidence interval is given by $\frac{1.96\sigma}{\sqrt{N}}$, where σ is the

standard deviation and N is the number of cooling runs. Finally, the number of IN per cubic meter air $IN(T)$ is estimated according to the following equation:

$$IN(T) = \frac{\left[c_{IN}(T) - f c_{Impurities}(T)\right] V_{Impinger}}{Q_s t} \qquad (5.\ 3)$$

where $c_{IN}(T)$ is the concentrations of IN in the impinger aerosol samples [IN per liter water) and $c_{Impurities}(T)$ is the initial concentration of impurities in NanoPure water, f is the scaling factor for the introduced impurities due to refilling of the impinger in the course of the experiments, $V_{Impinger}$ is the volume of the impinger, Q_s is the sample (volumetric) flow rate through the impinger and t is the sampling/operation time. Table 6 in the appendix gives an overview of the quantities used for the calculation of the number of IN per cubic meter air.

The concentrations of IN per liter water and per cubic meter air of the impinger aerosol samples and the blind test/mystery samples are displayed in the figures 39 and 40. In the impinger aerosol samples (figures 39A and 39B) were approximately 10^6 to 10^{10} IN per liter water and 10^5 to 10^8 IN per cubic meter air present. These IN concentrations are high compared to ambient IN concentrations of ~1 IN/m³ air at -20°C[159, 161], but these concentrations were necessary to deliver a constant aerosol flow for all the instruments participating in the intercomparison campaign. As can be seen from figure 39B, the background correction has the strongest impact on the illite NX, as illite NX is the least ice active material among the aerosol samples. The other aerosol samples are only marginally affected by the background correction. The blind test/mystery samples are in the same IN concentration range as the impinger aerosol samples (see figures 40A and 40B). However, the concentration of IN per m³ air of the mystery samples could not be calculated, because these samples are concentrated suspension (~1wt%) and were not sampled from the NAUA chamber via the impingers.

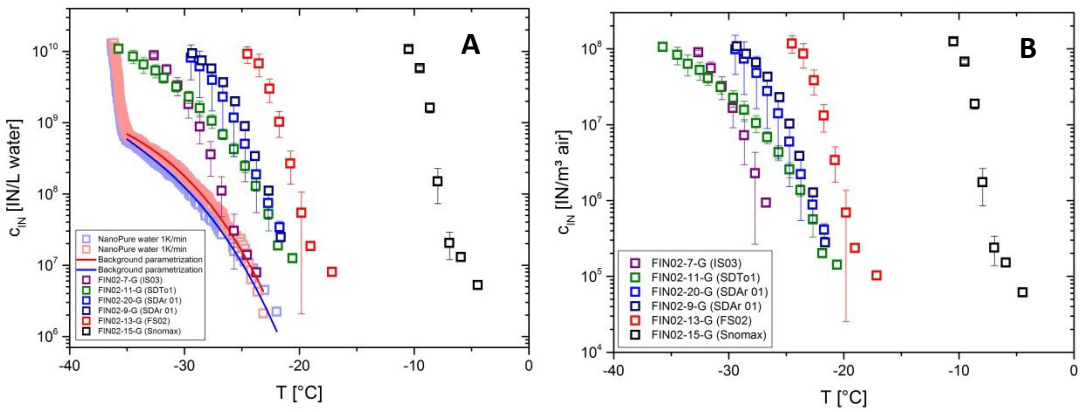

Figure 39: Estimated concentrations of IN A) per liter water and B) per cubic meter air of the aerosol impinger samples (non-formal intercomparison data). The blue and red solid lines indicate the parametrizations of the background (see text).

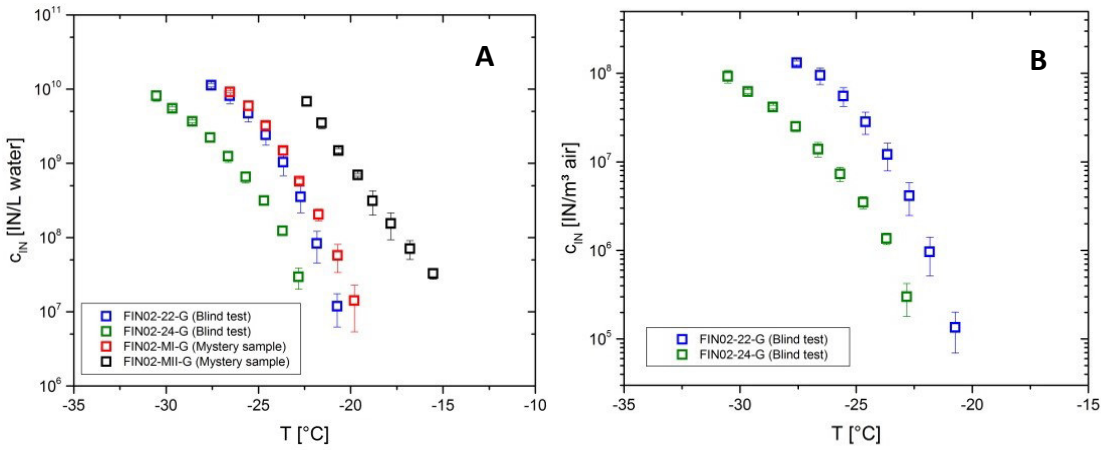

Figure 40: Estimated concentrations of IN A) per liter water and B) per cubic meter air of the blind test and mystery samples (formal intercomparison data).

5.2.4 Intercomparison of different off-line instruments

For the non-formal intercomparison, the results of the impinger aerosol samples were compared with those of the off-line instruments. Up to seven off-line techniques based on the measurements of IN efficiency of particles collected on filters in suspensions contributed data to the FIN02 intercomparison campaign. As apparent from the figures 41 and 42, the IN concentrations of the impinger aerosol samples measured with the KIT Cold stage are at the lower temperature end, which is reasonable considering that the KIT Cold stage is a nanoliter droplet freezing technique. The IN concentrations per liter water and per m³ air of the impinger aerosol samples (red data points in figures 41 and 42) are in fairly good agreement with the other off-line instruments. However, a few outliers were noted (e.g. TU Wien Cold Stage, CSU IS Filter/Mainz-AL for Snowmax® and soil dust). In general, the results of the off-line techniques agreed reasonably well on the log scale, but there are in some cases up to two orders of magnitude difference in IN concentrations. Hiranuma et al.[147] showed that the discrepancies for the reference mineral dust illite NX between nineteen measurement techniques were even larger (up to three orders of magnitude with respect to the INAS surface density (see section 2.4.3) or about 8°C in temperature difference). The reasons for the discrepancies are not fully understood. It is worth noting that the aerosol samples illite NX, K-feldspar and Tunisian soil/desert dust showed a linear increase of the IN concentrations per liter water and per m³ air indicating a single IN population, while for the aerosol samples Argentina soil and Snomax® a stepwise behavior of the IN concentrations were observed indicating the presence of multiple INPs. This behavior resembles that of FS01/02 on the one hand and FS04 on the other hand (see section 5.1). A good agreement was also obtained for the blind test and mystery samples in the formal intercomparison (not shown here). Blind test 22 and mystery sample II are ATD and blind test 24 and mystery sample I are Argentina dust. Both aerosol samples showed a non-linear temperature

dependence of the IN concentrations in the temperature range from 266K to 241K, which is consistent with multiple INPs activated at characteristic temperature regimes.

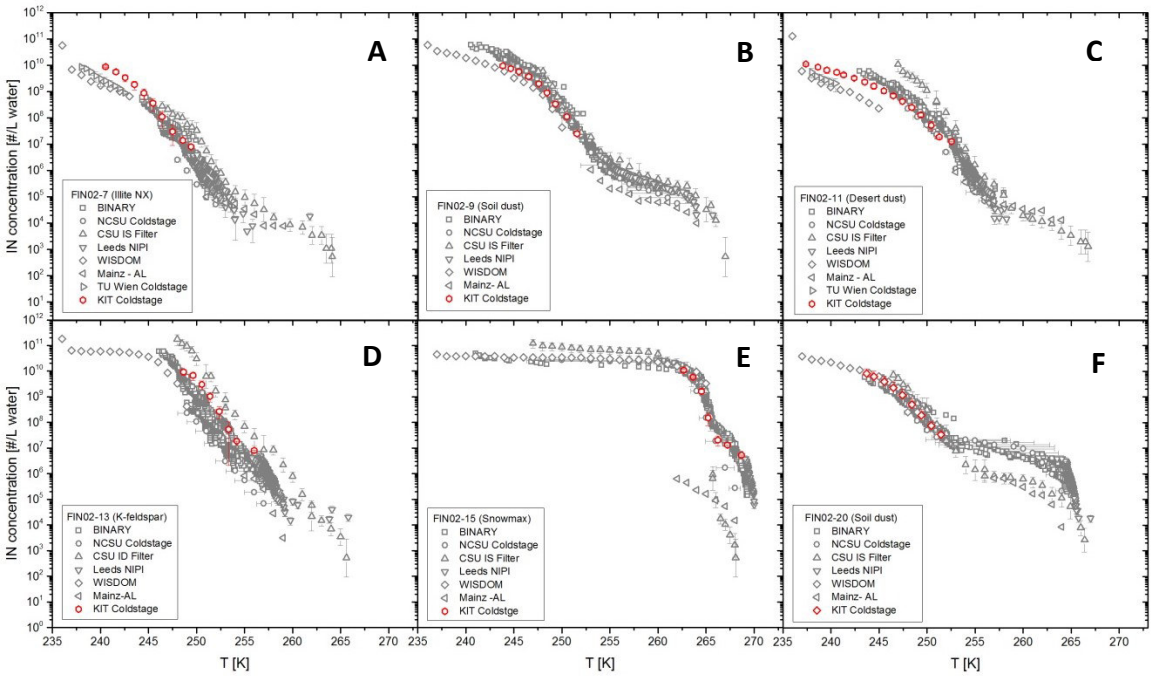

Figure 41: Estimated IN concentrations per liter water of A) illite NX (IS03), B) Soil Dust from Argentina (SDAr01), C) Tunisian Soil/Desert Dust (SDTo1), D) K-feldspar (microcline), E) Snomax® (0.5wt%) and F) Soil Dust from Argentina (SDAr 01) (formal intercomparison data).

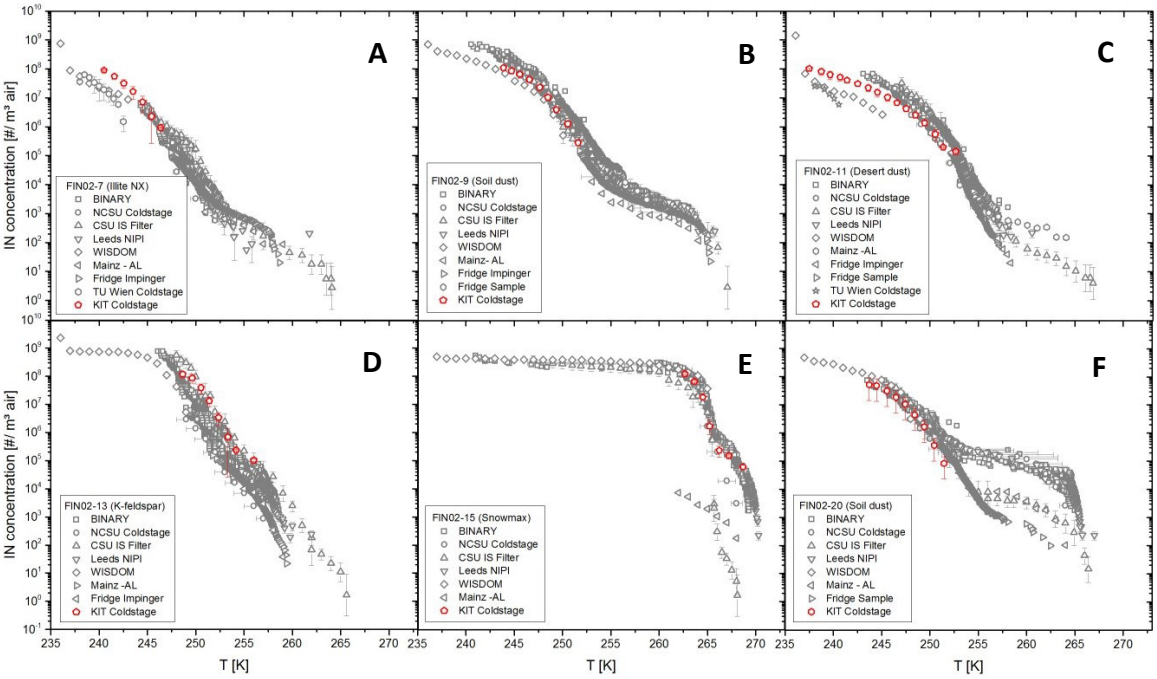

Figure 42: Estimated IN concentrations per cubic meter air of A) illite NX (IS03), B) Soil Dust from Argentina (SDAr01), C) Tunisian Soil/Desert Dust (SDTo1), D) K-feldspar (microcline), E) Snomax® (0.5wt%) and F) Soil Dust from Argentina (SDAr 01) (formal intercomparison data).

5.2.5 Suspension experiments with filtered feldspar particles

An analysis of the cooling rate dependence of the K-feldspar aerosol sample revealed that a 10-fold change in the cooling rate decreased the mean freezing temperature from $T_{0.5}$ (1K/min)=-21.74°C to $T_{0.5}$(10K/min)=-22.46°C(see figure 43B). This corresponds to a temperature shift of ΔT=0.72°C. The value of the temperature shift is very similar to the one derived for the unfiltered concentrated FS01/FS02 suspensions in section 5.1.5. The frozen fraction curves of the K-feldspar aerosol sample are closely related to the size distribution of the residual particles deposited onto the silicon substrate (see figure 43A). The mean projected area equivalent particle diameter is d_p=0.397µm assuming a lognormal distribution of particles. The results of the K-feldspar aerosol sample are compared with the frozen fraction curves and the corresponding size distributions of not filtered and filtered FS02 suspensions (figure 44). Not filtered concentrated FS02 suspensions (0.8wt%) featured a mean projected area equivalent particle diameter of d_p=0.644µm and a $T_{0.5}$ (1K/min) value of -20.66°C. In contrary, concentrated FS02 suspensions filtered with a 0.45µm and a 0.2µm syringe filter exhibited very narrow size distributions and $T_{0.5}$ (1K/min) values of -23.62°C and -25.57°C respectively. These findings demonstrate both that K-feldspar (microcline) particles are still ice active even below about 100nm[162] and that their size distribution strongly affects the position and shape of the frozen fraction curves. However, the cooling rate dependence appears to be less affected by the size distribution of the particles. The temperature shift of the not filtered FS02 suspensions is ΔT=0.66°C and of the filtered FS02 suspensions ΔT=0.82°C (0.45µm) and ΔT=0.64°C (0.2µm) for a 10-fold increase of the cooling rate. The deviating value of ΔT=0.82°C is mainly due to the limited temporal resolution of this 10K/min run (figure 44B, dark green curve).

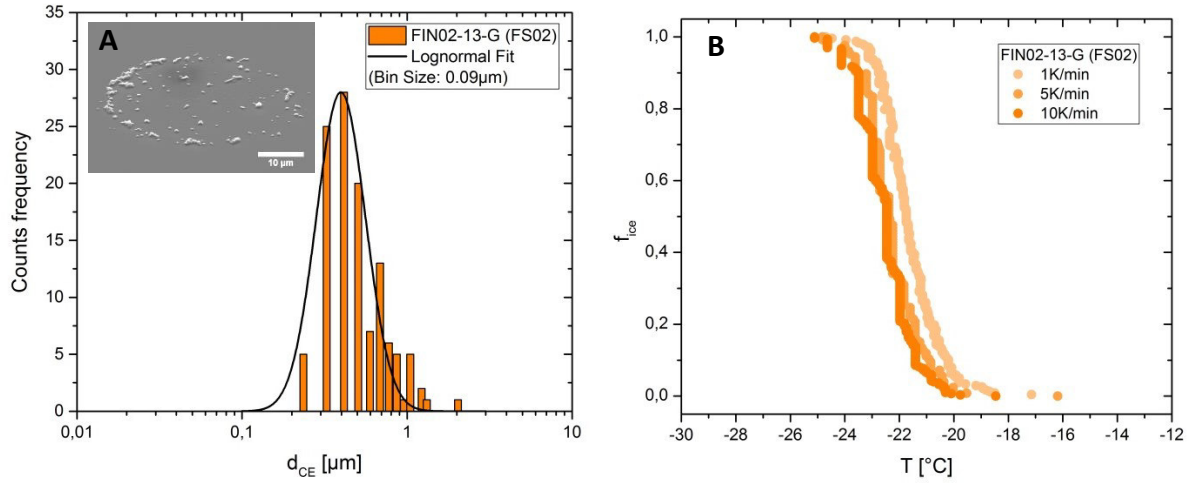

Figure 43: A) Size distribution of the aerosol impinger sample FIN02-13-G (K-feldspar). The inset shows deposited K-feldspar particles onto a silicon substrate. The size bar in the inset corresponds to 10µm. B) Fraction frozen curves of the same sample (FIN02-13-G) measured with different cooling rates (1, 5 and 10K/min).

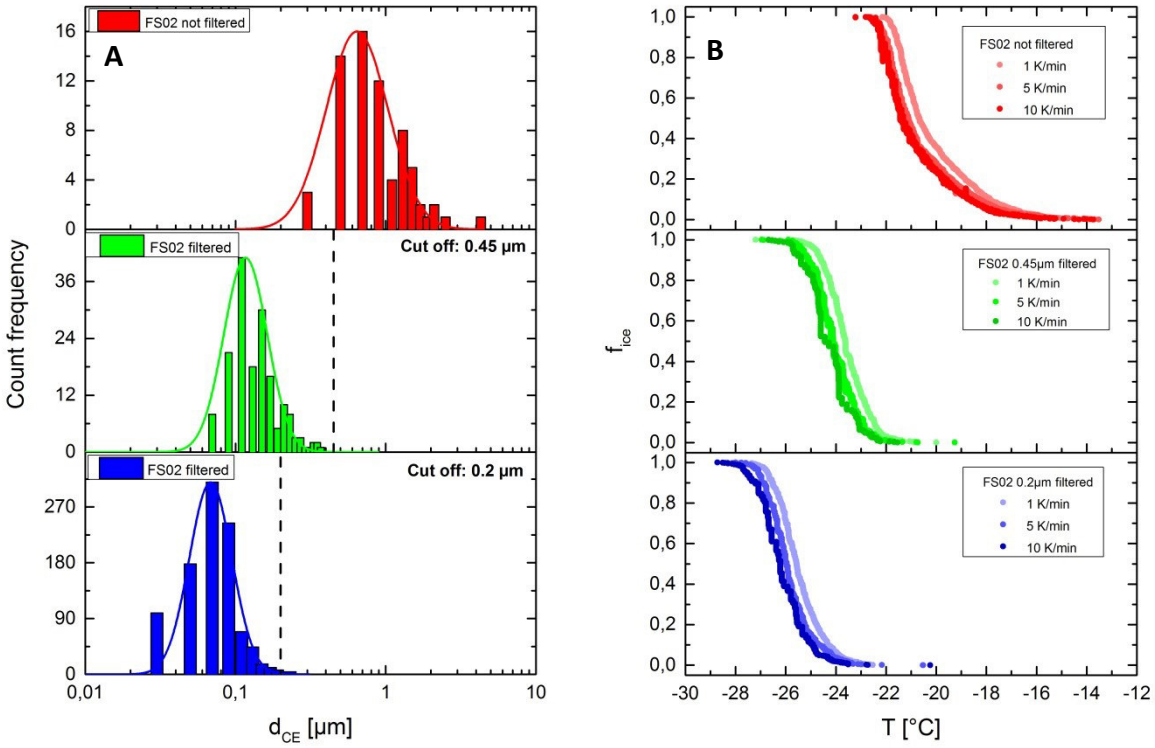

Figure 44: A) Size distributions of FS02 particles (red: not filtered, green: 0.45µm and blue: 0.2µm pore size of syringe filter). B) Fraction frozen curves of the corresponding FS02 suspensions. Note that the color coding indicates the cooling rate of suspension measurements.

Overall, the results of the formal and non-formal intercomparison revealed that the number of IN per liter water and per m³ air of different types of aerosol samples can be quantitatively analyzed with KIT Cold stage setup. The IN concentrations of aerosol samples and blind test/mystery samples were in good agreement with established off-line droplet freezing assays. The intercomparison campaign also showed that some limitations of the experimental setup exist: Below about -25°C a background correction needs to be applied. The sensitivity of the KIT Cold stage is strongly related to the total number of investigated droplets and is generally lower than ~1%, which is comparable to or even better than other off-line techniques. Furthermore, the temperature uncertainty of $\Delta T = 0.2$°C is very low due to the direct measure of the temperature (with a Pt-100 sensor) on top of the silicon substrate.

The KIT cold stage is a suitable tool for studying the ice nucleation efficiencies of various aerosol samples. This competitive technique allowed the determination of the IN concentrations of known and unknown aerosol samples in the temperature range from 0°C to -36°C (homogeneous freezing limit). Therefore, the FIN02 intercomparison campaign offered the unique opportunity to test and validate the experimental setup regarding to the IN concentrations of aerosol samples. The results are promising for future applications of the KIT Cold stage.

5.3 Water

5.3.1 Raman spectra of water at different temperatures

The bulk spectra of liquid water at ambient temperature exhibit in the high-frequency region from 3000 cm^{-1} to 3700 cm^{-1} a broad band originating from the asymmetric and symmetric OH stretching modes of water molecules[163] (see figure 45). The Raman spectra of supercooled water at -29°C is characterized by a strong contribution of a Raman band at approximately 3200 cm^{-1}. It has been proposed that the Raman band at 3200 cm^{-1} results from a Fermi resonance, a combination of normal and overtone modes[164]. The Raman band at 3200cm^{-1} increases with decreasing temperature[163]. In the literature, several approaches exist to deconvolve the OH stretching band. Up to five individual Gaussian-shaped components were used to represent the entire OH stretching band of liquid and supercooled water[165]. The amount of hydrated (tetrahedral-coordinated) and non-hydrated (free) water can be determined by this method. In the Raman spectra of frozen water at -40°C, a sharp peak at 3150cm^{-1} appeared. It is assumed that the Raman band is associated with an in-phase v_1 vibration[166, 167] and the two Raman bands at 3323cm^{-1} and 3420cm^{-1} are assigned to the v_3 LO (longitudinal optic) and v_1 out-of-phase vibrations of water molecules in the crystal lattice respectively[167]. The spectral features are characteristic for the formation of hexagonal ice (I_h).

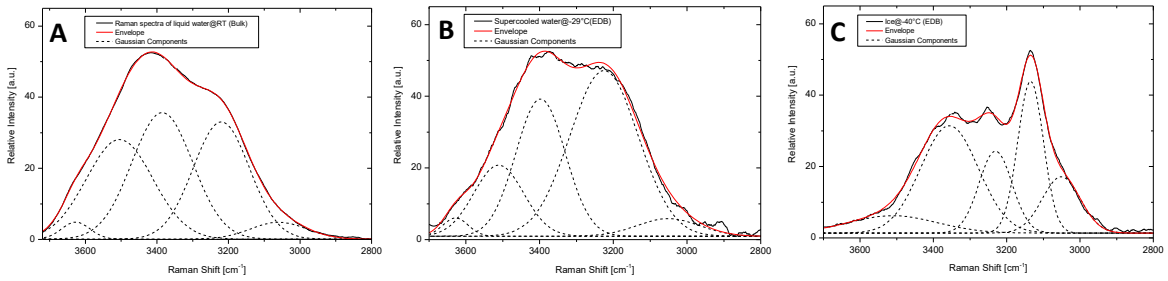

Figure 45: High-frequency region of the Raman spectra of A) liquid water at ambient temperature B) supercooled water at -29°C and C) frozen water at -40°C. The last two Raman spectra originate from particles suspended in the EDB. Together with the experimental Raman spectra (black solid line), the individual Gaussian components (black dotted lines) and the overall envelope (red solid line) are shown. The OH bending mode is not shown.

The low-frequency Raman spectra of liquid water at ambient temperature showed a band at ~183cm^{-1} after applying the Bose-Einstein correction due to the thermal distribution of vibrational states (see figure 46). This Raman band is related to the H-bond O-O stretching vibration[168]. However, the Raman band at ~50cm^{-1} (H-bond O-O-O bending vibration) could not be resolved due to the removal of the Rayleigh component by the Raman spectrometer. The intermolecular modes correspond to restricted translational motions perpendicular and

parallel to the water molecule's axis[169]. In the Raman spectra of supercooled water at -29°C a pronounced Raman band is located at ~200cm^{-1}, which is closely linked to the Raman band at ~183cm^{-1}. With decreasing temperature decreases the intermolecular H-bonded O-O distance. The decrease in temperature also implies that the force constant increases. As a consequence, the vibrational frequency rises from about 183cm^{-1} to 200cm^{-1} in the temperature range from 20°C to -29°C[168, 170]. Krishnamurthy et al.[168] pointed out that already in liquid water at low temperatures the shoulder at 260cm^{-1} becomes significantly more pronounced (which is hardly visible in figure 46B). The Raman spectra of frozen water showed two strong Raman bands at 230cm^{-1} and 293cm^{-1}. These peaks were interpreted in terms of the structural similarity of four-coordinated water molecules in the liquid and in the solid state. The peaks arise from the splitting into perpendicular and parallel components from clusters of tetrahedrally coordinated water molecules[168]. Note that for reasons of simplicity, the OH-bending region and the liberations (hindered rotational motions) of water molecules are not shown in the figures 45 and 46.

The Raman spectra of water at different temperatures were recorded with the intention to understand the effect of temperature on the Raman spectra. This procedure seems to be appropriate, as in the next section the influence of both temperature and additional ionic components on the Raman spectra of water and their impact on the nucleation behavior of the solutions are investigated.

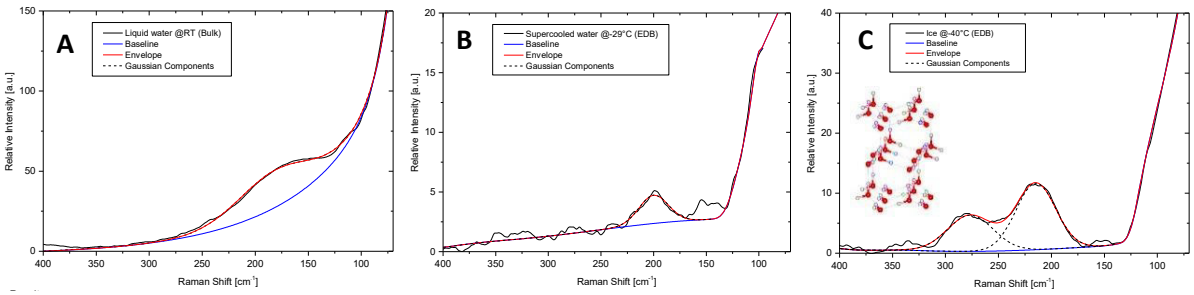

Figure 46: Low-frequency region of the Raman spectra of A) liquid water at ambient temperature B) supercooled water at -29°C and C) frozen water at -40°C. The last two Raman spectra originate from particles suspended in the EDB. Together with the experimental Raman spectra (black solid line), the individual Gaussian components (black dotted lines) and the overall envelope (red solid line) are shown. The inset in panel C shows an illustration of the crystal structure of hexagonal ice (I_h).

5.4 NaCl particles

5.4.1 Raman spectra of anhydrous NaCl and NaCl·2H_2O

The Raman spectra of a NaCl diyhrdate particle levitated in the EDB at -40°C showed three distinct Raman regions: In the high-frequency region (3000-3800cm^{-1}), two main peaks at 3424cm^{-1} with a shoulder at the low-frequency side (3410cm^{-1}) and a weaker peak at 3545cm^{-1} were observed, arising from the symmetric and asymmetric OH-stretching vibrations of water respectively. Two Raman bands with significant lower intensity were found at 3299cm^{-1} and 3320cm^{-1}. The OH-bending modes of crystalline water are centered at 1644cm^{-1} and 1664cm^{-1}. In the low-frequency region (200-800cm^{-1}) of the Raman spectra of NaCl dihydrate, lattice water molecules exhibit librational modes due to rotational vibrations, restricted in their motion by the interactions with neighboring lattice atoms. A pronounced librational vibration is located at 390cm^{-1} (see figure 47).

Dubessy et al.[171], Bakker et al.[172] and Baumgartner et al.[173] observed four different Raman bands in the OH-stretching region of NaCl dihydrate. A temperature-dependent study of the Raman spectra of NaCl dihydrate suggests that at higher temperatures the Raman bands are broadened and individual peaks merge into a broader band[172, 173]. This could explain the observation of two main Raman features. Additionally, an isotopic dilution technique (replacement of hydrogen atoms by deuterium atoms) proved the existence of four unequal OH-bonds[174].
The two OH-bending modes in NaCl dihydrate provide evidence for at least two distinct water molecules[171, 175]. X-ray diffraction measurements reveal that the structure of NaCl dihydrate consists of two crystallographically independent water molecules[176]. NaCl dihydrate (also known as hydrohalite) has a monoclinic crystal structure and belongs to the space group of $P2_1/c$ (see insets of figure 47). Note, that the literature about the low-frequency region of NaCl dihydrate is scarce.

Both Raman spectra of anhydrous NaCl collected at -20°C in the EDB and at room temperature (approximately 21°C) showed no spectral signatures. Only lattice vibrations in spectral range from 100cm^{-1} to 390cm^{-1} were observable. One prominent signal is located at 235cm^{-1}. These observations for a pure NaCl crystal are in agreement with findings of Möller et al.[177]. It is proposed that the strongest peak at 235cm^{-1} arise from combinations and overtones of longitudinal-acoustic (LA) and/or transverse-acoustic (TA) phonons (lattice vibrations) in the second-order Raman spectra (inelastic scattering of a photon by two phonons) of anhydrous NaCl[178].

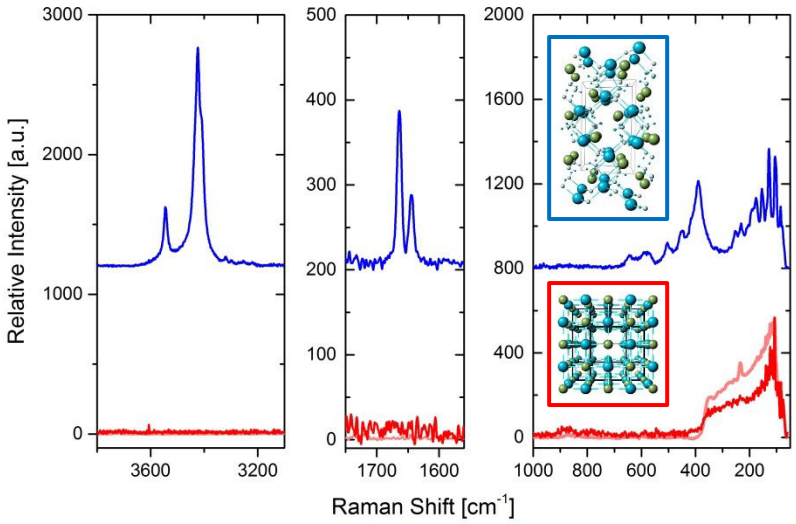

Figure 47: Raman spectra of a NaCl dihydrate particle at -40°C (blue), an anhydrous NaCl particle at -20°C (red) in the EDB and a conventional bulk Raman spectra of anhydrous NaCl crystals at room temperature (~21°C, light red Raman spectra). The insets show the corresponding crystal structures of NaCl dihydrate and anhydrous NaCl. Note that the Raman spectra are normalized to the lattice vibration of anhydrous NaCl at ~107cm^{-1}.

5.4.2 Liquid-solid phase transformations of NaCl particles

A thoroughly inspection of the Raman spectra collected in a RH-ramp efflorescence experiment at room temperature (~21°C) revealed that several spectral features changed with decreasing RH (see figure 48). The Raman band at ~3225cm^{-1} decreased in intensity, the OH-bending mode at 1640cm^{-1} (ν_2) remained nearly unchanged or increased slightly and the Raman band at ~450cm^{-1} increased in intensity. These spectral changes originate from a perturbation of the water structure, i.e. the fully dissolved ions of NaCl are not Raman-active, but they affect the interaction of water molecules[179]. The vibrations are elucidated in more detail below:

Walfrafen et al. [180] assigned the broad Raman band in range from 3000-3800cm^{-1} to the symmetric (ν_1) and asymmetric (ν_3) OH-stretching mode. The band at ~3225cm^{-1} is due to the Fermi resonance of ($2\nu_2$+ν_1). A fermi resonance is a coupling of vibrational frequencies and occurs between normal and overtone modes, i.e. the OH-stretching and the second excited state (overtone) of the OH-bending mode of water. Both vibrations exhibit nearly the same symmetry (i.e. point group) and energy. The Raman band at ~450cm^{-1} (ν_{L1}) is suggested to arise from librations of water molecules in the environment of electrolyte ions. The increase of concentration, i.e. a lower relative humidity leads to a disruption of the local framework of water molecules. An enhancement and a shift to higher frequencies of the asymmetric OH-stretching was observed and interpreted as an increase of free OH-bonds, i.e. H-bonds break down in the tetrahedral environment of water. As the H-bonds weaken,

the intensity of the Fermi resonance also decreases. The strength of the fermi resonance is strongly correlated to the strength of the H-bonds. The peak at 1640 cm^{-1} increased and its width diminished with increasing solute concentration. The spectral changes of the peak at ~450cm^{-1} are explained in terms of an increase of structural ion-water units. The introduction of high polarizable Cl^--ions to the water network causes the formation of O-H···Cl-bonds, which are less polar than the normal O-H···O-bonds in pure water. It was proposed that the O-H···Cl-bonds have a lower polarity, i.e. a higher polarizability and thus the intensity of the libration mode increased by lowering the relative humidity.

Terpestra et al.[181] ascribed the intensification of the liberation band at ~450cm^{-1} in the presence of electrolytes to the effect of the density of the salt solution. Electrolyte ions, in particular Cl^--ions do not only perturb the water structure, but also produce local ordering of water molecules around the ions (formation of hydration shells). The vibrations involving H-bonds between ions and water are more symmetric, i.e. more intensive compared to water-water vibrations.

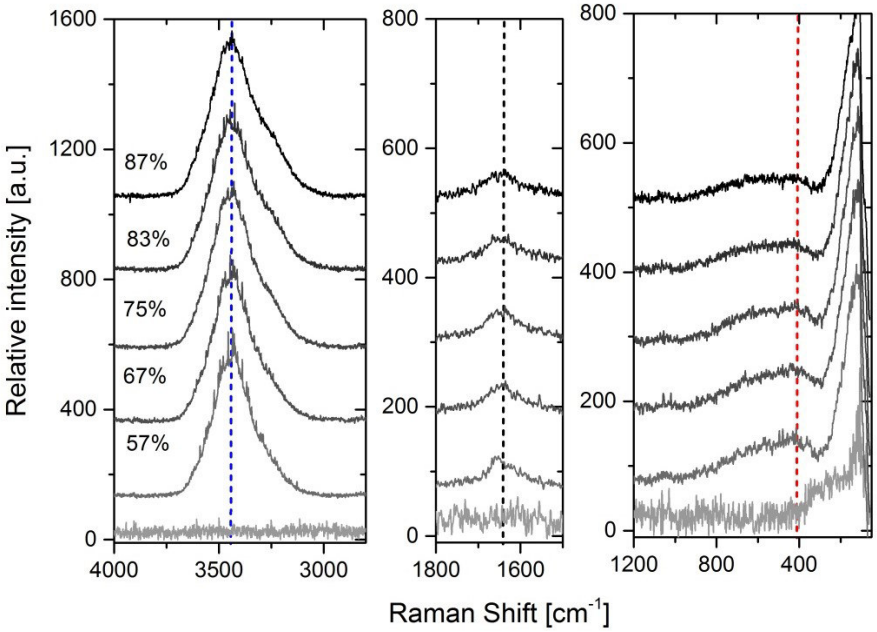

Figure 48: Raman spectra of an evaporating NaCl solution droplet levitated in the EDB at ambient temperature (~21°C). Note that the Raman spectra are normalized to the OH-stretching mode at ~3440cm^{-1}, expect of the Raman spectra of solid anhydrous NaCl (light grey Raman spectra).

5.4.3 Solid-solid phase transformations of NaCl dihydrate particles

Exposing NaCl dihydrate particles to dry conditions, i.e. RH values significant lower than the ERH value of NaCl induces solid-solid transformations from the dihydrate to the anhydrous form. The solid-solid phase changes are visible in both the high-frequency and the low-frequency region of the Raman spectra of NaCl dihydrate (see figure 49). The timescale of

this conversion is on the order of several minutes for different particles. In contrast, NaCl dihydrate particles exposed to RH values in the range of 38-45% over a period of 15 minutes showed no spectral changes. Only minor morphological changes (such as surface roughening) are observed from the shadow images of the NaCl particles.

Wise et al. reported that hydration water in the crystal lattice of NaCl dihydrate particles was removed when the RH in the environmental cell was dropped to 19.8% RH. The solid-solid transformation was accompanied by the cracking of the particle and the complete disappearance of spectral features in the Raman spectra[9]. A coexistence region of NaCl dihydrate and anhydrous NaCl is predicted by the phase diagram of $NaCl/H_2O$ starting at a composition of 61.87wt% (i.e. 16.1%RH at 273.25K)[182]. The phase transition should be thermodynamically induced, but obviously occurred at a slightly higher RH value as reported by Wise et al[9].

It is reasonable to assume that these solid-solid phase transformations of salt hydrates show virtually no or a low nucleation barrier because water molecules can intercalate into the crystal structure on a molecule-by-molecule basis in a diffusional process similar to the hydration or drying of clays[6]. A similar observation of successive hydration water loss in the dehydration process and hydration water incorporation in the humidification process of lithium iodide particles was reported by Kurtz et al[183].

The kinetic energy should exceed a certain amount so as to eject water molecules from the crystal lattice. The loss of hydration water then results in a collapse of the crystal structure or a rearrangement of the ions to a new stable crystalline form[184]. However, a disruption of the spherical shape of the NaCl dihydrate particles was not observed, perhaps due to the different experimental conditions of a charged and levitated NaCl particle in the EDB.

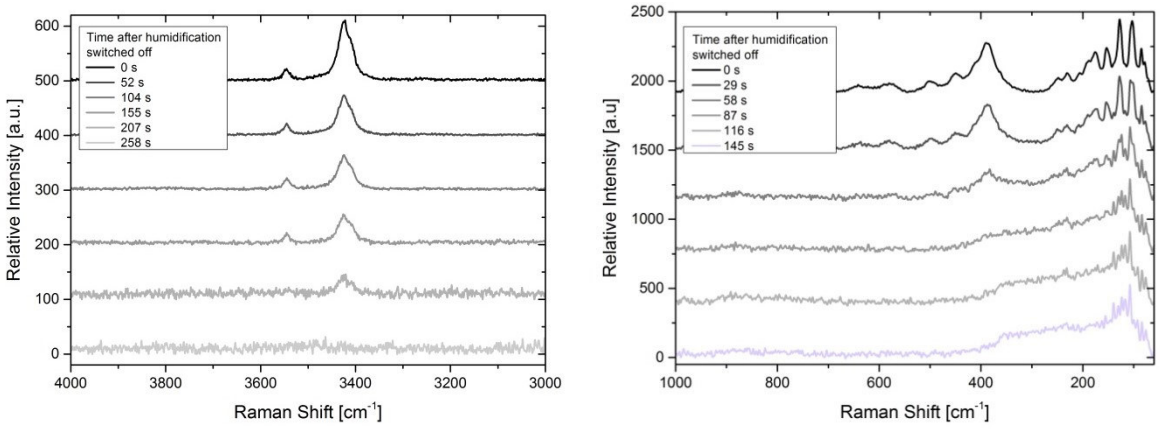

Figure 49: Temporal evolution of phase changes in the OH-stretching region of the Raman spectra (left panel) and in the lattice vibration region of the Raman spectra of a NaCl dihydrate particle (right panel). Note that the Raman spectra were collected from different NaCl dihydrate particles suspended in the EDB at -20°C.

5.4.4 DC voltage curves of anhydrous NaCl and NaCl dihydrate particles

The balancing DC voltage as a function of time for efflorescing NaCl solution droplets is depicted in figure 50 (see section 4.2.2 of the EDB layout). The crystallization usually occurred when the RH is lowered and the droplet underwent a liquid-solid phase transition. The phase transition is accompanied with a steep decrease in the DC voltage. The difference between the DC voltages immediately before crystallization and after crystallization was characteristic for the anhydrous NaCl particle and the NaCl dihydrate particle. This can be understood in terms of the release of water to the vapor phase at crystallization. NaCl dihydrate contains hydration water, which is incorporated in the lattice structure and cannot be released to the vapor phase. Effloresced NaCl particles can be distinguished due to their DC voltages curves after crystallization. Anhydrous NaCl particles were aspherical and rotated inside the EDB leading to sharps spikes in DC voltage curves, whereas the NaCl dihydrate particles were almost spherical and exhibited only slightly changing DC voltage curves. In the insets of figure 50, an enlargement of the nucleation event is displayed. The nucleation event can be recognized by a small increase of the compensating DC voltage, i.e. the scattered light intensity. After crystallization, the feedback mechanism of the height control requires time to adjust the DC voltage for the solid particle.

These observations are consistent with those of Cohen et al.[125]. It could be shown that the crystallization of NaCl at +20°C was very fast and was normally completed in less than 1s. Some of the NaCl particles did not directly transform to the dry solid state. These particles continued to lose water slowly until the dry state was reached. Based on the DC voltages before and after crystallization, the weight fraction of solute was calculated to be between 0.442 and 0.45 (i.e. ∼45% RH).

Braun et al.[73] investigated the efflorescence and deliquescence of NaCl solution droplets at -9.65°C (263.5K) in an EDB setup. A time of 2s has been required to completely crystallize the NaCl solution droplet. In contrast, a total time for efflorescence of less than 10ms was derived based on assumptions for the crystal growth rate and evaporation time. The apparent discrepancy was attributed to a diffusion barrier. It was proposed that after initial nucleation, a solid shell grows around the liquid core, which collapses due to mechanical stress resulting in the formation of an irregularly shaped solid NaCl particle. This description resembles the different freezing stages of supercooled water droplets[22].

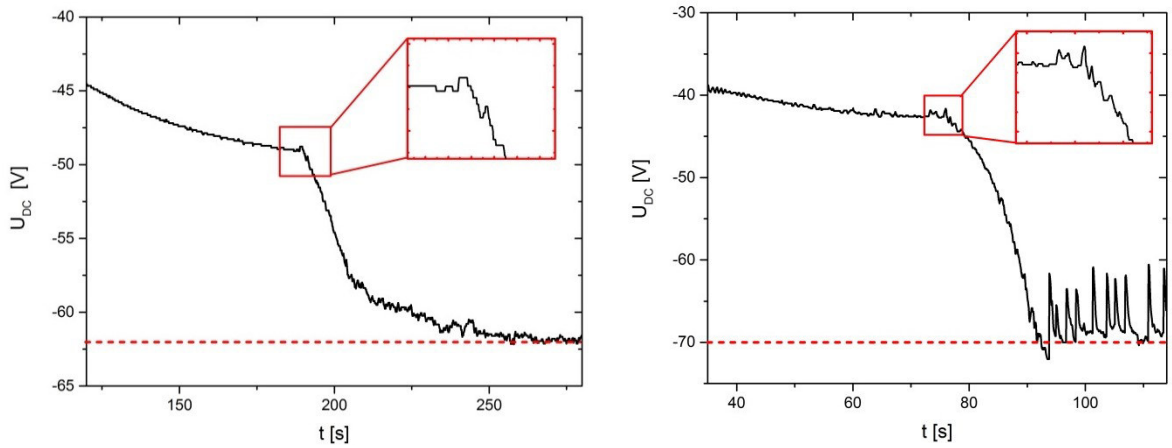

Figure 50: Left) DC voltage curves of a NaCl dihydrate particle and of Right) an anhydrous NaCl particle in EDB. The insets show an enlarged region of the DC voltage curves at the moment of nucleation.

5.4.5 Morphological characterization of residual particles

The vast majority of the effloresced anhydrous NaCl particles had a cubic shape (see figure 51). In addition, a few variously shaped NaCl particles were obtained, e.g. more elongated cubic-shaped particles and particles consisting of two and more interconnected cubes with different crystallographic orientations. The macroscopic single NaCl particles reflect the face-centered cubic (fcc) crystal structure of anhydrous NaCl. In this crystal structure each sodium ion (Na^+) and chloride ion (Cl^-) is octahedrally surrounded by its counterions. The morphology of the residual NaCl particles is in good agreement with previous measurements studying the shape of evaporating NaCl particles by wind tunnel experiments[185] and under the scanning electron microscope (SEM)[186, 187]. Furthermore, hollow crystalline NaCl particles were obtained by rapid drying of polydispersed NaCl droplets. The various particle shapes of anhydrous NaCl may be attributed to the experimental conditions, under which they were generated e.g. particle size, the rate of drying, concentration gradients within the evaporating droplets, etc.[22].

The NaCl dihydrate particles exhibited a nearly spherical shape. Some of the NaCl dihydrate particles showed small bulges und deformations probably due to the efflorescence process. Residual particles with a surface-roughened structure were also observed. The results are in line with measurements of Wise et al.[9]. Effloresced NaCl particles at 244K showed a round and bumpy appearance. The collected Raman spectra of these non-cubic particles confirmed the presence of NaCl dihydrate. Apparently, the observed morphology of the residual NaCl dihydrate particles does not reflect the monoclinic-prismatic crystal structure of NaCl dihydrate. In the crystal structure of NaCl dihydrate, four water molecules and two chloride ions surround one sodium ion[176]. The disagreement could be resolved by considering that the macroscopic spherical particle can be composed of several microscopic crystallites of NaCl dihydrate with a monocline-prismatic structure. These findings give rise to the assumption that supersaturated NaCl droplets effloresced into polycrystalline NaCl dihydrate

particles while maintaining the shape of the droplet. Similar to frozen water droplets, the polycrystallinity presumably could be due to the existence of more than one nucleation center[22].

The projection area of the residual NaCl particles has been determined with the program ImageJ 1.47v. The projection area can be either converted into an area-equivalent diameter or into a particle volume by assuming spherical geometry. To understand the difference in the size of the NaCl particles, the following considerations can be made: The average area-equivalent diameter of anhydrous NaCl particles is $d_p = 24.15\mu m$ ($V = 7.37 \cdot 10^{-9} cm^3$) with a specific density of $\rho(NaCl) = 2.165 g/cm^3$. The average area-equivalent diameter of NaCl dihydrate particles is $d_p = 30.98\mu m$ ($V = 1.55 \cdot 10^{-8} cm^3$). NaCl dihydrate has a lower specific density of $\rho(NaCl \cdot 2H_2O) = 1.61 g/cm^3$. If the ratio of the specific densities of the different solid forms of NaCl is taken into account, then the average diameter of NaCl dihydrate particles can be converted as follows:

$$d_p = \frac{1.61 g/cm^3}{2.17 g/cm^3} \cdot 30.98\mu m = 23.09\mu m \qquad (5.4)$$

The agreement between the calculated and measured average diameter of anhydrous NaCl particles is quite good within the uncertainty range ($\Delta d_p = \pm 1\mu m$) suggesting that the differences in size or volume are related to the crystal structures of the different solid forms of NaCl. Note that the derived sizes and volumes of the residual NaCl particles are at the upper end of the dominant modes of marine aerosols with diameters ranging from 0.1µm to 100µm (see section 2.1).

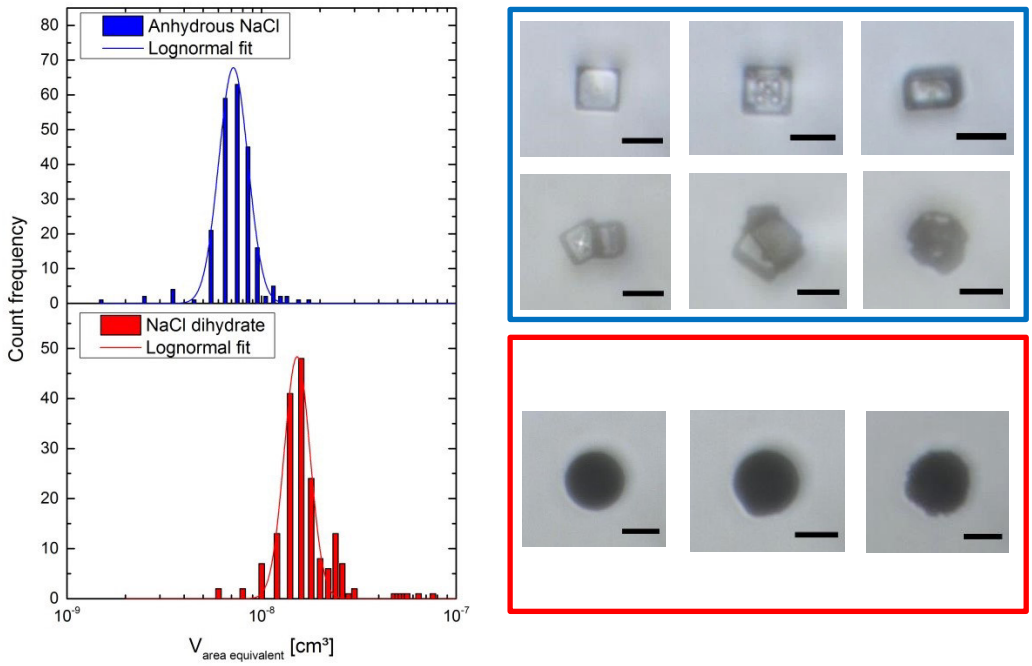

Figure 51: Left) Volume distributions of residual anhydrous NaCl and NaCl dihydrate particles. Right) Shadow images of residual anhydrous NaCl particles suspended in the EDB. Every size bar corresponds to 20µm.

5.4.6 Temperature-dependent formation of NaCl dihydrate

The NaCl dihydrate formation shows a strong temperature dependence, i.e. an increase in the NaCl dihydrate fraction with decreasing temperature. Above -20°C, virtually no formation of NaCl dihydrate particles was observed. The fraction of NaCl dihydrate began to rise at about -23°C and became one at -32°C. The transition between the anhydrous and the dihydrate form of NaCl proceeded in a narrow temperature range (see figure 52). In the following, the results of other measurements techniques are presented and compared with the EDB data.

Wise et al.[9] performed efflorescence experiments of NaCl particles in a RH and temperature controlled environmental cell coupled to a Raman spectrometer. NaCl particles with diameter of 1-10µm were studied in RH ramp experiments with rates of RH change from 1-10% RH per minute. It was found out, that no hydrated NaCl particles were obtained above -21.15°C (252K). At temperature between -21.15°C (252K) and -37.15°C (236K), a mixture of anhydrous and hydrated particles crystallized. At lower temperatures than -37.15°C exclusively NaCl dihydrate particles were formed. A linear relationship for the formation of NaCl dihydrate was suggested in the temperature range from -24.15 (249K) to -34.15°C (239K). It was pointed out that the linear dependence is not valid at higher temperatures between -21.15°C (252K) and -24.15°C (249K) and lower temperatures between -34.15°C (239K) and -37.15°C (236K). The results of Wise et al. are in good agreement with the EDB measurements. The curve of the formation of NaCl dihydrate reported by Wise et al. is slightly shifted to lower temperatures.

Wagner et al.[10] investigated the formation of NaCl dihydrate in the Aerosol Interaction and Dynamics in the Atmosphere (AIDA) cloud chamber by means of FTIR-spectroscopy. In the FTIR extinction spectra any evidence was found for the formation of NaCl dihydrate above -29.15°C (244K). A small NaCl dihydrate fraction (0.07) was obtained at -37.45°C (235.7K). At -57.15°C (216K), a fraction of 0.88 was reported. The curve of the formation of NaCl dihydrate is about 13°C shifted to lower temperatures when compared to the results of Wise et al. The discrepancies were attributed to the size of the particles (i.e. a narrow size distribution centered at 0.87µm was investigated in the AIDA), the influence of the substrate surface on the partitioning between the solid forms of NaCl and the efflorescence relative humidities, at which crystallization in the long-term AIDA experiments occurred (i.e. RH w.r.t. water was between 52% and 61%). The temperature regime of the formation of NaCl dihydrate is broader when compared to Wise et al. and the EDB measurements.

Cziczo et al.[79] studied the efflorescence of NaCl in the temperature range from +24.85°C (298K) to -20.15°C (253K) in an absorption cell attached to an IR aerosol spectrometer. The NaCl particles (mean radius of 0.18µm) were investigated either in efflorescence mode experiments (~30s residence time) or in static mode experiments (up to 30min residence time). The efflorescence experiments showed no indication of NaCl dihydrate. These

observations are reasonable due to very small size of the particles (i.e. longer observation times are needed) and the investigated temperature range.

Similarly, Koop et al.[74] examined the deliquescence and efflorescence of NaCl particles in the temperature range from -24.15°C (249K) to -0.15°C (273K) via flow cell microscopy. No evidence of NaCl dihydrate formation for particles ranging from 5µm to 25µm was found in efflorescence experiments, while NaCl dihydrate was clearly identified upon cooling of bulk and emulsion samples by differential scanning calorimetry (DSC). In the case of the bulk and emulsion measurements, NaCl dihydrate formation was ascribed to heterogeneous nucleation on ice surfaces after ice formation. It should be emphasized that a significant fraction of NaCl dihydrate starts to form at lower temperature than -24.15°C and the small fraction formed at -24.15°C has only a minor effect on the deliquescence experiments. In general, the two solid phases of NaCl can be discriminated by their DRH values (anhydrous NaCl: 75% and NaCl dihydrate: 85-87%)[9], but a precise discrimination of the NaCl particles can only be realized by spectroscopic techniques.

In freezing experiments of NaCl solutions on a sapphire substrate, the formation of NaCl dihydrate was also detected between -25°C and -30°C by sum frequency generation (SFG) spectroscopy[188, 189]. A detailed analysis of the factors influencing the formation of NaCl dihydrate is given in a subsequent section. It will be shown, how the different experimental findings can be reconciled.

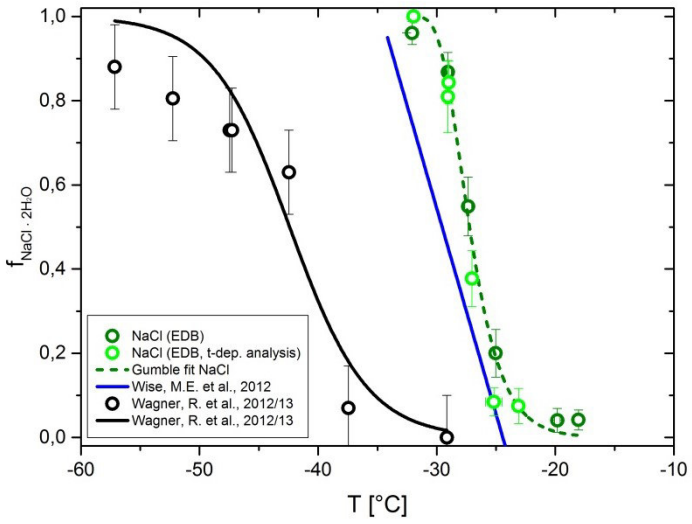

Figure 52: Temperature-dependent formation of NaCl dihydrate in the EDB.

5.4.7 Time-dependent analysis of NaCl crystallization

For the estimation of volume nucleation rates, a time-dependent analysis of the efflorescence of NaCl solution droplets was performed. Such an evaluation has already been applied for supercooled water droplets[108, 190] and NaCl solution droplets[86] in an electrodynamic levitator. In figure 53, the decay of the logarithm of the number of non-effloresced droplets N_i divided by the total number of droplets N_0 for different isothermal experiments is displayed. At time $t = 0s$, the droplets are injected in the EDB and hence $ln(N_i/N_0) = 0$. In the course of the efflorescence experiments, the droplets evaporate (see appendix for the determination of the evaporation rates) and adopt the final concentration and temperature. The temperature accommodation of the droplet is thought to be a very faster process and completed within a few seconds. The slope of the curve is at the beginning very flat indicating small nucleation rates. At a certain residence time, a steep decline of the curve is obtained. A linear decrease of the $ln(N_i/N_0)$ with increasing residence time is predicted by the CNT. At lower temperatures, the curves are shifted to longer residence times. It seems reasonable that this temperature effect is due to the lower partial vapor pressure of NaCl solution droplets at colder temperatures and hence a slower evaporation process. As expected, the slope of curves is affected by the temperature. However, when considering the uncertainties in the calculation of the slope, the temperature dependence of the slope is only weakly expressed.

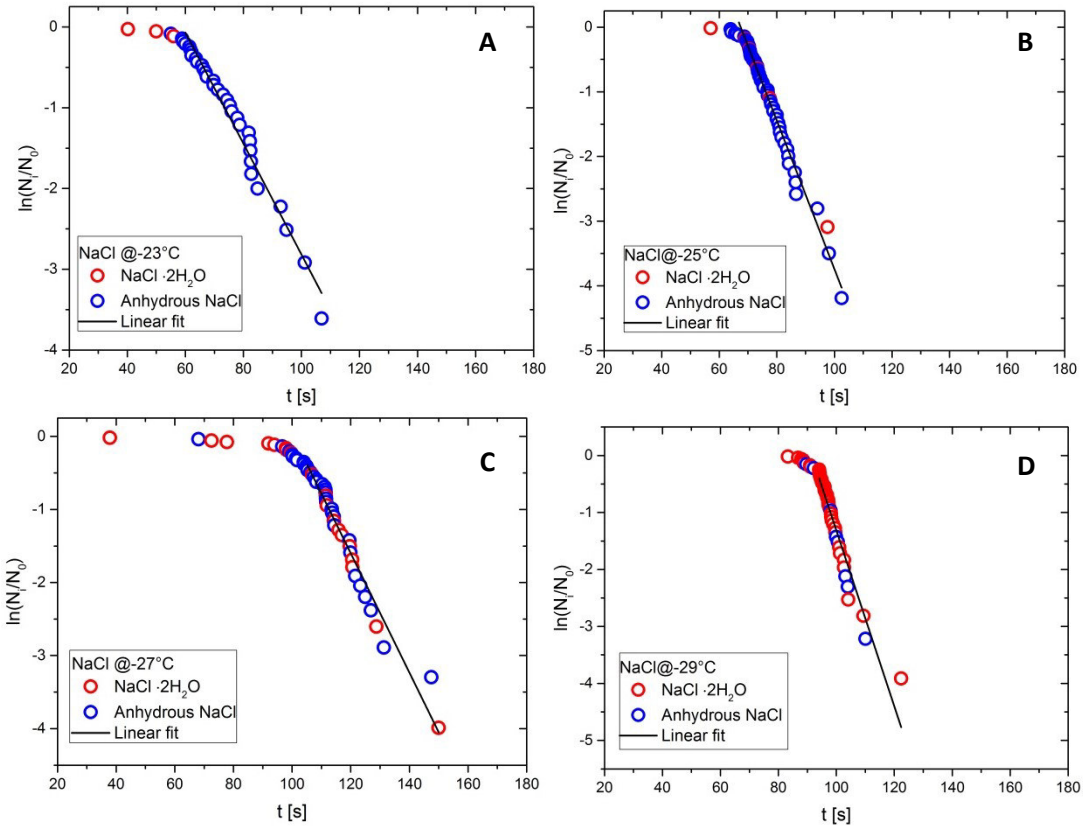

Figure 53: Time-dependent analysis of the efflorescence of NaCl particles at different temperatures in the EDB.

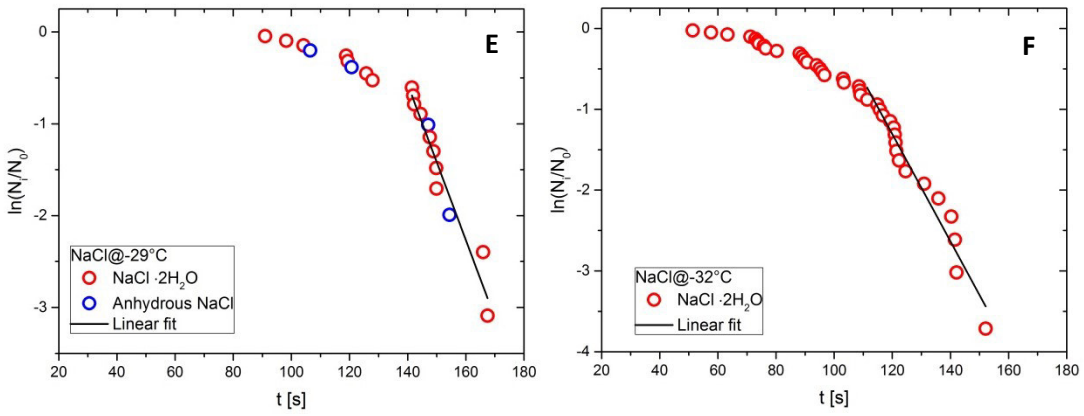

Figure 53: (continued).

The statistical analysis of the time-dependent nucleation of NaCl dihydrate is conducted as follows: A stochastic process, which gives two distinct possible outcomes and in which every single experiment has the same probability of either the one or the other outcome can be described by a binomial distribution:

$$P(n;k,p) = \binom{n}{k} p^k (1-p)^{n-k} \tag{5. 5}$$

In this formula p is the probability of getting the outcome i (i is the final phase state A or B of the effloresced residual particle) and n is the total number of trials. Then the term $P(n;k,p)$ denotes the probability to obtain exactly k times the outcome i. The expected value (first moment) is the product of the number of trials and the probability p:

$$\mu = n \cdot p \tag{5. 6}$$

The variance is given by the square of the standard deviation of the binomial distribution, where p_i denotes the fraction $f_i = p_i = N_i/N_0$ of the particular phase state:

$$\sqrt{Var} = \sigma = \sqrt{N_0 p_i (1-p_i)} = \sqrt{N_0 \left(\frac{N_i}{N_0}\right)\left(1-\frac{N_i}{N_0}\right)} \tag{5. 7}$$

It is assumed that the efflorescence process follows two nucleation paths depending on temperature for an ensemble of N_0 identical droplets. The nucleation paths A and B are associated with the nucleation rates J'_A and J'_B. Since both nucleation paths are assumed to be independent, the natural logarithm of the number of effloresced events N_i dividend by the total number of events N_0 can be expressed as the sum of nucleation rates coefficients J' multiplied by the volume $V$and nucleation time t according classical nucleation theory:

$$ln\left(\frac{N_i}{N_0}\right) = -J'Vt = -(J'_A + J'_B)Vt \tag{5. 8}$$

The nucleation time is not directly accessible for the measurement, therefore the observation time prior to nucleation is chosen for evaluation. For the number of nucleation

events it is not crucial which process leads to the nucleation due to the sum of nucleation rates. In a two path nucleation process nucleation occurs (whether A or B). Then the final state A or B of the droplet is related to the probabilities p_A and p_B. The sum of the probabilities is per definition equal to one ($p_A + p_A = 1$). The probabilities p_A and p_B can be stated as follows:

$$p_A = \frac{J'_A}{(J'_A + J'_B)} \text{ and } p_B = \frac{J'_B}{(J'_A + J'_B)} \tag{5. 9}$$

The number of expected results A and B is given by the product of the total number of events and the respective probability of occurrence of state A and B:

$$N_A = N_0 p_A = N_0 \frac{J'_A}{(J'_A + J'_B)} \text{ and } N_B = N_0 p_B = N_0 \frac{J'_B}{(J'_A + J'_B)} \tag{5. 10}$$

If equation (5.10) is rearranged and solved for the nucleation rate of the final state A or the final state B. The following equation can be obtained:

$$J_A = \frac{N_A}{N_0}(J'_A + J'_B) = \frac{N_A}{N_0} J' \text{ and } J_B = \frac{N_B}{N_0}(J'_A + J'_B) = \frac{N_B}{N_0} J' \tag{5. 11}$$

Form equation (5.11) it can be inferred that the determination of the total nucleation rate J' is sufficient for the evaluation of nucleation rates of ensembles A and B. To evaluate the homogeneous nucleation rate coefficients of the formation of NaCl dihydrate and anhydrous NaCl in efflorescing NaCl solution droplets the following equation based on the afore-mentioned considerations was applied:

$$J_i = \frac{f_i \cdot J'}{V_{drop}} \tag{5. 12}$$

In the formula (5.12) f_i denotes the fraction of NaCl dihydrate and anhydrous NaCl particles in an ensemble, J' is the slope of a $-ln(N_i/N_0)$ vs. t plot and V_{drop} is volume of the droplet prior to nucleation. The relative uncertainty in J_i is the sum of the relative uncertainties of the individual quantities in equation (5.12) and can be calculated according to the equation:

$$\frac{\Delta J_\mathrm{i}}{J_i} = \underbrace{\frac{\Delta f_i}{f_i}}_{\substack{Error \\ in\ fraction}} + \underbrace{\frac{\Delta J'}{J'}}_{\substack{Error \\ in\ slope}} + \underbrace{\frac{\Delta V_{drop}}{V_{drop}}}_{\substack{Error \\ in\ volume}} \tag{5. 13}$$

To be more explicit, relative uncertainty in the fraction is related to the standard deviation of the binomial distribution, the relative uncertainty in the slope of a $-ln(N_i/N_0)$ vs. t plot is the inverse of the root square of the total number of investigated droplets and the relative

uncertainty in the volume of droplets is the error in the determination of the radius of the droplet. An error of $\Delta r = \pm 0.5 \mu m$ is estimated based on image analysis:

$$\frac{\Delta f_i}{f_i} = \frac{\sqrt{N_0 \left(\frac{N_i}{N_0}\right)\left(1 - \frac{N_i}{N_0}\right)}}{N_i} = \sqrt{\left(\frac{1}{N_A}\right) - \left(\frac{1}{N_0}\right)} \tag{5. 14}$$

$$\frac{\Delta J'}{J'} = \frac{1}{\sqrt{N_0}} \tag{5. 15}$$

$$\frac{\Delta V_{drop}}{V_{drop}} = 3\frac{\Delta r}{r} \tag{5. 16}$$

By fitting $J_{NaCl \cdot 2H_2O}(T)$ to a function that increased exponentially with decreasing temperature, a simple parametric equation was obtained, which is, strictly speaking, only valid in the investigated temperature range from -23°C to -32°C:

$$J_{NaCl \cdot 2H_2O}(T) = exp(-0.272T + 6.670) \tag{5. 17}$$

The derived parametric equation (5.17) was used for the calculation of the theoretical fraction of NaCl dihydrate particles. Figure 54 shows the temperature dependence of the homogeneous nucleation rate coefficient of NaCl dihydrate. As it was expected, the homogeneous nucleation rate coefficient of NaCl dihydrate increased with decreasing temperature.

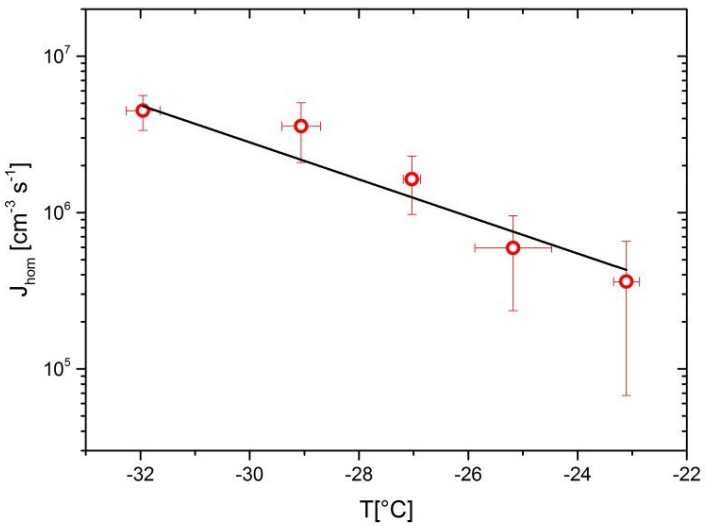

Figure 54: Temperature dependence of the homogeneous nucleation rate coefficient of NaCl dihydrate in NaCl solution droplets.

Several values for the product of the volume and time were derived by applying a standard fitting algorithm (Levenberg-Marquardt) to represent the data sets of the different experimental techniques (see figure 55). The following equation was used to calculate the fraction of NaCl dihydrate particles:

$$f_i(T) = 1 - exp\left(J_i(T)V_{drop}t\right) \quad (5.18)$$

where i denotes NaCl dihydrate. The derived parametrization for the temperature dependence of the homogeneous nucleation rate coefficient of NaCl dihydrate is used to scale the formation of NaCl dihydrate for different volumes and observation times of the NaCl solution droplets. To represent the results from the different experiment techniques, equation (5.18) is fitted to the data by using the parametrization from equation (5.17). In particular, a value of $Vt = 5.62 \cdot 10^{-7} cm^3 s$ is obtained for the EDB measurements. If the mean residence time is fixed to 94s estimated for the NaCl efflorescence experiments and a particle diameter of 22.5µm is assumed, then the fitting parameter $Vt = 5.62 \cdot 10^{-7} cm^3 s$ can be successfully recalculated bearing in mind that both variables (volume and time) have an identical effect on the formation of NaCl dihydrate. A slightly lower value of $Vt = 2.79 \cdot 10^{-7} cm^3 s$ is obtained for the measurements of Wise et al.[9] The authors reported a dry particle diameter between 1µm and 10 µm with typical values close to 5µm and a drying rate of 1-10% RH/min. The fitting parameter is best represented by assuming a particle diameter of 5µm and a residence time of 4264s (71min) or 10µm and 533s (9min) respectively. The last parameter set is more likely when considering the range of drying rates. A significant lower value of $Vt = 5.85 \cdot 10^{-9} cm^3 s$ resulted from the fitting procedure of the AIDA measurements. Wagner et al.[11] showed that the size distribution is in the range between 0.06µm and 1.1µm with a mean particle diameter of 0.85µm. By taking into account the particle diameter, the fitting parameter is best reproduced by an observation time of $1.82 \cdot 10^4$s (~5h), which is very close to the reported value of $2 \cdot 10^4 s$, at which the entire droplet population is crystallized[10]. A fully quantitative representation of the results of Wagner et al.[10] is not possible so far probably due to a different temperature and/or concentration dependence of the nucleation rate coefficient compared to equation (5.18). The temperature range of the formation of NaCl dihydrate reported by Wagner et al. is much broader suggesting that the nucleation rate coefficient is less steep. It should be mentioned that these calculations rely on the experimental accessible diameter of effloresced NaCl particles. It would be more appropriate to use the droplet diameter prior to efflorescence, because homogeneous efflorescence is a volume-dependent process and the size of the nucleating volume can certainly affect the nucleation rate. Nevertheless, these calculations suggest a volume and time dependence of the formation of NaCl dihydrate under the assumption of the same homogeneous nucleation rate coefficient.

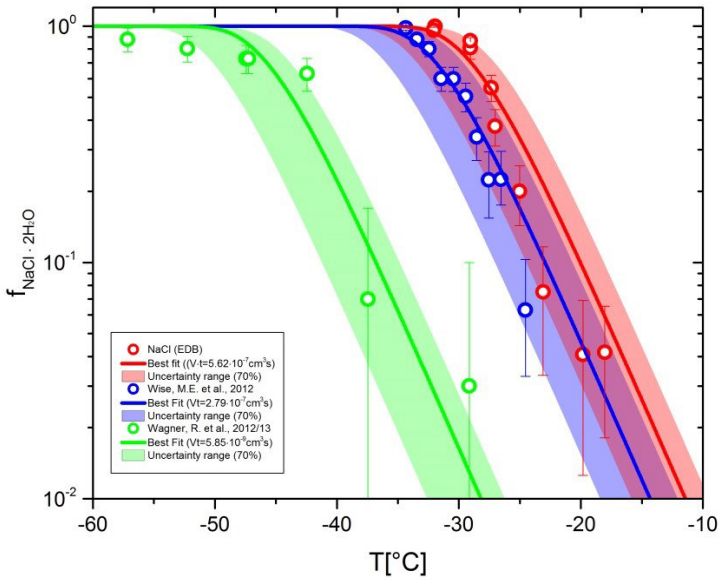

Figure 55: Temperature dependence of the fraction of NaCl dihydrate for different experimental techniques.

5.4.8 Concentration-dependent analysis of NaCl crystallization

As mentioned in the previous section 5.4.7, the nucleation rate strongly depends on the concentration of the efflorescing droplets. A high nucleation rate and thus a steep solid formation curve are expected for highly supersaturated droplets in the moment of crystallization and vice versa. To investigate the impact of concentration on the nucleation process of NaCl droplets, several trajectories of evaporating droplets were monitored by Mie scattering pattern (see section 3.3). Figure 56 shows the increase in the molar concentration with time for an efflorescing NaCl droplet at -25°C together with optical microscopy data. In the initial phase the evaporation rate is very high and slows down with time asymptotically reaching a final concentration until nucleation occurred. For the determination of the size of the droplets of fixed refractive index of 1.3512 (i.e. 10wt%) was used. Prior to crystallization, the concentration is increased to approximately 10.2 mol/L (i.e. 44wt%) corresponding to a refractive index of 1.4162 (see appendix for the calculation of the refractive index). The error introduced by assuming a fixed refractive index and neglecting the influence of temperature[191] on the refractive index is minimal, as the sizing is almost independent of the refractive index[73, 192]. However, Davis et al. argued that the usage of a fixed refractive index slightly underestimates the final size of the droplet and overestimates the slope of the process[193]. The experimental results of the evaporation of the NaCl droplet indicated that the NaCl droplet starts with an initial concentration of 1.832mol/L (i.e. 10wt%) and reaches a concentration very close to the efflorescence concentration (i.e. 10.2 mol/L)[125]. The results of the optical microscope measurements also showed an approximatively five-fold change in the volume ratio of the NaCl droplets at the end of the evaporation process. It cannot be ruled out that individual NaCl droplets nucleated before the efflorescence concentration is reached. Moreover, the curvature of the evaporation curve is strongly affected by the temperature, at which the isothermal experiment was conducted. At low temperatures, the evaporation process is slower and thus the evaporation curve is much broader.

The evaporation curve can be used to calculate the fraction of crystallized droplets as a function of concentration or supersaturation ($S_{Nacl} = c/c_{sat}$) with respect to anhydrous NaCl (i.e. c= 5.412mol/L at deliquescence). This means that the figures 53A-56F given in section 5.4.7 can be expressed in terms of concentration instead of time. The fraction of crystallized droplets increased steeply with increasing concentration depending on the functional relationship between concentration and time (see figure 57A and 57B). Similar results were obtained by Parsons et al., who investigated the efflorescence of pure ammonium sulfate and mixed ammonium sulfate/malonic acid droplets between 295K and 300K in the EDB[194]. The fraction of liquid ammonium sulfate droplets showed a sharp decrease in a quite narrow RH range, while the mixed droplets effloresced over a broad RH interval. Pant et al. reported on the crystallization of pure and with soot and kaolinite contaminated ammonium sulfate droplets in a flow cell coupled to an optical microscope. In all cases, very steep liquid fraction curves were obtained except for the kaolinite contaminated droplets, in which the liquid fraction curve is shifted to higher RH values[195].

These experiments demonstrate that the crystallization is strongly concentration-dependent and that the concentration dependence should be considered by the interpretation of the NaCl dihydrate formation curve (see section 5.4.6).

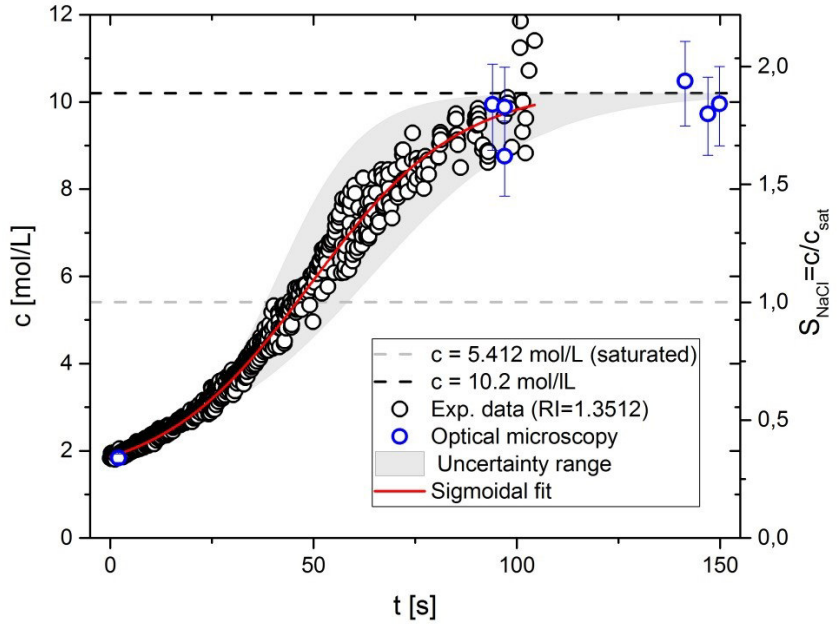

Figure 56: Change of molar concentration with time for an evaporating NaCl droplet in the EDB at -25°C.

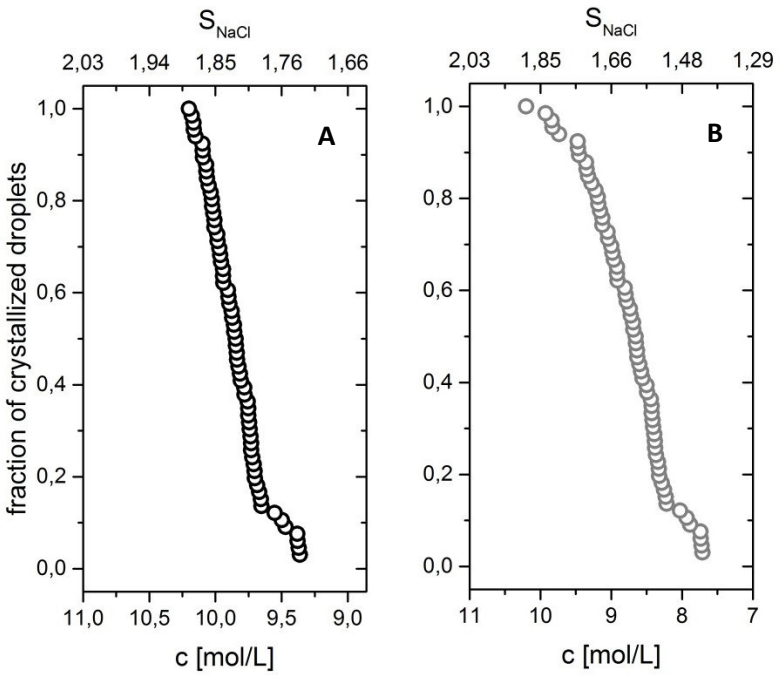

Figure 57: Fraction of crystallized NaCl droplets as a function of molar concentration. Correlation between concentration and time via A) Left side of the uncertainty range and B) Sigmoidal fit (red curve in figure 56).

5.5 Sea salt aerosol (SSA) particles

5.5.1 Chemical composition of SSA particles

Instant Ocean® is a simulated salt mixture and was chosen as a surrogate for sea salt aerosol. Detailed chemical analysis of Instant Ocean® revealed that the salt mixture accurately mimic the chemical composition of the major inorganic constituents of natural sea salt water[196](see figure 58). In-house ion chromatographic (IC) measurements confirmed this analysis, but slight deviations concerning the Na^+ and Cl^- ion concentrations were found. In previous laboratory studies[12, 74], Instant Ocean® was successfully used to investigate the liquid-solid phase transitions (i.e. homogeneous freezing and efflorescence) and the ice nucleation ability of SSA particles in deposition and immersion mode experiments. It is implicitly assumed that the chemical composition of SSA particles is similar to that of bulk sea water, which holds true for at least the major ionic species[14]. However, there is an enrichment of particular species either during the formation process of SSA particles or subsequent during their residence in the atmosphere due to chemical transformations. The enrichment includes inorganic components e.g. iodide and trace metals and organic components e.g. bacteria, viruses and surface-active material (surfactants) originating from the sea surface microlayer[14]. It is also well known that the enrichment of particular species affects the hygroscopic growth (CCN properties), phase transitions, optical and other properties compared to pure SSA particles composed of inorganic species[14].

The NaCl and SSA particles studied in this thesis are in the range of several tens of micrometers and therefore situated at the upper end of the marine aerosol size distribution. In this size range the organic material represents only a minor fraction of the particle composition. Ault et al.[197] demonstrated that in submicron-sized SSA particles the organic material is strongly enriched compared to supermicron-sized SSA particles, in which inorganic salts are the major components. By using the simulated sea salt mixture of Instant Ocean®, the influence of additional ionic species (i.e. Ca^{2+}, Mg^{2+},$K^+$and SO_4^{2-}) on the temperature-dependent formation of $NaCl \cdot 2H_2O$ in SSA droplets can be investigated, bearing in mind that natural SSA particles are much more complex in their chemical composition especially regarding to the organic and biological material.

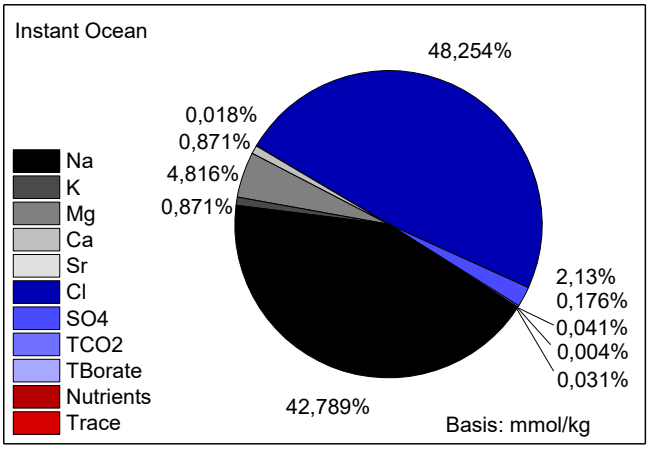

Figure 58: Elemental composition of the simulated sea salt mixture Instant Ocean®. The ion concentrations (mmol/kg water) are taken from Atkinson et al.[196].

The simulated SSA particles were generated by printing SSA solutions droplets onto Si(111)-wafer at ambient temperature and allowed them to evaporate. Scanning electron microscopic (SEM) and energy-dispersive X-ray (EDX) spectroscopic measurements of an exemplary SSA particle are depicted in figure 59. As can be seen from figure 59, the deposited SSA particle is constituted of NaCl cubes surrounded by an amorphous coating. The coating is mainly composed of Mg, S, O and Cl. Several rod-shaped inclusions within the amorphous layer were identified as $CaSO_4$ crystals. An unambiguous specification of the formation of $CaSO_4 \cdot 2H_2O$ and/or $CaSO_4 \cdot ½H_2O$ remains questionable. SEM images and EDX elemental maps were frequently used as an appropriate tool to investigate the chemical composition of laboratory-generated and collected SSA particles. The SEM/EDX analysis provide specific information about the mixing state of SSA particles and their complex internal chemical heterogeneity[198]. The experimental observations presented in figure 59 are in agreement with previous SEM/EDX analysis indicating a segregation of chemical species within the SSA particles[83, 187]. It is generally accepted that the cubic solid NaCl core is embedded in a mixture of hydrated Mg-rich and Ca-rich material[83, 187, 197, 199]. Differences in the composition of the exterior of the NaCl core were observed ranging from Mg-and K-rich chloride/sulfates coatings, over aggregated rod-like $CaSO_4$ crystals, $NaNO_3$ crystals and silicate grains[200] to organic material enriched on the surface of the NaCl core[197, 199]. The spatial segregation underlines that the nucleation of individual components during the evaporation process plays to crucial role for the mixing state and the morphology of the solid SSA particles.

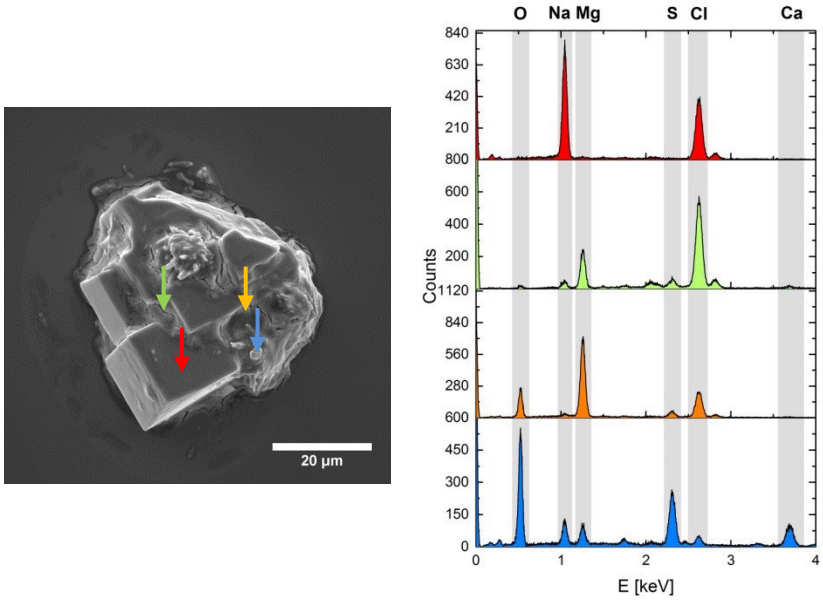

Figure 59: Left) SEM image of a deposited SSA particle onto a silicon substrate. Right) EDX spectra of the SSA particle. The arrows indicate the location of the EDX spectra.

5.5.2 Raman spectra of SSA particles

The $\nu_1(SO_4^{2-})$ stretching mode is of particular importance, as it is the most intense und visible vibration mode in the Raman spectra of sulfate containing solutions. The peak position and the width of the $\nu_1(SO_4^{2-})$ stretching mode critically depend on the chemical environment, i.e. the presence of Ca^{2+}/Mg^{2+}-ions, the concentration of the solution (or in other words the relative humidity) and the phase state.

Representative examples of selected SSA particles and their corresponding Raman spectra are displayed in figure 60. The analysis of the Raman spectra is basically focused on the $\nu(OH)$ stretching region and the $\nu_1(SO_4^{2-})$ stretching region due to the rapid identification of the effloresced SSA particles. To a limited extent, the $\delta(OH)$ bending mode is also taken into consideration. A comprehensive summary of the experimental observed vibrational frequencies and their assignment to functional moieties is given in table 4.

In case A, the Raman spectra of a concentrated liquid SSA droplet is shown, as apparent from the broad $\nu(OH)$-stretching band from 3000-3700cm^{-1} and the $\nu_1(SO_4^{2-})$ stretching mode centered at 985cm^{-1}. The examples B and C show the Raman spectra of the identical SSA particle. The Raman spectra B is immediately recorded after the nucleation of anhydrous NaCl in the SSA droplet. The remaining ionic species surrounding the NaCl crystal give rise to the $\nu(OH)$-stretching band and the $\nu_1(SO_4^{2-})$ stretching mode at 985cm^{-1} with a shoulder at 1006cm^{-1}. The band at 985cm^{-1} is attributed to free SO_4^{2-}-ions, while the band at 1006cm^{-1} corresponds to vibrations of contact ion pairs (CIPs) in highly concentrated $MgSO_4$ solution. Below a RH of ~40%, aqueous $MgSO_4$ turns into a gel-like phase state, in which the transport of water is limited and the response to changes in RH is retarded. With decreasing

RH or increasing residence time at low RHs, the $\nu_1(SO_4^{2-})$ stretching mode blue-shifts indicating the formation of complex CIPs in supersaturated $MgSO_4$ solution. In example C, the Raman spectra features a broad OH-stretching band and a $\nu_1(SO_4^{2-})$ stretching mode at 1012cm^{-1}, which is characteristic for the formation of CIPs due to the successive loss of aqueous water. The last example D depicts the exceptional formation of a lenticular-shaped SSA particle. The spectral characteristics are consistent with those of $NaCl \cdot 2H_2O$ effloresced from pure NaCl solution droplets. The SSA particle contains a small amount of aqueous species, as visible from the $\nu_1(SO_4^{2-})$ mode at 984cm^{-1}. The $\nu(OH)$-stretching region is clearly dominated by the two sharp OH-stretching modes of $NaCl \cdot 2H_2O$.

Schill et al[12]. investigated the water uptake of SSA particles at -58.15°C and showed that at approximately 0% RH, a sharp OH-stretching band (3400cm^{-1}) and a $\nu_1(SO_4^{2-})$ stretching mode at 1010cm^{-1} are visible in the Raman spectra. The peak at 1010cm^{-1} was assigned to $MgSO_4$ or $CaSO_4$ and their respective hydrates. An increase in the RH leads to water absorption of the SSA particle. At 17%RH, the shoulder of the $\nu(OH)$ stretching band at the low-frequency side (~3200cm^{-1}) und a small peak at 981cm^{-1} appeared. In the fully deliquesced SSA particle only the $\nu_1(SO_4^{2-})$ stretching mode at 981cm^{-1} was present. The residual aqueous $MgSO_4$ coating at low RHs may explains the deliquescence behavior in the temperature range from -38.15°C to -43.15°C. Furthermore, the Raman spectra presented by Schill et al. bear a strong resemblance to the one of carnallite crystals. Together with the $MgSO_4$ coating, these observations may help to understand the higher saturation ratio (S_{ice}) in the temperature range from -48.15°C to -58.15°C compared to the ice nucleation efficiency of $NaCl \cdot 2H_2O$ reported by Wise et al.[9] (S_{ice}= 1.08-1.18) and Wagner et al.[11] (S_{ice} =1.15-1.25) in deposition mode freezing experiments.

The formation of a thin layer of highly concentrated $MgSO_4$ solution on the surface of the precipitated NaCl crystals was also reported by Xiao et al.[201]. The $\nu_1(SO_4^{2-})$ stretching mode increased from 981cm^{-1} to 1036cm^{-1} when the RH was lowered from 55% to 4%. Overall, these findings support the interpretation of the concentration-dependent shift of the $\nu_1(SO_4^{2-})$ stretching mode in the presence of aqueous $MgSO_4$.

No spectral features of $CaSO_4 \cdot 2H_2O$ or $CaSO_4 \cdot ½H_2O$[202]were evident in the $\nu(OH)$ stretching region of the experimental Raman spectra of SSA particles. The detection of $CaSO_4$ is may be prevented by the NaCl formation enclosing the $CaSO_4$ crystals and the intensity of the signal of $CaSO_4$ is probably too low to be detected by the Raman spectrometer. Moreover, a slight drift of the SSA particle, which is not actively controlled in its height in the EDB during the acquisition of the Raman spectra complicates even more the detection of small $CaSO_4$ crystallites. In contrast, the SEM/EDX measurements presented in the previous section 5.5.1 prove the formation of $CaSO_4$ crystals. But the state of hydration of $CaSO_4$ (dihydrate or hemihydrate) could not be unambiguously determined by the EDX technique. Xiao et al.[201] described the precipitation of $CaSO_4 \cdot 2H_2O$ (3495cm^{-1}, 3406cm^{-1} and 1008cm^{-1}), $CaSO_4 \cdot ½H_2O$ (3596cm^{-1}, 3510cm^{-1} and 1012cm^{-1}) and carnallite (3430cm^{-1}, 3250cm^{-1} and 1643cm^{-1}) crystallites by means of spatially resolved micro-Raman

spectroscopy. In addition, a Raman spectroscopic analysis of a large number of size-selected SSA particles revealed that $CaSO_4 \cdot 2H_2O$ (3500cm^{-1}, 3400cm^{-1} and 1010cm^{-1}), carnallite (3250cm^{-1} and 3430cm^{-1}) and hydrated $MgCl_2/CaCl_2$ salts (3233cm^{-1}) were formed[197]. These findings emphasize that the precipitation of hydrated $CaSO_4$ crystals is a common feature in efflorescing SSA particles.

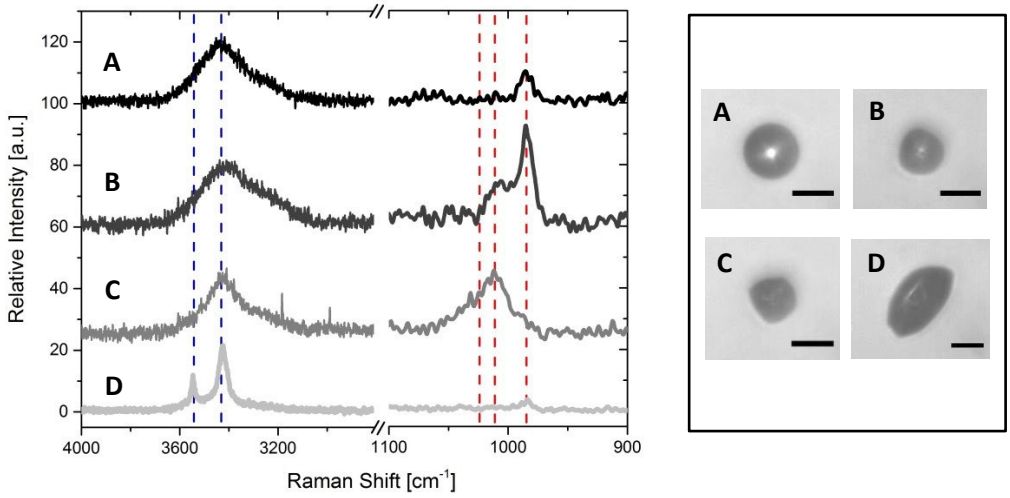

Figure 60: Left) Raman spectra of residual SSA particles. Right) Shadow images of residual SSA particles in the EDB. Note that the Raman spectra are normalized to the $\boldsymbol{\nu(OH)}$ stretching mode.

Table 4: Assignment of the vibrational modes in the Raman spectra of sea salt aerosol (SSA) particles.

	$\boldsymbol{\nu}$**(OH)** [cm^{-1}]	$\boldsymbol{\delta}$ **(OH)** [cm^{-1}]	$\boldsymbol{\nu_1(SO_4^{2-})}$ [cm^{-1}]	**Reference**
A	3434	1651	985	-
B	3426	1641	985, 1006	-
C	3426	1641	1012	-
D	3423, 3546	1665, 1645	984	-
Carnallite $\boldsymbol{(KMgCl_3 \cdot 6H_2O)}$	3250, 3430	1643	-	Xiao et al.[201]
Hydrohalite $\boldsymbol{(NaCl \cdot 2H_2O)}$	3424, 3545	1664, 1644	-	Dubessy et al.[171]

A minor fraction of the effloresced SSA particles was identified as carnallite crystals, a potassium and magnesium-rich double salt ($KMgCl_3 \cdot 6H_2O$), which is well known as a saline lake evaporite in sedimentary petrology[203]. The Raman spectra of the effloresced carnallite particles are depicted in figure 61. The Raman spectra exhibited the following common features: A sharp peak at 3430cm^{-1} with a shoulder at 3250cm^{-1}. These spectral features are attributed to the OH-stretching vibrations of water molecules confined in the lattice of the carnallite crystals. A weak $\delta(OH)$-bending mode is located at 1643cm^{-1}. Additionally, the Raman spectra contain the $\nu_1(SO_4^{2-})$ stretching modes of free dissolved aqueous SO_4^{2-}-ions and aqueous SO_4^{2-}-ions in the environment of Ca^{2+}/Mg^{2+}-ions. The experimental results are in good agreement with the reference spectra of carnallite taken from the online available RRUFF database[204]. This reference spectrum was measured with a Thermo Almega XR spectrometer (532nm, 150mW). Furthermore, the results are confirmed by efflorescence experiments of SSA solution droplets at ambient temperature (~22-24°C)[201]. The authors stated that their measurements are best interpreted in terms of the precipitation of carnallite on preexisting NaCl crystals at ~44%RH. The corresponding deliquescence of carnallite particles has been reported at ~52%RH.

The observed morphology of the carnallite particles does not totally reflect their orthorhombic-dipyramidal crystal structure consisting of a network of face-sharing KCl_6 octahedra and isolated $Mg(H_2O)_6$ octahedra with water molecules at the corner of the magnesium octrahedra[205]. A few carnallite particles exhibited an irregular particle shape. However, a single carnallite particle showed a nearly pseudohexagonal crystal habit (see right panel of figure 61, particle B). This hexagonal shape is in good agreement with the (001) basal plane of the carnallite crystal[206]. It should be noted, that the notation in the brackets describes the Miller indices of the planes in the crystal lattice, i.e. (001) is the plane parallel to the α axis with a thick tabular appearance in the macroscopic carnallite crystal.

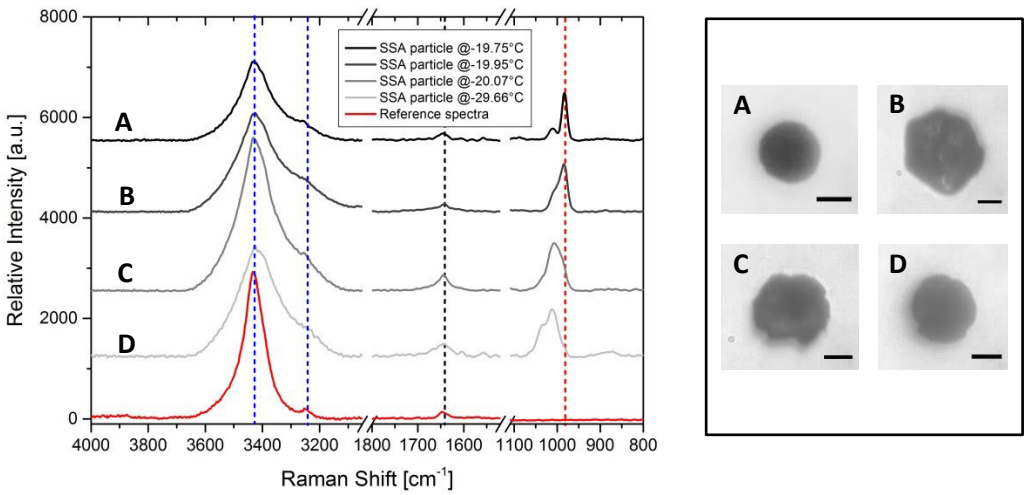

Figure 61: Left) Raman spectra of residual carnallite particles. Right) Shadow images of carnallite particles in the EDB. The red reference spectra of carnallite is taken from the RRUFF database[204].

Individual SSA particles exhibited an exceptional hexagonal shape. The corresponding Raman spectra are shown in figure 62. Based on the Raman spectra, it can be inferred that the particles are composed of $NaCl \cdot 2H_2O$ or a mixture of $NaCl \cdot 2H_2O$ and other hydrated salts e.g. carnallite. As stated above, $NaCl \cdot 2H_2O$ has a monoclinic-prismatic crystal structure and the observed morphology of the SSA particles is in accordance with this crystal structure. Bode et al.[207] demonstrated that the crystal growth of $NaCl \cdot 2H_2O$ is influenced by the orientation of the underlying cleaved NaCl crystal. The covering layer of $NaCl \cdot 2H_2O$ had the same alignment as the (100) face of the cleaved NaCl substrate. This result was explained by a higher growth rate of the (100) face of $NaCl \cdot 2H_2O$ compared to the tilted higher (011) and (111) side faces. The (100) face was identified as being responsible for the hexagonal appearance of the $NaCl \cdot 2H_2O$ crystals. This view is encouraged by a field study in the Death Valley core (California, USA), where Roberts et al.[208] found hexagonal-shaped saline lake deposits. These crystals were probably pseudomorphs of the low-temperature hydrous mineral hydrohalite ($NaCl \cdot 2H_2O$). The absence of hexagonal-shaped crystals in the efflorescence experiments of pure NaCl solution droplets (see section 5.4.5 for the description of the morphology of $NaCl \cdot 2H_2O$ particles) leads to the conclusion that propably solid inclusions initialize the precipitation of $NaCl \cdot 2H_2O$ in SSA droplets. Unlike the case of the perfect growth of $NaCl \cdot 2H_2O$ on top of the (100) NaCl subtrate, there is no unambiguous identification of the triggering solid inclusions in the SAA droplets possible.

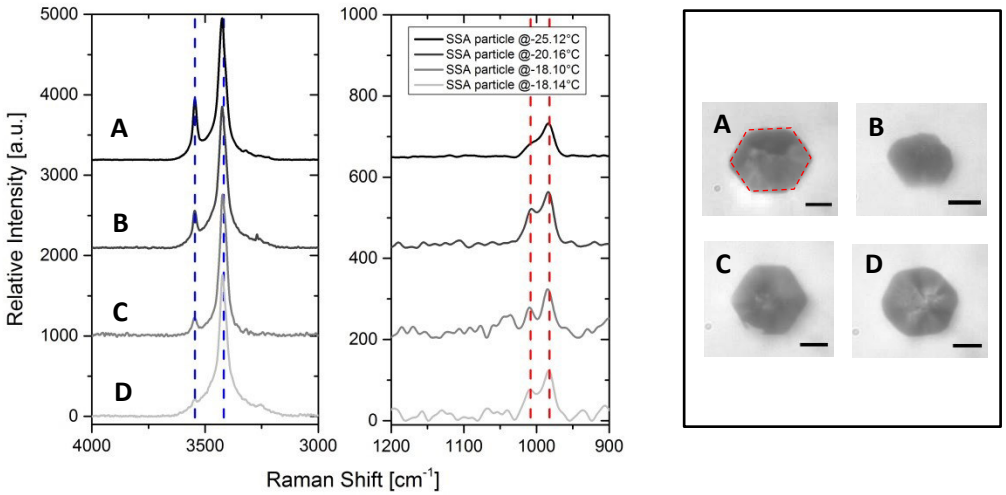

Figure 62: A) Raman spectra of residual SSA particles. Right) Shadow images of the residual SSA particles in the EDB.

5.5.3 DC voltage curves of SSA particles

Figure 63 shows the DC voltage curves of efflorescing SSA droplets. The DC voltage curves of SSA droplets nucleating $NaCl \cdot 2H_2O$ or anhydrous NaCl had a very similar appearance. A sharp decrease in the balancing DC voltage indicated the efflorescence. The efflorescence is accompanied by a loss a particulate mass due to the release of water to the gas phase, which is compensated by the balancing DC voltage restoring the particle in the center of the EDB.

Such a single step efflorescence of SSA droplets is expected, considering that the chemical composition of SSA droplets is dominated by NaCl. In contrast, a two-step efflorescence was experimentally verified for ternary mixtures consisting of NaCl/KCl/water[81] and NaCl/ $MgCl_2$/water[209].

Small fluctuations of the DC voltage are visible prior to the efflorescence. It might be argued that these fluctuations are caused by variations in the intensity of the elastically scattered light of the evaporating SSA droplets. Changes in the transparency due to precipitating material or morphological deformations of the SSA droplets may be reasonable explanations for the experimental observations. However, Tang et al.[82] investigated the evaporation of SSA droplets in the EDB and obtained a monotonically decreasing DC voltage curve until crystallization at ~ 45%RH occurred. It was suggested that the deposition of tiny salt crystals is hardly discernible with this detection technique, as the whole scattered light in the 90° direction is collected by the CCD-camera[201]. However, several studies demonstrated that small solid inclusions (~10% of the droplet radius) can be detected by the angle-resolved light scattering[210].

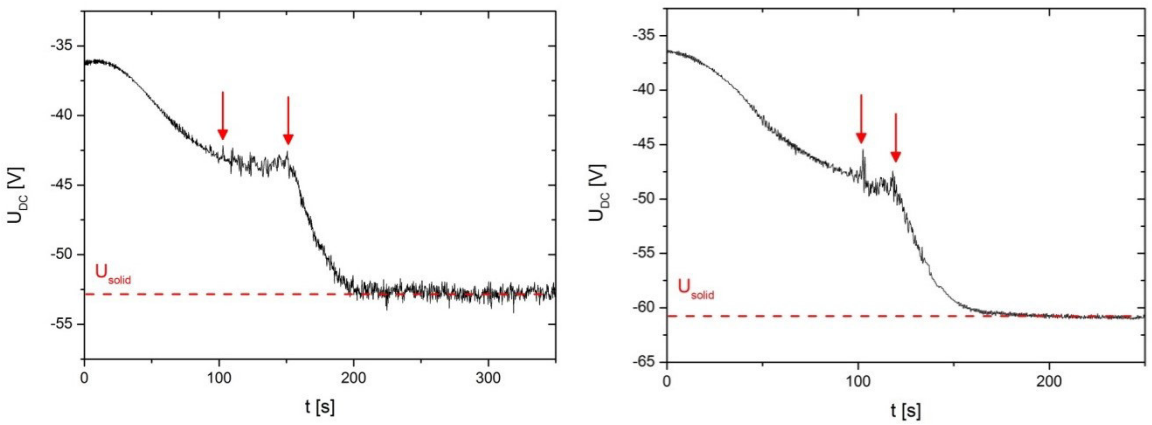

Figure 63: Balancing DC voltage curves of SSA particles in EDB. The red arrows indicate the beginning of the fluctuations of the DC voltage and the moment of crystallization respectively.

5.5.4 Morphological characterization

The derived volume distributions of SSA particles are subdivided in SSA droplets containing $NaCl \cdot 2H_2O$ or anhydrous NaCl, as already carrried out for the pure effloresced NaCl particles (see section 5.4.5). Figure 64 displays the volume distributions of SSA particles. As can be seen from figure 64, both volume distributions of residual SSA particles are shifted to larger volumes and are broader compared to the volume distributions of pure NaCl partilces. The presence of an amorphous coating consisting of hydrated $MgCl_2$ and $MgSO_4$ salts provides a reasonable explanation for the increased volume and size of the SSA particles. Tang et al.[82] stated that approximately 5-10wt% of residual water is found to be present in the dry SSA particles based on hygroscopic growth and evaporation measurements in the

EDB. The size conversion between anhydrous NaCl and $NaCl \cdot 2H_2O$ containing SSA particles is still applicable due to the fact that solid SSA particles have a comparable specific density ($\rho(SSA) = 2.25 g/cm^3$) as pure anhydrous NaCl particles ($\rho(NaCl) = 2.165 g/cm^3$)[22]. However, field studies indicate that the specific density of SSA particlces can vary over a larger range strongly depending on the sampling location[22].

The anhydrous NaCl containing SSA particles had a cubic shape with rounded edges due to the amorphous coating. Individual SSA particles were irregular-shaped. Schill et al.[12] reported that SSA particles deposited on a hydrophobically treated fused silica substrate exhibited an irregular, cuboidal shape and a bright opacity under the optical microscope due to light scattering. The $NaCl \cdot 2H_2O$ containing SSA particles retained their spherical appearance. The amorphous coating is probably embedded in the cavities (i.e. pores and veins) between the $NaCl \cdot 2H_2O$ crystallites and therefore did not significantly modify the morphology of the SSA particles. Several studies observed the formation of hollow NaCl and SSA particles deposited on hydrophobically coated substrates[211] or formed under free-fall conditions in wind tunnel experiments[185, 212, 213]. The hollow structure of SSA particles was attributed to the formation of a porous shell on the upstream side of the evaporating droplet and a continuous accumulation of salt material to the crust wall leaving behind an insufficiently filled volume[185]. On the other hand, non-hollow SSA particles were obtained after the evaporation of SSA solution droplets onto a hydrophilic quartz substrate[201]. These findings highlight that the experimental conditions have a considerable impact on the observed morphology of the SSA particles.

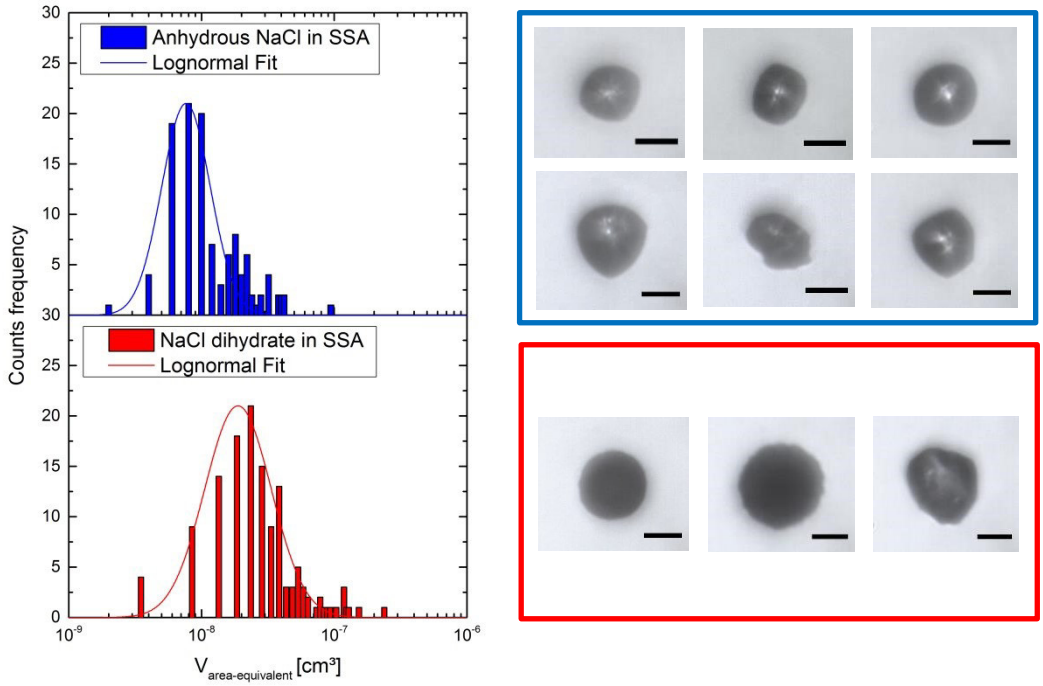

Figure 64: Left) Volume distributions of residual SSA particles containing anhydrous NaCl (blue) and NaCl dihydrate (red). Right) Shadow images of residual SSA particles suspended in the EDB. Every size bar corresponds to 20µm.

5.5.5 Temperature-dependent formation of NaCl dihydrate in SSA particles

The temperature-dependent formation of NaCl dihydrate in SSA solution droplets is displayed in figure 65. A significant fraction of NaCl dihydrate is already formed at -18°C and nearly all SSA solution droplets nucleated NaCl dihydrate at -30°C. The $f_{NaCl\cdot 2H_2O}(T)$ curve of SSA is shifted to higher temperatures compared to the pure NaCl case. The T_{50} values of the NaCl dihydrate formation curves of pure NaCl and SSA droplets are -27.22°C and -21.94°C respectively, with T_{50} being the temperature corresponding to $f_{NaCl\cdot 2H_2O}(T) = 0.5$. The temperature shift ΔT between the $f_{NaCl\cdot 2H_2O}(T)$ curves of pure NaCl and SSA is about 5.28°C. Based on these observations, it is argued that heterogeneous nucleation of NaCl dihydrate is responsible for the enhanced formation of NaCl dihydrate in SSA solution droplets. Due to the lack of data, a direct comparison with published literature is not possible. Therefore, indirect evidences are provided which support the hypothesis of an enhanced formation of NaCl dihydrate in SSA solution droplets by solid inclusions.

Several laboratory studies[201, 211, 214] have shown that less soluble components e.g. $CaSO_4 \cdot 2H_2O$ and $CaSO_4 \cdot ½H_2O$ crystalized prior to the nucleation of NaCl in SSA droplets deposited on hydrophilic and hydrophobic substrates. In the course of the efflorescence experiments, the sequential crystallization of $CaSO_4 \cdot ½H_2O$ (~90%), $CaSO_4 \cdot 2H_2O$ (~78%), NaCl (~55%), $KMgCl_3 \cdot 6H_2O$ (~44%) and hydrated $MgSO_4$ salts (<5%) was observed for 80-100µm SSA droplets onto a quartz substrate[201]. It was pointed out that the observed ERH of NaCl is in disagreement with previous measurements[82] of the ERH of SSA droplets (45-48%) suggesting that heterogeneous nucleation initiated the NaCl nucleation in SSA droplets. A related study investigated the efflorescence of SSA droplets by means of high-speed imaging and micro-Raman spectroscopy and mainly confirmed the previous findings[211]. It was emphasized that either gypsum ($CaSO_4 \cdot 2H_2O$) or omongwaite ($Na_2Ca_5(SO_4)_6 \cdot 3H_2O$) have been crystallized in SSA droplets strongly depending on the drying rate[211]. $CaSO_4 \cdot 2H_2O$ precipitated at 82% RH during slow efflorescence experiments and $Na_2Ca_5(SO_4)_6 \cdot 3H_2O$ was formed during rapid efflorescence experiments. The dependence of the nature of the substrate was stressed leading to nucleation either at the liquid-solid interface in the case of quartz or at the gas-liquid surface in the case of polytetrafluoroethylene (PTFE) substrates. The main disadvantage of these studies is that they were performed at ambient temperature (~22-24°C) and hence only the formation of anhydrous NaCl was observed.

This picture is also supported by the sequence of evaporative precipitation of seawater minerals[215]. The sequence starts with calcium carbonate, followed by calcium sulfate (gypsum or anhydrite), sodium chloride, magnesium sulfate and finally magnesium and potassium chlorides. The sequence based on the chemical composition of seawater and the mineral solubilities predicted by the Pitzer's ion interaction model[216, 217]. In particular, the solubility of $CaSO_4 \cdot 2H_2O$ is increased in the presence of low NaCl concentrations due to the increase of the ionic strength of the solution[218]. The solubility of $CaSO_4 \cdot 2H_2O$ is relatively insensitive to changes in temperature and is roughly 0.014mol/kg water at 20°C.

By adding more NaCl to the solution, the solubility is approximately four-fold increased (~0.055mol/kg water at ~3mol NaCl/kg water)[216, 218]. A further addition of NaCl again reduced the solubility due to the competition for hydration water molecules and thus the probability of precipitation of $CaSO_4 \cdot 2H_2O$ is increased. Richardson et al. reported that early studies suggested the precipitation of $CaSO_4 \cdot 2H_2O$ from seawater starting at -17°C. The author concluded that the proposed $CaSO_4 \cdot 2H_2O$ precipitation is confirmed by nuclear magnetic resonance (NMR) measurements[219]. In addition, a similar effect on the solubility of $CaSO_4 \cdot 2H_2O$ through the addition of $MgCl_2$ to the ternary $CaSO_4$- $NaCl$- H_2O system has been recently described[220]. However, Lewis et al. objected that the sequence of precipitation based on equilibrium conditions and that the temperature dependencies of the solubilities of the salt components are not well-established[14]. Thus these considerations are hardly transferable to SSA droplets below deliquescence relative humidity.

Additional support for the heterogeneous nucleation of NaCl dihydrate is provided by the study of Koop et al.[74]. They observed the formation of NaCl dihydrate in bulk and emulsion experiments, while no hints of $NaCl \cdot 2H_2O$ were obtained from flow tube experiments. An ice surface mediated crystallization of NaCl dihydrate was proposed by the authors, as apparent from differential scanning calorimetry (DSC) curves in emulsion freezing experiments. Wagner et al.[221] investigated the crystallization of ternary solution droplets composed of oxalic acid (OA), NaCl and water in the AIDA cloud chamber at -29.15°C. In the FTIR extinction spectra, the appearance of NaCl dihydrate was visible in the second efflorescence experiment. It was suggested that in the first efflorescence experiment oxalic acid crystals were formed, which did not deliquesced in the subsequent expansion run (i.e. the solubility of solid oxalic acid crystals is very close to water saturation). In the second efflorescence experiment, the formation of NaCl dihydrate was triggered by the surface of immersed oxalic acid crystals. In comparison, Wagner et al.[10] showed that no NaCl dihydrate was formed in pure NaCl solution droplets at -29.15°C (see section 5.4.6 for more details). Following the line of reasoning, the enhanced formation of NaCl dihydrate in effloresing SSA droplets could be related to the presence of solid inclusions in the SSA droplets.

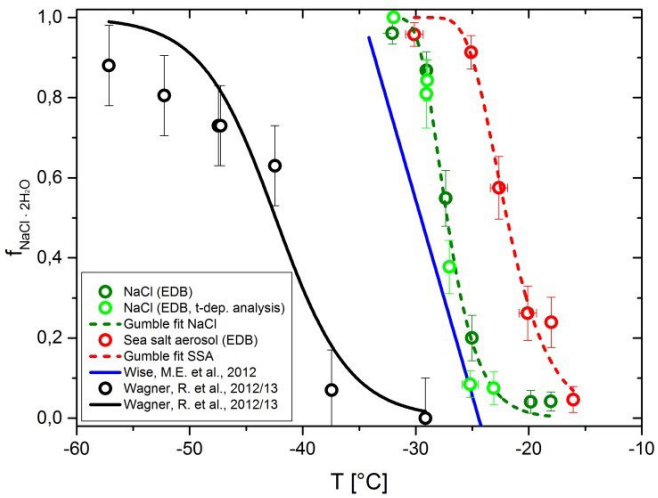

Figure 65: Temperature-dependent formation of NaCl dihydrate in levitated SSA droplets.

5.5.6 Number of nucleating sites per dry SSA mass

In analogy to equation (2.19), the cumulative number of nucleating sites n_m per unit mass of dry sea salt can be calculated as follows:

$$n_m(T) = \frac{-ln(1 - f_{NaCl \cdot 2H_2O}(T))}{C_m V_{drop}} \quad (5.\ 19)$$

where C_m is the mass concentration of SSA in the examined droplets and V_{drop} is the droplet volume. The following values were used: $C_m(SSA) = 0.11 g/mL$ (i.e. 10wt%) and $V_{drop} = 1.705 \cdot 10^{-8} mL$. $n_m(T)$ is extensively used for the characterization of the ice nucleation efficiency of soil dusts[150] and bacterial ice nuclei[145]. Therefore, the usage of $n_m(T)$ represents an alternative approach to overcome the necessity of knowing the surface area of the nucleating particles. The surface area is required for the determination of the heterogeneous nucleation rate coefficient.

As apparent from figure 66, the $n_m(T)$ curve shows a steep linear increase with decreasing temperature. The total uncertainty of $n_m(T)$ is the sum of the errors of the $NaCl \cdot 2H_2O$ fraction, the concentration and the droplet volume:

$$\frac{\Delta n_m}{n_m} = \frac{\Delta f_i}{f_i} + \frac{\Delta C_m}{C_m} + \frac{\Delta C_m}{C_m} \quad (5.\ 20)$$

The error of the concentration is mainly an instrument-based error depending on ΔV_{mc} (V_{mc} is the volume of the measuring cylinder) and Δm_{SSA}. The uncertainty of the temperature is given by two standard deviations (2σ), derived from the temperatures of individual nucleation events.

$$\frac{\Delta C_m}{C_m} = \frac{\Delta V_{mc}}{V_{mc}} + \frac{\Delta m_{SSA}}{m_{SSA}} \quad (5.\ 21)$$

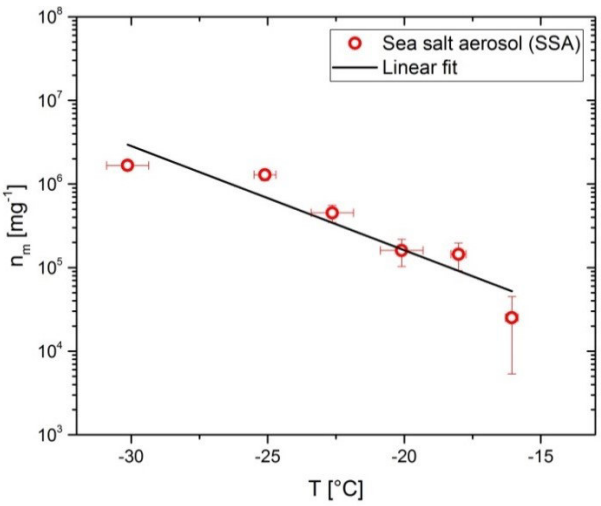

Figure 66: Temperature dependence of the number of nucleating sites per dry SSA mass.

5.6 Liquid-liquid phase separations in levitated C6/AS/H_2O particles

5.6.1 Hygroscopic properties

The experiments described in the following sections 5.6.1 to 5.6.3 were performed during the research stay at the ETH Zurich (Institute for Atmospheric and Climate Science, IAC, Research group of Prof. Thomas Peter). The research stay was financially supported by the graduate school for climate and environment (GRACE) at the Karlsruhe Institute of Technology (KIT). The experimental EDB setup is similar to the one in section 4.2. The basic components of the EDB have been described previously in detail[122, 222]. Briefly, the EDB is mounted in a double-jacketed glass chamber. In the inner walls circulates a cooling fluid and in the outer walls an isolating vacuum is maintained. The internal pressure of the EDB can be varied between 150hPa and 1000hPa. A well calibrated RH and temperature sensor is directly mounted in close vicinity to the levitated droplet. Four different methods are available to investigate the phase behavior of the levitated droplets: 1) The DC voltage measures the mass changes upon drying and humidification of the aerosol. 2) The two dimensional angle-resolved optical scattering pattern can be used to detect phase changes of the aerosol. 3) The low resolution Mie resonance spectroscopy with a LED point source (red) allows to track size changes of the aerosol. 4) The high resolution (TDL) Mie resonance spectroscopy can simultaneously determine the refractive index and the size of the droplet.

The left panel of figure 67 shows the typical profile of temperature, relative humidity and the DC voltage in the course of a drying and humidification cycle experiment (see figures 67A-67C). In the right panel, the hydroscopic behavior (expressed as the mass fraction of solute (mfs) vs. the water activity (a_w)) of pure ammonium sulfate (AS, blue), dicarboxylic acids/water mixture (C6/H_2O, red) and dicarboxylic acids/ammonium sulfate/water mixture (C6/AS/H_2O, black) containing equal amounts of AS and C6 by weight are displayed (see figure 67D). Regarding to the dehydration cycle, the C6/H_2O mixture was always in the liquid state even at very dry conditions (i.e. no efflorescence). A slight deviation between the experimental data and the AIOMFAC model (that is a thermodynamic UNIFAC-based group contribution model for the estimation of activity coefficients in organic/inorganic/water mixtures[223]) predictions can be recognized from figure 67D. In contrast, AS showed a liquid-solid phase transition in the range from 35% RH to 40% RH. The experimental data taken from Tang et al.[224] are in excellent agreement with the AIOMFAC model predictions. The C6/AS/H_2O droplets were exposed to changes in RH to undergo LLPS and internal morphological changes of the involved liquid phases, but typically avoiding efflorescence (i.e. the dehydration cycle was restricted to ~46%RH). Song et al. reported that the ERH for the C6/AS/H_2O mixture is between 35-48% RH[13]. The corresponding mfs (a_w) curve is closer to the AS curve indicating that the hygroscopic behavior is strongly affected by the inorganic AS component. The AIOMFAC model correctly predicts the mfs (a_w) curve for the C6/AS/H_2O mixture.

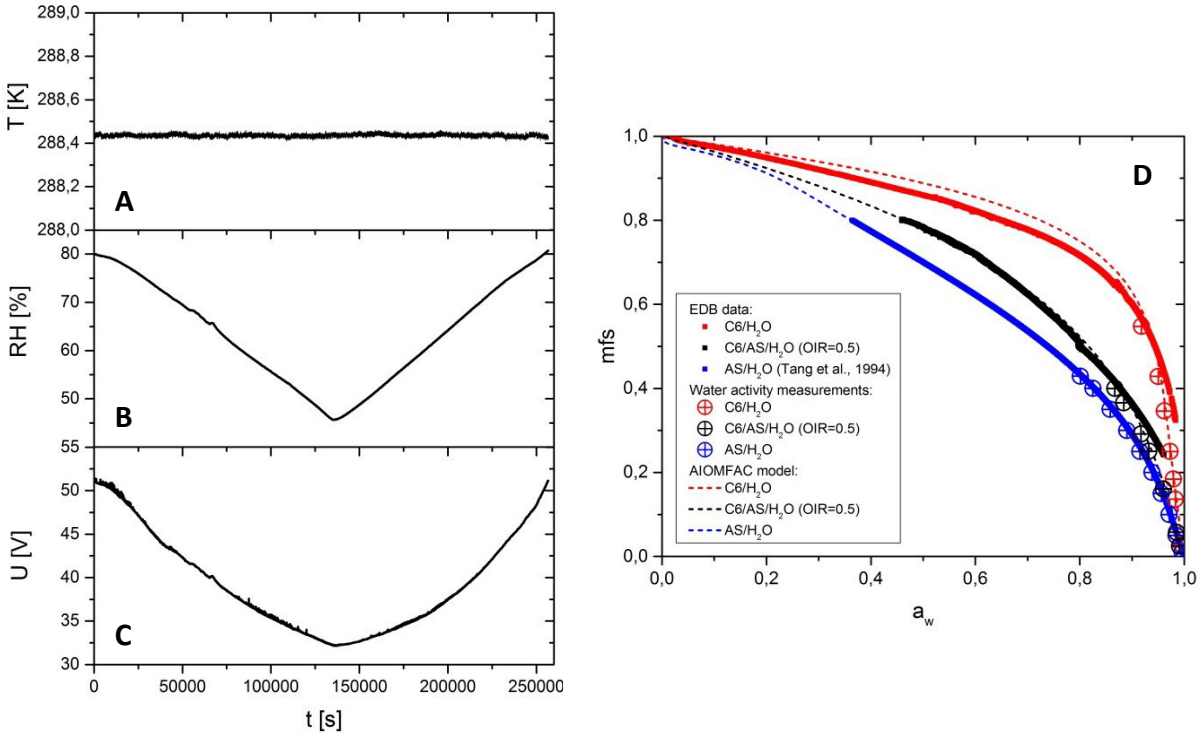

Figure 67: Experimental run for a C6/AS/H_2O particle suspended in the EDB. Temporal evolution of A) temperature, B) relative humidity and C) DC voltage for compensating of the gravitational force. D) Mass fraction of solute (mfs) vs. water activity (a_w). The open crossed circles denote water activity measurements of bulk solutions. The solid squares and the dashed lines represent EDB data and AIOMFAC model results respectively. Color coding: AS/H_2O (blue), C6/H_2O mixture (red) and C6/AS/H_2O mixture (OIR=0.5, black).

5.6.2 Light emitting diode (LED) spectra

A false color intensity map of the Mie resonance spectra of a C6/AS/H_2O droplet is displayed in figure 68. It is shown how the Mie resonances evolve with changing RH. A single Mie resonance can be used to monitor the size changes of the C6/AS/H_2O droplet. From these data the vapor pressure at different temperatures and the vaporization enthalpy can be derived[225]. The right panel of figure 68 shows the LED spectra at selected RHs (indicated as vertical lines in the left panel of figure 68). The characteristic Mie resonances of a homogeneous (i.e. liquid) particle are visible at 76.7% RH in the drying cycle. However, at a slightly lower RH of 75.2%, the LED spectra appeared nearly structureless with only broad Mie resonances present in the LED spectra indicating that LLPS occurred upon drying of the C6/AS/H_2O droplet. In the subsequent humidification cycle, the LED spectra featured several Mie resonances at 61% RH. Between 63.2% RH and 71.6% RH only broad Mie resonances appeared, similar to the drying cycle. At 73.4% RH, the LED spectra indicated the presence of a homogeneous droplet. The LED spectra at the beginning of the drying cycle and at the end of the humidification cycle had a similar appearance. The transition from structured to broad featureless LED spectra is attributed to the transition from a homogeneous to a phase-separated C6/AS/H_2O droplet and vice versa. The next paragraph describes the spectral changes in the TDL spectra.

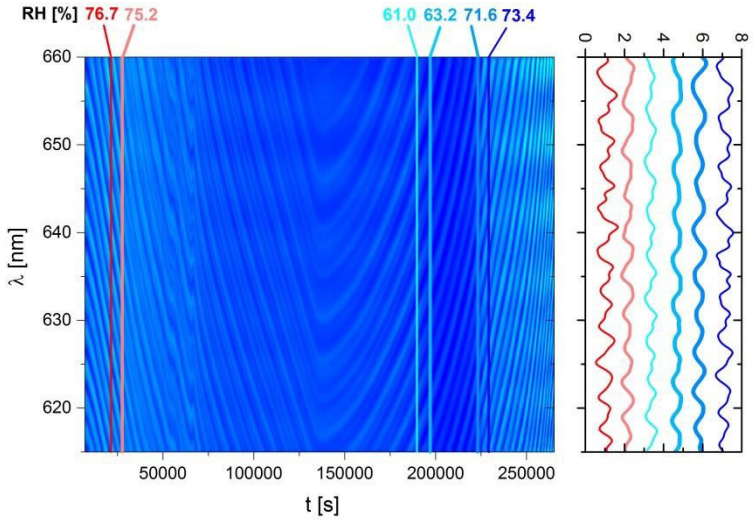

Figure 68: Left) False color intensity map of Mie resonance spectra measured with the LED (red). The dark and bright blue colors denote low and high intensity respectively. Right) LED spectra for selected relative humidities (as indicated by the vertical lines in the false color intensity map).

5.6.3 Tunable diode laser (TDL) spectra

Figure 69 shows a series of TDL spectra upon drying and humidification of a C6/AS/H_2O droplet. Two characteristic resonances can be identified in the TDL spectra of a fully deliquesced C6/AS/H_2O droplet at 84.9% RH. The sharp resonance indicates a low mode order (i.e. the Mie resonance is closer to the surface of the droplet). The broad resonance can be attributed to a higher mode order (i.e. the Mie resonance penetrates further into the droplet). With decreasing RH, the broad resonance continuously shifted toward the center (figure 69A). At 74.4% RH, the sharp resonance suddenly disappeared. The quenching of resonance modes is suggested to be a consequence of the distortion of the spherical shape of the droplet due to the formation of small liquid inclusions upon LLPS. At about 66.6% RH, two sharp low intensity resonances reappeared. These resonances are more pronounced at 64.2%RH and they shifted toward the central peak with decreasing RH. The first sharp resonance even vanished at 45.6% RH. The reappearance of sharp resonances can be understood in terms of the partial coalescence of liquid inclusions and the restoration of the spherical symmetry of the droplet. In the subsequent humidification cycle, the two sharp resonances are suppressed at about 61.9% RH and even completely disappeared at 64.8% RH (figure 69B). In the RH range from 64.8% to 69.8%, no visible changes can be noted in the TDL spectra. Again, at 74.3% RH a weak resonance appeared and this sharp resonance shifted from the center with increasing RH. The transition regime in the humidification cycle slightly differs from the one in the drying cycle, as one might expect, since the phase behavior of the liquid components is not identical in both cycles. Finally, at 84.9% RH the two characteristic resonances are observed indicating the presence of a homogeneous (i.e.

liquid) droplet. Song et al.[226] reported TDL spectra of a C6/AS/H_2O particle subjected to drying and humidification cycles. In the RH range from 65.6% to 61.9%, a significant increase of noise and a scatter of the spectral positions were observed, which was attributed to the transition from a core-shell to a partially engulfed configuration. In the humidification cycle, the transition from a noisy to a non-distorted TDL spectra occurred at around 66% RH. Similar observations of noisy TDL spectra at 61.5% RH for a smaller C6/AS/H_2O droplet are shown in the appendix (see figure 84). Another experimental study investigated the phase separation of C6/AS/H2O droplets for two different compositions (DCA:AS, 1:2 and 1:5)[227]. The authors came to the conclusion that the C6/AS/H_2O droplets underwent both a change of mode offset (CMO) and a quenching of modes (QM). These spectral indicators were associated with a core-shell morphology and a partially engulfed morphology respectively. Unfortunately, the observed phase separation relative humidity (SRH) values for the two compositions were significantly higher than the SRH values reported by Song et al.[226]. It was stressed that probably inaccuracies in the determination of the water activity derived from the refractive index could account for the deviations of the SRH value.

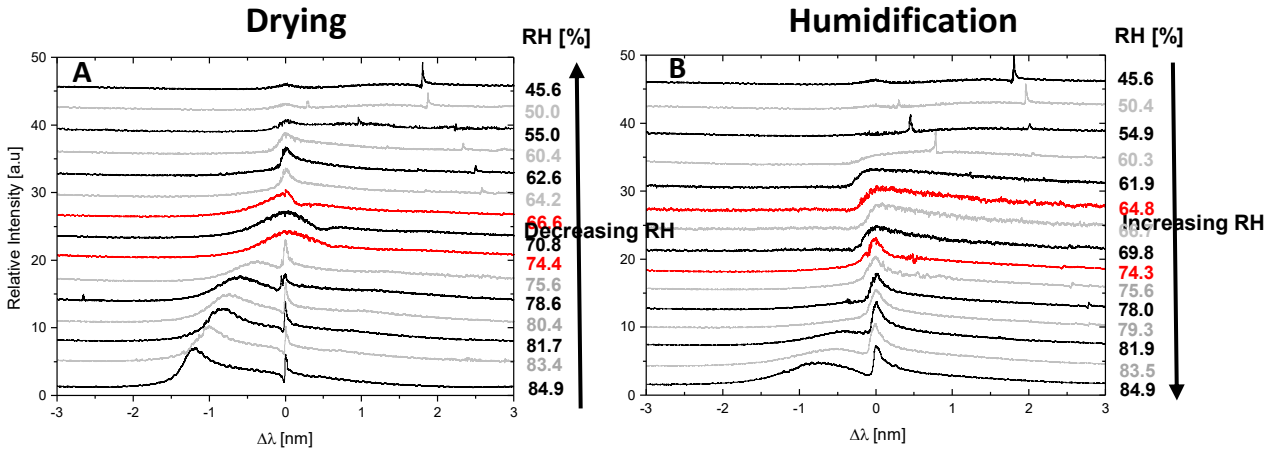

Figure 69: Series of TDL spectra (TE-polarization) upon slow A) drying and B) humidification of a levitated C6/AS/H_2O particle. The scattered intensity is normalized to the maximum intensity in the spectra and the wavelength scale is relative to the peak center. At the right side of each panel the relative humidities are given, at which the TDL spectra were recorded.

5.6.4 Raman spectra of C6/AS/H_2O particles

The experiments described in the following sections 5.6.4 to 5.6.6 were carried out with the EDB setup at the Institute of Meteorology and Climate Research – Atmospheric aerosol research (IMK-AAF) at KIT. The experiments complement the results of the EDB setup at the ETH in Zurich. The same chemical composition of substances (C6/AS/H_2O, OIR=0.5) was used for the experiments, but the instrumentation for the characterization was different and provided additional information about the phase behavior.

The figure 70 shows a series of Raman spectra of an evaporating C6/AS/H_2O droplet at 15°C in the EDB. At high relative humidity, several spectral features can be identified in the Raman spectra (see table 5): An intense broad band in the range from 3000-3700cm^{-1} is ascribed to the asymmetric and symmetric $\nu(OH)$-stretching vibration of water molecules. Three distinct Raman bands at 2976cm^{-1}, 2926cm^{-1} and 2878cm^{-1} indicate the $\nu(CH)$-stretching vibrations of dicarboxylic acid molecules. The $\nu(CO)$-stretching vibration appears as relatively broad band at 1702cm^{-1}. In addition, the characteristic stretching modes of the $\nu(SO_4^{2-})$-ion are visible in the Raman spectra: The asymmetric stretching mode $\nu_3(SO_4^{2-})$ at 1095cm^{-1}, the intense symmetric stretching mode $\nu_1(SO_4^{2-})$ at 981cm^{-1} and the two bending modes $\nu_4(SO_4^{2-})$ and $\nu_2(SO_4^{2-})$ at 616cm^{-1} and 457cm^{-1} respectively[118]. The spectral features and their assignment is in accordance with Song et al.[13], who investigated the phase separation of deposited C6/AS/H_2O droplets on hydrophobically coated glass coverslides by means of optical microscopy and Raman spectroscopy. With decrease of the relative humidity, the broad OH-band decreased and the other spectral features intensified. However, a small amount of water was still detectable prior to the efflorescence of the C6/AS/H_2O droplet. At about ~71%, LLPS occurred (red Raman spectra in figure 70), as determined from the 2D angle-resolved optical scattering pattern and shadow images. The chemical composition of the separated phases could not be identified properly due to the random motion of the inclusions within the droplet. For this reason, the Raman spectra are collected from the center of the C6/AS/H_2O droplet. A detailed spectral analysis of the $\nu_1(SO_4^{2-})$ stretching mode evolving with decreasing relative humidity is shown in figure 71. Reducing the relative humidity caused to a continuous decrease of the vibrational frequency from 981cm^{-1} to 978cm^{-1} and to an increase of the linewidth from 8cm^{-1} to 12cm^{-1} in the RH range from ~90% to 31%. A sudden decrease of both the vibrational frequency (975cm^{-1}) and the linewidth (5cm^{-1}) is accompanied with the efflorescence of the droplet. An enhanced intensity and a narrow linewidth are characteristic for the solid state Raman spectra of AS. A similar analysis of the phase transitions was performed for several internally mixed dicarboxylic acids (DCA)/AS/H_2O droplets deposited on hydrophobic substrates[228, 229]. Note that the apparently low ERH value is due to the stepwise drying process. After equilibrium has been reached at 37.8% and the Raman spectra was collected, the RH was further lowered. Crystallization of AS was observed immediately at the beginning of the drying step. Song et al.[13] stated that for mfs (AS)≥0.5, the efflorescence occurred in a rather broad range from 35-48%, which is in line with the observed ERH value of the C6/AS/H_2O droplet.

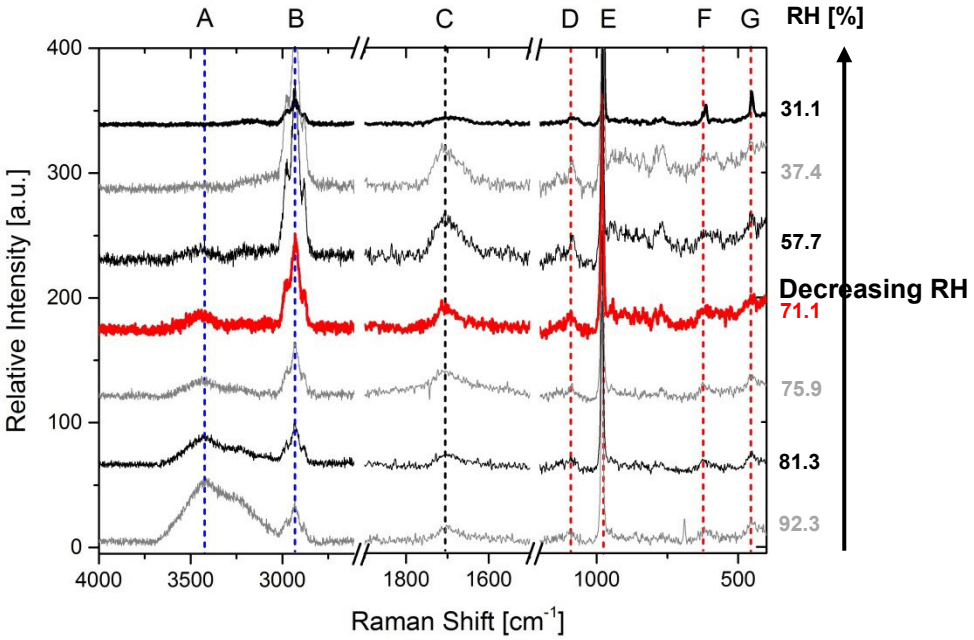

Figure 70: Raman spectra of an evaporating C6/AS/H_2O solution droplet (OIR=0.5) in the EDB at ~15°C. Note that the Raman spectra are normalized to the $\boldsymbol{\nu_1(SO_4^{2-})}$ stretching mode at 981cm^{-1}. The Raman spectra are vertically shifted for a better visibility. The corresponding relative humidities are given at the right side of the panel. The red highlighted Raman spectra indicates LLPS at ~71%RH.

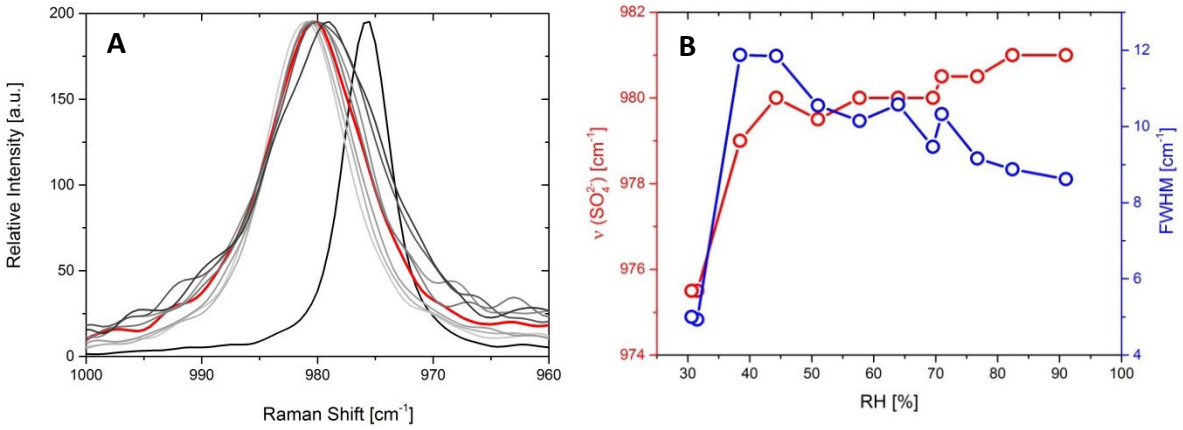

Figure 71: A) Raman spectra of the $\boldsymbol{\nu_1(SO_4^{2-})}$ stretching region (from 960cm^{-1} to 1000cm^{-1}). B) Analysis of the frequency shift of $\boldsymbol{\nu_1(SO_4^{2-})}$ stretching mode (red open symbols) and the full width at half maximum (FWHM, blue open symbols) upon slow dehydration of a C6/AS/H_2O particle in the EDB at ~15°C.

Table 5: Assignment of the vibrational modes in the Raman spectra of fully deliquesced C6/AS/H_2O particles.

Label	ν [cm^{-1}]	Assignment	Reference
A	3700-3030	$\nu(OH)$	Song et al.[13]
B	2976, 2926, 2878	$\nu(CH)$	Song et al.[13]
C	1702	$\nu(CO)$	Song et al.[13]
D	1095	$\nu_3(SO_4^{2-})$	Pye et al.[230]
E	981	$\nu_1(SO_4^{2-})$	Pye et al.[230]
F	619	$\nu_4(SO_4^{2-})$	Pye et al.[230]
G	457	$\nu_2(SO_4^{2-})$	Pye et al.[230]

5.6.5 2D angle-resolved scattering pattern

The drying of a C6/AS/H_2O mixture started with a liquid droplet. Size and phase changes of the droplet were continuously monitored by two-dimensional (2D) angle resolved optical scattering pattern (TAOS) pattern. A homogeneous liquid droplet showed regularly arranged vertical interference stripes indicating that a perpendicular polarized laser beam illuminates the spherical droplet in the same plane as the elastically scattered light is detected by the CCD-camera (90° scattering geometry). In the corresponding optical shadow images, a fully deliquesced droplet can be seen (see figure 72A). As the RH is lowered, the droplet shrinked in its size and the distance between the fringes became wider. Technically speaking, the distance between adjacent intensity maxima and minima is a good indicator for the size of the droplet provided that the concentration and thus the refractive index (RI) are known at all times. At about ∼71% RH, a second scattering pattern with broader fringes is superimposed on the regular pattern (figure 72H). A closer look on the scattering pattern revealed that the background fringes are slightly distorted. In the optical shadow image was an inclusion at the right edge of the droplet visible (see darker region in figure 72C). The optical images coincided nicely with the TAOS pattern demonstrating that LLPS has been occurred at ∼71% RH. Short timescale changes of the superimposed fringes in position and shape are probably associated with the movement of the liquid inclusion within the host droplet. With decreasing RH, the second scattering pattern is slightly distorted and the fringes are bended (figure 72I). In the corresponding optical shadow images, the two liquid phases cannot be easily distinguished from each other due to the limited contrast of the images. Finally, the scattering pattern of the effloresced C6/AS/H_2O droplet is characterized by a totally irregular structure fluctuating with time due to the diffuse reflection of light at the solid AS crystallites (figure 72J). The spherical shape is preserved by the effloresced

C6/AS/H_2O particle, probably being indicative of the formation of polycrystalline AS (figure 72E). The organic material could be enclosed in the pores and veins of the inorganic matrix.

To put this in context, Secker et al.[231] measured the forward scattering pattern and optical images of phase-separated oleic acid/water droplets and observed secondary scattering fringes superimposed on the normal concentric rings originating from the homogeneous spherical droplet. The oleic acid/water droplets adopted a partially engulfed structure with a liquid water inclusion residing at the edge of the oleic acid host droplet. Further evidence for the formation of a secondary ring structure was also provided by modelling simulations, in which the secondary pattern was described as the result of host internal fields, which are scattered by the inclusion[232]. It has been shown that the frequency of the secondary ring structure correlates with the size of the inclusion. Overall, the experimental results showed that the onset of LLPS and the evolution of the separated liquid phases as well as their phase transitions can be tracked by 2D angle-resolved scattering pattern and optical images.

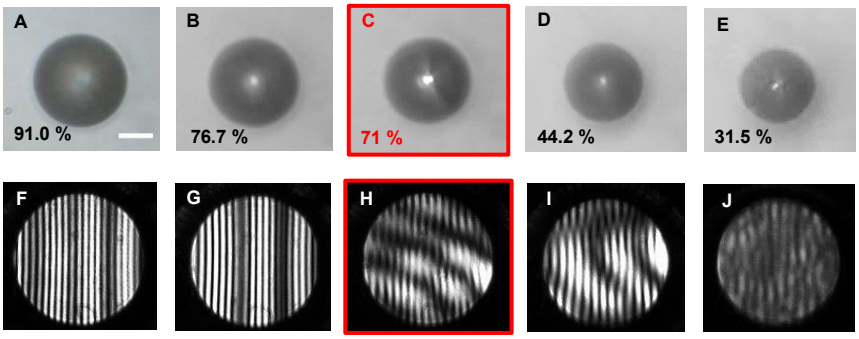

Figure 72: Upper panels: Shadow images of an evaporating C6/AS/H_2O particle in the EDB at ~15°C. The scale bar given in the first image is about 20µm. Lower panels: 2D angle-resolved scattering pattern of the same particle C6/AS/H_2O at the indicated relative humidities.

5.6.6 Morphology of phase-separated C6/AS/H_2O particles

Some representative examples of phase-separated C6/AS/H_2O particles are depicted in figure 73. It appears that the phase-separated particles are built up of multiple liquid inclusions floating around within the host droplets due to the moisture flow through the EDB (see figures 73A and 73B) or of two liquid phases in a partially engulfed configuration (see figures 73C and 73D). In none of the cases, a core-shell or completely engulfed configuration of the C6/AS/H_2O droplets was observed. These findings slightly deviate from substrate-supported observations[13]. It was pointed out that after the initial stage (i.e. the formation of small separated regions and subsequent partial coalescence of inclusions) a major AS-rich inclusion surrounded by an organic-rich phase tented to move from the center toward the edge of the host droplet in the RH range from 71.9% to 67.2%, which is equivalent to the transition from a core-shell to a partially engulfed configuration. The obtained morphologies

are also confirmed by optically levitated droplets[233]. Dependig on the volume ratio of the NaCl and decane phase, the droplets adopted different morphologies ranging from core-shell to partially engulfed structures with a single or mupliple inclusions.The adoption of a specific morphology has been interpreted in terms of the spreading coefficient of the organic phase on the aqueous phase[8, 226]. A speading coefficient with a positive sign (i.e. larger than zero) results in a core-shell morphology, while a spreading coefficient with a negative sign (i.e. smaller than zero) gives a partially engulfed morphology. The RH can critically influence the interfacial tension of the AS and organic phase. With decreasing RH, the interfacial tension of the AS and organic phase increases and thus the transition from a core-shell to a partially engulfed morphology is more likely to occur.

In conclusion, the experiments revealed that LLPS in C6/AS/H_2O droplets is a moisture-induced process, which can be unambiguously observed with different EDB setups and detection methods (i.e. low and high resolution Mie resonance spectroscopy on the one hand and Mie scattering pattern and optical microscopy on the other hand). Furthermore, the temporal evolution of separated liquid phases and their phase transitions can be monitored by using these detection techniques.

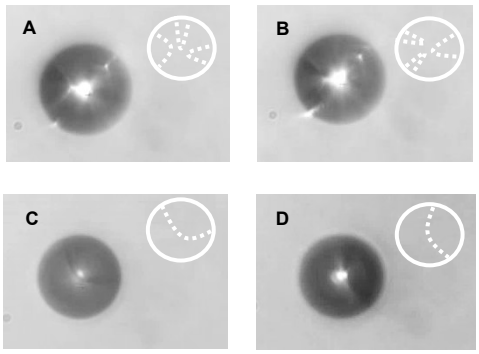

Figure 73: A compilation of shadow images of different C6/AS/H_2O particles suspended in the EDB at ~15°C. The insets show the tentative representation of the internal structure of the C6/AS/H_2O particles.

6. Summary and conclusions

Heterogeneous nucleation phenomena in metastable atmospheric systems like supercooled cloud droplets or liquid aerosol particles have been studied. Three systems have been chosen representing the different classes of atmospheric aerosol particles: supercooled suspension of feldspar, that has been recently identified as a very efficient ice nucleating mineral[5], supersaturated solution of sea salt, being the most abundant marine aerosol source, and ternary mixtures of dicarboxylic acid/ammonium sulfate/water representing the complex organic/inorganic aerosol systems as a possible pathway of the secondary organic aerosol formation.

Specifically, the aim of this work was to perform different types of nucleation experiments beyond those carried out with steady cooling in order to provide evidence to distinguish between time-independent (singular) and time-dependent (stochastic) interpretations of heterogeneous ice nucleation[67, 140]. The current understanding of the variability in the ice nucleating efficiencies of the feldspar group members is insufficient and needs to be investigated. In addition, previous measurements indicated a large discrepancy in the temperature-dependent partitioning between anhydrous NaCl and NaCl dihydrate[9, 10]. The objective of the current work was to elucidate this disagreement and to understand the effect of additional ionic species on the formation of NaCl dihydrate in simulated sea salt aerosol (SAA) particles. Furthermore, the influence of the substrate on the internal configuration of phase separated organic/inorganic aerosols was questioned and in this study verified. For this purpose, two techniques, a novel droplet freezing assay instrument and a combination of an electrodynamic balance (EDB) coupled to a Raman microscope were used in order to address these issues.

A cold stage apparatus was used to study the heterogeneous ice nucleation ability of feldspar suspensions. Up to 1000 individual suspension droplets were printed onto a silicon substrate and covered with silicone oil. The nucleation events were detected via a sudden change in the reflected light of the particles. By using this droplet freezing assay a variety of complementary nucleation tests were performed allowing for measurements of the ice nucleation active site (INAS) surface density $n_s(T)$. The INAS surface density is a quantitative measure of the ice nucleating efficiency of aerosol particles regardless of the experimental measurement conditions[63, 66]. It was found out that concentrated feldspar suspensions showed a steep temperature dependence of the INAS surface density, whereas diluted suspensions showed a flattening of $n_s(T)$ with decreasing temperature approaching a limiting value n_s^*. The K-rich feldspar samples FS01 and FS02 and the Na/Ca-rich feldspar FS05 showed a weak cooling rate dependence on the order of 0.6K shift of the median freezing temperature over a ten-fold change in the cooling rate, whereas the median freezing temperature of FS04 suspensions was shifted by only 0.2K by increasing the cooling from 1K/min to 10K/min. Isothermal freezing experiments have been conducted for concentrated FS02 suspensions at four temperatures from 253K to 256K and for FS04 suspensions at two temperatures of 266K and 267K. The fraction of liquid droplets has been found to decay in a nonlinear fashion for the FS02 sample and in a quite linear fashion for

the FS04 sample. It was argued that the FS02 sample featured a greater heterogeneity of ice active sites as compared to the FS04 sample. To explore the relationship between stochastic and singular ice nucleation repeated freeze-thaw cycle experiments have been performed clearly demonstrating the stochastic nature of heterogeneous ice nucleation (i.e. two subsequent cooling ramp experiments are not perfectly correlated).

The results have been described within the classical nucleation theory (CNT)-based theoretical framework (the so called Soccer ball model, SBM). It could be shown that the levelling off of the INAS surface density at low temperature can be correctly predicted by the SBM. Even more, both the cooling ramp experiments and thus the $n_s(T)$ curves and the isothermal experiments can be described by a unique set of SBM fit parameters. The different types of nucleation experiments allowed to constrain the variability of SBM fit parameters arising if only one type of nucleation experiment results (e.g. frozen fraction curves) is used for fitting.

One particular K-feldspar FS04 showed an exceptional high ice activity, starting already at 268K. The INAS surface density of this feldspar sample showed a bimodal distribution of ice active sites with a high temperature mode in the range from 255K to 268K and a low temperature mode in the range below 255K. Chemical treatment of FS04 suspensions with 30% hydrogen peroxide (H_2O_2) solution resulted in the deactivation of the anomalous IN mode and the reduction of ice activity down to that of the generic K-rich feldspar. The proteinaceous origin of the these highly active IN entities could be excluded by heating the suspensions up to 95°C without any observable change of the IN efficacy. Applying the SBM fit to the temperature jump and isothermal decay experiments, a very high mean contact angle was obtained, which was previously found for bacterial INPs (i.e. Snomax®), the most active ice nucleating particles so far[145]. The number of high temperature active sites per mass of feldspar was found being too high to be explained by surface contaminations of the feldspar specimen prior to milling. It is concluded that the presence of the high temperature IN sites should be an inherent property of this particular feldspar specimen. However, the nature of these ice nucleation sites could not be clarified.

The understanding of heterogeneous ice nucleation induced by feldspar particles can be improved by implementing multiple and non-symmetric contact angle distributions in the SBM, which allow to accurately represent the observed nucleation behavior. From an experimental point of view, further studies dealing with the variety of ice nucleation properties of the complex feldspar group encompassing the plagioclase solid solution series, ternary feldspars etc. should be performed, as suggested by the work of Harrison et al.[234]. The chemical identification of the ice active sites responsible for the anomalous high ice activity of the FS04 sample is strongly needed in order to understand the complexity of ice nucleation of feldspar particles on a microscopic level.

The participation in the intercomparison campaign (Fifth international ice nucleation workshop, FIN02) revealed that the Cold stage apparatus is capable to quantify the number

concentration of ice nuclei per liter water and per unit volume of air for several aerosol samples including Snomax, K-feldspar, Argentinian soil dust, Tunisian desert dust and illite NX. Background correction was only relevant for aerosol samples showing ice nucleation very close to the homogeneous freezing limit (e.g. illite NX). As a part of the FIN02 intercomparison campaign, the experimental setup demonstrated its reliability and reproducibility of the frozen fraction curves for the entire temperature range from 273K to 236K. The results are in good agreement with the data obtained with the well-established off-line ice nucleation instruments[5, 143, 145, 147, 150, 160]. The objective of the FIN02 campaign was not only to compare off-line and on-line methods at predefined temperatures and aerosol types, but also to measure the IN concentrations of unknown aerosol types. The cold stage apparatus was also able to correctly predict the IN concentrations of unknown aerosol suspensions.

To investigate the factors governing the solute nucleation of NaCl dihydrate in pure NaCl and SSA solution droplets, efflorescence experiments were carried out with an EDB equipped with a relative humidity and temperature control system. Identical solution droplets were suspended in the EDB maintained at isothermal and isohumid conditions. After the crystallization, the differentiation between NaCl dihydrate and anhydrous NaCl particles has been done by confocal Raman spectroscopy. The two crystalline forms of NaCl could also be distinguished due to their different morphological appearance (i.e. cubic vs. spherical particles) and their Mie scattering patterns. The temperature-dependent formation of NaCl dihydrate was observed in the temperature range from 250K to 241K. The results are comparable with the observations of deposited NaCl solution droplets reported by Wise et al.[9]. In contrast, the temperature-dependent formation curve of NaCl dihydrate from the AIDA cloud chamber could not be reproduced. The efflorescence occurred in a narrow temperature interval, rather than covering a broad temperature range (several tens of degrees centigrade) as described in Wagner et al.[10]. A time-dependent statistical analysis of the NaCl efflorescence revealed that the nucleation process is stochastic in nature and governed by a temperature dependent volumetric nucleation rate coefficient. The derived homogeneous nucleation rate coefficients of NaCl dihydrate were used to scale the temperature-dependent formation of NaCl dihydrate for different system sizes (i.e. droplet volumes) and observation times. A quantitative representation of the previous results was obtained by choosing reasonable values for the droplet volume and observation time.

Furthermore, simulated SSA particles were analyzed by means of SEM/EDX measurements indicating a complex internal heterogeneity of the SSA particles with NaCl-rich and $CaSO_4$-rich regions surrounded by an amorphous matrix containing $MgCl_2$ and $MgSO_4$. The temperature-dependent formation of NaCl dihydrate was observed in the temperature range from 255K to 243K, as compared to 250K to 241K for pure NaCl droplets. The enhanced formation of NaCl dihydrate in the SSA particles is attributed to the earlier crystallization of solid inclusions (probably $CaSO_4 \cdot 2H_2O$ formed during the evaporation process) which could be trigger the heterogeneous nucleation of NaCl dihydrate.

Additional experiments with smaller NaCl solution droplets (i.e. lower initial concentrations) may help to understand the different results of the experimental approaches (i.e. AIDA cloud chamber, environmental cell and EDB). By adding defined amounts of impurities of less soluble and less ice active material (e.g. $CaSO_4 \cdot 2H_2O$ or $CaCO_3$) to the NaCl solution, the heterogeneous efflorescence process can be studied in detail and heterogeneous nucleation rates can be derived. As an instrument-based improvement, an in-situ relative humidity and temperature sensor in proximity to the levitated droplet would have the advantage to determine the efflorescence relative humidity (ERH) and thus the supersaturation with respect to the solute right at the location of the NaCl solution droplet. These measurements could complement the concurrent dew point mirror (DPM) data recording.

Finally, the liquid-liquid phase separation (LLPS) behavior of the ternary dicarboxylic acid/ammonium sulfate/water mixture (C6/AS/H_2O) with an organic to inorganic ratio (OIR) of 0.5 was investigated with two different EDB setups (at KIT and ETH Zurich) and several spectroscopic and optical techniques. It has been shown that the onset of LLPS could be unambiguously identified by low and high resolution Mie resonance spectroscopy on the one hand and angle-resolved scattering pattern and optical shadow images on the other hand. The onset RH of phase separation (SRH) is in the range from 74-75% (derived from low and high resolution Mie resonance spectroscopic measurements) to ~71% (derived from Mie scattering pattern and optical images). The observed SRHs confirm previous findings for C6/AS/H_2O droplets deposited on a hydrophobically coated substrate reported by Song et al.[13]. The transition from the core-shell to the partially engulfed configuration is expected to occur at much lower RH values (i.e. 63-66%). However, the influence of the temperature on the transition from the core-shell to the partially engulfed morphology was intended to be studied with both EDB setups, but could only be realized at 288K. Further studies are needed to examine the temperature sensitivity of the internal morphological transformation and the variability in the SRH values during the drying and humidification process.

By using the described experimental approaches, existing measurements of the aerosol systems could not only be reproduced, but also described within theoretical formalisms considering the stochastic nature of nucleation. New findings of a highly ice active K-rich feldspar and for simulated SSA particles were observed expanding the knowledge of phase transitions in atmospheric aerosols.

7. Appendix

To determine the size of the deposited droplets on the Cold Stage, a calibration of the microscopic image from the CCD camera was performed. For this propose, a stage micrometer mounted on a glass slide (Nikon) and an etched silicon wafer with a distance between two adjacent grooves of 100µm were placed under the microscope. Both calibration standards revealed that 12Pixel of the microscopic image correspond to 100µm. This relationship was used to calculate the diameter and volume of the deposited droplets. As can be seen from figure 74, the size of the droplets is well reproduced by a Gaussian-shaped distribution with a mean value of 107 µm.

The volumes of the droplets on the silicon substrate have been evaluated using the equation for the spherical cap geometry[235]:

$$V = \frac{\pi r^3 (2 - 3cos\alpha + cos^3\alpha)}{3(sin^3\alpha)} \qquad (7.\ 1)$$

where r being the apparent radius of the droplet projection on a plane and α the stationary contact angle of water on the substrate. The contact angle was measured optically with the droplets on the substrate cooled down to the dew point temperature of the lab air to avoid the evaporation and was found to be 74°±10°. The projection area equivalent diameter (apparent diameter) was measured using the image of the droplet array recorded by the video camera regularly used in the cold stage setup. The distribution of the apparent diameter was found to be centered around (107±14)µm (see figure 74). Based on these measurements, the average volume of the droplet was evaluated as (215±70) pL.

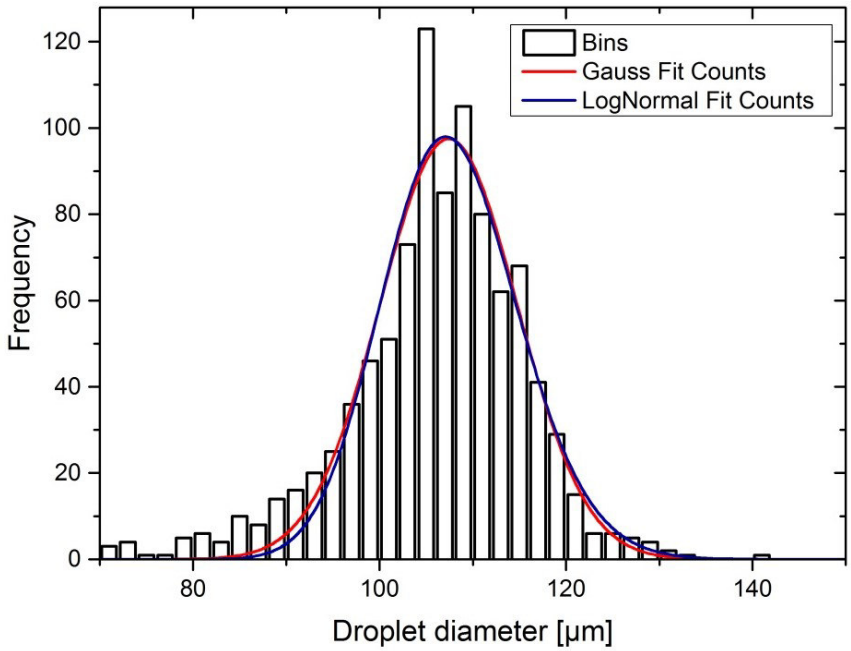

Figure 74: Size distribution of FS02 suspension droplets deposited onto a silicon water.

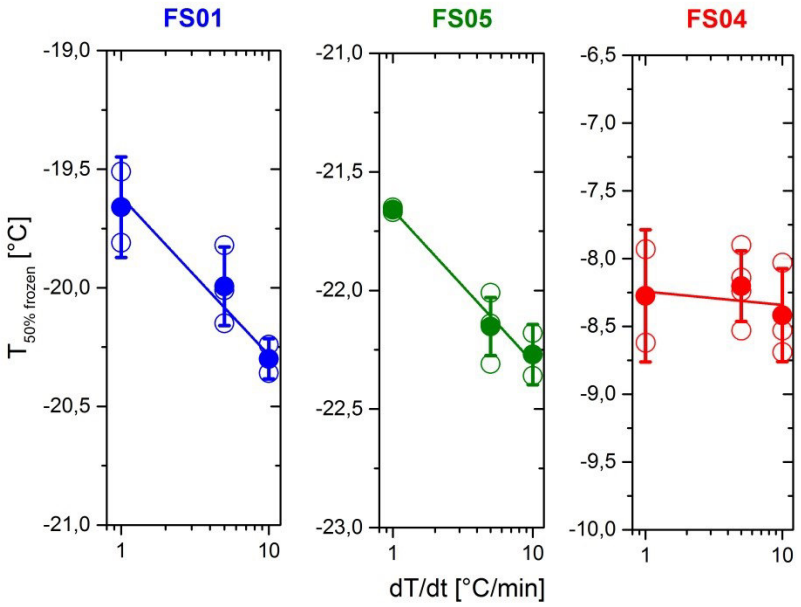

Figure 75: Median freezing temperature $\boldsymbol{T_{0.5}}$ for the aqueous 0.8wt% suspensions of FS01 und FS05 and FS04. Open circles correspond to median freezing temperatures for different runs with the same cooling rate. The solid circles are averaged median freezing temperatures. Straight lines are non-weighted linear regressions of the averaged $\boldsymbol{T_{0.5}}$ values for three different cooling rates.

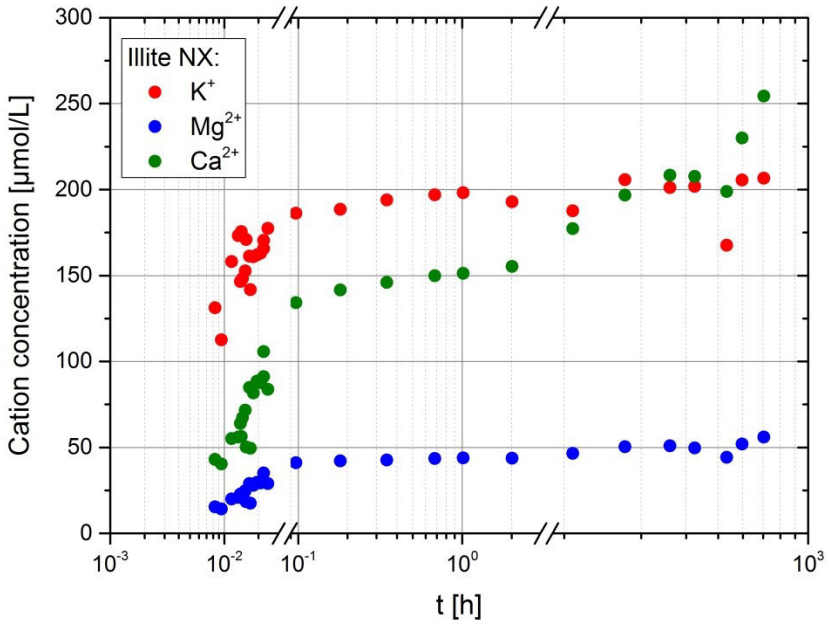

Figure 76: Evolution of the cation concentration in aqueous suspension of 0.1 g illite NX in 10mL deionized water with time. The scaling of the time-axis is different for three different subsections of the time series[147].

The concentration of impurities was calculated as follows:

$$c_{Impurities}(T) = 10^{(A+BT+CT^2+DT^3)} \quad (7.\ 2)$$

where $c_{IN}(T)$ is the concentration of IN per picoliter (pL). The coefficients are $A = -44.649$, $B = -3.470$, $C = -0.099$ and $D = -9.863 \cdot 10^{-4}$. In addition, a second parametrization with $A = -13.602$, $B = -0.485$, $C = -0.005$ and $D = -5.609 \cdot 10^{-7}$ was determined. The first parametrization was used for the calculation of IN per m³ air due to the higher background level.

For the calculation of the IN concentration per m³ air the droplet volume $V_{drop} = 523.59pL$ (corresponding to a 100µm diameter droplet) was used. The sample (volumetric) flow rate was $\mathrm{Q_s} = 12.5\mathrm{L/min}$ throughout the measurements. The scaling factor f is calculated as follows:

$$f = \frac{\sum_i V_{i,added} + V_{Impinger}}{V_{Sample}} \quad (7.\ 3)$$

where $V_{i,added}$ is the amount of added water to refill the impinger. $V_{Impinger}$ and V_{Sample} are the volumes of the impinger and the sample respectively. The concentrations of IN per m³ air of the impinger aerosol samples were estimated according to equation (5.3) and the parameters given in Table 6.

Table 6: Quantities for the calculation of the concentration of IN per cubic meter air

	Scaling factor f	**Sampling time t [min]**	**Sample volume $V_{Impinger}$**
Illite NX	2.083	256	36
Soil dust 1	2.155	242.39	36
Desert dust	2.277	251.21	36.7
K-feldspar	2.332	240.97	38.6
Snomax®	2.261	238.87	34.8
Soild dust 2	2.158	233.84	36.6
Blind test sample 1	2.324	250.78	37
Blind test sample 2	2.349	241.05	36.6

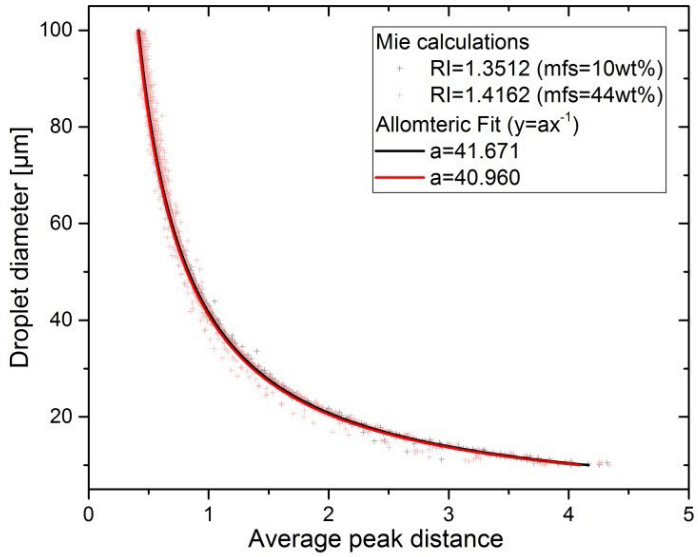

Figure 77: Droplet diameter as a function of the average peak distance. The following parameters were chosen to perform the Mie calculations: excitation laser wavelength: 632.8nm, polarization: perpendicular, peak width: 3, angular range: 16.46°, angle between incident laser beam and CCD-camera: 90°.

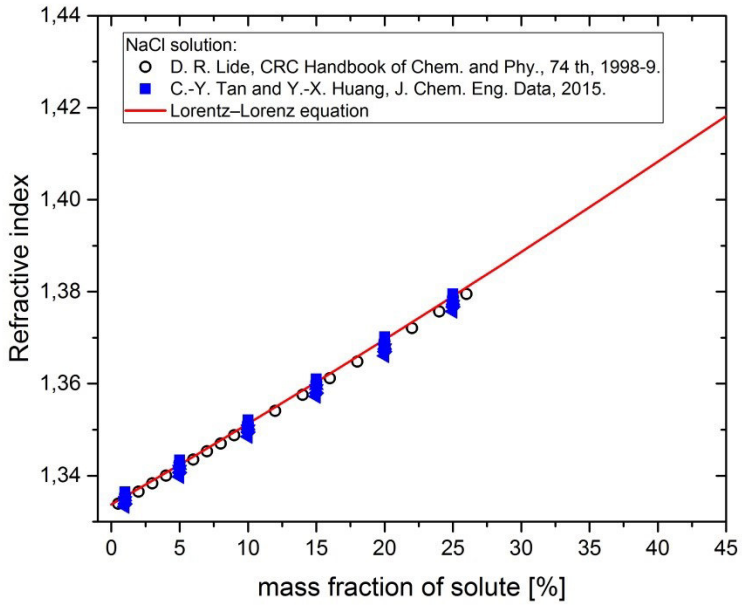

Figure 78: Refractive index (RI) as a function of mass fraction of solute (mfs). The RI was measured at 589.3nm (sodium D line) in D.R. Lide, 1998-1999 and in C.-Y. Tan and Y.-X. Huang, 2015. The molar refractivities of H_2O (3.72) and NaCl (9.26) were used for the calculation of the RI according to the Lorentz-Lorenz equation.

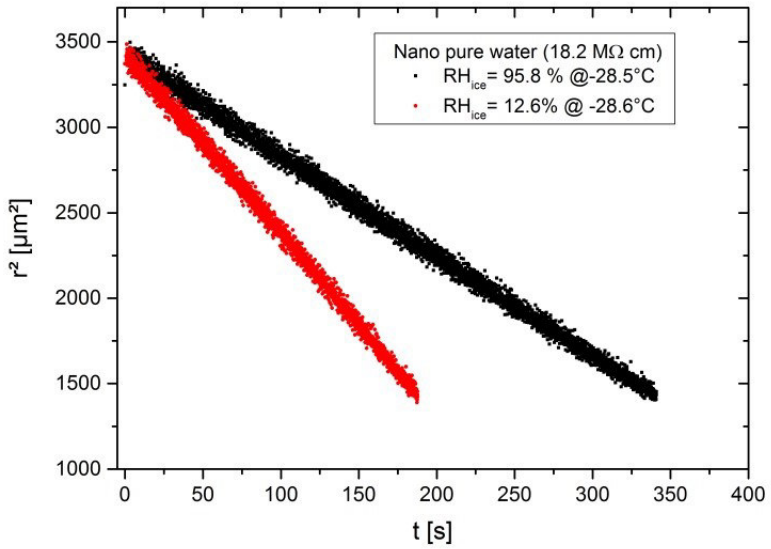

Figure 79: Time dependencies of the radius squared for evaporating water droplets in the EDB. The water droplets evaporate into humidified air at a temperature of -28.5°C.

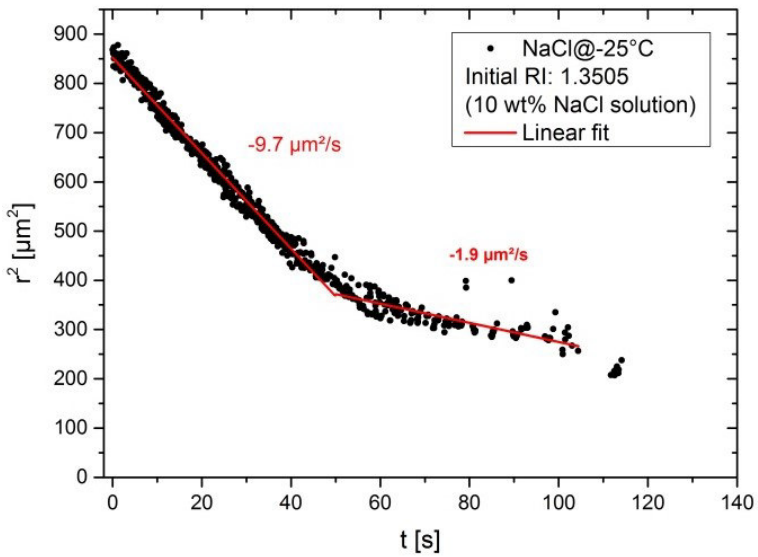

Figure 80: Time dependence of the radius squared for an evaporating NaCl solution droplet in the EDB. The EDB is maintained at -25°C. The initial concentration of the bulk NaCl solution was 10wt%.

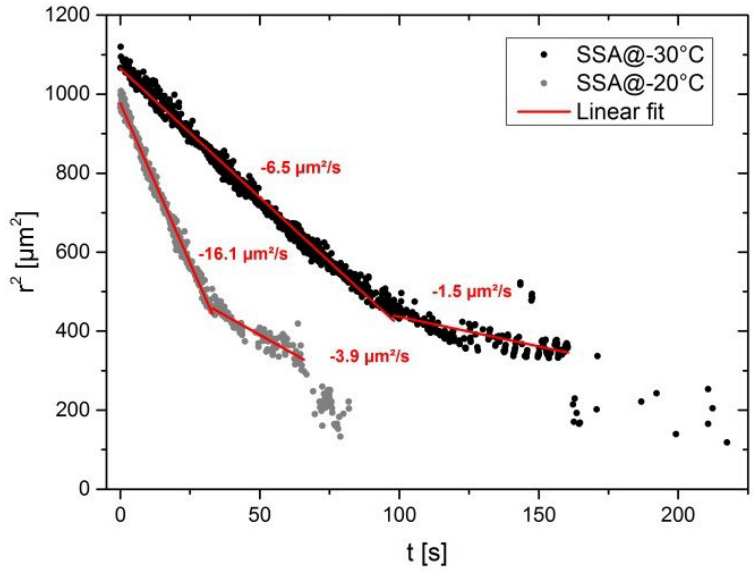

Figure 81: Time dependencies of the radius squared for evaporating SSA droplets at two different temperatures in the EDB. The initial concentration of the bulk SSA solution was 10wt%.

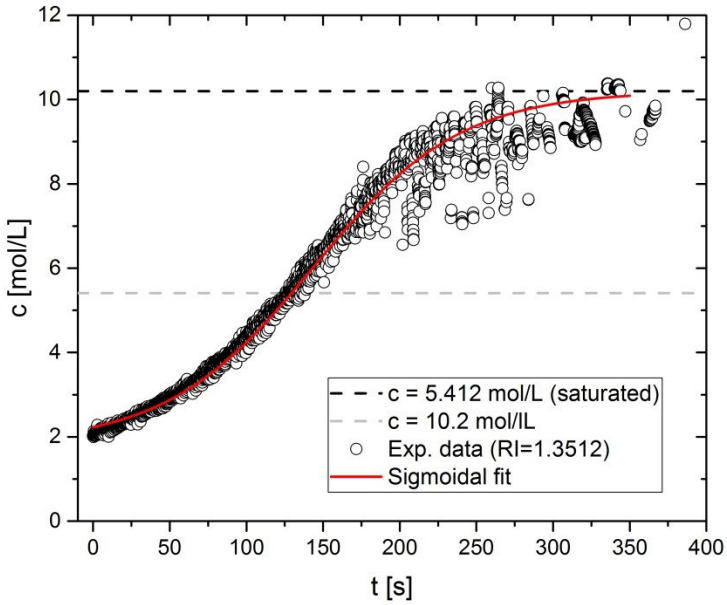

Figure 82: Change of molar concentration with time for an evaporating NaCl droplet in the EDB at -30°C.

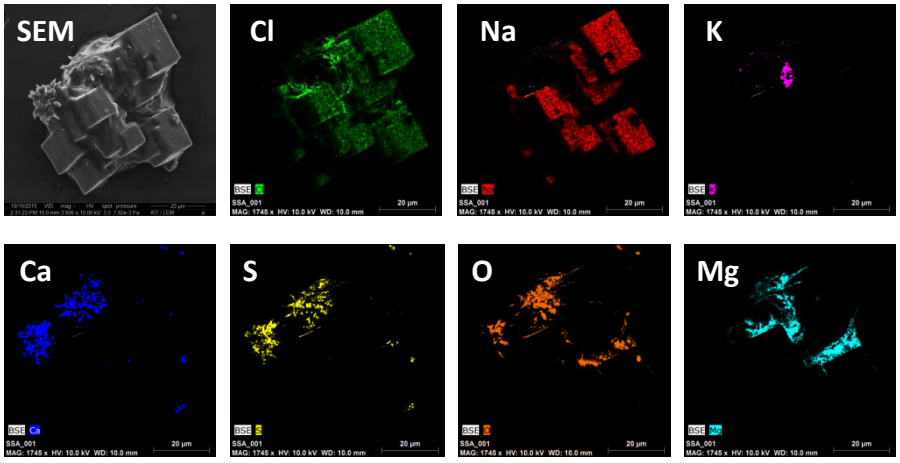

Figure 83: SEM image (upper left panel) and EDX elemental maps of a deposited SSA particle onto a silicon wafer. The residual SSA particles exhibit a complex internal heterogeneity of chemical species. The chemical elements Na/Cl and Ca/S/O are directly correlated. Mg is located in the space between the NaCl cubes.

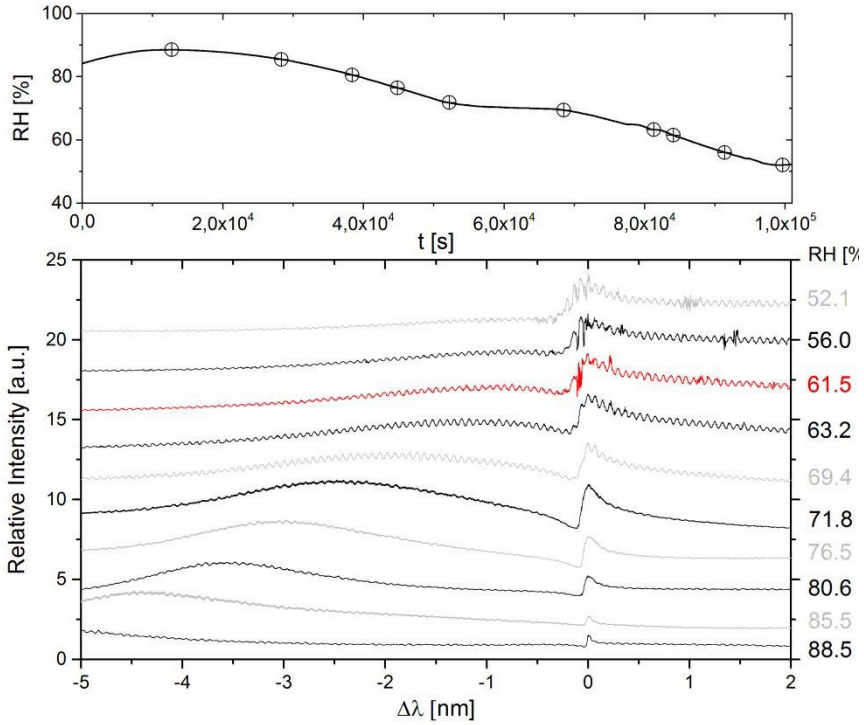

Figure 84: The upper panel shows the change in RH with time. The symbols mark the times and humidities at which the TDL spectra in the lower panel were recorded. The lower panel shows a series of TDL spectra (TE-polarization) upon drying from 88.5% RH to 52.1% RH. The scattered intensity is normalized to the maximum intensity in the TDL spectra; the wavelength scale is relative to the peak center.

8. List of figures

9. List of tables

10. Bibliography

1. V. Ramaswamy, in *Climate Change 2001: The Scientific Basis. Contribution of Working Group I to the Third Assessment Report of the Intergovernmental Panel on Climate Change*, ed. J. T. Houghton, Cambridge University Press, Cambridge, United Kingdom and New York, NY, USA, 2001, pp. 349-416.
2. T. F. Stocker, D. Qin, G.-K. Plattner, M. Tignor, S. K. Allen, J. Boschung, A. Nauels, Y. Xia, V. Bex and P. M. Midgley, *Climate Change 2013: The Physical Science Basis. Contribution of Working Group I to the Fifth Assessment Report of the Intergovernmental Panel on Climate Change*, Cambridge University Press, Cambridge [u.a.], 2013.
3. M. D. Petters and S. M. Kreidenweis, *Atmos. Chem. Phys.*, **2007**, 7, 1961-1971.
4. U. Lohmann and C. Hoose, *Atmos. Chem. Phys.*, **2009**, 9, 8917-8934.
5. J. D. Atkinson, B. J. Murray, M. T. Woodhouse, T. F. Whale, K. J. Baustian, K. S. Carslaw, S. Dobbie, D. O'Sullivan and T. L. Malkin, *Nature*, **2013**, 498, 355-358.
6. S. T. Martin, *Chemical Reviews*, **2000**, 100, 3403-3454.
7. T. Koop, J. Bookhold, M. Shiraiwa and U. Poschl, *Physical Chemistry Chemical Physics*, **2011**, 13, 19238-19255.
8. U. K. Krieger, C. Marcolli and J. P. Reid, *Chemical Society Reviews*, **2012**, 41, 6631-6662.
9. M. E. Wise, K. J. Baustian, T. Koop, M. A. Freedman, E. J. Jensen and M. A. Tolbert, *Atmospheric Chemistry and Physics*, **2012**, 12, 1121-1134.
10. R. Wagner, O. Möhler and M. Schnaiter, *Journal of Physical Chemistry A*, **2012**, 116, 8557-8571.
11. R. Wagner and O. Möhler, *Journal of Geophysical Research: Atmospheres*, **2013**, 118, 4610-4622.
12. G. P. Schill and M. A. Tolbert, *Journal of Physical Chemistry C*, **2014**, 18, 29234–29241.
13. M. Song, C. Marcolli, U. K. Krieger, A. Zuend and T. Peter, *Atmospheric Chemistry and Physics*, **2012**, 12, 2691-2712.
14. E. R. Lewis and S. E. Schwartz, *Sea salt aerosol production : mechanisms, methods, measurements, and models; a critical review*, American Geophysical Union, Washington, DC, 2004.
15. J. H. Seinfeld and S. N. Pandis, *Atmospheric chemistry and physics : from air pollution to climate change*, Wiley, Hoboken, NJ, 2. ed. edn., 2006.
16. T. Kouimtzis, C. Samara and S. Biegalski, *Airborne Particulate Matter*, Springer, Berlin, 1995.
17. B. J. Murray, D. O'Sullivan, J. D. Atkinson and M. E. Webb, *Chemical Society Reviews*, **2012**, 41, 6519-6554.
18. H. Grythe, J. Ström, R. Krejci, P. Quinn and A. Stohl, *Atmos. Chem. Phys.*, **2014**, 14, 1277-1297.
19. E. L. Andreas, *Journal of Geophysical Research: Oceans*, **1992**, 97, 11429-11441.
20. E. L. Andreas, *Journal of Physical Oceanography*, **1998**, 28, 2175-2184.
21. M. D. Anguelova, Doctoral thesis, University of Delaware, 1997.
22. H. R. Pruppacher and J. D. Klett, *Microphysics of clouds and precipitation*, Kluwer, Dordrecht [u.a.], 2., rev. and enl. ed. edn., 1997.
23. U. Baltensperger, *Science*, **2010**, 329, 1474-1475.
24. F. Zimmermann, S. Weinbruch, L. Schütz, H. Hofmann, M. Ebert, K. Kandler and A. Worringen, *Journal of Geophysical Research: Atmospheres*, **2008**, 113, D23204.
25. J. D. Yakobi-Hancock, L. A. Ladino and J. P. D. Abbatt, *Atmospheric Chemistry and Physics*, **2013**, 13, 11175-11185.
26. T. F. Whale, B. J. Murray, D. O'Sullivan, T. W. Wilson, N. S. Umo, K. J. Baustian, J. D. Atkinson, D. A. Workneh and G. J. Morris, *Atmos. Meas. Tech.*, **2015**, 8, 2437-2447.
27. T. Zolles, J. Burkart, T. Häusler, B. Pummer, R. Hitzenberger and H. Grothe, *The Journal of Physical Chemistry A*, **2015**, 119, 2692-2700.

28. D. Niedermeier, S. Augustin-Bauditz, S. Hartmann, H. Wex, K. Ignatius and F. Stratmann, *Journal of Geophysical Research: Atmospheres*, **2015**, 120, 5036-5046.
29. G. P. Schill, K. Genareau and M. A. Tolbert, *Atmos. Chem. Phys.*, **2015**, 15, 7523-7536.
30. S. Augustin-Bauditz, H. Wex, S. Kanter, M. Ebert, D. Niedermeier, F. Stolz, A. Prager and F. Stratmann, *Geophysical Research Letters*, **2014**, 41, 7375-7382.
31. G. Kulkarni, C. Sanders, K. Zhang, X. Liu and C. Zhao, *Journal of Geophysical Research: Atmospheres*, **2014**, 119, 9993-10011.
32. C. Emersic, P. J. Connolly, S. Boult, M. Campana and Z. Li, *Atmos. Chem. Phys.*, **2015**, 15, 11311-11326.
33. J. Niehaus, J. G. Becker, A. Kostinski and W. Cantrell, *Journal of the Atmospheric Sciences*, **2014**, 71, 3659-3667.
34. A. B. Ronov and A. A. Yaroshevsky, in *The Earth's Crust and Upper Mantle*, AGU, Washington, DC, 1969, vol. 13, pp. 37-57.
35. K. Kandler, L. Schütz, C. Deutscher, M. Ebert, H. Hofmann, S. Jäckel, R. Jaenicke, P. Knippertz, K. Lieke, A. Massling, A. Petzold, A. Schladitz, B. Weinzierl, A. Wiedensohler, S. Zorn and S. Weinbruch, *Tellus B*, **2011**, 61.
36. K. Kandler, L. Schütz, S. Jäckel, K. Lieke, C. Emmel, D. Müller-Ebert, M. Ebert, D. Scheuvens, A. Schladitz, B. Šegvić, A. Wiedensohler and S. Weinbruch, *Tellus B*, **2011**, 63.
37. S. Nickovic, A. Vukovic, M. Vujadinovic, V. Djurdjevic and G. Pejanovic, *Atmospheric Chemistry and Physics*, **2012**, 12, 845-855.
38. G. Y. Jeong, *Journal of Geophysical Research: Atmospheres*, **2008**, 113, D02208.
39. R. C. Schnell and G. Vali, *Journal of the Atmospheric Sciences*, **1976**, 33, 1554-1564.
40. R. C. Schnell and G. Vali, *Tellus*, **1975**, 27, 321-323.
41. R. C. Schnell, *Geophysical Research Letters*, **1975**, 2, 500-502.
42. R. Fall and R. C. Schnell, *Journal of Marine Research*, **1985**, 43, 257-265.
43. L. V. Parker, C. W. Sullivan, T. W. Forest and S. F. Ackley, *Antarctic Journal*, **1985**, 20, 126–127.
44. P. A. Alpert, J. Y. Aller and D. A. Knopf, *Atmos. Chem. Phys.*, **2011**, 11, 5539-5555.
45. D. A. Knopf, P. A. Alpert, B. Wang and J. Y. Aller, *Nature Geosci*, **2011**, 4, 88-90.
46. P. A. Alpert, J. Y. Aller and D. A. Knopf, *Physical Chemistry Chemical Physics*, **2011**, 13, 19882-19894.
47. T. W. Wilson, L. A. Ladino, P. A. Alpert, M. N. Breckels, I. M. Brooks, J. Browse, S. M. Burrows, K. S. Carslaw, J. A. Huffman, C. Judd, W. P. Kilthau, R. H. Mason, G. McFiggans, L. A. Miller, J. J. Najera, E. Polishchuk, S. Rae, C. L. Schiller, M. Si, J. V. Temprado, T. F. Whale, J. P. S. Wong, O. Wurl, J. D. Yakobi-Hancock, J. P. D. Abbatt, J. Y. Aller, A. K. Bertram, D. A. Knopf and B. J. Murray, *Nature*, **2015**, 525, 234-238.
48. L. A. Ladino, J. D. Yakobi-Hancock, W. P. Kilthau, R. H. Mason, M. Si, J. Li, L. A. Miller, C. L. Schiller, J. A. Huffman, J. Y. Aller, D. A. Knopf, A. K. Bertram and J. P. D. Abbatt, *Atmospheric Environment*, **2016**, 132, 1-10.
49. P. J. DeMott, T. C. J. Hill, C. S. McCluskey, K. A. Prather, D. B. Collins, R. C. Sullivan, M. J. Ruppel, R. H. Mason, V. E. Irish, T. Lee, C. Y. Hwang, T. S. Rhee, J. R. Snider, G. R. McMeeking, S. Dhaniyala, E. R. Lewis, J. J. B. Wentzell, J. Abbatt, C. Lee, C. M. Sultana, A. P. Ault, J. L. Axson, M. Diaz Martinez, I. Venero, G. Santos-Figueroa, M. D. Stokes, G. B. Deane, O. L. Mayol-Bracero, V. H. Grassian, T. H. Bertram, A. K. Bertram, B. F. Moffett and G. D. Franc, *Proceedings of the National Academy of Sciences*, **2015**.
50. K. A. Prather, T. H. Bertram, V. H. Grassian, G. B. Deane, M. D. Stokes, P. J. DeMott, L. I. Aluwihare, B. P. Palenik, F. Azam, J. H. Seinfeld, R. C. Moffet, M. J. Molina, C. D. Cappa, F. M. Geiger, G. C. Roberts, L. M. Russell, A. P. Ault, J. Baltrusaitis, D. B. Collins, C. E. Corrigan, L. A. Cuadra-Rodriguez, C. J. Ebben, S. D. Forestieri, T. L. Guasco, S. P. Hersey, M. J. Kim, W. F. Lambert, R. L. Modini, W. Mui, B. E. Pedler, M. J. Ruppel, O. S. Ryder, N. G. Schoepp, R. C. Sullivan and D. Zhao, *Proceedings of the National Academy of Sciences*, **2013**, 110, 7550-7555.

51. S. M. Burrows, C. Hoose, U. Pöschl and M. G. Lawrence, *Atmos. Chem. Phys.*, **2013**, 13, 245-267.
52. H. C. Price, B. J. Murray, J. Mattsson, D. O'Sullivan, T. W. Wilson, K. J. Baustian and L. G. Benning, *Atmos. Chem. Phys.*, **2014**, 14, 3817-3830.
53. B. J. Murray, T. W. Wilson, S. Dobbie, Z. Cui, S. M. R. K. Al-Jumur, O. Mohler, M. Schnaiter, R. Wagner, S. Benz, M. Niemand, H. Saathoff, V. Ebert, S. Wagner and B. Karcher, *Nature Geosci*, **2010**, 3, 233-237.
54. T. W. Wilson, B. J. Murray, R. Wagner, O. Möhler, H. Saathoff, M. Schnaiter, J. Skrotzki, H. C. Price, T. L. Malkin, S. Dobbie and S. M. R. K. Al-Jumur, *Atmos. Chem. Phys.*, **2012**, 12, 8611-8632.
55. D. J. Cziczo, K. D. Froyd, C. Hoose, E. J. Jensen, M. Diao, M. A. Zondlo, J. B. Smith, C. H. Twohy and D. M. Murphy, *Science*, **2013**, 340, 1320-1324.
56. K. A. Pratt, P. J. DeMott, J. R. French, Z. Wang, D. L. Westphal, A. J. Heymsfield, C. H. Twohy, A. J. Prenni and K. A. Prather, *Nature Geosci*, **2009**, 2, 398-401.
57. B. Zobrist, T. Koop, B. P. Luo, C. Marcolli and T. Peter, *The Journal of Physical Chemistry C*, **2007**, 111, 2149-2155.
58. L. Ickes, A. Welti, C. Hoose and U. Lohmann, *Physical Chemistry Chemical Physics*, **2015**, 17, 5514-5537.
59. G. Vali, P. J. DeMott, O. Möhler and T. F. Whale, *Atmos. Chem. Phys.*, **2015**, 15, 10263-10270.
60. V. I. Khvorostyanov and J. A. Curry, *Thermodynamics, Kinetics and Microphysics of Clouds*, Cambridge University Press, New York (NY), 2004.
61. J. Levine, *Statistical explanation of spontaneous freezing of water droplets*, 1950.
62. E. J. Langham and B. J. Mason, *Proceedings of the Royal Society of London A: Mathematical, Physical and Engineering Sciences*, **1958**, 247, 493-504.
63. P. J. Connolly, O. Möhler, P. R. Field, H. Saathoff, R. Burgess, T. Choularton and M. Gallagher, *Atmospheric Chemistry and Physics*, **2009**, 9, 2805-2824.
64. D. Niedermeier, S. Hartmann, R. A. Shaw, D. Covert, T. F. Mentel, J. Schneider, L. Poulain, P. Reitz, C. Spindler, T. Clauss, A. Kiselev, E. Hallbauer, H. Wex, K. Mildenberger and F. Stratmann, *Atmospheric Chemistry and Physics*, **2010**, 10, 3601-3614.
65. S. Brunauer, P. H. Emmett and E. Teller, *Journal of the American Chemical Society*, **1938**, 60, 309-319.
66. P. J. DeMott, *Atmospheric Research*, **1995**, 38, 63-99.
67. G. Vali, *Atmos. Chem. Phys.*, **2014**, 14, 5271-5294.
68. S. L. Broadley, B. J. Murray, R. J. Herbert, J. D. Atkinson, S. Dobbie, T. L. Malkin, E. Condliffe and L. Neve, *Atmospheric Chemistry and Physics*, **2012**, 12, 287-307.
69. C. Marcolli, S. Gedamke, T. Peter and B. Zobrist, *Atmos. Chem. Phys.*, **2007**, 7, 5081-5091.
70. D. Niedermeier, R. A. Shaw, S. Hartmann, H. Wex, T. Clauss, J. Voigtländer and F. Stratmann, *Atmos. Chem. Phys.*, **2011**, 11, 8767-8775.
71. D. Niedermeier, B. Ervens, T. Clauss, J. Voigtländer, H. Wex, S. Hartmann and F. Stratmann, *Geophysical Research Letters*, **2014**, 41, 736-741.
72. S. L. Clegg, P. Brimblecombe and A. S. Wexler, *The Journal of Physical Chemistry A*, **1998**, 102, 2155-2171.
73. C. Braun and U. K. Krieger, *Opt. Express*, **2001**, 8, 314-321.
74. T. Koop, A. Kapilashrami, L. T. Molina and M. J. Molina, *Journal of Geophysical Research: Atmospheres*, **2000**, 105, 26393-26402.
75. I. N. Tang, H. R. Munkelwitz and J. G. Davis, *Journal of Aerosol Science*, **1977**, 8, 149-159.
76. M. D. Cohen, R. C. Flagan and J. H. Seinfeld, *The Journal of Physical Chemistry*, **1987**, 91, 4563-4574.
77. D. J. Cziczo, J. B. Nowak, J. H. Hu and J. P. D. Abbatt, *Journal of Geophysical Research: Atmospheres*, **1997**, 102, 18843-18850.
78. D. D. Weis and G. E. Ewing, *Journal of Geophysical Research: Atmospheres*, **1999**, 104, 21275-21285.

79. D. J. Cziczo and J. P. D. Abbatt, *The Journal of Physical Chemistry A*, **2000**, 104, 2038-2047.
80. T. Koop and B. Zobrist, *Physical Chemistry Chemical Physics*, **2009**, 11, 10839-10850.
81. I. N. Tang and H. R. Munkelwitz, *Atmospheric Environment. Part A. General Topics*, **1993**, 27, 467-473.
82. I. N. Tang, A. C. Tridico and K. H. Fung, *Journal of Geophysical Research: Atmospheres*, **1997**, 102, 23269-23275.
83. M. E. Wise, E. J. Freney, C. A. Tyree, J. O. Allen, S. T. Martin, L. M. Russell and P. R. Buseck, *Journal of Geophysical Research: Atmospheres*, **2009**, 114, n/a-n/a.
84. C.-T. Lee and W.-C. Hsu, *Journal of Aerosol Science*, **2000**, 31, 189-197.
85. Y. Ming and L. M. Russell, *Journal of Geophysical Research: Atmospheres*, **2001**, 106, 28259-28274.
86. A. P. Olsen, R. C. Flagan and J. A. Kornfield, *Review of Scientific Instruments*, **2006**, 77, 073901.
87. I. N. Tang and H. R. Munkelwitz, *Journal of Colloid and Interface Science*, **1984**, 98, 430-438.
88. Y. Gao, S. B. Chen and L. E. Yu, *Atmospheric Environment*, **2007**, 41, 2019-2023.
89. K. Hämeri, A. Laaksonen, M. Väkevä and T. Suni, *Journal of Geophysical Research: Atmospheres*, **2001**, 106, 20749-20757.
90. G. Biskos, A. Malinowski, L. M. Russell, P. R. Buseck and S. T. Martin, *Aerosol Science and Technology*, **2006**, 40, 97-106.
91. S. Oatis, D. Imre, R. McGraw and J. Xu, *Geophysical Research Letters*, **1998**, 25, 4469-4472.
92. D. Chakraborty and G. N. Patey, *Chemical Physics Letters*, **2013**, 587, 25-29.
93. D. Chakraborty and G. N. Patey, *The Journal of Physical Chemistry Letters*, **2013**, 4, 573-578.
94. D. Zahn, *Physical Review Letters*, **2004**, 92, 040801.
95. S. A. Hassan, *The Journal of Chemical Physics*, **2011**, 134, 114508.
96. N. E. R. Zimmermann, B. Vorselaars, D. Quigley and B. Peters, *Journal of the American Chemical Society*, **2015**, 137, 13352-13361.
97. C. B. Richardson and T. D. Snyder, *Langmuir*, **1994**, 10, 2462-2465.
98. R. D. Davis, S. Lance, J. A. Gordon, S. B. Ushijima and M. A. Tolbert, *Proceedings of the National Academy of Sciences*, **2015**.
99. R. D. Davis, S. Lance, J. A. Gordon and M. A. Tolbert, *Analytical Chemistry*, **2015**, 87, 6186-6194.
100. A. Zuend, C. Marcolli, T. Peter and J. H. Seinfeld, *Atmospheric Chemistry and Physics*, **2010**, 10, 7795-7820.
101. Y. You, L. Renbaum-Wolff, M. Carreras-Sospedra, S. J. Hanna, N. Hiranuma, S. Kamal, M. L. Smith, X. Zhang, R. J. Weber, J. E. Shilling, D. Dabdub, S. T. Martin and A. K. Bertram, *Proceedings of the National Academy of Sciences*, **2012**, 109, 13188-13193.
102. G. P. Schill and M. A. Tolbert, *Atmospheric Chemistry and Physics*, **2013**, 13, 4681-4695.
103. D. Gebauer, M. Kellermeier, J. D. Gale, L. Bergstrom and H. Colfen, *Chemical Society Reviews*, **2014**, 43, 2348-2371.
104. A. Peckhaus, S. Grass, L. Treuel and R. Zellner, *Journal of Physical Chemistry A*, **2012**, 116, 6199-6210.
105. L. Treuel, A. Sandmann and R. Zellner, *ChemPhysChem*, **2011**, 12, 1109-1117.
106. W. Paul and M. Raether, *Zeitschrift für Physik*, **1955**, 140, 262-273.
107. E. J. Davis and G. Schweiger, *The airborne microparticle : its physics, chemistry, optics, and transport phenomena*, Springer, Berlin, 2002.
108. D. Duft, Doctoral thesis, Technical University Illmenau, 2010.
109. N. Hoffmann, Doctoral thesis, University Heidelberg, 2015.
110. A. Smekal, *Naturwissenschaften*, **1923**, 11, 873-875.
111. C. V. Raman and K. S. Krishnan, *Nature*, **1928**, 121, 501-502.
112. G. Landsberg and L. Mandetstam, *Naturwissenschaften*, **1928**, 16, 557-558.

113. C. J. H. Schutte, *The Theory of Molecular Spectroscopy Volume1: The Quantum Mechanics and Group Theory of Vibrating and Rotating Molecules*, North-Holland Publishing Company, Amsterdam, 1976.
114. E. Bright Wilson, J. C. Decius and P. C. Cross, *Molecular Vibrations: The Theory of Infrared and Raman Vibrational Spectra*, Dover Publications, Inc., New York, 1955.
115. B. Schrader, *Infrared and Raman Spectroscopy: Methods and Applications*, Wiley-VCH, Weinheim, 1995.
116. E. Smith and G. Dent, *Modern Raman Spectroscopy: A Practical Approach*, John Wiley & Sons, Chichester, 2004.
117. S. Graß, Doctoral thesis, University Duisburg-Essen, 2015.
118. K. Ben Mabrouk, T. H. Kauffmann, H. Aroui and M. D. Fontana, *Journal of Raman Spectroscopy*, **2013**, 44, 1603-1608.
119. G. Mie, *Annalen der Physik*, **1908**, 330, 377-445.
120. C. F. Bohren and D. R. Huffman, *Absorption and Scattering of Light by Small Particles*, John Wiley & Sons, Inc., New York, 1983.
121. R. Symes, R. M. Sayer and J. P. Reid, *Physical Chemistry Chemical Physics*, **2004**, 6, 474-487.
122. S. S. Steimer, U. K. Krieger, Y. F. Te, D. M. Lienhard, A. J. Huisman, B. P. Luo, M. Ammann and T. Peter, *Atmos. Meas. Tech.*, **2015**, 8, 2397-2408.
123. A. Peckhaus, A. Kiselev, T. Hiron, M. Ebert and T. Leisner, *Atmos. Chem. Phys. Discuss.*, **2016**, 2016, 1-43.
124. I. Steinke, Doctoral thesis, Heidelberg University, 2013.
125. M. D. Cohen, R. C. Flagan and J. H. Seinfeld, *The Journal of Physical Chemistry*, **1987**, 91, 4583-4590.
126. D. Rzesanke, J. Nadolny, D. Duft, R. Muller, A. Kiselev and T. Leisner, *Physical Chemistry Chemical Physics*, **2012**, 14, 9359-9363.
127. D. M. Murphy and T. Koop, *Quarterly Journal of the Royal Meteorological Society*, **2005**, 131, 1539-1565.
128. C. Klein and A. R. Philpotts, *Earth materials : introduction to mineralogy and petrology*, Cambridge University Press, Cambridge [u.a.], 2013.
129. W. A. Deer, R. A. Howie and J. Zussman, *Rock Forming Minerals: Single Chain Silicates*, Geological Society of London, 2nd ed edn., 1978.
130. J. J. Freeman, A. Wang, K. E. Kuebler, B. L. Jolliff and L. A. Haskin, *The Canadian Mineralogist*, **2008**, 46, 1477-1500.
131. P. Makreski, G. Jovanovski and B. Kaitner, *Journal of Molecular Structure*, **2009**, 924–926, 413-419.
132. T. P. Mernagh, *Journal of Raman Spectroscopy*, **1991**, 22, 453-457.
133. T. P. Wright, M. D. Petters, J. D. Hader, T. Morton and A. L. Holder, *Journal of Geophysical Research: Atmospheres*, **2013**, 118, 10,535-510,543.
134. J. M. Campbell, F. C. Meldrum and H. K. Christenson, *The Journal of Physical Chemistry C*, **2015**, 119, 1164-1169.
135. G. Vali, *Atmos. Chem. Phys.*, **2008**, 8, 5017-5031.
136. T. P. Wright and M. D. Petters, *Journal of Geophysical Research: Atmospheres*, **2013**, 118, 3731-3743.
137. A. P. Fornea, S. D. Brooks, J. B. Dooley and A. Saha, *Journal of Geophysical Research: Atmospheres*, **2009**, 114, n/a-n/a.
138. B. J. Murray, S. L. Broadley, T. W. Wilson, J. D. Atkinson and R. H. Wills, *Atmospheric Chemistry and Physics*, **2011**, 11, 4191-4207.
139. K. Diehl, M. Debertshäuser, O. Eppers, H. Schmithüsen, S. K. Mitra and S. Borrmann, *Atmos. Chem. Phys.*, **2014**, 14, 12343-12355.
140. R. J. Herbert, B. J. Murray, T. F. Whale, S. J. Dobbie and J. D. Atkinson, *Atmos. Chem. Phys.*, **2014**, 14, 8501-8520.

141. A. Welti, F. Lüönd, Z. A. Kanji, O. Stetzer and U. Lohmann, *Atmos. Chem. Phys.*, **2012**, 12, 9893-9907.
142. S. A. Yankofsky, Z. Levin, T. Bertold and N. Sandlerman, *Journal of Applied Meteorology*, **1981**, 20, 1013-1019.
143. C. Budke and T. Koop, *Atmos. Meas. Tech.*, **2015**, 8, 689-703.
144. S. Augustin, H. Wex, D. Niedermeier, B. Pummer, H. Grothe, S. Hartmann, L. Tomsche, T. Clauss, J. Voigtländer, K. Ignatius and F. Stratmann, *Atmos. Chem. Phys.*, **2013**, 13, 10989-11003.
145. H. Wex, S. Augustin-Bauditz, Y. Boose, C. Budke, J. Curtius, K. Diehl, A. Dreyer, F. Frank, S. Hartmann, N. Hiranuma, E. Jantsch, Z. A. Kanji, A. Kiselev, T. Koop, O. Möhler, D. Niedermeier, B. Nillius, M. Rösch, D. Rose, C. Schmidt, I. Steinke and F. Stratmann, *Atmos. Chem. Phys.*, **2015**, 15, 1463-1485.
146. S. Hartmann, S. Augustin, T. Clauss, H. Wex, T. Šantl-Temkiv, J. Voigtländer, D. Niedermeier and F. Stratmann, *Atmos. Chem. Phys.*, **2013**, 13, 5751-5766.
147. N. Hiranuma, S. Augustin-Bauditz, H. Bingemer, C. Budke, J. Curtius, A. Danielczok, K. Diehl, K. Dreischmeier, M. Ebert, F. Frank, N. Hoffmann, K. Kandler, A. Kiselev, T. Koop, T. Leisner, O. Möhler, B. Nillius, A. Peckhaus, D. Rose, S. Weinbruch, H. Wex, Y. Boose, P. J. DeMott, J. D. Hader, T. C. J. Hill, Z. A. Kanji, G. Kulkarni, E. J. T. Levin, C. S. McCluskey, M. Murakami, B. J. Murray, D. Niedermeier, M. D. Petters, D. O'Sullivan, A. Saito, G. P. Schill, T. Tajiri, M. A. Tolbert, A. Welti, T. F. Whale, T. P. Wright and K. Yamashita, *Atmos. Chem. Phys.*, **2015**, 15, 2489-2518.
148. S. Hartmann, H. Wex, T. Clauss, S. Augustin-Bauditz, D. Niedermeier, M. Rösch and F. Stratmann, *Journal of the Atmospheric Sciences*, **2016**, 73, 263-278.
149. D. Niedermeier, S. Hartmann, T. Clauss, H. Wex, A. Kiselev, R. C. Sullivan, P. J. DeMott, M. D. Petters, P. Reitz, J. Schneider, E. Mikhailov, B. Sierau, O. Stetzer, B. Reimann, U. Bundke, R. A. Shaw, A. Buchholz, T. F. Mentel and F. Stratmann, *Atmos. Chem. Phys.*, **2011**, 11, 11131-11144.
150. D. O'Sullivan, B. J. Murray, T. L. Malkin, T. F. Whale, N. S. Umo, J. D. Atkinson, H. C. Price, K. J. Baustian, J. Browse and M. E. Webb, *Atmos. Chem. Phys.*, **2014**, 14, 1853-1867.
151. C. Zhu, *Geochimica et Cosmochimica Acta*, **2005**, 69, 1435-1453.
152. C. Zhu and P. Lu, *Geochimica et Cosmochimica Acta*, **2009**, 73, 3171-3200.
153. I. Parsons, *Feldspars and their reactions : [proceedings of the NATO Advanced Study Institute on Feldspars and Their Reactions, Edinburgh, United Kingdom, June 29 - July 10, 1993]*, Kluwer, 1994.
154. S. Pouleur, C. Richard, J.-G. Martin and H. Antoun, *Applied and Environmental Microbiology*, **1992**, 58, 2960-2964.
155. B. G. Pummer, H. Bauer, J. Bernardi, S. Bleicher and H. Grothe, *Atmos. Chem. Phys.*, **2012**, 12, 2541-2550.
156. D. O'Sullivan, B. J. Murray, J. F. Ross, T. F. Whale, H. C. Price, J. D. Atkinson, N. S. Umo and M. E. Webb, *Scientific Reports*, **2015**, 5, 8082.
157. B. G. Pummer, C. Budke, S. Augustin-Bauditz, D. Niedermeier, L. Felgitsch, C. J. Kampf, R. G. Huber, K. R. Liedl, T. Loerting, T. Moschen, M. Schauperl, M. Tollinger, C. E. Morris, H. Wex, H. Grothe, U. Pöschl, T. Koop and J. Fröhlich-Nowoisky, *Atmos. Chem. Phys.*, **2015**, 15, 4077-4091.
158. M. Schnaiter, M. Gimmler, I. Llamas, C. Linke, C. Jäger and H. Mutschke, *Atmos. Chem. Phys.*, **2006**, 6, 2981-2990.
159. J. D. Hader, T. P. Wright and M. D. Petters, *Atmos. Chem. Phys.*, **2014**, 14, 5433-5449.
160. M. Niemand, O. Möhler, B. Vogel, H. Vogel, C. Hoose, P. Connolly, H. Klein, H. Bingemer, P. DeMott, J. Skrotzki and T. Leisner, *Journal of the Atmospheric Sciences*, **2012**, 69, 3077-3092.
161. M. D. Petters and T. P. Wright, *Geophysical Research Letters*, **2015**, 42, 8758-8766.
162. L. Ickes, A. Welti and U. Lohmann, *Atmos. Chem. Phys. Discuss.*, **2016**, 2016, 1-38.
163. D. M. Carey and G. M. Korenowski, *Journal of Chemical Physics*, **1998**, 108, 2669-2675.

164. A. Sokołowska and Z. Kęcki, *Journal of Raman Spectroscopy*, **1986**, 17, 29-33.
165. Q. Sun, *Vibrational Spectroscopy*, **2009**, 51, 213-217.
166. B. Minceva-Sukarova, W. F. Sherman and G. R. Wilkinson, *Journal of Physics C: Solid State Physics*, **1984**, 17, 5833.
167. E. Whalley, *Canadian Journal of Chemistry*, **1977**, 55, 3429-3441.
168. S. Krishnamurthy, R. Bansil and J. Wiafe-Akenten, *The Journal of Chemical Physics*, **1983**, 79, 5863-5870.
169. M. Paolantoni, P. Sassi, A. Morresi and S. Santini, *The Journal of Chemical Physics*, **2007**, 127, 024504.
170. G. E. Walrafen, M. R. Fisher, M. S. Hokmabadi and W. H. Yang, *The Journal of Chemical Physics*, **1986**, 85, 6970-6982.
171. J. Dubessy, D. Audeoud, R. Wilkins and C. Kosztolanyi, *Chemical Geology*, **1982**, 37, 137-150.
172. R. J. Bakker, *The Canadian Mineralogist*, **2004**, 42, 1283-1314.
173. M. Baumgartner and R. J. Bakker, *Chemical Geology*, **2010**, 275, 58-66.
174. J. Schiffer, Doctoral thesis, Princeton University, 1964.
175. M. Falk and O. Knop, in *Water in Crystalline Hydrates Aqueous Solutions of Simple Nonelectrolytes*, ed. F. Franks, Springer US, 1973, vol. 2, ch. 2, pp. 55-113.
176. B. Klewe and B. Pedersen, *Acta Crystallographica Section B*, **1974**, 30, 2363-2371.
177. W. Möller and R. Kaiser, in *Zeitschrift für Naturforschung A*, 1970, vol. 25, p. 1024.
178. E. Burstein, F. A. Johnson and R. Loudon, *Physical Review*, **1965**, 139, A1239-A1245.
179. I. Đuričković, M. Marchetti, R. Claverie, P. Bourson, J.-M. Chassot and M. D. Fontana, *Applied Spectroscopy*, **2010**, 64, 853-857.
180. G. E. Walrafen, *Journal of Chemical Physics*, **1962**, 36, 1035-1042.
181. P. Terpstra, D. Combes and A. Zwick, *The Journal of Chemical Physics*, **1990**, 92, 65-70.
182. R. Bakker, *Central European Journal of Geosciences*, **2012**, 4, 238-245.
183. C. A. Kurtz and C. B. Richardson, *Chemical Physics Letters*, **1984**, 109, 190-194.
184. J. Colvin and J. Hume, *Transactions of the Faraday Society*, **1938**, 34, 969-976.
185. S. K. Mitra, J. Brinkmann and H. R. Pruppacher, *Journal of Aerosol Science*, **1992**, 23, 245-256.
186. M. Wise, G. Biskos, S. Martin, L. Russell and P. Buseck, *Aerosol Science and Technology*, **2005**, 39, 849-856.
187. M. E. Wise, T. A. Semeniuk, R. Bruintjes, S. T. Martin, L. M. Russell and P. R. Buseck, *Journal of Geophysical Research: Atmospheres*, **2007**, 112, n/a-n/a.
188. E. Anim-Danso, Y. Zhang and A. Dhinojwala, *Journal of the American Chemical Society*, **2013**, 135, 8496-8499.
189. Y. Zhang, E. Anim-Danso and A. Dhinojwala, *Journal of the American Chemical Society*, **2014**, 136, 14811-14820.
190. D. Duft and T. Leisner, *Atmos. Chem. Phys.*, **2004**, 4, 1997-2000.
191. C.-Y. Tan and Y.-X. Huang, *Journal of Chemical & Engineering Data*, **2015**, 60, 2827-2833.
192. E. J. Davis and R. Periasamy, *Langmuir*, **1985**, 1, 373-379.
193. J. F. Davies, A. E. Haddrell and J. P. Reid, *Aerosol Science and Technology*, **2012**, 46, 666-677.
194. M. T. Parsons, J. L. Riffell and A. K. Bertram, *The Journal of Physical Chemistry A*, **2006**, 110, 8108-8115.
195. A. Pant, M. T. Parsons and A. K. Bertram, *The Journal of Physical Chemistry A*, **2006**, 110, 8701-8709.
196. M. J. Atkinson and C. Bingman, *J. Aquari. & Aqua. Sci.*, **1997**, VIII, 39-43.
197. A. P. Ault, D. Zhao, C. J. Ebben, M. J. Tauber, F. M. Geiger, K. A. Prather and V. H. Grassian, *Physical Chemistry Chemical Physics*, **2013**, 15, 6206-6214.
198. A. Laskin, R. C. Moffet, M. K. Gilles, J. D. Fast, R. A. Zaveri, B. Wang, P. Nigge and J. Shutthanandan, *Journal of Geophysical Research: Atmospheres*, **2012**, 117, n/a-n/a.
199. A. P. Ault, R. C. Moffet, J. Baltrusaitis, D. B. Collins, M. J. Ruppel, L. A. Cuadra-Rodriguez, D. Zhao, T. L. Guasco, C. J. Ebben, F. M. Geiger, T. H. Bertram, K. A. Prather and V. H. Grassian, *Environmental Science and Technology*, **2013**, 47, 5603-5612.

200. J. W. Chi, W. J. Li, D. Z. Zhang, J. C. Zhang, Y. T. Lin, X. J. Shen, J. Y. Sun, J. M. Chen, X. Y. Zhang, Y. M. Zhang and W. X. Wang, *Atmos. Chem. Phys.*, **2015**, 15, 11341-11353.
201. H.-S. Xiao, J.-L. Dong, L.-Y. Wang, L.-J. Zhao, F. Wang and Y.-H. Zhang, *Environmental Science & Technology*, **2008**, 42, 8698-8702.
202. N. Prieto-Taboada, O. Gómez-Laserna, I. Martínez-Arkarazo, M. Á. Olazabal and J. M. Madariaga, *Analytical Chemistry*, **2014**, 86, 10131-10137.
203. R. G. Bryant, B. W. Sellwood, A. C. Millington and N. A. Drake, *Sedimentary Geology*, **1994**, 90, 269-291.
204. B. Lafuente, R. T. Downs, H. Yang and S. N., in *Highlights in Mineralogical Crystallography*, eds. T. Armbruster and R. M. Danisi, W. De Gruyter, Berlin, 2015, pp. pp 1-30.
205. E. O. Schlemper, P. K. Sen Gupta and T. Zoltai, *American Mineralogist*, **1985**, 70, 1309-1313.
206. J. Podder, S. Gao, R. W. Evitts, R. W. Besant and D. Matthews, *International Journal of Materials Research*, **2013**, 105, 308-313.
207. A. A. C. Bode, P. G. M. Pulles, M. Lutz, W. J. M. Poulisse, S. Jiang, J. A. M. Meijer, W. J. P. van Enckevort and E. Vlieg, *Crystal Growth & Design*, **2015**, 15, 3166-3174.
208. S. M. Roberts, R. J. Spencer, W. Yang and H. R. Krouse, *Journal of Paleolimnology*, **1997**, 17, 101-130.
209. D. Gupta, H. J. Eom, H. R. Cho and C. U. Ro, *Atmos. Chem. Phys.*, **2015**, 15, 11273-11290.
210. U. K. Krieger, C. Braun, L. Imbach, T. Koop, T. Corti and G. Videen, *Journal of Quantitative Spectroscopy and Radiative Transfer*, **2003**, 79–80, 873-880.
211. H.-J. Tong, Z.-G. Qian, J. Reid and Y.-H. Zhang, *Acta Physico-Chimica Sinica*, **2011**, 27, 2521-2527.
212. R. J. Cheng, D. C. Blanchard and R. J. Cipriano, *Atmospheric Research*, **1988**, 22, 15-25.
213. F. Baumgärtner, A. Zanier and K. Krebs, *Journal of Aerosol Science*, **1989**, 20, 883-886.
214. Z. Qian, F. Wang, Y. Zheng, J. Yu and Y. Zhang, *Chinese Science Bulletin*, **2012**, 57, 591-594.
215. L. A. Hardie, *Annual Review of Earth and Planetary Sciences*, **1991**, 19, 131-168.
216. C. E. Harvie and J. H. Weare, *Geochimica et Cosmochimica Acta*, **1980**, 44, 981-997.
217. C. E. Harvie, N. Møller and J. H. Weare, *Geochimica et Cosmochimica Acta*, **1984**, 48, 723-751.
218. D. Freyer and W. Voigt, *Monatshefte für Chemie / Chemical Monthly*, 134, 693-719.
219. C. Richardson, *J. Glaciol.*, **1976**, 17, 507-519.
220. S. Ben Ahmed, M. M. Tlili, M. Amami and M. Ben Amor, *Industrial & Engineering Chemistry Research*, **2014**, 53, 9554-9560.
221. R. Wagner, O. Möhler, H. Saathoff, M. Schnaiter and T. Leisner, *Atmospheric Chemistry and Physics*, **2011**, 11, 2083-2110.
222. D. M. Lienhard, A. J. Huisman, D. L. Bones, Y.-F. Te, B. P. Luo, U. K. Krieger and J. P. Reid, *Physical Chemistry Chemical Physics*, **2014**, 16, 16677-16683.
223. A. Zuend, C. Marcolli, B. P. Luo and T. Peter, *Atmos. Chem. Phys.*, **2008**, 8, 4559-4593.
224. I. N. Tang and H. R. Munkelwitz, *Journal of Geophysical Research: Atmospheres*, **1994**, 99, 18801-18808.
225. A. A. Zardini, U. K. Krieger and C. Marcolli, *Opt. Express*, **2006**, 14, 6951-6962.
226. M. Song, C. Marcolli, U. K. Krieger, D. M. Lienhard and T. Peter, *Faraday Discussions*, **2013**, 165, 289-316.
227. D. J. Stewart, C. Cai, J. Nayler, T. C. Preston, J. P. Reid, U. K. Krieger, C. Marcolli and Y. H. Zhang, *The Journal of Physical Chemistry A*, **2015**, 119, 4177-4190.
228. M. C. Yeung and C. K. Chan, *Aerosol Science and Technology*, **2010**, 44, 269-280.
229. M. C. Yeung, A. K. Y. Lee and C. K. Chan, *Aerosol Science and Technology*, **2009**, 43, 387-399.
230. C. C. Pye and W. W. Rudolph, *The Journal of Physical Chemistry A*, **2001**, 105, 905-912.
231. D. R. Secker, P. H. Kaye, R. S. Greenaway, E. Hirst, D. L. Bartley and G. Videen, *Appl. Opt.*, **2000**, 39, 5023-5030.
232. G. Videen, W. Sun, Q. Fu, D. R. Secker, R. S. Greenaway, P. H. Kaye, E. Hirst and D. Bartley, *Appl. Opt.*, **2000**, 39, 5031-5039.

233. J. Buajarern, L. Mitchem and J. P. Reid, *The Journal of Physical Chemistry A*, **2007**, 111, 9054-9061.
234. A. D. Harrison, T. F. Whale, M. A. Carpenter, M. A. Holden, L. Neve, D. O'Sullivan, J. Vergara Temprado and B. J. Murray, *Atmos. Chem. Phys. Discuss.*, **2016**, 2016, 1-26.
235. C. Bourges-Monnier and M. E. R. Shanahan, *Langmuir*, **1995**, 11, 2820-2829.

11. Acknowledgements

First of all, I would like to thank Prof. Dr. Thomas Leisner for the opportunity to prepare my doctoral thesis at the Institute of Meteorology and Climate Research - Atmospheric Aerosol Research (IMK-AAF) at the Karlsruhe Institute of Technology (KIT). Prof. Dr. Thomas Leisner is also acknowledged for his role as first referee. I would like to thank Prof. Dr. Hans-Robert Volpp, who agreed to act as the second referee of the doctoral thesis.

A great praise is expressed to Dr. Alexei Kiselev for his constant readiness for scientific discussions, for the performance of SEM/EDX measurements and for the proofreading of the doctoral thesis.

Special thanks go to Dr. Denis Duft who supported me in the analysis of the time-dependent behavior of homogeneous nucleation. Dr. Denis Duft and Mr. Jens Nadolny are acknowledged for their programming of Labview to control the technical equipment and to analyze the measurement data. At this point, I would particularly give thanks to my colleagues Dr. Thomas Pander and Dr. Nadine Hofmann, who worked with me in the Paul trap laboratory at the same time and advised me in practical issues. Last but not least, I thank all colleagues and technical members of the IMK-AAF for the pleasant working atmosphere and their intellectual and practical support during my research time.

The Graduate School for Climate and Environment (GRACE) at the KIT is thanked for the financial support of summer schools and the research stay at the ETH Zurich.